UNIVERSITY OF OKLAHOMA

GRADUATE COLLEGE

TIME-DEPENDENT QUANTUM REACTIVE SCATTERING IN HYPERSPHERICAL COORDINATES

A DISSERTATION

SUBMITTED TO THE GRADUATE FACULTY

in partial fulfillment of the requirements for the

Degree of

DOCTOR OF PHILOSOPHY

By

JEFFREY JAMES CRAWFORD
Norman, Oklahoma
2013

TIME-DEPENDENT QUANTUM REACTIVE SCATTERING IN HYPERSPHERICAL COORDINATES

A DISSERTATION APPROVED FOR THE
HOMER L. DODGE DEPARTMENT OF PHYSICS AND ASTRONOMY

BY

Dr. Gregory A. Parker, Chair

Dr. Kerry V. Magruder

Dr. Eric R. I. Abraham

Dr. James P. Shaffer

Dr. Deborah Watson

Acknowledgements

I would like to thank my Ph.D. advisor Dr. Gregory Parker. He has been an exceptional mentor, providing me with everything I could need to be successful. His everlasting patience, constant encouragement, and wealth of knowledge provided relief when the difficulties of research brought frustration and slow progress. He has prepared me to take on any challenges that are set before me. I will always fondly remember the hours spent in helpful chalkboard debate, trying to reconcile hyperspherical time-independent and time-dependent theories.

I would also like to thank Dr. James Shaffer for introducing me to proper research in physics. The knowledge and skills acquired while working for him have been invaluable in my graduate education and will continue to assist me in my new job.

I would like to thank my advising committee members, Dr. Eric Abraham, Dr. Kerry Magruder, Dr. James Shaffer, and Dr. Deborah Watson. They have provided me with plenty of helpful advice and direction, consistently making themselves available for whatever I needed. Many thanks also go to Dr. Neil Shafer-Ray. He served on my committee for the majority of my tenure at OU, providing constant support and motivation through his kind words and enthusiasm for physics. Also, I would like to thank Dr. Michael Morrison for assisting me in every aspect of my education. His instruction, advice, and friendship have been invaluable.

I owe a large debt of gratitude to my fellow research group members. Dan Brue and Xuan Li were instrumental in my development as a theorist, always offering their advice and experience. I am grateful to Zac Eldredge and Joe Hart for their efforts in testing and improving my software.

Thank you, Mr. Zac Crawford. Your random thoughts and smiling face have always provided respite and refreshment when I was exhausted, especially when preparing this manuscript. I would like to thank my parents, Mark and Catheen Bilbrey, and my grandparents, James and Patricia Isbell, for their constant encouragement and love.

Most importantly, my thanks and love go to my wife Mindy. I am grateful to her for her love, encouragement, and inspiration. I could not have done any of this without her. She has patiently tolerated my graduate education, knowing it would pay dividends in the end. It is to her that I dedicate this work.

Contents

List of Figures

List of Tables

Abstract

We present a time-dependent hyperspherical, wave packet method for calculating three atom state-to-state S-matrix elements. The wave packet is propagated in time using adiabatically adjusting, principal axes hyperspherical (APH) coordinates that treat all arrangement channels equivalently, allowing the simultaneous analysis of the products in all three arrangement channels. We take advantage of the symmetry of the potential energy surface and decompose the initial wave packet into its component irreducible representations, propagating each component separately. Each packet is analyzed by projecting it onto the hyperspherical basis at a fixed, asymptotic hyperradius, and irreducible representation dependent S-matrix elements are obtained by matching the hyperspherical projections to symmetry-adapted Jacobi coordinate boundary conditions. We obtain arrangement channel-dependent S-matrix elements as linear combinations of the irreducible representation dependent elements. We derive and implement a new three-dimensional Sylvester-like algorithm that reduces the number of multiplications required to apply the Hamiltonian to the wave packet, dramatically increasing the computational efficiency. A convergence study is presented to show the behavior of the results as the initial parameters are varied and to determine the values of those parameters that give accurate results. State-to-state $\mathrm{H} + \mathrm{H}_2$ and $\mathrm{F} + \mathrm{H}_2$ results for zero total angular momentum are presented and show excellent agreement with time-independent bechmark results.

CHAPTER 1

INTRODUCTION

We are interested in three-body reactions of the form

$$\mathrm{A+BC} \rightleftharpoons \begin{cases} \mathrm{A+BC} & \text{(a)} \\ \mathrm{AB+C} & \text{(b)} \\ \mathrm{AC+B} & \text{(c)} \\ A+B+C & \text{(d).} \end{cases} \tag{1.1}$$

The products in Eq. (1.1a) correspond to non-reactive collisions, where the diatom can be in the same or different rovibrational state as the reactants. The products in Eqs. (1.1b) and (1.1c) correspond to reactive (or rearrangement) collisions, where the diatomic molecule dissociates and one of its constituents binds with the free atom. The products in Eq. (1.1d) correspond to collision-induced dissociation (CID) reactions, where the three atoms separate after the collision. The time-reversed reaction of CID corresponds to three-body recombination, which is very important in cold and ultracold physics.

The quantum mechanical treatment of three-body scattering processes is key to understanding chemical reaction dynamics and inter-particle interactions, and has attracted recent attention in the field of cold and ultracold atomic gases [3]. Non-reactive collisions are important for understanding the dynamics of ultracold atom-molecule systems at the mean field level, and in these systems reactive collisions affect the lifetime of Feshbach molecules [4, 5, 6]. An understanding of three-body recombination collisions provides information on the lifetimes and stability of ultracold gas samples, especially in Bose-Einstein condensates [7, 8].

Initial progress in full-dimensional triatomic quantum reactive scattering was dominated by time-independent (TI) methods that calculate the entire S-matrix at a given energy [9, 10, 11, 12, 13, 1], and has resulted in the development of accurate and efficient hyperspherical, coupled channel TI methods [1, 14, 15, 16] that are ideal for low energy scattering in systems with a small number of basis functions. TI methods require multiplication of two matrices of dimension $N_B \times N_B$, where N_B is the number of basis functions, for each propagation step and for each energy. The number of floating-point operations required is proportional to $N_E N_P N_B^3$, where N_E is the number of energies and N_P is the number of propagation steps (dimension of the propagation coordinate grid). This scaling makes TI methods inefficient at high energies, where a large number of channels are open, and for systems with deep wells, such as $H + O_2$ or $Cs + Cs_2$ that support a large number of available bound states.

Time-dependent wave packet (TDWP) methods [17, 18, 19, 20, 21, 22, 23, 24, 25] provide an intuitive picture of the scattering dynamics. While TDWP methods only calculate one column of the S-matrix at a time, corresponding to a single initial state, they do so for a range of energies defined by the initial wave packet. As a result, a single propagation in time produces scattering information over a range of energies, making it easier to locate scattering resonances than with TI methods. TDWP methods require the multiplication of a matrix and a vector of dimension $N_P N_B$ for each initial state. The number of floating-point operations required is proportional to $N_t \left(N_P N_B\right)^2$, where N_t is the number of time propagation steps. The ratio of the TI to TDWP scalings is $N_E N_B / N_t N_P N_i$. Typically, we are only interested in a single initial state,

$N_i = 1$, and $N_E \approx N_t$, giving a ratio of N_B/N_P. Therefore, when the number of basis functions required is larger than the dimension of the scattering coordinate grid, the TDWP method scales better than the TI method.

The majority of TDWP methods are Jacobi coordinate-based [17, 18, 19, 20, 21, 22]. A major advantage of Jacobi methods is that the coordinate grids are evenly spaced and the computational time scales as $N \ln N$, where N is the number of grid points. Note that our hyperspherical grid is also evenly spaced and may have the same scaling as the Jacobi methods. However, we have not proved that relationship. A better approach for a hyperspherical method may be a non-uniform grid which drastically decreases the number of grid points.

Jacobi TDWP methods possess two primary drawbacks: First, different coordinate sets are needed for each arrangement channel, and separate propagations are required for each unique set of reaction products. Second, Jacobi coordinates are not optimal for treating products with three free atoms, referred to as collision-induced dissociation (CID), or its time reversal, three-body recombination, due to the double continuum [26, 27, 28]. Although Jacobi-coordinate based methods to overcome the first drawback have been developed by Althorpe [18] and Sun, et al. [22], hyperspherical coordinate methods offer a favorable alternative.

By propagating the wave packet using a hyperspherical coordinate set that treats all arrangement channels equally, scattering information can be obtained in all arrangement channels with a single propagation. Also, the double continuum is reduced to a single continuum, providing a proper treatment of products consisting of three free atoms (CID). As a result, hyperspherical methods can overcome both of the previously discussed drawbacks associated with Jacobi methods. The propagating hyperspherical wave packet can be matched to a set of mixed-boundary conditions at a constant value of the hyperradius, [29] with Jacobi basis functions for the atom-diatom products and hyperspherical basis functions for CID products.

Here, we will use the adiabatically adjusting, principal axes hyperspherical (APH) coordinate system [1]. For systems containing two or more identical atoms, the symmetry of the potential energy surface (PES) can be exploited, and the wave packet can be decomposed into its component irreducible representations. This offers an increase in computational efficiency, since each irreducible representation wave packet can be propagated using a fraction of the total coordinate space.

Other hyperspherical TDWP methods [23, 24, 25] have been presented. These methods use Johnson's hyperspherical coordinates and a different asymptotic matching method. Furthermore, they do not take advantage of the symmetry of the potential energy surface. Results from these methods [25] are not as accurate as those presented here, especially at higher energies. This is most likely due to their use of a different method to match onto asymptotic states.

In this thesis, we introduce a hyperspherical, time-dependent wave packet method for calculating state-to-state S-matrix elements for scattering processes of the form in Eq. (1.1). Similar to other time-dependent approaches, our method involves three primary steps [30]: (i) definition of an initial wave packet, (ii) propagation of the wave packet in time, (iii) analysis of the wave packet. An initial wave packet is obtained that appropriately describes the reactants. Prior to propagation, the wave packet is mapped onto APH coordinates and decomposed into its component irreducible representations. Each irreducible representation of the wave packet is propagated in time using the APH Hamiltonian, which treats all three arrangement channels equivalently. The wave packet is analyzed in the asymptotic region of the PES to extract irreducible representation dependent S-matrix elements. After each irreducible representation has been analyzed, the arrangement channel dependent S-matrix elements are calculated as linear combinations of the irreducible representation S-matrix elements.

This thesis is organized as follows: In Chapter 2, we begin by discussing the Jacobi and APH coordinate systems, reviewing their derivations and their basis set expansions. We then discuss a time-dependent method for obtaining state-to-state probabilities where APH coordinates are used to propagate the wave packet in time and Jacobi coordinates are used to represent the reactants and products. In Chapter 5, state-to-state probabilities for the $\mathrm{H}+\mathrm{H}_2$ and $\mathrm{F}+\mathrm{H}_2$ reaction with zero total angular momentum are presented and compared to previous time-independent results. In Chapter 6, we present our conclusions.

CHAPTER 2

THEORY

2.1 Introduction

In this chapter, we present a hyperspherical-TDWP (h-TDWP) method for obtaining state-to-state S-matrix elements. The method propagates the wave packet in hyperspherical (APH) coordinates, treating all arrangement channels equivalently. As the APH wave packet evolves, scattering information can be obtained in all arrangement channels. Moreover, the three-atom PES is symmetric with respect to a single APH coordinate, and symmetry adapted wave functions can be readily obtained. Noting that APH coordinates cover configuration space twice, the PES for systems of three identical atoms, two identical atoms, or no identical atoms, belongs to the C_{6v}, C_{2v}, or C_2 point groups, respectively. The wave packet can be decomposed into components labeled by the irreducible representations of its parent point group, and can be represented on a reduced coordinate grid, providing and efficient means to propagate and analyze the wave packet.

Initially ignoring symmetry, the basic steps of the h-TDWP method are as follows: (1) An initial wave packet is constructed and transformed to APH coordinates. (2) The wave packet is propagated in time according to the APH Hamiltonian, and, after each time step, the scattered wave packet is projected onto the APH basis at a constant asymptotic hyperradius. (3) The time-dependent APH projections are converted to energy-dependent projections via a Fourier transform. (4) The S-matrix elements are obtained by matching the energy-dependent APH projections to a set of appropriate boundary conditions.

To include symmetry, the APH wave packet in step (1) is split into its component irreducible representations via projection operators [31]. Then, steps (2)–(4) are carried out for each irreducible representation component of the initial wave packet, giving S-matrix elements labeled by irreducible representation rather than arrangement channel. Note that the boundary conditions in step (4) are rewritten as irreducible representation dependent linear combinations of the arrangement channel dependent conditions. After obtaining the S-matrix elements for all irreducible representations present in the initial wave packet, the arrangement channel dependent S-matrix elements are obtained by a simple transformation.

In Sec. 2.2, we briefly review mass-scaled Jacobi and APH coordinates and their basis functions. We also include a brief discussion of the symmetry of the potential energy surface in APH coordinates. We provide the details of the wave packet propagation in APH coordinates in Sec. 2.3 and define the initial wave packet in Sec. 2.4. The extraction of the state-to-state S matrix elements is presented in Sec. 2.5.

2.2 Coordinates and Basis Functions

Although detailed descriptions of the Jacobi and APH coordinate systems and their basis functions have been presented previously [1], a brief summary is presented here in order to provide consistent notation and to illustrate the complementary relationship between them.

2.2.1 Jacobi Coordinates

Consider a system of three atoms A, B, and C, with masses m_A, m_B and m_C and positions X_A, X_B, and X_C with respect to a space-fixed axis. After separating the center-of-mass motion, the Jacobi coordinates are given by

$$\mathbf{r}_\tau = \mathbf{X}_{\tau+2} - \mathbf{X}_{\tau+1}, \tag{2.1a}$$

$$\mathbf{R}_\tau = \mathbf{X}_\tau - \frac{m_{\tau+1}\mathbf{X}_{\tau+1} + m_{\tau+2}\mathbf{X}_{\tau+2}}{m_{\tau+1} + m_{\tau+2}}, \tag{2.1b}$$

where τ, $\tau+1$, and $\tau+2$ are any cyclic permutation of A, B, and C for a given τ. Each pair of Jacobi coordinates describes a unique arrangement channel of the system, labeled A, B, or C. For arrangement A, $\mathbf{r}_A$ is the vector pointing from B to C and $\mathbf{R}_A$ is the vector pointing from the center-of-mass of B and C towards A.

The mass-scaled Jacobi coordinates are given by

$$\mathbf{s}_\tau = d_\tau^{-1}\mathbf{r}_\tau, \tag{2.2a}$$

$$\mathbf{S}_\tau = d_\tau\mathbf{R}_\tau, \tag{2.2b}$$

where the scaling factor d_τ and the three-body reduced mass μ are given by

$$d_\tau = \left[\frac{m_\tau}{\mu}(1 - \frac{m_\tau}{M})\right]^{1/2}, \tag{2.3}$$

$$\mu = \left(\frac{m_A\, m_B\, m_C}{M}\right)^{1/2}, \tag{2.4}$$

and $M = m_A + m_B + m_C$ is the total mass of all three particles.

An advantage of mass-scaled Jacobi coordinates is that transformations between the different sets are kinematic rotations,

$$\begin{pmatrix} \mathbf{S}_{\tau+1} \\ \mathbf{s}_{\tau+1} \end{pmatrix} = \mathbf{T}(\chi_{\tau+1,\tau})\begin{pmatrix} \mathbf{S}_\tau \\ \mathbf{s}_\tau \end{pmatrix} \tag{2.5}$$

where the transformation matrix $\mathbf{T}$ is

$$\mathbf{T}(\chi_{\tau+1,\tau}) = \begin{pmatrix} \cos\chi_{\tau+1,\tau} & \sin\chi_{\tau+1,\tau} \\ -\sin\chi_{\tau+1,\tau} & \cos\chi_{\tau+1,\tau} \end{pmatrix} \otimes \mathbf{I} \tag{2.6}$$

where $\mathbf{I}$ is a 3×3 identity matrix. The kinematic angles $\chi_{\tau+1,\tau}$ are negative, obtuse angles given by

$$\cos\chi_{\tau+1,\tau} = -\frac{\mu}{d_\tau d_{\tau+1} m_{\tau+2}} \tag{2.7a}$$

and

$$\sin\chi_{\tau+1,\tau} = -\frac{1}{d_\tau d_{\tau+1}}, \tag{2.7b}$$

with $\chi_{\tau,\tau} = 0$ and $\chi_{\tau,\tau+1} = -\chi_{\tau+1,\tau}$. Since the mass-scaled Jacobi coordinates will be used exclusively, they will be referred to simply as Jacobi coordinates.

The positions of the three atoms can be described with respect to either a space-fixed (SF) or a body-fixed (BF) set of axes. The six Jacobi SF coordinates consist of the magnitude and two orientation angles of each Jacobi vector: (s_τ, θ_{s_τ}, ϕ_{s_τ}, S_τ, θ_{S_τ}, ϕ_{S_τ}). The BF coordinates consist of the magnitudes of each Jacobi vector, a relative angle between the Jacobi vectors, and three Euler angles: (s_τ, S_τ, Θ_τ, α_τ, β_τ, γ_τ). The relative angle Θ_τ is given by

$$\cos\Theta_\tau = \frac{\mathbf{s}_\tau \cdot \mathbf{S}_\tau}{s_\tau S_\tau}, \tag{2.8}$$

with $0 \leq \Theta_\tau \leq \pi$. The Euler angles describe the orientation of the BF axes of arrangement channel τ with respect to the SF axes.

The set of Jacobi BF axes corresponding to arrangement channel τ will be referred to as the BF$_\tau$ system. The BF$_\tau$ systems share a common y axis that is perpendicular to the triatomic plane, and the z axis for each system points along its respective $\mathbf{S}_\tau$ vector. Transformations between the three sets of BF axes consist of rotations about this common y axis.

The Jacobi kinetic energy operator is given by

$$T = -\frac{\hbar^2}{2\mu}\left(\frac{1}{S_\tau}\frac{\partial^2}{\partial S_\tau^2}S_\tau + \frac{1}{s_\tau}\frac{\partial^2}{\partial s_\tau^2}s_\tau\right) + \frac{\boldsymbol{\mathcal{L}}_\tau^2}{2\mu S_\tau^2} + \frac{\boldsymbol{\mathcal{J}}_\tau^2}{2\mu s_\tau^2}, \tag{2.9}$$

where $\boldsymbol{\mathcal{L}}_\tau$ is the orbital angular momentum operator of the atom τ about the center-of-mass of the other two atoms, and $\boldsymbol{\mathcal{J}}_\tau$ is the rotational angular momentum operator of the $\tau+1$ and $\tau+2$ atoms. The total angular momentum operator of the system is given by $\mathbf{J} = \boldsymbol{\mathcal{L}}_\tau + \boldsymbol{\mathcal{J}}_\tau$.

2.2.2 APH Coordinates

Consider the kinematic rotation

$$\begin{pmatrix} \mathbf{Q} \\ \mathbf{q} \end{pmatrix} = \mathbf{T}(\chi_\tau)\begin{pmatrix} \mathbf{S}_\tau \\ \mathbf{s}_\tau \end{pmatrix}, \tag{2.10}$$

where χ_τ is a continuous variable with the range $0 \leq \chi_\tau \leq 2\pi$. We choose the angle's origin to be along the A arrangement channel, denoted as the initial or reactant channel:

$$\chi_\tau = \chi_i - \chi_{\tau i}, \tag{2.11}$$

where the $\chi_{\tau i}$ are the Jacobi kinematic angles of Eq. (2.7).

The kinematic angle χ_τ is chosen to maximize the magnitude of $\mathbf{Q}$ so that the vector $\mathbf{Q}$ will approach the vector $\mathbf{S}_\xi$ of any atom ξ that leaves the other two. Q is maximized when

$$\tan(2\chi_\tau) = \frac{2\mathbf{S}_\tau \cdot \mathbf{s}_\tau}{S_\tau^2 - s_\tau^2}, \tag{2.12}$$

where $\chi_\tau \in [-\pi, \pi]$.

Similar to the BF$_\tau$ set, we choose a BF$_Q$ set of axes in which the z axis points along $\mathbf{Q}$, and the y axis is perpendicular to the triatomic plane. The BF$_Q$ system is an instantaneous principal axis system [1], since $\mathbf{Q}$ and $\mathbf{q}$ always lie along the smallest and second smallest principal moments of inertia, respectively. As a result, the BF$_Q$ axes swing smoothly from reactants to products.

Transformations from the BF$_\tau$ systems to the BF$_Q$ system consist of rotations $\beta_{Q\tau}$ about their common y axis. The rotation $\beta_{Q\tau}$ is given by

$$\sin\beta_{Q\tau} = \frac{s_\tau \sin\chi_\tau \sin\Theta_\tau}{Q} \tag{2.13a}$$

and

$$\cos\beta_{Q\tau} = \frac{S_\tau \cos\chi_\tau + s_\tau \sin\chi_\tau \cos\Theta_\tau}{Q}, \tag{2.13b}$$

where

$$\begin{aligned} Q = \Big[& s_\tau^2 \sin^2\chi_\tau \sin^2\Theta_\tau \\ & + \left(S_\tau \cos\chi_\tau + s_\tau \sin\chi_\tau \cos\Theta_\tau\right)^2 \Big]^{1/2}. \end{aligned} \tag{2.13c}$$

This is an important connection between the Jacobi and APH systems and will be used to map wave functions from one system to the other.

The internal coordinates of the APH system are the hyperradius ρ, and the two angles θ and χ_i. The hyperradius ρ and angle θ are given by

$$\rho = \left(q^2 + Q^2\right)^{1/2}, \tag{2.14a}$$

$$\theta = \pi/2 - 2\tan^{-1}(q/Q), \tag{2.14b}$$

where $0 \leq \rho \leq \infty$, $0 \leq \theta \leq \pi/2$. The kinematic angle χ_i is given in Eq. (2.11). These internal coordinates treat all arrangement channels equivalently. The remaining three coordinates are the Euler angles α_Q, β_Q, and γ_Q that describe the orientation of the BF$_Q$ system with respect to the SF axes.

The APH internal coordinates in terms of Jacobi coordinates are given by

$$\rho = \left(s_\tau^2 + S_\tau^2\right)^{1/2}, \tag{2.15a}$$

$$\tan\theta = \frac{\left[\left(S_\tau^2 - s_\tau^2\right)^2 + \left(2\mathbf{S}_\tau \cdot \mathbf{s}_\tau\right)^2\right]^{1/2}}{2S_\tau s_\tau \sin\Theta_\tau}, \tag{2.15b}$$

and

$$\tan\left[2\left(\chi_i - \chi_{\tau i}\right)\right] = \frac{2\mathbf{S}_\tau \cdot \mathbf{s}_\tau}{S_\tau^2 - s_\tau^2}. \tag{2.15c}$$

Alternatively, the Jacobi coordinates in terms of the APH coordinates are

$$S_\tau = \frac{\rho}{\sqrt{2}}\Big\{1 + \sin\theta\cos\left[2\left(\chi_i - \chi_{\tau i}\right)\right]\Big\}^{1/2}, \tag{2.16a}$$

$$s_\tau = \frac{\rho}{\sqrt{2}}\Big\{1 - \sin\theta\cos\left[2\left(\chi_i - \chi_{\tau i}\right)\right]\Big\}^{1/2}, \tag{2.16b}$$

and

$$\cos\Theta_\tau = \frac{\sin\theta\sin\left[2\left(\chi_i - \chi_{\tau i}\right)\right]}{\Big\{1 - \sin^2\theta\cos^2\left[2\left(\chi_i - \chi_{\tau i}\right)\right]\Big\}^{1/2}}. \tag{2.16c}$$

The hyperradius describes the size of the three-atom system and the hyperangles describe its shape. As the hyperradius ρ increases, the interatomic separation increases, causing S_τ and s_τ to increase. The angle θ is a "bending" angle, which varies the triatomic shape from an equilateral triangle ($\theta = 0$) to a collinear geometry ($\theta = \pi/2$). For collinear geometries, the kinematic angle χ_i describes the ratio of s_τ to S_τ for a fixed value of ρ, where, for example, $s_A/S_A \to 0$ as $\chi_i \to 0$.

The APH kinetic energy operator is

$$\begin{aligned}
T = &- \frac{\hbar^2}{2\mu\rho^{5/2}}\frac{\partial^2}{\partial\rho^2}\rho^{5/2} + \frac{15\hbar^2}{8\mu\rho^2} \\
&- \frac{\hbar^2}{2\mu\rho^2}\left[\frac{4}{\sin 2\theta}\frac{\partial}{\partial\theta}\sin 2\theta\frac{\partial}{\partial\theta} + \frac{1}{\sin^2\theta}\frac{\partial^2}{\partial\chi_i^2}\right] \\
&+ \frac{1}{\mu\rho^2}\left[\frac{\mathcal{A}_\theta + \mathcal{B}_\theta}{2}J^2 + \left(\mathcal{C}_\theta - \frac{\mathcal{A}_\theta - \mathcal{B}_\theta}{2}\right)J_z^2\right], \\
&- \frac{1}{2\mu\rho^2}\left[\frac{\mathcal{A}_\theta - \mathcal{B}_\theta}{2}\left(J_+^2 + J_-^2\right) + \hbar\mathcal{D}_\theta\left(J_- - J_+\right)\frac{\partial}{\partial\chi_i}\right]
\end{aligned} \tag{2.17}$$

where J is the total angular momentum operator,

$$J_\pm = J_x \mp iJ_y, \tag{2.18}$$

are the raising and lowering operators, J_i are the components of the total angular momentum with respect to the BF_Q system, and

$$\mathcal{A}_\theta = \frac{1}{1+\sin\theta}, \tag{2.19a}$$

$$\mathcal{B}_\theta = \frac{1}{2\sin^2\theta}, \tag{2.19b}$$

$$\mathcal{C}_\theta = \frac{1}{1-\sin\theta}, \tag{2.19c}$$

$$\mathcal{D}_\theta = \frac{\cos\theta}{\sin^2\theta}. \tag{2.19d}$$

Note that $\mathcal{A}_\theta = \mu\rho^2/2I_x$ and $\mathcal{C}_\theta = \mu\rho^2/2I_z$, but $\mathcal{B}_\theta \neq \mu\rho^2/2I_y$, for principal moments of inertia I_x, I_y, and I_z. Therefore, the APH Hamiltonian is that of a fluid rotor, rather than a rigid asymmetric top rotor [1].

For $\theta > 40°$, the diagonal terms of the APH kinetic energy operator dominate. When using basis set methods, one must be careful in choosing rapidly converging basis functions. However, since we are using a grid-based method we don't have to take this into account.

2.2.3 Symmetry of the Potential Energy Surface

The symmetries present in the potential energy surface (PES) are important because they allow a reduction in the coordinate space required to represent the wave functions. The APH coordinates provide a good illustration of the symmetries present at a constant APH ρ value. The potential energy surface for H_3 at a constant ρ is given in Fig. 2.1. The plot shows the PES as a function of APH θ and χ_i at a constant hyperradius, $\rho = 6$ bohr. The X and Y coordinates are given by [1]

$$X = \tan\left(\frac{\theta}{2}\right)\cos\chi_i \tag{2.20}$$

$$Y = \tan\left(\frac{\theta}{2}\right)\sin\chi_i. \tag{2.21}$$

The APH θ coordinate is the radial coordinate, since it provides the distance from the center of the plot, and APH χ_i is the polar angle measured from the positive x-axis.

The symmetry of the $\mathrm{H} + \mathrm{H}_2$ surface is readily evident in Fig. 2.1 and exhibits symmetry elements belonging to the C_{6v} point group [31]. Fig. 2.2 shows the location of the arrangement channels on the constant APH ρ surface;

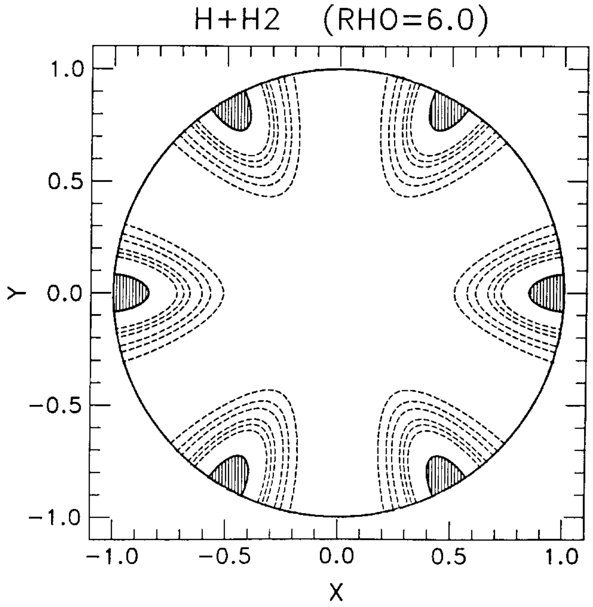

Figure 2.1: PKH3 potential energy surface at $\rho = 6$ bohr [1]. The shaded areas show the repulsive region of the PES and the contours show the well region. The contours are at 0.1, 0.38, and 1.0 eV.

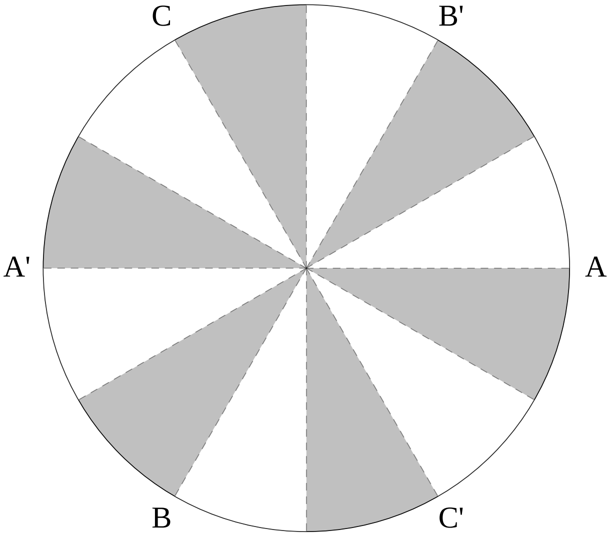

Figure 2.2: Location of the potential energy surface arrangement channels and symmetry elements of C_{6v}.. Each dashed line represents a reflection plane and are located at successive $\chi_i = \pi/6$ rotations. The shaded areas illustrate the rotational symmetry and are located at succesive $\chi_i = \pi/3$ rotations.

dashed lines are used to illustrate the symmetry elements in C_{6v}. Note that each arrangement channel is listed twice, since the APH coordinates cover configuration space twice. This is done to avoid using half-integer angular momentum. Each dashed line represents a reflection plane. These planes are located at succesive $\chi_i = \pi/6$ rotations. The PES is symmetric with respect to reflections through these planes. The shaded areas illustrate the rotational symmetry and are located at succesive $\chi_i = \pi/3$ rotations. The PES is symmetric with respect to $\pi/3$, $2\pi/3$, π, $4\pi/3$, $5\pi/3$, and 2π rotations of the APH χ_i coordinate.

The PES for $F + H_2$ at a constant ρ is given in Fig. 2.3. The plot shows the PES projected on the top hemisphere of a hypersphere of radius $\rho = 10.5$ bohr. The $F + H_2$ surface is less symmetric than the $H + H_2$ surface and exhibits symmetry elements belonging to the C_{2v} point group [31]. Fig. 2.4 shows the location of the arrangement channels on the constant APH ρ surface; dashed lines are used to illustrate the symmetry elements in C_{2v}. Each dashed line represents a reflection plane. These planes are located at succesive $\chi_i = \pi/2$ rotations. The PES is symmetric with respect to reflections through these planes. The shaded areas illustrate the rotational symmetry. The PES is symmetric with respect to π rotations of the APH χ_i coordinate.

The important feature is that the PES is symmetric with respect to a single APH coordinate, χ_i. As a result, the wave function can be represented on a fraction of the total space, making computation more efficient. C_{6v} contains four one-dimensional and two two-dimensional irreducible representations (IR) [31]. If the wave function is an eigenfunction of a C_{6v}, it only needs to be represented from $\chi_i = 0$ to $\pi/6$ for a one-dimensional IR and from $\chi_i = 0$ to $\pi/3$ for a two-dimensional IR. C_{2v} contains four one-dimensional IR's, so an eigen-

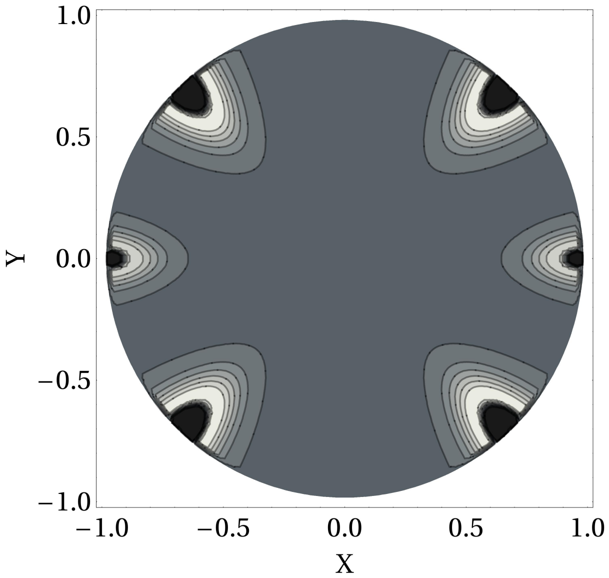

Figure 2.3: Stark-Werner FH2 potential energy surface at $\rho = 10.5$ bohr [2]. The shading runs from dark to light, with the darkest shading showing the highest potential energy.

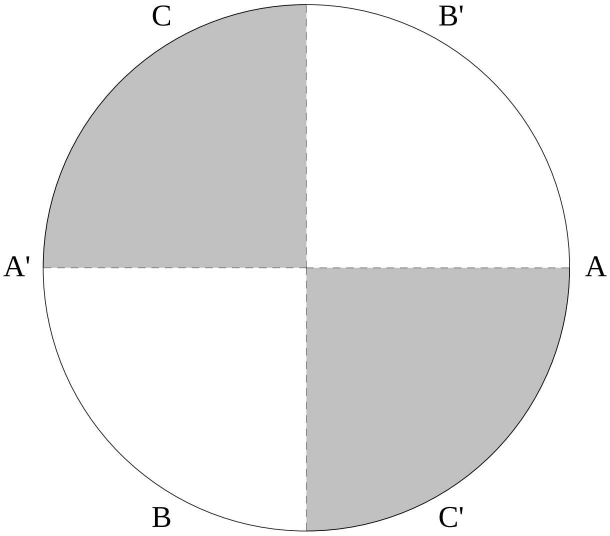

Figure 2.4: Location of the potential energy surface arrangement channels and symmetry elements of C_{2v}.. Each dashed line represents a reflection plane and are located at successive $\chi_i = \pi/2$ rotations. The shaded areas illustrate the rotational symmetry and are located at succesive $\chi_i = \pi$ rotations.

function only needs to be represented from $\chi_i = 0$ to $\pi/2$ [31]. In this work, we will take advantage of the ability to expand the wave functions in terms of the IR eigenfunctions, in order to increase the computational efficiency.

2.2.4 Jacobi Basis

For a given total angular momentum J and its SF z component M, the time independent Schrödinger equation (TISE) is given by

$$(E - \mathcal{H})\, \Psi^{JMi} = 0, \tag{2.22}$$

where i is labels the initial state. To define the Jacobi basis, the Hamiltonian $\mathcal{H} = T + V$ is formed from the kinetic energy operator in Eq. (2.9) and the potential energy $V = V(S_\tau, s_\tau, \Theta_\tau)$. The wave function can be expanded in SF Jacobi coordinates as a sum over the final states:

$$\Psi^{JMi} = \sum_{\tau\nu j\ell} \frac{1}{s_\tau S_\tau}\, G^{Ji}_{\tau\nu j\ell}(S_\tau)\, \mathcal{X}_{\tau\nu j}(s_\tau)\, \mathscr{Y}^{JM}_{\tau j\ell}(\hat{s}_\tau, \hat{S}_\tau), \tag{2.23}$$

where $\hat{s}_\tau = (\theta_{s_\tau},\, \phi_{s_\tau})$, $\hat{S}_\tau = (\theta_{S_\tau},\, \phi_{S_\tau})$, τ labels the arrangement channel, ν labels the diatomic vibrational state, j labels the diatomic rotational state, and ℓ labels the angular momentum state of the atom about the diatom.

The functions $\mathcal{X}_{\tau\nu j}(s_\tau)$ are the vibrational eigenfunctions of the diatom formed by atoms $\tau + 1$ and $\tau + 2$ and satisfy

$$\left[-\frac{\hbar^2}{2\mu}\frac{\partial^2}{\partial s_\tau^2} + \frac{\hbar^2 j(j+1)}{2\mu s_\tau^2} + v_\tau(s_\tau) - \epsilon_{\tau\nu j}\right] \mathcal{X}_{\tau\nu j}(s_\tau) = 0, \tag{2.24}$$

where $v_\tau(s_\tau)$ is the diatomic potential between atoms $\tau + 1$ and $\tau + 2$ and $\epsilon_{\tau\nu j}$ is the vibration-rotation energy. We obtain the solutions to Eq. (2.24) using a distributed approximating functional (DAF) representation [32, 33, 34, 35, 36, 37] for the s_τ kinetic energy operator.

The angular functions $\mathscr{Y}^{JM}_{\tau j\ell}(\hat{s}_\tau, \hat{S}_\tau)$ for each arrangement channel are eigenfunctions of $\mathbf{J}^2$, $\mathbf{J}_z$, $\boldsymbol{\mathcal{L}}^2_\tau$, and $\boldsymbol{\mathcal{J}}^2_\tau$ formed by coupling eigenfunctions of $\boldsymbol{\mathcal{L}}^2_\tau$ and $\boldsymbol{\mathcal{J}}^2_\tau$,

$$\begin{aligned}\mathscr{Y}^{JM}_{\tau j\ell}(\hat{s}_\tau, \hat{S}_\tau) = &\sum_m C(j, \ell, J; m, M-m, M)\\ &\times Y_{jm}(\hat{s}_\tau) Y_{l,M-m}(\hat{S}_\tau),\end{aligned} \tag{2.25}$$

where the Y functions are spherical harmonics, and C is a Clebsch-Gordan coefficient [38].

The functions $G^{Ji}_{\tau\nu j\ell}(S_\tau)$ satisfy the asymptotic boundary condition

$$\begin{aligned}G^{Ji}_{\tau\nu j\ell}(S_\tau) \xrightarrow[S_\tau \to \infty]{} &\left(\frac{\mu}{2\pi\hbar^2 k_{\tau\nu j}}\right)^{1/2}\\ &\times \Bigg\{ \delta_{\tau\tau_i}\delta_{\nu\nu_i}\delta_{jj_i}\delta_{\ell\ell_i}\, \mathscr{H}^{(2)}_\ell(k_{\tau\nu j} S_\tau)\\ &- \mathcal{S}^J_{\tau\nu j\ell,\tau_i\nu_i j_i\ell_i}(E)\, \mathscr{H}^{(1)}_\ell(k_{\tau\nu j} S_\tau) \Bigg\},\end{aligned} \tag{2.26}$$

where

$$k_{\tau\nu j} = \sqrt{\frac{2\mu}{\hbar^2}(E - \epsilon_{\tau\nu j})}, \tag{2.27}$$

E is the total energy, $\mathcal{S}^J$ is the scattering matrix (S matrix), and $\mathscr{H}^{(k)}_\ell$, with $k = 1, 2$, are Riccati-Hankel functions [39]. These boundary conditions will be applied at sufficiently large values of S_τ such that the wave packet is outside the interaction region of the potential energy surface, but the centrifugal potential will not necessarily be negligible.

In terms of BF$_\tau$ Jacobi coordinates, the angular momentum functions can be expanded as [40]

$$\begin{aligned}\mathscr{Y}^{JM}_{\tau j\ell}(\hat{s}_\tau, \hat{S}_\tau) =& \left(\frac{2\ell+1}{2J+1}\right)^{1/2} \sum_{\Omega} C(j\,\ell\,J;\,\Omega\,0\,\Omega) \\ & \times \hat{\mathcal{P}}_{j\Omega}(\Theta_\tau)\,\hat{D}^J_{\Omega M}(\alpha_\tau, \beta_\tau, \gamma_\tau),\end{aligned} \tag{2.28}$$

where Ω is the BF$_\tau$ z-component of the total angular momentum J, with values from $-\min(j, J)$ to $+\min(j, J)$. The basis function $\hat{\mathcal{P}}_{j\Omega}(\Theta_\tau)$ is a normalized spherical harmonic, and $\hat{D}^J_{\Omega M}(\alpha_\tau, \beta_\tau, \gamma_\tau)$ is a normalized Wigner D function [41]:

$$\hat{\mathcal{P}}_{j\Omega}(\Theta_\tau) = (2\pi)^{1/2}\, Y_{j\Omega}(\Theta_\tau, 0) \tag{2.29}$$

$$\hat{D}^J_{\Omega M}(\alpha_\tau, \beta_\tau, \gamma_\tau) = \left(\frac{2J+1}{8\pi^2}\right)^{1/2} D^J_{\Omega M}(\alpha_\tau, \beta_\tau, \gamma_\tau). \tag{2.30}$$

Substituting Eq. (2.28) into Eq. (2.23) gives

$$\begin{aligned}\Psi^{JMi} =& \sum_{\tau\nu j\Omega} \frac{1}{s_\tau S_\tau}\, G^{Ji}_{\tau\nu j\Omega}(S_\tau)\, \mathcal{X}_{\tau\nu j}(s_\tau) \\ & \times \hat{\mathcal{P}}_{j\Omega}(\Theta_\tau)\, D^J_{\Omega M}(\alpha_\tau, \beta_\tau, \gamma_\tau),\end{aligned} \tag{2.31}$$

where

$$G^{Ji}_{\tau\nu j\Omega}(S_\tau) = \sum_{\ell} \left(\frac{2\ell+1}{2J+1}\right)^{1/2} C(j\,\ell\,J;\,\Omega\,0\,\Omega)\, G^{Ji}_{\tau\nu j\ell}(S_\tau). \tag{2.32}$$

Here we will choose to represent the initial and final states using the expansion in Eq. (2.23) with the angular momentum functions expanded according to Eq. (2.28). This choice of basis takes advantage of the SF boundary conditions in Eq. (2.26) and, as shown in Sec. 2.4, offers a simple transformation between

Jacobi and APH coordinates via the Euler angle $\beta_{Q\tau}$ defined in Eq. (2.13).

2.2.5 APH Basis

To define the APH basis, the Hamiltonian is formed from the kinetic energy operator in Eq. (2.17) and the potential energy $V(\rho, \theta, \chi_i)$. The solutions to the APH Schrödinger equation can be expanded as functions of good parity p as [42],

$$\Psi^{JMp} = \sum_{\kappa\Lambda} \frac{4}{\rho^{5/2}}\, \psi^{Jp}_{\kappa\Lambda}(\rho)\, \Phi^{Jp}_{\kappa\Lambda}(\theta, \chi_i; \rho_\xi)\, \hat{D}^{Jp}_{\Lambda M}(\alpha_Q, \beta_Q, \gamma_Q), \tag{2.33}$$

where Λ is the BF$_Q$ z-component of J. The functions $\hat{D}^{Jp}_{\Lambda M}(\alpha_Q, \beta_Q, \gamma_Q)$ are normalized Wigner D functions with definite parity, defined as

$$\begin{aligned} &\hat{D}^{Jp}_{\Lambda M}(\alpha_Q, \beta_Q, \gamma_Q) \\ &= \left[\frac{2J+1}{16\pi^2(1+\delta_{\Lambda 0})}\right]^{1/2} \Big[\hat{D}^{J}_{\Lambda M}(\alpha_Q, \beta_Q, \gamma_Q) \\ &\qquad + (-1)^{J+\Lambda+p}\, \hat{D}^{J}_{-\Lambda M}(\alpha_Q, \beta_Q, \gamma_Q)\Big]. \end{aligned} \tag{2.34}$$

The basis functions $\Phi^{Jp}_{\kappa\Lambda}(\theta, \chi_i; \rho_\xi)$ satisfy [1]

$$\begin{aligned} \Bigg\{ &-\frac{\hbar^2}{2\mu\rho_\xi^2}\left[\frac{4}{\sin 2\theta}\frac{\partial}{\partial\theta}\sin 2\theta\frac{\partial}{\partial\theta} + \frac{1}{\sin^2\theta}\frac{\partial^2}{\partial\chi^2}\right] + \frac{15\hbar^2}{8\mu\rho_\xi^2} \\ &+ \frac{1}{\mu\rho^2}\left[\frac{\mathcal{A}_\theta + \mathcal{B}_\theta}{2}\hbar^2 J(J+1) + \left(\mathcal{C}_\theta - \frac{\mathcal{A}_\theta + \mathcal{B}_\theta}{2}\right)\hbar^2\Lambda^2\right] \\ &+ V(\theta, \chi_i; \rho_\xi) - \mathcal{E}^{Jp}_{\kappa\Lambda}\Bigg\}\Phi^{Jp}_{\kappa\Lambda}(\theta, \chi_i; \rho_\xi) = 0, \end{aligned} \tag{2.35}$$

where $\mathcal{A}_\theta$, $\mathcal{B}_\theta$, and $\mathcal{C}_\theta$ are defined in Eq. (2.19), and $V(\theta, \chi_i; \rho_\xi)$ is the potential energy for a fixed value of $\rho = \rho_\xi$. Since the functions $\Phi^{Jp}_{\kappa\Lambda}(\theta, \chi_i; \rho_\xi)$ are defined on the surface of a hypersphere of radius ρ_ξ, they will be referred to as *surface* functions.

For the h-TDWP method, we will only need to calculate surface functions at a single ρ value located in the asymptotic region of the PES, that we will refer to as ρ_∞. The wave packet will be analyzed on surface located at $\rho = \rho_\infty$.

The surface functions are obtained by diagonalizing the Hamiltonian in Eq. (2.35), where we use a discrete variable representation (DVR) [43, 44] for the θ kinetic energy operator and periodic DAF (PDAF) representation [32, 33, 34, 35, 36, 37] for the χ_i kinetic energy operator.

If the symmetry of the triatomic PES is taken into account, which is symmetric in the χ_i coordinate, we can calculate symmetry-adapted (SA) surface functions $\Phi_{\kappa\Lambda}^{Jp\Gamma}(\theta, \chi_i; \rho_\xi)$ that are labeled by the irreducible representations Γ of the appropriate point group. The basis set expansion in Eq. (2.33) can be rewritten as

$$\Psi^{JMp} = \sum_{\Gamma\kappa\Lambda} \frac{4}{\rho^{5/2}} \, \psi_{\kappa\Lambda}^{Jp\Gamma}(\rho) \, \Phi_{\kappa\Lambda}^{Jp\Gamma}(\theta, \chi_i; \rho_\xi) \, \hat{D}_{\Lambda M}^{Jp}(\alpha_Q, \beta_Q, \gamma_Q). \tag{2.36}$$

The SA surface functions are obtained by using a SA-DAF representation [45, 46] of the χ_i kinetic energy operator. The SA χ_i kinetic energy operator, and corresponding surface functions only need to be represented on a fraction of the total coordinate grid located in the interval $0 \leq \chi_i \leq 2\pi l_\Gamma / h$, where h is the order of the group, and l_Γ is the dimension of irreducible representation Γ [31].

2.3 Evolution of the Wave Packet in APH Coordinates

The wave packet will evolve in time according to the time-dependent Schrödinger equation,

$$i\hbar \frac{\partial}{\partial t} \varphi^{JMp}(t) = \mathcal{H}\, \varphi^{JMp}(t), \tag{2.37}$$

and, for a time-independent Hamiltonian $\mathcal{H}$, the solution is given by

$$\varphi^{JMp}(t) = e^{-i\mathcal{H}(t-t_0)/\hbar}\, \varphi^{JMp}(t_0). \tag{2.38}$$

Propagation of the wave packet is carried out using the Chebyshev method [47], where the time-evolution operator $e^{-i\mathcal{H}(t-t_0)/\hbar}$ is expanded as a sum of Chebyshev polynomials. This will require evaluating the result of operation of the Hamiltonian on the wave packet: $\mathcal{H}\varphi^{JMp}(t)$.

To propagate the wave packet in APH internal coordinates, (ρ, θ, χ_i), we expand the wave packet as

$$\varphi^{JMp}(t) = \sum_{\Lambda'} \frac{4}{\rho^{5/2}}\, \varphi^{J\Lambda' p}(\rho, \theta, \chi_i, t)\, \hat{D}^{Jp}_{\Lambda' M}(\alpha_Q, \beta_Q, \gamma_Q), \tag{2.39}$$

where $\hat{D}^{Jp}_{\Lambda' M}(\alpha_Q, \beta_Q, \gamma_Q)$ are defined in Eq. (2.34). The action of the APH

Hamiltonian on the Λ component of the wave packet is

$$\begin{aligned}
\mathcal{H}\varphi^{J\Lambda p}&(\rho,\theta,\chi_i,t) = \\
&\left\{-\frac{\hbar^2}{2\mu}\frac{\partial^2}{\partial\rho^2}+\frac{15\hbar^2}{8\mu\rho^2}+V(\rho,\theta,\chi_i)\right\}\varphi^{J\Lambda p}(\rho,\theta,\chi_i,t) \\
&-\left\{\frac{\hbar^2}{2\mu\rho^2}\left[\frac{4}{\sin 2\theta}\frac{\partial}{\partial\theta}\sin 2\theta\frac{\partial}{\partial\theta}+\frac{1}{\sin^2\theta}\frac{\partial^2}{\partial\chi_i^2}\right]\right\}\varphi^{J\Lambda p}(\rho,\theta,\chi_i,t) \\
&+\left\{\frac{1}{\mu\rho^2}\left[\frac{\mathcal{A}_\theta+\mathcal{B}_\theta}{2}\hbar^2 J(J+1)\right\}\varphi^{J\Lambda p}(\rho,\theta,\chi_i,t)\right. \\
&+\left\{\frac{1}{\mu\rho^2}\left(\mathcal{C}_\theta-\frac{\mathcal{A}_\theta+\mathcal{B}_\theta}{2}\right)\hbar^2\Lambda^2\right]\right\}\varphi^{J\Lambda p}(\rho,\theta,\chi_i,t) \\
&-\frac{1}{2\mu\rho^2}\sum_{\Lambda'=0}^{J}\left\langle \hat{D}^{Jp}_{\Lambda M}\left|\frac{\mathcal{A}_\theta-\mathcal{B}_\theta}{2}\left(J_+^2+J_-^2\right)\right|\hat{D}^{Jp}_{\Lambda' M}\right\rangle\varphi^{J\Lambda' p}(\rho,\theta,\chi_i,t) \\
&-\frac{1}{2\mu\rho^2}\sum_{\Lambda'=0}^{J}\left\langle \hat{D}^{Jp}_{\Lambda M}\left|\hbar\mathcal{D}_\theta\left(J_--J_+\right)\frac{\partial}{\partial\chi_i}\right|\hat{D}^{Jp}_{\Lambda' M}\right\rangle\varphi^{J\Lambda' p}(\rho,\theta,\chi_i,t),
\end{aligned} \tag{2.40}$$

where $\mathcal{A}_\theta$, $\mathcal{B}_\theta$, $\mathcal{C}_\theta$, $\mathcal{D}_\theta$ are given in Eq. (2.19).

The matrix elements in Eq (2.40) can be solved analytically [1]:

$$\begin{aligned}
\langle\hat{D}^{Jp}_{\Lambda M}&\,|\,J_+^2+J_-^2\,|\,\hat{D}^{Jp}_{\Lambda' M}\rangle \\
&=\hbar^2\Big[(1+\delta_{\Lambda,0})(1+\delta_{\Lambda',0})\Big]^{-1/2} \\
&\quad\times\Big[\lambda^+_{J,\Lambda}\lambda^+_{J,\Lambda+1}\delta_{\Lambda',\Lambda+2}-\lambda^-_{J,\Lambda}\lambda^-_{J,\Lambda-1}\delta_{\Lambda',\Lambda-1} \\
&\quad+(-1)^{J+\Lambda+p}\lambda^-_{J,\Lambda}\lambda^-_{J,\Lambda-1}\delta_{\Lambda',2-\Lambda}\Big],
\end{aligned} \tag{2.41}$$

and

$$\begin{aligned}&\left\langle \hat{D}^{Jp}_{\Lambda M} \,\middle|\, J_- - J_+ \,\middle|\, \hat{D}^{Jp}_{\Lambda' M} \right\rangle \\ &\quad =\hbar\Big[(1+\delta_{\Lambda,0})(1+\delta_{\Lambda',0})\Big]^{-1/2}\Big[\lambda^+_{J,\Lambda}\delta_{\Lambda',\Lambda+1} \\ &\qquad - \lambda^-_{J,\Lambda}\delta_{\Lambda',\Lambda-1} + (-1)^{J+\Lambda+p}\lambda^-_{J,\Lambda}\delta_{\Lambda',1-\Lambda}\Big] \end{aligned} \tag{2.42}$$

where [48, 49]

$$\lambda^{\pm}_{J,\Lambda} = \Big[(J \pm \Lambda + 1)(J \mp \Lambda)\Big]^{1/2}. \tag{2.43}$$

The results in Eqs. (2.42) and (2.41) are referred to as the asymmetric top and Coriolis coupling coefficients, respectively [**?**]. Each Λ component of the wave packet is coupled to its $\Lambda \pm 1$ and $\Lambda \pm 2$ components, and J or $J+1$ Λ components of the initial wave packet must be propagated, depending on the parity [21, 50].

The number of terms that must be used in the Chebychev expansion of the time-evolution operator is dependent upon the eigenvalue range of the Hamiltonian [47]. For small values of θ, the presence of $1/\sin 2\theta$ and $1/\sin^2\theta$ terms in the θ and χ_i kinetic energy operators result in very large eigenvalues. Furthermore, similar issues exist for the angular momentum operators that contain $\mathcal{B}_\theta$, $\mathcal{C}_\theta$, and $\mathcal{D}_\theta$. To avoid these large eigenvalues, we set energy cutoffs that limit the maximum eigenvalues of terms that do not couple different Λ values. The coupling terms are ignored when the sum of the $J(J+1)$ and Λ^2 terms are cutoff [51]. The computational details concerning these points will be discussed in Sec. 3.3.

As discussed in Sec. 2.2.5, the PES symmetry can be exploited to reduce the coordinate space required to represent the wave packet and χ_i derivatives by decomposing them into the irreducible representations Γ of the appropriate point group. Rather than propagating the wave packet over the full APH coordinate space, we propagate the irreducible representation wave packets using Hamiltonians that belong to the same irreducible representation. The only terms affected in the APH Hamiltonian operation, in Eq. (2.40), are the χ_i derivatives, represented using the SA-PDAF representation [45, 46].

2.4 The Initial Wave Packet

In general, the initial wave packet can be constructed in any coordinate basis that appropriately represents the reactants of the system, assuming a transformation between the coordinate system and APH coordinates exists. To be propagated using the Chebyshev method with Eq. (2.40), a general initial wave packet $\varphi_i^{JM}(t=0)$ is expanded according to Eq. (2.39), giving

$$\varphi_i^{J\Lambda p}(\rho, \theta, \chi_i, t=0) = \frac{\rho^{5/2}}{4} \int \mathrm{d}Q\, \hat{D}^{Jp*}_{\Lambda M}\, \varphi_i^{JMp}(t=0), \tag{2.44}$$

where the index i denotes a set of initial quantum numbers and

$$\mathrm{d}Q = \mathrm{d}\alpha_Q\, \sin\beta_Q\, \mathrm{d}\beta_Q\, \mathrm{d}\gamma_Q. \tag{2.45}$$

To calculate state-to-state transition probabilties, we choose an initial wave packet that obeys the SF boundary conditions discussed in Sec. 2.2.4:

$$\begin{aligned}\varphi^{JMp}_{\tau_i\nu_i j_i\ell_i}(t=0) =& \frac{1}{s_{\tau_i}S_{\tau_i}}\, g_{\tau_i}(S_{\tau_i})\, \mathcal{X}_{\tau_i\nu_i j_i}(s_{\tau_i}) \\ &\times \left(\frac{2\ell+1}{2J+1}\right)^{1/2} \sum_{\Omega\geq 0} C(j\,\ell\,J;\,\Omega\,0\,\Omega) \\ &\times \hat{\mathcal{P}}_{j_i\Omega_i}(\Theta_{\tau_i})\, \hat{D}^{Jp}_{\Omega_i M}(\alpha_{\tau_i},\beta_{\tau_i},\gamma_{\tau_i}). \end{aligned} \tag{2.46}$$

Note that Eq. (2.46) has been written as a function of definite parity, where

$$\begin{aligned}&\hat{D}^{Jp}_{\Omega_i M}(\alpha_{\tau_i},\beta_{\tau_i},\gamma_{\tau_i}) \\ &= \left[\frac{2J+1}{16\pi^2(1+\delta_{\Lambda 0})}\right]^{1/2} \Big[D^{J}_{\Omega_i M}(\alpha_{\tau_i},\beta_{\tau_i},\gamma_{\tau_i}) \\ &\qquad + (-1)^{J+\Lambda+p}\, D^{J}_{-\Omega_i M}(\alpha_{\tau_i},\beta_{\tau_i},\gamma_{\tau_i})\Big]. \end{aligned} \tag{2.47}$$

The translational function $g_{\tau_i}(S_{\tau_i})$ is a normalized Gaussian defined as

$$g_{\tau_i}(S_{\tau_i}) = \left(\frac{1}{2\pi\sigma^2}\right)^{1/4} e^{-\left(S_{\tau_i}-S^0_{\tau_i}\right)^2/4\sigma^2} e^{-ik_0 S_{\tau_i}}. \tag{2.48}$$

The initial wave packet is centered at $S^0_{\tau_i}$, chosen to be large enough that the packet is located in the asymptotic region of the reactant arrangement channel PES, and is centered at $\hbar k_0$ in momentum space, chosen such that $k_0 > 0$, so the packet is traveling toward the interaction region. In other words, the initial wave packet is constructed so the atom and diatom are initially well separated (large $S^0_{\tau_i}$), are not interacting, and are given an initial momentum such that they are initially approaching each other. It is important to choose an appropriate width parameter σ that keeps the momentum space distribution narrow enough to contain only incoming waves and keeps the coordinate distribution narrow enough to ensure that the whole packet is initially localized in the asymptotic region of the potential energy surface.

Substituting Eq. (2.46) into Eq. (2.44), the integral can be solved by taking advantage of the orthogonality of the Wigner D functions. We transform from the BF$_\tau$ system to the BF$_Q$ system by a $\beta_{Q\tau}$ rotation about their common y-axis, where $\beta_{Q\tau}$ is defined in Eq. (2.13), using the relationship [1]

$$\hat{D}^{Jp}_{\Omega M}(\alpha_\tau, \beta_\tau, \gamma_\tau) = \sum_{\Lambda} d^{Jp}_{\Omega\Lambda}(\beta_{Q\tau})\, \hat{D}^{Jp}_{\Lambda M}(\alpha_Q, \beta_Q, \gamma_Q). \tag{2.49}$$

The Λ component of the initial wave packet is given by

$$\begin{aligned} \varphi^{J\Lambda p}_{\tau_i \nu_i j_i \ell_i}(\rho, \theta, \chi_i, t = 0) = & \frac{\rho^{5/2}}{4 s_{\tau_i} S_{\tau_i}}\, g_{\tau_i}(S_{\tau_i})\, \mathcal{X}_{\tau_i \nu_i j_i}(s_{\tau_i}) \\ & \times \left(\frac{2\ell + 1}{2J + 1}\right)^{1/2} \sum_{\Omega} C(j\, \ell\, J;\, \Omega\, 0\, \Omega) \\ & \times \hat{\mathcal{P}}_{j_i \Omega_i}(\Theta_{\tau_i}) d^{Jp}_{\Omega_i \Lambda}(\beta_{Q\tau_i}), \end{aligned} \tag{2.50}$$

where

$$d^{Jp}_{\Omega_i \Lambda}(\beta_{Q\tau}) = \frac{d^{J}_{\Omega_i \Lambda}(\beta_{Q\tau}) + \big(-1\big)^{J+\Lambda+p}\, d^{J}_{\Omega_i -\Lambda}(\beta_{Q\tau})}{\Big[2\big(1 + \delta_{\Lambda,0}\big)\Big]^{1/2}}. \tag{2.51}$$

Eq. (2.50) shows that the Λ components of the initial wave packet can be formed directly from the Jacobi basis functions and mapped to APH coordinates using Eq. (2.16).

If we consider symmetry, the initial wave packet will need to be decomposed into its component irreducible representations. Since the initial wave packet in the Jacobi basis has been mapped to internal APH coordinates, this can be done using projection operators [31]:

$$\varphi^{J\Lambda p\Gamma}_{\tau_i\nu_i j_i\ell_i}(\theta,\chi_i,t=0;\rho_\infty) = P^\Gamma \varphi^{J\Lambda p}_{\tau_i\nu_i j_i\ell_i}(\theta,\chi_i,t=0;\rho_\infty). \tag{2.52}$$

The projection operators are defined as [31]

$$P^\Gamma = \frac{\ell_\Gamma}{h}\sum_R X(R)^\Gamma \hat{R}, \tag{2.53}$$

where ℓ_Γ is the dimension of the irreducible representation Γ, h is the order of the point group, R is a symmetry operation of the group, and $X(R)^\Gamma$ is the character of the symmetry operation R for irreducible representation Γ. Each irreducible representation wave packet will be propagated and analyzed separately.

The values of the rotational quantum number j and parity p will limit the number of component irreducible representations present in the initial wave packet. As a result, the region of coordinate space over which we must propagate the wave packet is reduced. For example, for the reactants $H + H_2$ with $j = 0$ and even parity, the initial wave packet will have A_1 and E_{2A} irreducible representation components of the C_{6v} point group. Propagation of the A_1 component requires $0 \leq \chi_i \leq \pi/6$, and the E_{2A} component requires $0 \leq \chi_i \leq \pi/3$, which is 1/4 of the coordinate space that would be required if the full wave packet were propagated.

At this point, we have defined an initial Jacobi wave packet that is localized in the asymptotic region of the potential energy surface and that consists of only incoming waves. We can propagate it in APH coordinates from $t = 0$ to a time t_{max} when the reaction has concluded and the entire wave packet has exited the interaction region. The scattering information can be extracted by analyzing the wave packet at each time step as it re-enters the asymptotic region.

2.5 Wave Packet Analysis

Let $\varphi_i^{JM}(t=0)$ be an initial wave packet, where i denotes the initial state, that is localized in the asymptotic region of the PES. As the wave packet propagates in time, it will enter the interaction region, scatter, and exit into the asymptotic region. Once the packet has returned to the asymptotic region, it can be analyzed after each time step by projecting it onto the APH basis states at a constant ρ surface, which we label ρ_∞. The S-matrix can be extracted by Fourier transforming the APH projection coefficients and matching them to the appropriate Jacobi boundary conditions.

First we present the analysis assuming no symmetry, so S-matrix elements are labeled by arrangement channel. Then we present the analysis taking into account symmetry, so the S-matrix elements are labeled by irreducible representation, and show how to transform to arrangement channel dependent S-matrix elements.

At any time t, the Λ component of the propagating wave packet can be expressed in terms of it's stationary state components,

$$\varphi_i^{J\Lambda p}(\rho,\theta,\chi_i,t) = \frac{1}{2\pi\hbar}\int_0^\infty \mathrm{d}E\, e^{-iEt/\hbar}\,\eta_i(E)\,\Psi^{J\Lambda ip}, \tag{2.54}$$

with $\Psi^{J\Lambda ip} = \left\langle \hat{D}^{Jp}_{\Lambda M}(\alpha_Q,\beta_Q,\gamma_Q)\,\middle|\,\Psi^{JMi}\right\rangle$, where Ψ^{JMi} is defined in Sec. 2.2.4, and $\eta_i(E)$ is the total energy distribution,

$$\eta_i(E) = \sqrt{\frac{\mu}{2\pi\hbar^2 k_i}}\int_0^\infty \mathrm{d}S_{\tau_i}\,\mathscr{H}^{(1)}_{\ell_i}(k_i S_{\tau_i})\,g_{\tau_i}(S_{\tau_i}), \tag{2.55}$$

determined from the initial Gaussian, where $\mathscr{H}^{(1)}_{\ell_i}(k_i S_{\tau_i})$ is a Ricatti-Hankel function [39].

We project the wave packet onto the surface of a hypersphere of radius $\rho = \rho_\infty$, where ρ_∞ is located in the asymptotic region of the potential energy surface, and project this portion of the wave packet onto the APH surface functions $\Phi^{Jp}_{\kappa\Lambda}(\theta, \chi_i; \rho_\infty)$. This is done by multiplying both sides of Eq. (2.54) by $\delta(\rho - \rho_\infty)\Phi^{Jp}_{\kappa\Lambda}(\theta, \chi_i; \rho_\xi)$ and integrating over the APH internal coordinates [52], giving

$$\begin{aligned}\int_0^\infty \mathrm{d}\rho\, \delta(\rho - \rho_\infty) \int_0^{\pi/2} \sin 2\theta\, \mathrm{d}\theta \int_0^{2\pi} \mathrm{d}\chi_i\, \Phi^{Jp}_{\kappa\Lambda}(\theta, \chi_i; \rho_\xi)\, \varphi^{J\Lambda p}_i(\rho, \theta, \chi_i, t)&\\ = \frac{1}{2\pi\hbar} \int_0^\infty \mathrm{d}E\, e^{-iEt/\hbar}\, \eta_i(E) \int_0^\infty \mathrm{d}\rho\, \delta(\rho - \rho_\infty) \int_0^{\pi/2} \sin 2\theta\, \mathrm{d}\theta&\\ \times \int_0^{2\pi} \mathrm{d}\chi_i\, \Phi^{Jp}_{\kappa\Lambda}(\theta, \chi_i; \rho_\xi)\, \Psi^{J\Lambda ip}.&\end{aligned} \tag{2.56}$$

The left-hand side (LHS) of Eq. (2.56) contains the overlap of the wave packet with the APH surface functions, and the right-hand side (RHS) contains the overlap of the surface functions with the Jacobi stationary state basis functions.

We seek the S-matrix contained in the boundary conditions of $\Psi^{J\Lambda ip}$. Since ρ_∞ has been chosen to be in the asymptotic region, the boundary conditions, such as those in Eq. (2.26) for an asymptotic value of S_τ, can be applied. The stationary state wave functions $\Psi^{J\Lambda ip}$ can be expanded as

$$\Psi^{J\Lambda ip}(\rho_\infty) = -\sum_f \mathcal{S}^J_{f,i}(E)\, \Psi^{J\Lambda ip}_f(E; \rho_\infty), \tag{2.57}$$

where the composite index f labels the final product states in all arrangement channels, and $\mathcal{S}^J_{f,i}(E)$ is the S-matrix element for a transition from an initial state i to a final state f. Notice the absence of the incoming boundary condition in Eq. (2.57). For this equation to be valid, we can either choose ρ_∞ to be large enough that the initial wave packet is localized in the region $\rho < \rho_\infty$ or we can choose to start the analysis at a time $t_{delay} > 0$ such that the initial wave packet no longer has any significant amplitude along $\rho \geq \rho_\infty$.

At energies below dissociation, the final state wave functions $\Psi_f^{J\Lambda ip}(E;\rho_\infty)$ are constructed from Jacobi basis functions. If the wave packet energy range includes both bound and dissociative final states, the final state wave functions are constructed as a sum of Jacobi and hyperspherical basis functions, satisfying a set of mixed-boundary conditions [29].

Substituting Eq. (2.57) into Eq. (2.56) and evaluating the ρ integral gives

$$\begin{aligned} F^J_{\kappa\Lambda,i}(t;\rho_\infty) = \frac{1}{2\pi\hbar}\int_0^\infty \mathrm{d}E\, e^{-iEt/\hbar}\,\eta_i(E) \\ \times \sum_f \mathcal{S}^J_{f,i}(E)\, A^J_{\kappa\Lambda,f}(E;\rho_\infty), \end{aligned} \tag{2.58}$$

where

$$\begin{aligned} F^J_{\kappa\Lambda,i}(t;\rho_\infty) = \int_0^{\pi/2} \mathrm{d}\theta\, \sin 2\theta \\ \times \int_0^{2\pi} \mathrm{d}\chi_i\, \Phi^{Jp}_{\kappa\Lambda}(\theta,\chi_i;\rho_\infty)\, \varphi_i^{J\Lambda p}(\theta,\chi_i,t;\rho_\infty) \end{aligned} \tag{2.59}$$

and

$$\begin{aligned} A^J_{\kappa\Lambda,f}(E;\rho_\infty) = \int_0^{\pi/2} \mathrm{d}\theta\, \sin 2\theta \\ \times \int_0^{2\pi} \mathrm{d}\chi_i\, \Phi^{Jp}_{\kappa\Lambda}(\theta,\chi_i;\rho_\infty)\, \Psi_f^{J\Lambda ip}(E,\rho_\infty). \end{aligned} \tag{2.60}$$

To extract the S-matrix elements from the integral, we perform a time-to-energy Fourier transformation on Eq. (2.58) and rearrange to get

$$\sum_f \mathcal{S}^J_{f,i}(E)\, A^J_{\kappa\Lambda,f}(E;\rho_\infty) = F^J_{\kappa\Lambda,i}(E;\rho_\infty), \tag{2.61}$$

where

$$F^J_{\kappa\Lambda,i}(E;\rho_\infty) = \frac{1}{\eta_i(E)} \int_0^\infty \mathrm{d}t\, e^{iEt/\hbar}\, F^J_{\kappa\Lambda,i}(t;\rho_\infty), \tag{2.62}$$

and $A^J_{\kappa\Lambda,f}(E;\rho_\infty)$ is defined in Eq. (2.60).

If we have N_f open final states and N_s APH surface functions at a given total energy E, Eq. (2.61) can be written in matrix form as

$$\mathbf{A}^J \boldsymbol{\mathcal{S}}^J = \mathbf{F}^J, \tag{2.63}$$

where $\mathbf{A}^J$ is an $N_f \times N_s$ matrix, $\boldsymbol{\mathcal{S}}^J$ is a vector of length N_f, and $\mathbf{F}^J$ is a vector of length N_s. The number of energetically accessible final states will depend upon the value of the total energy at which Eq. (2.63) will be solved. The number of APH surface functions must be large enough to fully represent all the energetically accessible final states. Since the matrix $\mathbf{A}^J$ will not necessarily be square, we multiply both sides of Eq. (2.63) by $(\mathbf{A}^J)^T$ and solve for $\boldsymbol{\mathcal{S}}^J$ as

$$\boldsymbol{\mathcal{S}}^J = \left[\mathbf{A}^T\mathbf{A}\right]^{-1}\mathbf{A}^T\mathbf{F}, \tag{2.64}$$

where the J superscripts on the right-hand side have been suppressed for clarity.

In deriving Eq. (2.63), we made no use of symmetry. To extract the S-matrix elements, taking advantage of symmetry, we first expand the Γ component of the initial wave packet in terms of the Γ components of the Jacobi stationary state functions:

$$\varphi_i^{J\Lambda p\Gamma}(\rho,\theta,\chi_i,t) = \frac{1}{2\pi\hbar}\int_0^\infty \mathrm{d}E\, e^{-iEt/\hbar}\,\eta_i(E)\,\Psi^{J\Lambda i\Gamma}, \tag{2.65}$$

as in Eq. (2.54). We can decompose the stationary state functions, which have been mapped to APH coorddinates, in the same way we decoposed the initial wave packet in Eq. (2.52). Expanding $\Psi^{J\Lambda i\Gamma}$ over final states f', excluding the sum over the arrangement channel τ, and projecting the wave packet onto the SA-APH surface functions corresponding to irreducible representation Γ at $\rho = \rho_\infty$, gives

$$\sum_{f'} \mathcal{S}^{J\Gamma}_{f',i}(E)\, A^{J\Gamma}_{\kappa\Lambda,f'}(E;\rho_\infty) = F^{J\Gamma}_{\kappa\Lambda,i}(E;\rho_\infty), \tag{2.66}$$

where

$$F^{J\Gamma}_{\kappa\Lambda,i}(E;\rho_\infty) = \frac{1}{\eta_i(E)}\int_0^\infty \mathrm{d}t\, e^{iEt/\hbar}\, F^{J\Gamma}_{\kappa\Lambda,i}(t;\rho_\infty), \tag{2.67}$$

$$\begin{aligned} F^{J\Gamma}_{\kappa\Lambda,i}(t;\rho_\infty) = &\int_0^{\pi/2} \mathrm{d}\theta\, \sin 2\theta \\ &\times \int_0^{2\pi l_\Gamma/h} \mathrm{d}\chi_i\, \Phi^{Jp\Gamma}_{\kappa\Lambda}(\theta,\chi_i;\rho_\infty)\, \varphi_i^{J\Lambda p\Gamma}(\theta,\chi_i,t;\rho_\infty), \end{aligned} \tag{2.68}$$

and

$$\begin{aligned} A^{J\Gamma}_{\kappa\Lambda,f'}(E;\rho_\infty) = &\int_0^{\pi/2} \mathrm{d}\theta\, \sin 2\theta \\ &\times \int_0^{2\pi l_\Gamma/h} \mathrm{d}\chi_i\, \Phi^{Jp\Gamma}_{\kappa\Lambda}(\theta,\chi_i;\rho_\infty)\, \Psi^{J\Lambda i\Gamma}_{f'}(E,\rho_\infty). \end{aligned} \tag{2.69}$$

The S-matrix elements labeled by irreducible representation are obtained by solving Eq. (2.66) using Eq. (2.64). The S-matrix elements indexed by arrangement channel are linear combinations of those indexed by irreducible representation:

$$\mathcal{S}^{J}_{f,i}(E) = \sum_{\Gamma'} \bar{P}^{\Gamma}_{ff'}\, \mathcal{S}^{J\Gamma}_{f',i}(E), \tag{2.70}$$

where $\bar{P}^{\Gamma}_{f}$ are the matrix elements

$$\bar{P}^{\Gamma}_{f} = \left\langle\, \Psi^{J\Lambda ip}_{f} \,\middle|\, P^{\Gamma} \,\middle|\, \Psi^{J\Lambda i\Gamma}_{f'} \,\right\rangle, \tag{2.71}$$

and P^{Γ} is a projection operator for irreducible representation Γ [31].

A negative imaginary potential (NIP) [53, 54] is used to absorb the wave packet after it crosses the analysis surface at ρ_{∞}. The NIP is applied beginning at the $\rho_{NIP} > \rho_{\infty}$ surface, and has the form

$$V_{NIP} = -iU_{NIP}\left(\frac{\rho - \rho_{NIP}}{\rho_{max} - \rho_{NIP}}\right)^{3} \tag{2.72}$$

for $\rho_{NIP} < \rho \leq \rho_{max}$ and is zero, otherwise. U_{NIP} is the strength of the potential, and is adjusted according to the range of kinetic energies contained in the initial wave packet [54].

CHAPTER 3

COMPUTATION

3.1 Introduction

This chapter discusses the details of implementing the time-dependent hyperspherical method, specifically the computational methods and algorithms used. The majority of the computational time is used to propagate the wave packet in time, so the primary goal of this chapter is to discuss how the wave packet is propagated, how to make the propagation more efficient, and how much computational time is required to run the program for various input parameters.

First, the Chebychev method used to propagate the wave packet will be discussed. This method will require multiple matrix-vector multiplications, as the Hamiltonian is applied to the wave packet. Next, a Sylvester-like algorithm, which is used to make the matrix-vector multiplications more efficient, will be discussed. Finally, the computational times required to run the program will be discussed.

3.2 Chebychev Method

The wave packet is propagated in time, for an interval $\Delta t = t - t_0$, by applying the time-evolution operator:

$$\varphi^{JMp}(t) = e^{-i\mathcal{H}\Delta t/\hbar}\,\varphi^{JMp}(t_0), \tag{3.1}$$

The kinetic energy operators in the Hamiltonian are not diagonal, so we will approximate the time-evolution operator as sum of Chebychev polynomials

[39]. The operation of the time evolution operator can be expanded as [47, 55]:

$$e^{-i\mathcal{H}\Delta t/\hbar}\,\varphi^{JMp}(t_0) = e^{i(E_{max}-E_{min})\Delta t/2\hbar}\sum_{n=0}^{N_C}(2-\delta_{n0})i^n J_n(R)T_n(-i\bar{\mathcal{H}})\,\varphi^{JMp}(t_0), \tag{3.2}$$

where $T_n(-i\bar{\mathcal{H}})$ are the Chebychev polynomials [39], $J_n(R)$ is a regular Bessel function [39], and

$$R = \frac{1}{2\hbar}(E_{max}-E_{min})\Delta t, \tag{3.3}$$

$$\bar{\mathcal{H}} = \frac{2\mathcal{H}-(E_{max}+E_{min})}{E_{max}-E_{min}}. \tag{3.4}$$

E_{min} and E_{max} are the minimum and maximum eigenvalues of the unscaled Hamiltonian, respectively.

The sum requires $N_C + 1$ terms to converge. The quantity N_C depends on the eigenvalue range of the unscaled Hamiltonian and the time interval over which the wave packet is propagated: $N_C = \alpha R$ for $\alpha > 1$. The operator $\bar{\mathcal{H}}$ is the scaled Hamiltonian, and its has been scaled so that its eigenvalues range between -1 and 1. This scaling is done to match the interval over which the Chebychev polynomials are defined.

The Chebychev polynomials are functions of the scaled Hamiltonian operator, so we will calculate their action on the wave packet as

$$\phi_n = T_n(-i\bar{\mathcal{H}})\,\varphi^{JMp}(t_0). \tag{3.5}$$

The terms in the sum are calculated according to the Chebychev recurrence relation [39]

$$\phi_n = -2i\bar{\mathcal{H}}\phi_{n-1} - \phi_{n-2}, \tag{3.6}$$

where $\phi_0 = \varphi^{JMp}(t_0)$ and $\phi_1 = -i\bar{\mathcal{H}}\varphi^{JMp}(t_0)$.

According to Eq. (3.3), the number of terms required increases as the eigenvalue range increases and as the time interval increases. When the eigenvalue range becomes too large, the large value of N_C can cause a large computational cost. Therefore, it is important that the eigenvalue range is accurately determined. To determine the eigenvalue range, we diagonalize the discretized kinetic energy operators in the APH Hamiltonian and sum the maximum eigenvalues. To this we add the maximum value of the potential energy and angular momentum terms. Note that we restrict the maximum value of the potential by setting a cut-off value V_{cut}. We can do this because the wave function will not have amplitude in regions of the PES that are above V_{cut}. We have determined that the minimum number of terms required for the Chebychev sum to converge is about 25 terms, even if the predicted N_C is less than this value.

The Chebychev method is preferred over other methods because its accuracy is dominated by the accuarcy of the computer [56]. The reason for this is that as the order n of the Bessel functions becomes larger than the argument R, the Bessel functions decay exponentially. The error is equally distributed over the entire range of eigenvalues [56]. Furthermore, the method is not limited by the time interval chosen, providing results of the same accuracy as long as enough terms are included in the sum.

3.3 Constraining the Eigenvalue Range

The previous section discussed the importance of the eigenvalue range in determining the computational efficiency of the Chebychev method. Since the time propagation of the wave packet is the most computationally expensive part of the program, it is important to limit the eigenvalue range when it exceeds the physically relevant region of interest.

Referencing Eq. (2.40), the θ and χ_i kinetic energy operators are given by

$$-\frac{\hbar^2}{2\mu\rho^2}\left[\frac{4}{\sin 2\theta}\frac{\partial}{\partial\theta}\sin 2\theta\frac{\partial}{\partial\theta}+\frac{1}{\sin^2\theta}\frac{\partial^2}{\partial\chi_i^2}\right]. \tag{3.7}$$

For small values of θ, the presence of $1/\sin 2\theta$ and $1/\sin^2\theta$ terms in the θ and χ_i kinetic energy operators result in very large eigenvalues. These eigenvalues may exceed the physically relevant energies for a particular scattering experiment and unnecessarily increase the required number of terms in the Chebychev sum. To remove these eigenvalues, the eigenvalues associated with the high energy eigenvectors can be set to a determined energy cut-off value E_{cut}. In the program, E_{cut} is the same as the potential energy cut-off value, V_{cut}.

First, the discretized kinetic energy operator is diagonalized to obtain the eigenvalues and eigenvectors. Then, the kinetic energy matrix operator $\mathbf{T}$ can be written as

$$\mathbf{T}=\sum_{i=1}^{N}\epsilon_i\,\psi_i^{\dagger}\psi_i, \tag{3.8}$$

where ϵ_i is the eigenvalue of the i^{th} eigenvector ψ_i, and N is the dimension of the grid. The first step is to determine which values of i correspond to eigenvalues above E_{cut}, such that the eigenvalues to be kept lie between $i = 0$ and i_{cut}. Next, the terms in the sum with $i > i_{cut}$ are removed from the kinetic energy operator and replaced with $\epsilon_i = E_{cut}$ to give

$$\mathbf{T}_{cut}=\mathbf{T}-\sum_{j=i_{cut}}^{N}\epsilon_j\,\psi_j^{\dagger}\psi_j+\sum_{k=i_{cut}}^{N}E_{cut}\,\psi_k^{\dagger}\psi_k. \tag{3.9}$$

Now the maximum eigenvalue of the kinetic energy operator $\mathbf{T}_{cut}$ is equal to

E_{cut}.

It is important to note that there will not be one specific value of i_{cut} associated with each kinetic energy operator. The θ kinetic energy operator is also a function of ρ^{-2}, so the eigenvalues will be ρ dependent. Therefore, the θ kinetic energy operator eigenvector replacement will have to be done at each ρ grid point. Similarly, the χ_i kinetic energy operator depends on ρ and θ, so the replacement will need to be completed at each ρ and θ grid point. Fortunately, the eigenvalues only exceed E_{cut} at a few grid points, when θ is small, and kinetic energy operators can be used without replacement. Because of this fact, this eigenvalue replacement method is much more efficient than retaining the eigenvalues above E_{cut}.

Similar issues exist for the angular momentum operators that contain $\mathcal{B}_\theta$, $\mathcal{C}_\theta$, and $\mathcal{D}_\theta$, which are defined in Eq. (2.19). These also have large eigenvalues at small values of θ. The best way to eliminate the large energies associated with these terms is to look at the diagonal angular momentum terms in Eq. (2.40):

$$\frac{1}{\mu\rho^2}\left[\frac{\mathcal{A}_\theta+\mathcal{B}_\theta}{2}\hbar^2 J(J+1)+\left(\mathcal{C}_\theta-\frac{\mathcal{A}_\theta+\mathcal{B}_\theta}{2}\right)\hbar^2\Lambda^2\right]. \tag{3.10}$$

Since the matrix associated with these terms is diagonal, there is no need to resolve it into its eigenvectors. We can just replace any energy above E_{cut} with E_{cut}. At points where the energies are replaced, we ignore the asymmetric-top and Coriolis terms, since they will also exceed E_{cut}.

3.4 Efficient Three-Dimensional Sylvester-Like Algorithm for Applying the APH Hamiltonian

3.4.1 Introduction

The most time consuming portion of the program is the time propagation of the wave packet. Since the propagation is facilitated by repeatedly applying the Hamiltonian to the time-dependent wave function, reducing the number of multiplications needed for this matrix-vector multiplication will have a significant effect on the computational efficiency.

In this section, a three-dimensional Sylvester-like algorithm for applying the APH Hamiltonian to the time-dependent wave packet is derived. A detailed derivation is presented since this is a new algorithm I developed by extending the two-dimensional Sylvester algorithm [57]. First, the relevant operators and notation will be introduced and discussed. Next, a proof of the two-dimensional Sylvester algorithm will be presented and applied to the two-dimensional APH Hamiltonian used in time-independent reactive scattering theories. Last, the three-dimensional Sylvester-like algorithm will be derived and its computational efficiency discussed.

3.4.2 Operators and Notation

Matrices and vectors will be denoted by boldface letters (eg. $\mathbf{A}$, $\mathbf{B}$), while scalar quantities will be denoted by math italic text (eg. A, B). Since subscripts will be used as identifying labels, the traditional method for labeling the elements of rank 2 matrices (eg. $A_{i,j}$ for the element of A in row i and column j) will be replaced by the notation $A[i, j]$. For rank 3 matrices, we will use the notation $A[i, j, k]$. To represent a single row or column of a matrix $\mathbf{A}$, the notation $\mathbf{A}[i,:]$ for the i^{th} row and $\mathbf{A}[:,j]$ for the j^{th} column will be used. The colon represents every element contained in the corresponding index. For example, if $\mathbf{A}$ is an $(n_A \times m_A)$ matrix, then

$$\mathbf{A}[i,:] = \begin{pmatrix} A[i,1] & A[i,2] & \cdots & A[i,m_A] \end{pmatrix} \tag{3.11}$$

and

$$\mathbf{A}[:,j] = \begin{pmatrix} A[1,j] \\ A[2,j] \\ \vdots \\ A[n_A,j] \end{pmatrix}. \tag{3.12}$$

For rank 3 matrices, let $\mathbf{B}$ be an $(n_B \times m_B \times p_B)$ matrix. Then, the use of one colon gives a vector:

$$\mathbf{B}[:,j,k] = \begin{pmatrix} B[1,j,k] \\ B[2,j,k] \\ \vdots \\ B[n_B,j,k] \end{pmatrix} \tag{3.13a}$$

$$\mathbf{B}[i,:,k] = \begin{pmatrix} B[i,1,k] \\ B[i,2,k] \\ \vdots \\ B[i,m_B,k] \end{pmatrix} \tag{3.13b}$$

$$\mathbf{B}[i,j,:] = \begin{pmatrix} B[i,j,1] \\ B[i,j,2] \\ \vdots \\ B[i,j,p_B] \end{pmatrix}. \tag{3.13c}$$

The use of two colons gives a rank 2 matrix:

$$\mathbf{B}[:,:,k] = \begin{pmatrix} B[1,1,k] & B[1,2,k] & \cdots & B[1,m_B,k] \\ B[2,1,k] & B[2,2,k] & \cdots & B[2,m_B,k] \\ \vdots & \vdots & \ddots & \vdots \\ B[n_B,1,k] & B[n_B,2,k] & \cdots & B[n_B,m_B,k] \end{pmatrix} \tag{3.14a}$$

$$\mathbf{B}[:,j,:] = \begin{pmatrix} B[1,j,1] & B[1,j,2] & \cdots & B[1,j,p_B] \\ B[2,j,1] & B[2,j,2] & \cdots & B[2,j,p_B] \\ \vdots & \vdots & \ddots & \vdots \\ B[n_B,j,1] & B[n_B,j,2] & \cdots & B[n_B,j,p_B] \end{pmatrix} \tag{3.14b}$$

$$\mathbf{B}[i,:,:] = \begin{pmatrix} B[i,1,1] & B[i,1,2] & \cdots & B[i,1,p_B] \\ B[i,2,1] & B[i,2,2] & \cdots & B[i,2,p_B] \\ \vdots & \vdots & \ddots & \vdots \\ B[i,m_B,1] & B[i,m_B,2] & \cdots & B[i,m_B,p_B] \end{pmatrix}. \tag{3.14c}$$

Let **A** and **B** be matrices with, $\mathbf{A} \in \Re^{n_A \times n_A}$ and $\mathbf{B} \in \Re^{n_B \times n_B}$. The Kronecker product of **A** and **B** is given by [57]

$$\mathbf{A} \otimes \mathbf{B} = \begin{pmatrix} A[1,1]\mathbf{B} & A[1,2]\mathbf{B} & \cdots & A[1,n_A]\mathbf{B} \\ A[2,1]\mathbf{B} & A[2,2]\mathbf{B} & \cdots & A[2,n_A]\mathbf{B} \\ \vdots & \vdots & \ddots & \vdots \\ A[n_A,1]\mathbf{B} & A[n_A,2]\mathbf{B} & \cdots & A[n_A,n_A]\mathbf{B} \end{pmatrix}, \tag{3.15}$$

an $n_A n_B \times n_A n_B$ matrix.

For a two dimensional case, let **X** be a matrix with $\mathbf{X} \in \Re^{n_A \times n_B}$. Applying the vec operator [57] to **X** stacks the columns of **X** into a vector of length

$n_A n_B$:

$$\operatorname{vec}(\mathbf{X}) = \begin{pmatrix} X[1,1] \\ \vdots \\ X[n_A,1] \\ X[1,2] \\ \vdots \\ X[n_A,2] \\ \vdots \\ \vdots \\ X[1,n_B] \\ \vdots \\ X[n_A,n_B] \end{pmatrix} = \begin{pmatrix} \mathbf{X}[:,1] \\ \mathbf{X}[:,2] \\ \vdots \\ \mathbf{X}[:,n_B] \end{pmatrix} \tag{3.16}$$

For a three dimensional case, let $\mathbf{X}$ be a matrix with $\mathbf{X} \in \Re^{n_A \times n_B \times n_C}$. Applying the vec operator gives a vector of length $n_A n_B n_C$:

$$\operatorname{vec}(\mathbf{X}) = \begin{pmatrix} \mathbf{X}[:,1,1] \\ \vdots \\ \mathbf{X}[:,1,n_C] \\ \mathbf{X}[:,2,1] \\ \vdots \\ \mathbf{X}[:,2,n_C] \\ \vdots \\ \vdots \\ \mathbf{X}[:,n_B,1] \\ \vdots \\ \mathbf{X}[:,n_B,n_C] \end{pmatrix} \tag{3.17}$$

Other useful ways to write Eqn. (3.17), which will be used later, are

$$\mathrm{vec}(\mathbf{X}) = \begin{pmatrix} \mathrm{vec}(\mathbf{X}[:, 1, :]) \\ \mathrm{vec}(\mathbf{X}[:, 2, :]) \\ \vdots \\ \mathrm{vec}(\mathbf{X}[:, n_B, :]) \end{pmatrix} \tag{3.18}$$

and

$$\mathrm{vec}(\mathbf{X}) = \mathrm{vec} \begin{pmatrix} \mathbf{X}[:, :, 1] \\ \mathbf{X}[:, :, 2] \\ \vdots \\ \mathbf{X}[:, :, n_C] \end{pmatrix} \tag{3.19}$$

3.4.3 Operations in Two Dimensions

In this section, we will be dealing with discretized two-dimensional operations of the form

$$\mathbf{Cx} = (\mathbf{B} \otimes \mathbf{A})\mathrm{vec}(\mathbf{X}), \tag{3.20}$$

where $\mathbf{B} \in \Re^{n_B \times n_B}$, $\mathbf{A} \in \Re^{n_A \times n_A}$, $\mathbf{X} \in \Re^{n_A \times n_B}$, $\mathbf{C} \in \Re^{n_A n_B \times n_A n_B}$, $\mathbf{x} \in \Re^{n_A n_B \times 1}$, and $\mathbf{x} = \mathrm{vec}(\mathbf{X})$. The operation of $\mathbf{C}$ on $\mathbf{x}$ requires $2n_A^2 n_B^2$ multiplications. The number of multiplications can be reduced by rewriting Eq. (3.20) as [57]

$$(\mathbf{B} \otimes \mathbf{A})\mathrm{vec}(\mathbf{X}) = \mathrm{vec}(\mathbf{AXB}^{\mathrm{T}}), \tag{3.21}$$

which requires $n_A^2 n_B + n_A n_B^2$ multiplications. Eq. (3.21) is the Sylvester identity [57].

Proof of Eq. (3.21): (See Ref. [57]) We begin with the k^{th} column of the product $\mathbf{AXB}^T$, denoted $(\mathbf{AXB}^T)[:,k]$,

$$\begin{aligned}(\mathbf{AXB}^T)[:,k] &= \mathbf{A}(\mathbf{XB}^T)[:,k]\\ &= \mathbf{AXB}^T[:,k]\\ &= \mathbf{A}\sum_{i=1}^{n_B}\mathbf{X}[:,k]\ B^T[i,k]\\ &= (\mathbf{A}B[1,k]\,\mathbf{A}B[2,k]\ \cdots\mathbf{A}B[n_B,k])\,\mathrm{vec}(\mathbf{X})\\ &= (\mathbf{B}[:,k]\otimes\mathbf{A})\mathrm{vec}(\mathbf{X}). \qquad (3.22)\end{aligned}$$

Including all n_B columns of $\mathbf{B}$ gives

$$\mathrm{vec}(\mathbf{AXB}^T) = \begin{pmatrix}\mathbf{B}[:,1]\otimes\mathbf{A}\\ \mathbf{B}[:,2]\otimes\mathbf{A}\\ \vdots\\ \mathbf{B}[:,n_B]\otimes\mathbf{A}\end{pmatrix}\mathrm{vec}(\mathbf{X}) = (\mathbf{B}\otimes\mathbf{A})\mathrm{vec}(\mathbf{X}). \qquad (3.23)$$

The expression in Eq. (3.21) can be used in time-independent three-atom quantum reactive scattering (QRS) calculations to reduce the number of multiplications involved in applying the Hamiltonian operator to the wave function [58]. In this case, the adiabatically adjusting, principal axes hyperspherical (APH) coordinates [1] will be used. The APH kinetic energy operator for total angular momentum $J = 0$ is given by

$$T = -\frac{\hbar^2}{2\mu\rho^5}\frac{\partial}{\partial\rho}\rho^5\frac{\partial}{\partial\rho} - \frac{\hbar^2}{2\mu\rho^2}\frac{4}{\sin 2\theta}\frac{\partial}{\partial\theta}\sin 2\theta\frac{\partial}{\partial\theta} - \frac{\hbar^2}{2\mu\rho^2}\frac{1}{\sin^2\theta}\frac{\partial^2}{\partial\chi_i^2}. \qquad (3.24)$$

Solutions for the terms containing only the θ and χ derivatives, with ρ as a parameter, are useful in QRS problems [58, 45], and the two-dimensional kinetic energy operator is given by

$$T_{2D} = -\frac{\hbar^2}{2\mu\rho_\xi^2}\frac{4}{\sin 2\theta}\frac{\partial}{\partial\theta}\sin 2\theta\frac{\partial}{\partial\theta} - \frac{\hbar^2}{2\mu\rho_\xi^2}\frac{1}{\sin^2\theta}\frac{\partial^2}{\partial\chi_i^2}, \tag{3.25}$$

where ρ_ξ is a fixed value. Adding the potential energy operator provides the full Hamiltonian:

$$H_{2D} = h_\theta + f_\theta h_\chi + \tilde{V}_{2D}, \tag{3.26}$$

where

$$h_\theta = -\frac{\hbar^2}{2\mu\rho_\xi^2}\frac{4}{\sin 2\theta}\frac{\partial}{\partial\theta}\sin 2\theta\frac{\partial}{\partial\theta} \tag{3.27a}$$

$$h_\chi = -\frac{\hbar^2}{2\mu\rho_\xi^2}\frac{\partial^2}{\partial\chi_i^2} \tag{3.27b}$$

$$f_\theta = \frac{1}{\sin^2\theta} \tag{3.27c}$$

$$\tilde{V}_{2D} = V(\rho_\xi, \theta, \chi_i) + \frac{15\hbar^2}{8\mu\rho_\xi^2}. \tag{3.27d}$$

Solutions for H_{2D} are obtained via the Schrödinger equation

$$H_{2D}\phi_i = \mathcal{E}_i\phi_i, \tag{3.28}$$

where ϕ_i are the eigenfunctions and $\mathcal{E}_i$ are the energy eigenvalues. Discretizing the application of the Hamiltonian to the wave function, with n_ρ, n_θ, and n_χ representing the number of grid points for each coordinate, the left-hand side of Eq. (3.28) gives an expression with terms that are analogous to Eq. (3.20):

$$\mathbf{H}_{2D}\phi_i = (\mathbf{f}_\theta \otimes \mathbf{h}_\chi + \mathbf{h}_\theta \otimes \mathbf{I}_\chi + \tilde{\mathbf{V}}_{2D})\mathrm{vec}(\mathbf{\Phi}_\mathrm{i}). \tag{3.29}$$

In Eq. (3.29), $\{\mathbf{f}_\theta, \mathbf{h}_\theta\} \in \Re^{n_\theta \times n_\theta}$, $\mathbf{h}_\chi \in \Re^{n_\chi \times n_\chi}$, $\tilde{\mathbf{V}}_{2D} \in \Re^{n_\theta n_\chi \times n_\theta n_\chi}$, $\mathbf{\Phi}_i \in \Re^{n_\chi \times n_\theta}$, $\phi_i \in \Re^{n_\chi n_\theta \times 1}$, and $\mathbf{I}_\chi$ is an $(n_\chi \times n_\chi)$ identity matrix. Note that $\tilde{\mathbf{V}}_{2D}$ and $\mathbf{f}_\theta$ are both diagonal matrices and that $\phi_i = \mathrm{vec}(\mathbf{\Phi}_\mathrm{i})$. This Kronecker product form requires $2n_\theta n_\chi^2 + 2n_\theta^2 n_\chi + n_\theta n_\chi$ multiplications, not counting multiplications by zero. Using the Sylvester identity in Eq. (3.21) gives

$$(\mathbf{f}_\theta \otimes \mathbf{h}_\chi)\mathrm{vec}(\mathbf{\Phi}_\mathrm{i}) = \mathrm{vec}(\mathbf{h}_\chi \mathbf{\Phi}_i \mathbf{f}_\theta) \tag{3.30}$$

$$(\mathbf{h}_\theta \otimes \mathbf{I}_\chi)\mathrm{vec}(\mathbf{\Phi}_\mathrm{i}) = \mathrm{vec}(\mathbf{I}_\chi \mathbf{\Phi}_i \mathbf{h}_\theta^T) = \mathrm{vec}(\mathbf{\Phi}_i \mathbf{h}_\theta^T), \tag{3.31}$$

which provides

$$\mathbf{H}_{2D}\phi_i = \mathrm{vec}(\mathbf{h}_\chi \mathbf{\Phi}_i \mathbf{f}_\theta + \mathbf{\Phi}_i \mathbf{h}_\theta^T) + \tilde{\mathbf{V}}_{2D}\mathrm{vec}(\mathbf{\Phi}_i), \tag{3.32}$$

requiring $n_\theta n_\chi^2 + n_\theta^2 n_\chi + 2n_\theta n_\chi$ multiplications, not counting multiplications by zero. The new form requires $n_\theta n_\chi^2 + n_\theta^2 n_\chi - n_\theta n_\chi$ less multiplications than the Kronecker product form.

3.4.4 Operations in Three Dimensions

The three-dimensional Hamiltonian that is applied to the wave packet is given in Eq. 2.40. It can be rewritten as

$$\begin{aligned} H_{3D} =& h_\rho + f_\rho h_\theta + f_\rho f_\theta h_\chi + \tilde{V} \\ & + f_\rho(\mathcal{A}_\theta + \mathcal{B}_\theta)J(J+1) + f_\rho(\mathcal{C}_\theta - \mathcal{A}_\theta - \mathcal{B}_\theta)\Lambda^2 \\ & - g_2 f_\rho \left(\frac{\mathcal{A}_\theta - \mathcal{B}_\theta}{2\hbar^2}\right) - g_1 f_\rho \left(\frac{\mathcal{D}_\theta}{\hbar}\right) h^1_{\chi_i}, \end{aligned} \tag{3.33}$$

where $\mathcal{A}_\theta$, $\mathcal{B}_\theta$, $\mathcal{C}_\theta$, and $\mathcal{D}_\theta$ are given in Eq. (2.19), and

$$h_\rho = -\frac{\hbar^2}{2\mu}\frac{\partial^2}{\partial\rho^2} \tag{3.34a}$$

$$h_\theta = -\frac{4}{\sin 2\theta}\frac{\partial}{\partial\theta}\sin 2\theta\frac{\partial}{\partial\theta} \tag{3.34b}$$

$$h_\chi = -\frac{\partial^2}{\partial\chi^2} \tag{3.34c}$$

$$h_\chi^1 = -\frac{\partial}{\partial\chi} \tag{3.34d}$$

$$f_\rho = \frac{\hbar^2}{2\mu\rho^2} \tag{3.34e}$$

$$f_\theta = \frac{1}{\sin^2\theta} \tag{3.34f}$$

$$\tilde{V} = V(\rho,\theta,\chi) + \frac{15\hbar^2}{8\mu\rho^2} \tag{3.34g}$$

$$g_1 = \sum_{\Lambda'=0}^{J}\big\langle \hat{D}^{Jp}_{\Lambda M}\,\big|\, i\hbar J_y \,\big|\, \hat{D}^{Jp}_{\Lambda' M}\big\rangle \tag{3.34h}$$

$$g_2 = \sum_{\Lambda'=0}^{J}\big\langle \hat{D}^{Jp}_{\Lambda M}\,\big|\, J_x^2 - J_y^2 \,\big|\, \hat{D}^{Jp}_{\Lambda' M}\big\rangle. \tag{3.34i}$$

Note that the definitions of h_θ and h_χ are different than in the 2D case.

Propagation of the time-dependent wave packet ϕ_t is facilitated by applying the Hamiltonian, as shown in Eq. (2.40). Here, the wave packet is represented by ϕ_t to avoid a large number of indices. The only index of importance that is suppressed is Λ, which couples off-diagonal terms. This will be referenced when necessary.

Discretizing the application of the Hamiltonian on the wave function gives an expression with terms that are analogous to Eq. (3.29):

$$\begin{aligned}
\mathbf{H}_{3D}\psi_t = {} & (\mathbf{f}_\rho \otimes \mathbf{f}_\theta \otimes \mathbf{h}_\chi + \mathbf{f}_\rho \otimes \mathbf{h}_\theta \otimes \mathbf{I}_\chi + \mathbf{h}_\rho \otimes \mathbf{I}_\theta \otimes \mathbf{I}_\chi + \tilde{\mathbf{V}})\mathrm{vec}(\mathbf{\Psi}_\mathrm{t}) \\
& + J(J+1)\left[\mathbf{f}_\rho \otimes (\mathcal{A}_\theta + \mathcal{B}_\theta) \otimes \mathbf{I}_\chi\right]\mathrm{vec}(\mathbf{\Psi}_t) \\
& + \Lambda^2\left[\mathbf{f}_\rho \otimes (2\mathcal{C}_\theta - \mathcal{A}_\theta - \mathcal{B}_\theta) \otimes \mathbf{I}_\chi\right]\mathrm{vec}(\mathbf{\Psi}_t) \\
& - \left\{\frac{g_2}{2\hbar^2}\left[\mathbf{f}_\rho \otimes (\mathcal{A}_\theta - \mathcal{B}_\theta) \otimes \mathbf{I}_\chi\right] + \frac{g_1}{\hbar}\left[\mathbf{f}_\rho \otimes \mathcal{D}_\theta \otimes h^1_\chi\right]\right\}\mathrm{vec}(\mathbf{\Psi}_t), \quad (3.35)
\end{aligned}$$

with $\{\mathbf{f}_\rho, \mathbf{h}_\rho\} \in \Re^{n_\rho \times n_\rho}$, $\{\mathbf{f}_\theta, \mathbf{h}_\theta, \mathcal{A}_\theta, \mathcal{B}_\theta, \mathcal{C}_\theta, \mathcal{D}_\theta\} \in \Re^{n_\theta \times n_\theta}$, $\{\mathbf{h}_\chi, \mathbf{h}^1_\chi\} \in \Re^{n_\chi \times n_\chi}$, $\tilde{\mathbf{V}} \in \Re^{n_\rho n_\theta n_\chi \times n_\rho n_\theta n_\chi}$, $\mathbf{\Psi}_t \in \Re^{n_\chi \times n_\rho \times n_\theta}$, and $\psi_t \in \Re^{n_\chi n_\rho n_\theta \times 1}$. Also, $\mathbf{I}_\theta$ and $\mathbf{I}_\chi$ are $(n_\theta \times n_\theta)$ and $(n_\chi \times n_\chi)$ identity matrices, respectively. Note that $\tilde{\mathbf{V}}$, $\mathbf{f}_\rho$, $\mathbf{f}_\theta$, $\mathcal{A}_\theta$, $\mathcal{B}_\theta$, $\mathcal{C}_\theta$, $\mathcal{D}_\theta$ are all diagonal matrices.

We seek to reduce the number of multiplications needed to compute $\mathbf{H}_{3D}\psi_t$. As with the potential energy term, the $J(J+1)$ and Λ^2 terms are diagonal and do not require attention to make them more efficient. Furthermore, the matrices that form the asymmetric top term are all diagonal with respect to the coordinate grid and do not require attention either. The terms of interest contain the ρ kinetic energy operator, the θ kinetic energy operator, the χ_i kinetic energy operator, and the χ_i first derivative Coriolis coupling operator.

The right-hand side of Eq. (3.35) can be written as

$$\mathbf{H}_{3D}\psi_t = \mathrm{vec}(\mathbf{Y}) + \mathbf{Z}\mathrm{vec}(\mathbf{\Psi}_\mathrm{t}), \quad (3.36)$$

where $\mathbf{Z}$ is a diagonal matrix containing the terms that do not need attention. The term $\mathbf{Y} \in \Re^{n_\chi \times n_\rho \times n_\theta}$ is a rank 3 tensor obtained by regular matrix multiplication, rather than by Kronecker product, and can be written as

$$\mathbf{Y} = \mathbf{Y}_\chi + \mathbf{Y}_\theta + \mathbf{Y}_\rho + \mathbf{Y}_\chi^1 \tag{3.37}$$

$$\mathrm{vec}(\mathbf{Y}) = \mathrm{vec}(\mathbf{Y}_\chi) + \mathrm{vec}(\mathbf{Y}_\theta) + \mathrm{vec}(\mathbf{Y}_\rho) + \mathrm{vec}(\mathbf{Y}_\chi^1). \tag{3.38}$$

The χ_i, θ, and ρ components of $\mathbf{Y}$ satisfy the equations

$$(\mathbf{f}_\rho \otimes \mathbf{f}_\theta \otimes \mathbf{h}_\chi)\mathrm{vec}(\mathbf{\Psi}_t) = \mathrm{vec}(\mathbf{Y}_\chi) \tag{3.39a}$$

$$(\mathbf{f}_\rho \otimes \mathbf{h}_\theta \otimes \mathbf{I}_\chi)\mathrm{vec}(\mathbf{\Psi}_t) = \mathrm{vec}(\mathbf{Y}_\theta) \tag{3.39b}$$

$$(\mathbf{h}_\rho \otimes \mathbf{I}_\theta \otimes \mathbf{I}_\chi)\mathrm{vec}(\mathbf{\Psi}_t) = \mathrm{vec}(\mathbf{Y}_\rho) \tag{3.39c}$$

$$\frac{g_1}{\hbar}(\mathbf{f}_\rho \otimes \mathcal{D}_\theta \otimes h_\chi^1)\mathrm{vec}(\mathbf{\Psi}_t) = \mathrm{vec}(\mathbf{Y}_\chi^1). \tag{3.39d}$$

The individual $\mathbf{Y}_i$ terms can be determined by rearranging the left-hand sides of the expressions in Eq. (3.39), as was done in the two-dimensional case.

First, we will find $\mathbf{Y}_\chi$ using Eqn. (3.39a). Rewriting the terms on the left-hand side gives

$$(\mathbf{f}_\rho \otimes \mathbf{f}_\theta \otimes \mathbf{h}_\chi) =$$

$$\begin{pmatrix} f_\rho[1,1](\mathbf{f}_\theta \otimes \mathbf{h}_\chi) & 0 & \cdots & 0 \\ 0 & f_\rho[2,2](\mathbf{f}_\theta \otimes \mathbf{h}_\chi) & \cdots & 0 \\ \vdots & \vdots & \ddots & \vdots \\ 0 & 0 & \cdots & f_\rho[n_\rho,n_\rho](\mathbf{f}_\theta \otimes \mathbf{h}_\chi) \end{pmatrix}, \tag{3.40a}$$

$$\mathrm{vec}(\mathbf{\Psi}_t) = \begin{pmatrix} \mathrm{vec}(\mathbf{\Psi}_t[:,1,:]) \\ \mathrm{vec}(\mathbf{\Psi}_t[:,2,:]) \\ \vdots \\ \mathrm{vec}(\mathbf{\Psi}_t[:,n_\rho,:]) \end{pmatrix}. \tag{3.40b}$$

The product of these can be written

$$(\mathbf{f}_\rho \otimes \mathbf{f}_\theta \otimes \mathbf{h}_\chi)\mathrm{vec}(\mathbf{\Psi}_t) = \begin{pmatrix} f_\rho[1,1](\mathbf{f}_\theta \otimes \mathbf{h}_\chi)\mathrm{vec}(\mathbf{\Psi}_t[:,1,:]) \\ f_\rho[2,2](\mathbf{f}_\theta \otimes \mathbf{h}_\chi)\mathrm{vec}(\mathbf{\Psi}_t[:,2,:]) \\ \vdots \\ f_\rho[n_\rho,n_\rho](\mathbf{f}_\theta \otimes \mathbf{h}_\chi)\mathrm{vec}(\mathbf{\Psi}_t[:,n_\rho,:]) \end{pmatrix}. \tag{3.41}$$

Using the two-dimensional relation from Eq. (3.21), each row of the right-hand side of Eq. (3.41) can be written as

$$f_\rho[j,j](\mathbf{f}_\theta \otimes \mathbf{h}_\chi)\mathrm{vec}(\mathbf{\Psi}_t[:,j,:]) = \mathrm{vec}(f_\rho[j,j]\mathbf{h}_\chi \mathbf{\Psi}_t[:,j,:]\mathbf{f}_\theta), \tag{3.42}$$

giving

$$\begin{aligned}(\mathbf{f}_\rho \otimes \mathbf{f}_\theta \otimes \mathbf{h}_\chi)\mathrm{vec}(\mathbf{\Psi}_t) &= \begin{pmatrix} \mathrm{vec}\left(f_\rho[1,1]\mathbf{h}_\chi \mathbf{\Psi}_t[:,1,:]\mathbf{f}_\theta\right) \\ \mathrm{vec}\left(f_\rho[2,2]\mathbf{h}_\chi \mathbf{\Psi}_t[:,2,:]\mathbf{f}_\theta\right) \\ \vdots \\ \mathrm{vec}\left(f_\rho[n_\rho,n_\rho]\mathbf{h}_\chi \mathbf{\Psi}_t[:,n_\rho,:]\mathbf{f}_\theta\right) \end{pmatrix} \\ &= \begin{pmatrix} \mathrm{vec}\left(\mathbf{Y}_\chi[:,1,:]\right) \\ \mathrm{vec}\left(\mathbf{Y}_\chi[:,2,:]\right) \\ \vdots \\ \mathrm{vec}\left(\mathbf{Y}_\chi[:,n_\rho,:]\right) \end{pmatrix} = \mathrm{vec}(\mathbf{Y}_\chi). \end{aligned} \tag{3.43}$$

Then, $\mathbf{Y}_\chi$ is given by

$$\mathbf{Y}_\chi[:, j, :] = f_\rho[j, j]\mathbf{h}_\chi \mathbf{\Psi}_t[:, j, :]\mathbf{f}_\theta. \tag{3.44}$$

Obtaining $\mathbf{Y}_\chi$ using Eq. (3.44) requires $n_\rho(n_\theta n_\chi^2 + n_\theta n_\chi + 1)$ multiplications However, this form is not the most efficient, though it is more efficient than the Kronecker form. We compute the χ vectors of $\mathbf{Y}_\chi$ for each set of ρ and θ values according to

$$\begin{aligned} \mathbf{Y}_\chi[:, j, k] &= f_\rho[j, j]\mathbf{h}_\chi \mathbf{\Psi}_t[:, j, :]\mathbf{f}_\theta[:, k] && (3.45) \\ &= f_\rho[j, j]\mathbf{h}_\chi \mathbf{\Psi}_t[:, j, k] f_\theta[k, k], && (3.46) \end{aligned}$$

where Eq. (3.46) arises since $\mathbf{f}_\theta$ is diagonal. This requires $n_\rho n_\theta(n_\chi^2 + 2)$ multiplications to obtain the full $\mathbf{Y}_\chi$, which is $n_\rho(n_\theta n_\chi - 2n_\theta + 1)$ less than for Eq. (3.44). Therefore, computation of $\mathbf{Y}_\chi$ is most efficient when its components are calculated via

$$\mathbf{Y}_\chi[:, j, k] = f_\rho[j, j] f_\theta[k, k]\mathbf{h}_\chi \mathbf{\Psi}_t[:, j, k], \tag{3.47}$$

which requires $n_\rho n_\theta(n_\chi^2+2)$ multiplications to obtain the full $\mathbf{Y}_\chi$, not including multiplications by zero.

Since Eq. (3.39d) is similar to Eq. (3.39a), with diagonal ρ and θ terms in the Kronecker product, the expression for $\mathbf{Y}_\chi^1$ can be found using a similar procedure. Referencing Eq. (3.48), the expression for $\mathbf{Y}_\chi^1$ is given by

$$\mathbf{Y}_\chi^1[:, j, k] = \frac{g_1}{\hbar} f_\rho[j, j]\mathcal{D}_\theta[k, k]\mathbf{h}_\chi^1 \mathbf{\Psi}_t[:, j, k], \tag{3.48}$$

requiring the same number of multiplications as $\mathbf{Y}_\chi$

Next, we will find $\mathbf{Y}_\theta$ using Eq. (3.39b). Rewriting the terms on the left-hand side gives

$$(\mathbf{f}_\rho \otimes \mathbf{h}_\theta \otimes \mathbf{I}_\chi) = \\ \begin{pmatrix} f_\rho[1,1](\mathbf{h}_\theta \otimes \mathbf{I}_\chi) & 0 & \cdots & 0 \\ 0 & f_\rho[2,2](\mathbf{h}_\theta \otimes \mathbf{I}_\chi) & \cdots & 0 \\ \vdots & \vdots & \ddots & \vdots \\ 0 & 0 & \cdots & f_\rho[n_\rho,n_\rho](\mathbf{h}_\theta \otimes \mathbf{I}_\chi) \end{pmatrix}, \tag{3.49a}$$

$$\text{vec}(\boldsymbol{\Psi}_t) = \begin{pmatrix} \text{vec}(\boldsymbol{\Psi}_t[:,1,:]) \\ \text{vec}(\boldsymbol{\Psi}_t[:,2,:]) \\ \vdots \\ \text{vec}(\boldsymbol{\Psi}_t[:,n_\rho,:]) \end{pmatrix}. \tag{3.49b}$$

The product of these can be written as

$$(\mathbf{f}_\rho \otimes \mathbf{h}_\theta \otimes \mathbf{I}_\chi)\text{vec}(\boldsymbol{\Psi}_t) = \begin{pmatrix} f_\rho[1,1](\mathbf{h}_\theta \otimes \mathbf{I}_\chi)\text{vec}(\boldsymbol{\Psi}_t[:,1,:]) \\ f_\rho[2,2](\mathbf{h}_\theta \otimes \mathbf{I}_\chi)\text{vec}(\boldsymbol{\Psi}_t[:,2,:]) \\ \vdots \\ f_\rho[n_\rho,n_\rho](\mathbf{h}_\theta \otimes \mathbf{I}_\chi)\text{vec}(\boldsymbol{\Psi}_t[:,n_\rho,:]) \end{pmatrix}. \tag{3.50}$$

Using the two-dimensional relation from Eq. (3.21), each row of the right-hand side of Eq. (3.50) can be written as

$$\begin{aligned} f_\rho[j,j](\mathbf{h}_\theta \otimes \mathbf{I}_\chi)\mathrm{vec}(\boldsymbol{\Psi}_t[:,j,:]) &= f_\rho[j,j]\mathrm{vec}(\mathbf{I}_\chi \boldsymbol{\Psi}_t[:,j,:]\mathbf{h}_\theta^T) \\ &= \mathrm{vec}(f_\rho[j,j]\boldsymbol{\Psi}_t[:,j,:]\mathbf{h}_\theta^T), \end{aligned} \tag{3.51}$$

giving

$$\begin{aligned} (\mathbf{f}_\rho \otimes \mathbf{h}_\theta \otimes \mathbf{I}_\chi)\mathrm{vec}(\boldsymbol{\Psi}_t) &= \begin{pmatrix} \mathrm{vec}\left(f_\rho[1,1]\boldsymbol{\Psi}_t[:,1,:]\mathbf{h}_\theta^T\right) \\ \mathrm{vec}\left(f_\rho[2,2]\boldsymbol{\Psi}_t[:,2,:]\mathbf{h}_\theta^T\right) \\ \vdots \\ \mathrm{vec}\left(f_\rho[n_\rho,n_\rho]\boldsymbol{\Psi}_t[:,n_\rho,:]\mathbf{h}_\theta^T\right) \end{pmatrix} \\ &= \begin{pmatrix} \mathrm{vec}\left(\mathbf{Y}_\theta[:,1,:]\right) \\ \mathrm{vec}\left(\mathbf{Y}_\theta[:,2,:]\right) \\ \vdots \\ \mathrm{vec}\left(\mathbf{Y}_\theta[:,n_\rho,:]\right) \end{pmatrix} = \mathrm{vec}(\mathbf{Y}_\theta). \end{aligned} \tag{3.52}$$

Then $\mathbf{Y}_\theta$ is given by

$$\mathbf{Y}_\theta[:,j,:] = f_\rho[j,j]\boldsymbol{\Psi}_t[:,j,:]\mathbf{h}_\theta^T. \tag{3.53}$$

Obtaining $\mathbf{Y}_\theta$ using Eq. (3.53) requires $n_\rho(n_\theta^2 n_\chi + 1)$ multiplications. This is the most efficient form.

Finally, we will find $\mathbf{Y}_\rho$ using Eq. (3.39c). Rewriting the terms on the left-hand side gives

$$(\mathbf{h}_\rho \otimes \mathbf{I}_\theta \otimes \mathbf{I}_\chi)\mathrm{vec}(\boldsymbol{\Psi}_t) = (\mathbf{h}_\rho \otimes \mathbf{I}_{\chi\theta})\mathrm{vec}\begin{pmatrix} \boldsymbol{\Psi}_t[:,:,1] \\ \boldsymbol{\Psi}_t[:,:,2] \\ \vdots \\ \boldsymbol{\Psi}_t[:,:,n_\theta] \end{pmatrix}. \tag{3.54}$$

The $\mathbf{I}_{\chi\theta}$ term is an $(n_\theta n_\chi \times n_\theta n_\chi)$ identity matrix obtained from

$$\mathbf{I}_\theta \otimes \mathbf{I}_\chi = \mathbf{I}_{\chi\theta}, \tag{3.55}$$

and we use

$$\mathrm{vec}(\boldsymbol{\Psi}_t) = \mathrm{vec}\begin{pmatrix} \boldsymbol{\Psi}_t[:,:,1] \\ \boldsymbol{\Psi}_t[:,:,2] \\ \vdots \\ \boldsymbol{\Psi}_t[:,:,n_\theta] \end{pmatrix}, \tag{3.56}$$

as shown in Eq. (3.19). Using the two-dimensional relation from Eq. (3.21), the right-hand side of Eq. (3.54) can be written as

$$\begin{aligned}(\mathbf{h}_\rho \otimes \mathbf{I}_{\chi\theta})\mathrm{vec}\begin{pmatrix} \boldsymbol{\Psi}_t[:,:,1] \\ \boldsymbol{\Psi}_t[:,:,2] \\ \vdots \\ \boldsymbol{\Psi}_t[:,:,n_\theta] \end{pmatrix} &= \mathrm{vec}\left\{\mathbf{I}_\chi \begin{pmatrix} \boldsymbol{\Psi}_t[:,:,1] \\ \boldsymbol{\Psi}_t[:,:,2] \\ \vdots \\ \boldsymbol{\Psi}_t[:,:,n_\theta] \end{pmatrix} \mathbf{h}_\rho^T \right\} \\ &= \mathrm{vec}\begin{pmatrix} \boldsymbol{\Psi}_t[:,:,1]\mathbf{h}_\rho^T \\ \boldsymbol{\Psi}_t[:,:,2]\mathbf{h}_\rho^T \\ \vdots \\ \boldsymbol{\Psi}_t[:,:,n_\theta]\mathbf{h}_\rho^T \end{pmatrix},\end{aligned} \tag{3.57}$$

and

$$(\mathbf{h}_\rho \otimes \mathbf{I}_\theta \otimes \mathbf{I}_\chi)\mathrm{vec}(\boldsymbol{\Psi}_t) = \mathrm{vec}\begin{pmatrix} \boldsymbol{\Psi}_t[:,:,1]\mathbf{h}_\rho^T \\ \boldsymbol{\Psi}_t[:,:,2]\mathbf{h}_\rho^T \\ \vdots \\ \boldsymbol{\Psi}_t[:,:,n_\theta]\mathbf{h}_\rho^T \end{pmatrix}$$

$$= \begin{pmatrix} \mathrm{vec}\left(\mathbf{Y}_\rho[:,:,1]\right) \\ \mathrm{vec}\left(\mathbf{Y}_\rho[:,:,2]\right) \\ \vdots \\ \mathrm{vec}\left(\mathbf{Y}_\rho[:,:,n_\theta]\right) \end{pmatrix} = \mathrm{vec}(\mathbf{Y}_\rho). \tag{3.58}$$

Then $\mathbf{Y}\rho$ is given by

$$\mathbf{Y}_\rho[:,:,k] = \boldsymbol{\Psi}_t[:,:,k]\mathbf{h}_\rho^T. \tag{3.59}$$

Obtaining $\mathbf{Y}_\rho$ using Eq. (3.59) requires $n_\rho^2 n_\theta n_\chi$ multiplications, and this is the most efficient form.

The expressions for all four $\mathbf{Y}_i$ terms are

$$\begin{aligned} \mathbf{Y}_\chi[:,j,k] &= f_\rho[j,j] f_\theta[k,k]\mathbf{h}_\chi \boldsymbol{\Psi}_t[:,j,k] \\ \mathbf{Y}_\theta[:,j,:] &= f_\rho[j,j]\boldsymbol{\Psi}_t[:,j,:]\mathbf{h}_\theta^T \\ \mathbf{Y}_\rho[:,:,k] &= \boldsymbol{\Psi}_t[:,:,k]\mathbf{h}_\rho^T \\ \mathbf{Y}_\chi^1[:,j,k] &= \frac{g_1}{\hbar} f_\rho[j,j]\mathcal{D}_\theta[k,k]\mathbf{h}_\chi^1 \boldsymbol{\Psi}_t[:,j,k]. \end{aligned}$$

For later comparisons, we will compare the number of multiplications required for the $J = 0$ Hamiltonian, which consists of the ρ, θ, and χ_i kinetic energy terms and the potential energy. The kronecker form requires $2n_\rho n_\theta n_\chi^2 + 2n_\rho n_\theta^2 n_\chi + 2n_\rho^2 n_\theta n_\chi + n_\rho n_\theta n_\chi$ multiplications, while the matrix multiply form requires $n_\rho n_\theta(n_\chi^2+2)+n_\rho(n_\theta^2 n_\chi+1)+n_\rho^2 n_\theta n_\chi+n_\rho n_\theta n_\chi$ multiplications. The matrix multiply form requires $n_\rho^2 n_\theta n_\chi+n_\rho n_\theta^2 n_\chi+n_\rho n_\theta n_\chi^2-n_\rho n_\theta-n_\rho$ fewer multiplications than the Kronecker form.

Fig. 3.1 compares the scaling of the number of multiplications required for the Kronecker and Sylvester-like methods when the total angular momentum is $J=0$. Figs. 3.1a and 3.1b compare the scaling as a function of N_ρ for $N_\theta=31$, $N_{\chi_i}=241$ and $N_\theta=65$, $N_{\chi_i}=481$, respectively. Not only does the Sylvester-like method require far fewer multiplications at any given value of N_ρ, but the slope of the Sylvester-like scaling is greatly reduced.

Figs. 3.1c and 3.1d compare the scaling as a function of N_θ for $N_\rho=100$, $N_{\chi_i}=241$ and $N_\rho=150$, $N_{\chi_i}=481$, respectively. Figs. 3.1e and 3.1f compare the scaling as a function of N_{χ_i} for $N_\rho=100$, $N_\theta=31$ and $N_\rho=150$, $N_\theta=65$, respectively. As before, the Sylvester-like method requires much fewer multiplications at any given value of N_{χ_i} and the scaling still has a smaller slope than the Kronecker counterpart.

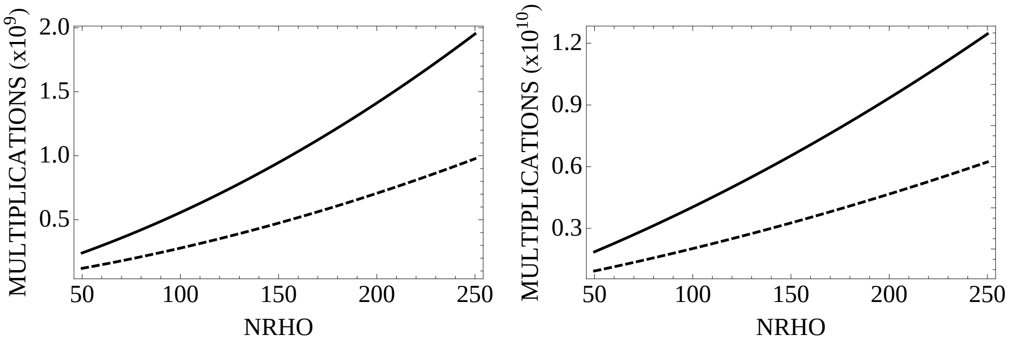

(a) $N_\theta = 31$, $N_{\chi_i} = 241$ (b) $N_\theta = 65$, $N_{\chi_i} = 481$

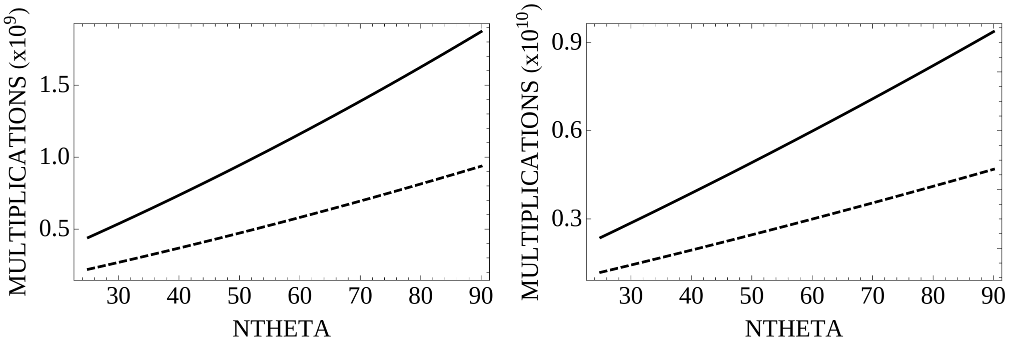

(c) $N_\rho = 100$, $N_{\chi_i} = 241$ (d) $N_\rho = 150$, $N_{\chi_i} = 481$

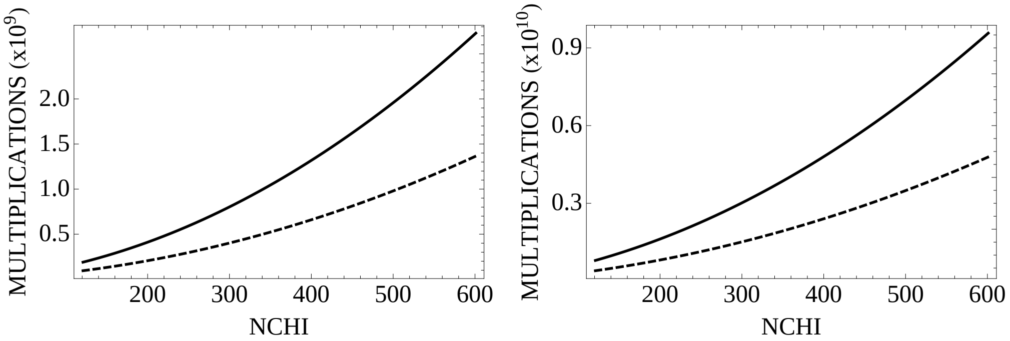

(e) $N_\rho = 100$, $N_\theta = 31$ (f) $N_\rho = 150$, $N_\theta = 65$

Figure 3.1: Comparisons of the number of multiplications required using the Kronecker and Sylvester-like matrix-multiply methods to apply the Hamiltonian operator. The solid lines show the Kronecker scaling and the dashed lines show the Sylvester-like scaling.

3.5 Scaling of Computational Time

This section presents the computational times required to run the program and how they scale for various input parameters. It is important to determine these scalings so that priority can be assigned to determine which parameters can be changed without a dramatic gain in computational cost.

Fig. 3.2 shows the computational times and scalings associated with the APH grid parameters. There are two plots associated with each APH grid parameter: one for a modest number of grid points and another for a dense number of grid points. Fits to the curves are listed above each plot.

Figs. 3.2a and 3.2b show the times and scalings for N_ρ. Both plots show a linear scaling as N_ρ increases. Note that there is about a six-fold increase in the slope of the fits as the number of grid points increase from $N_\theta = 31$, $N_{\chi_i} = 241$ to $N_\theta = 65$, $N_{\chi_i} = 481$, a dramatic increase in computational cost as the grid density increases. The linear fits show better scaling than the slightly quadratic nature of Figs. 3.1a and 3.1b, which show the estimated number of multiplications required.

Figs. 3.2c and 3.2d show the times and scalings for N_θ. Both plots show a small quadratic scaling, with small quadratic fit coefficients, as N_θ increases. However, the fits show a strong linear character. Note that there is about a five-fold increase in the linear slope, and the quadratic coefficient of the denser grid is about 1.5 times that of the more sparse grid. The fits show a less favorable scaling than the linear nature of Figs. 3.1c and 3.1d, which show the estimated number of multiplications required.

Figs. 3.2e and 3.2f show the times and scalings for N_{χ_i}. Both plots show a small quadratic scaling as N_{χ_i} increases. However, the fits show a dominant

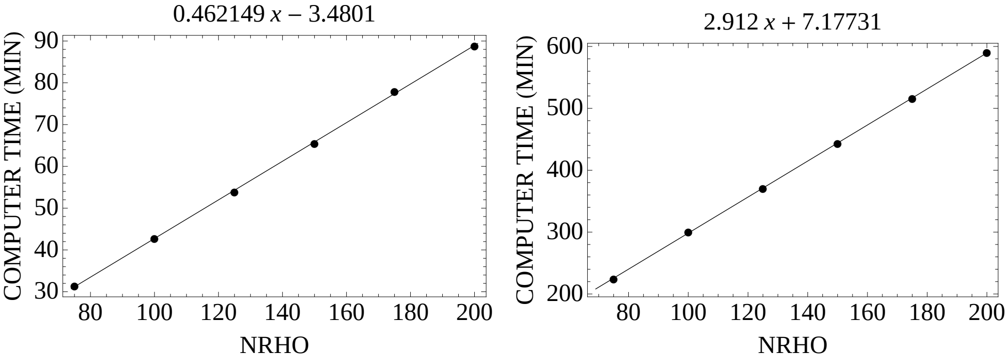

(a) $N_\theta = 31$, $N_{\chi_i} = 241$ (b) $N_\theta = 65$, $N_{\chi_i} = 481$

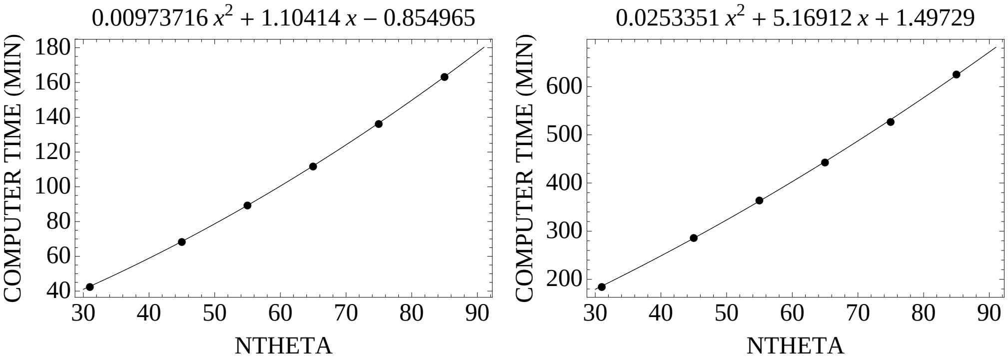

(c) $N_\rho = 100$, $N_{\chi_i} = 241$ (d) $N_\rho = 150$, $N_{\chi_i} = 481$

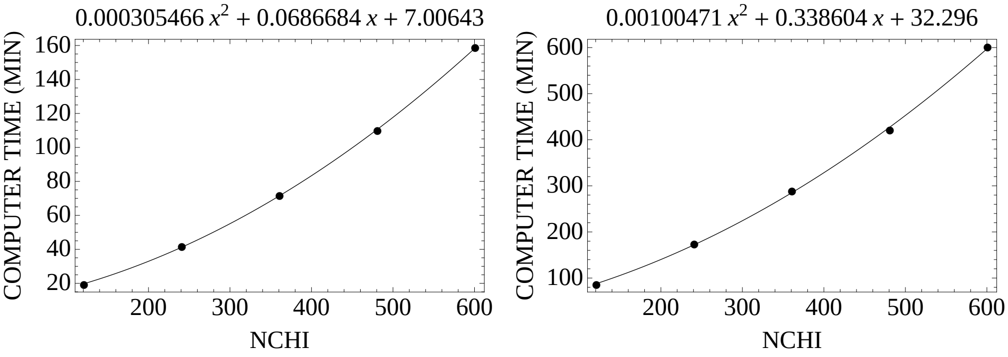

(e) $N_\rho = 100$, $N_\theta = 31$ (f) $N_\rho = 150$, $N_\theta = 65$

Figure 3.2: Fits of the computational time vs. APH coordinate grid points. The data points are the computational times and the solid lines are the fits to the points.

linear character. Note that there is about a five-fold increase in the linear slope, and the quadratic coefficient of the denser grid is about 3 times that of the more sparse grid. The fits show a similar scaling when compared to Figs. 3.1e

Label	Coefficient	Label	Coefficient
c_1	457.4	c_2	1725
b_1	0.3273	b_2	0.3883
d_1	138.2	d_2	492.2
f_1	0.0688	f_2	0.3221
g_1	-5.328	g_2	-21.38

Table 3.1: Coefficients of the Δt fit.

and 3.1f, which show the estimated number of multiplications required. It is evident that increasing N_θ has the greatest effect on the computational scaling, due to the larger quadratic and linear coefficients. These plots show that it is important to determine the minimum values of N_ρ, N_θ, and N_{χ_i}, since the computational times significantly increases as these parameters increase. Convergence of these parameters will be discussed in Chapter 4.

Fig. 3.3 shows the computational times and scalings associated with the propagation time parameters. Again, there are two plots associated with each time parameter: one for a modest number of coordinate grid points and another for a dense coordinate grid. Fits to the curves are listed above each plot.

Figs. 3.3a and 3.3b show the times and scalings for t_{max}. Both plots show a linear scaling as t_{max} increases. Note that there is about a two-fold increase in the slope of the fits as the number of grid points increase from $N_\rho = 150$,$N_\theta = 45$, $N_{\chi_i} = 361$ to $N_\rho = 150$, $N_\theta = 65$, $N_{\chi_i} = 481$, an increase in computational cost as the grid density increases.

Figs. 3.3c and 3.3d show the times and scalings for N_t. Both plots show a linear scaling as N_t increases. Note that there is about a three-fold increase in the slope of the fits as the number of grid points increase from $N_\rho = 100$,$N_\theta = 45$, $N_{\chi_i} = 361$ to $N_\rho = 150$, $N_\theta = 65$, $N_{\chi_i} = 481$.

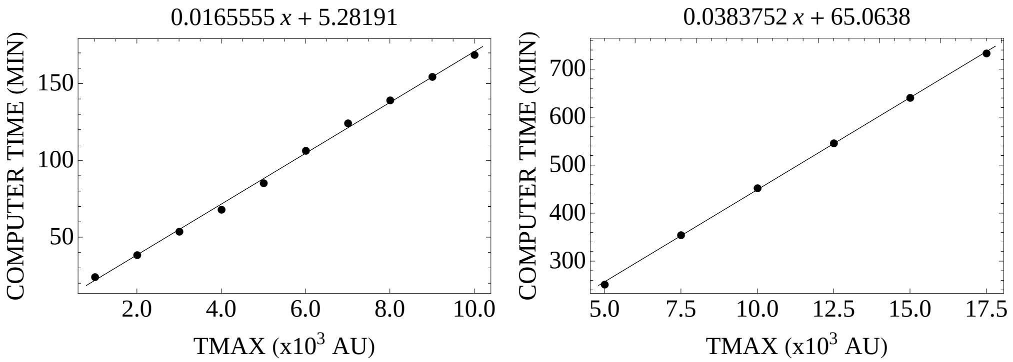

(a) $N_\rho = 150$, $N_\theta = 45$, $N_{\chi_i} = 361$ (b) $N_\rho = 150$, $N_\theta = 65$, $N_{\chi_i} = 481$

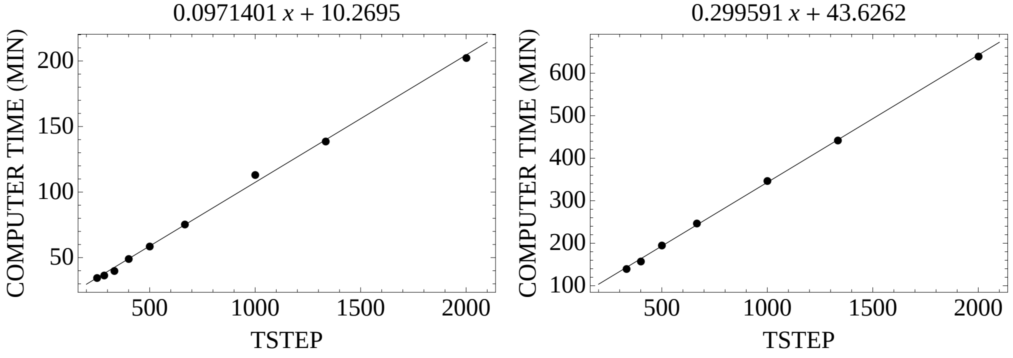

(c) $N_\rho = 100$, $N_\theta = 45$, $N_{\chi_i} = 361$ (d) $N_\rho = 150$, $N_\theta = 55$, $N_{\chi_i} = 481$

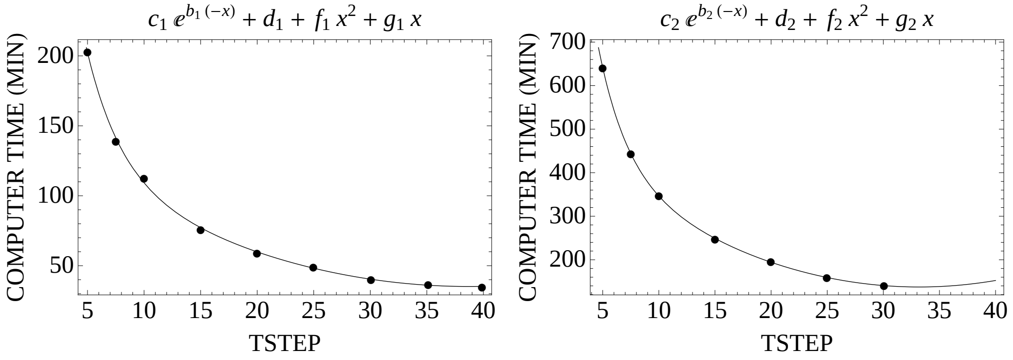

(e) $N_\rho = 100$, $N_\theta = 45$, $N_{\chi_i} = 361$ (f) $N_\rho = 150$, $N_\theta = 55$, $N_{\chi_i} = 481$

Figure 3.3: Fits of the computational time vs. propagation time parameters. The data points are the computational times and the solid lines are the fits to the points.

Figs. 3.3e and 3.3f show the times and scalings for the time grid spacing, Δt. Both plots show a decaying exponential scaling as N_t increases, but also have linear and quadratic terms. The fit coefficients are listed in Table 3.1.

According to fit coefficients, the exponential behavior of the more dense grid is similar to that of the more sparse grid but shifted to longer computational time.

CHAPTER 4

CONVERGENCE

4.1 Introduction

This chapter discusses the convergence of the scattering results produced by the h-TDWP program. We will analyze the behavior of the h-TDWP results as the input parameters are varied and compare them with benchmark TI results produced by the ABC program [15]. The input parameters and their descriptions are listed in Table 4.1.

A convergence study will not be presented for all the parameters listed in Table 4.1. The atom masses, M_A, M_B, and M_C, are determined by the system being studied, so that we use the same values as those used in the benchmark calculations. The inner boundary of the hyperradius grid, ρ_{min}, is determined by the shape of the electronic PES, and we choose the same value used in the benchmark calculations. Similarly, the PES cut-off V_{cut} is chosen to be large enough such that convergence isn't in question. The negative imaginary potential parameters, ρ_{NIP} and U_{NIP}, are primarily determined by an independent study conducted by Vibok and Balint-Kurti [54], with ρ_{NIP} also depending on ρ_∞, where the wave packet is analyzed. The energy grid parameters, E_{dim}, E_{min}, and E_{max}, are chosen by considering the Gaussian parameters, which determine the energy region of interest where the results will be accurate. For the purposes of illustrating the behavior of the results outside the appropriate energy regions-of-interest, the energy grid parameters will be chosen to cover a much larger range than what would be determined by considering the Gaussian parameters. The maximum number of rotational states, j_{max}, is determined by the maximum energy, E_{max}, being considered.

Table 4.1: List and descriptions of input parameters used in the h-TDWP program. The first column lists the symbol for the parameter used in this document and the second column lists the symbol for the parameter used in the program.

Parameter	Name	Description
M_A	amass	Mass of atom A
M_B	bmass	Mass of atom B
M_C	cmass	Mass of atom C
N_ρ	nrho	Number of APH ρ grid points
N_θ	ntheta	Number of APH θ grid points
N_χ	nchi	Number of APH χ grid points
ρ_{min}	rhomin	Minimum of APH ρ grid
ρ_{max}	rhomax	Maximum of APH ρ grid
ρ_∞	rho_infty_user	Value of ρ where wave packet is analyzed
t_{max}	tmax	Total propagation time: The wave packet is propagated from $t = 0$ to t_{max}.
N_t	tstep	Number of time step intervals
t_{delay}	tdelay	Time to begin analyzing wave packet: The wave packet is analyzed from $t = t_{delay}$ to t_{max}.
$S^0_{\tau_i}$	s0	Spatial center of initial Gaussian wave packet in mass-scaled Jacobi S
k_0	k0	Momentum center of initial Gaussian wave packet
σ_0	sigma	Width parameter of initial Gaussian wave packet
j_{max}	jmax	Largest number of diatomic rotational states used in asymptotic final state analysis
V_{cut}	vcut	Potential energy cut-off. Also used to limit the maximum eigenvalues of the APH θ and χ kinetic energy operators.
ρ_{NIP}	rho_nip	Value of APH ρ where negative imaginary potential region begins
U_{NIP}	unip	Amplitude of negative imaginary potential
N_E	edim	Number of energy points where S matrix is evaluated
E_{min}	emin	Minimum of energy grid
E_{max}	emax	Maximum of energy grid

We begin by studying the behavior of the results as the Gaussian initial wave packet parameters σ, k_0, and $S^0_{\tau_i}$ are varied. We continue by varying the number of APH grid points, N_ρ, N_θ, and N_{χ_i}, to find the minimum grid densities required to accurately represent the wave packet. Next, the convergence of the results with respect to t_{max} will be presented, discussing which parameters have a significant effect on the maximum propagation time. To study the behavior of the results, we will present probabilities for the initial state given by $\mathrm{H}+\mathrm{H}_2(\nu_i = j_i = 0)$ for zero total angular momentum. The total non-reactive probabilities, total reactive probabilities, and the total probability (normalization) will be presented along with their precent difference with respect to the benchmark ABC results [15]. The percent difference plots of the normalization data will be the precent difference from unity. The term "accurate" will be used to classify results that have a difference of $\leq 1\%$ with respect to the benchmark ABC results.

4.2 Gaussian Initial Wave Packet Parameters

The expression for the Gaussian initial wave packet was given previously in Sec. 2.4 by Eq. (2.48) as

$$g_{\tau_i}(S_{\tau_i}) = \left(\frac{1}{2\pi\sigma^2}\right)^{1/4} e^{-\left(S_{\tau_i}-S^0_{\tau_i}\right)^2/4\sigma^2} e^{-ik_0 S_{\tau_i}},$$

and has an initial momentum distribution given by

$$\eta_i(k_i) = \sqrt{\frac{1}{2\pi\hbar^2}} \int_0^\infty \mathrm{d}S_{\tau_i}\, \mathscr{H}^{(1)}_{\ell_i}(k_i S_{\tau_i})\, g_{\tau_i}(S_{\tau_i}), \tag{4.1}$$

with

$$k_i = \sqrt{2\mu\,(E - \epsilon_i)}, \tag{4.2}$$

where E is the total energy, and ϵ is the vibrational-rotational energy of the diatom. As shown in Sec. 2.5, the initial energy distribution is given by $\eta_i(E) = (\mu/k_i)^{1/2}\,\eta_i(k_i)$, with the explicit expression given previously in Eq. (2.55).

Since the results presented in this section are for the initial state with $J = 0$ and $\nu_i = j_i = \ell_i = 0$, the energy distribution is given by

$$\eta_i(E) = \left(\frac{2\sigma^2\mu^2}{\pi\hbar^4 k^2}\right)^{1/4} e^{-(k_i-k_0)^2\sigma^2} e^{iS^0_{\tau_i}(k_i-k_0)}. \tag{4.3}$$

The shape of the initial energy distribution determines the energy region of interest, where accurate results can be obtained, and also provides information concerning the initial momentum distribution. The energy region of interest boundaries are located where the energy distribution is 1% of its maximum. We will discuss the behavior of the plots with respect to the shape of the total energy distribution, since the results are presented with respect to total energy. As will be shown, the shape of the inverse of the initial energy distribution is also important, since the Fourier transformed time-dependent analysis coefficients are multiplied by $\eta_i(E)^{-1}$, shown in Sec. 2.5. The inverse of the energy distribution diverges outside the region of interest, outside of which, results are no longer accurate.

There are three input parameters that determine the characteristics of the initial wave packet and its energy distribution: σ, k_0, and $S^0_{\tau_i}$. The parameter σ determines the width of the wave packet in coordinate and in energy (and momentum) space. The parameter k_0 determines the center of the wave packet in momentum space, p_0, where $p_0 = \hbar k_0$, and, along with σ, determines the center and shape of the total energy distribution.

4.2.1 Behavior for changing σ

The input parameter σ determines the width of the Gaussian initial wave packet in coordinate and energy (or momentum) space. Fig. 4.1 shows the envelope of the initial wave packet for different values of σ, centered at $S^0_{\tau_i} =$ 9.5 bohr. The wave packet is narrow at smaller values of σ and broadens as σ increases. The narrowest allowable initial wave packet is desirable so that it will be completely located in the asymptotic region of the PES but not overlap the NIP region.

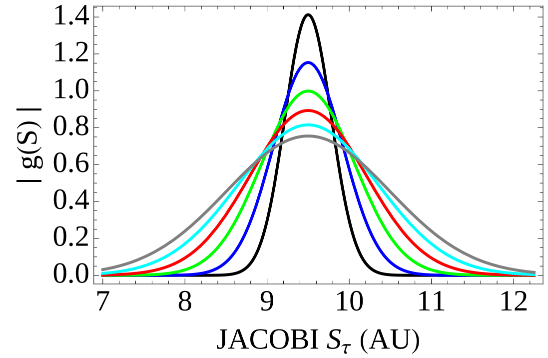

Figure 4.1: Envelope of the Gaussian initial wave packet for different values of σ centered at $S^0_{\tau_i} = 9.5$ bohr.
LEGEND: (BLACK : $\sigma = 0.2$), (BLUE : $\sigma = 0.3$), (GREEN : $\sigma = 0.4$), (RED : $\sigma = 0.5$), (CYAN : $\sigma = 0.6$), (GRAY : $\sigma = 0.7$).

Fig. 4.2 shows the envelope of the initial total energy distribution and its inverse for different values of σ, centered at $k_0 = 4.5$, 8.5, and 12.5 au in momentum space. Note that the curves originate at the energy of the diatomic ground state $\epsilon_i = 0.269$ eV, where $\nu_i = j_i = 0$, since this is the zero of the kinetic energy. The energy distribution is broad at smaller values of σ and narrows as σ increases. We want the broadest energy distribution allowable so that we can obtain results over a large range of energies. As discussed in

σ	$k_0 = 4.5$ au	$k_0 = 8.5$ au	$k_0 = 12.5$ au
0.2	0.269 - $>$ 3.0	0.269 - $>$ 3.0	0.269 - $>$ 3.0
0.3	0.269 - 2.35	0.269 - $>$ 3.0	0.45 - $>$ 3.0
0.4	0.269 - 1.75	0.3 - 3.0	0.75 - $>$ 3.0
0.5	0.269 - 1.45	0.4 - 2.6	0.95 - $>$ 3.0
0.6	0.269 - 1.25	0.5 - 2.35	1.15 - $>$ 3.0
0.7	0.3 - 1.15	0.55 - 2.15	1.25 - $>$ 3.0

Table 4.2: Energy regions of interest, in eV, for different values of σ for $k_0 =$ 4.5, 8.5, and 12.5 au

Sec. 2.4, we want the initial wave packet to contain only momenta directed toward the interaction region of the PES, so that the entire wave packet propagates into that region. When the initial wave packet contains both positive and negative momenta, a portion of the wave packet will propagate away from the interaction region. This creates two primary issues: First, a portion of the wave packet never enters the interaction region of the potential and can still cross the ρ_∞ surface, causing incorrect results due to the analysis of the unreacted wave packet. Second, since the momentum distribution crosses zero, the presence of very small momentum components can cause the value of t_{delay} to be too large, such that the reacted portion of the propagating wave packet crosses the analysis surface before the unreacted amplitude has left.

We can estimate an appropriate value of σ by studying the energy distribution and its inverse in Fig. 4.2. For the energy distribution plots in Figs. 4.2a, 4.2c, and 4.2e, the curves that go to zero as $E \to 0$ contain the appropriate momentum distribution. For the inverse plots in Figs. 4.2b,4.2d, and 4.2f, the divergence of the curves determines the energy region of interest, and energies outside this region are not accurate. We will estimate the energy region of interest boundaries to be where $\eta_i(E)^{-1} = 100$ eV^{-1}, and these are given in

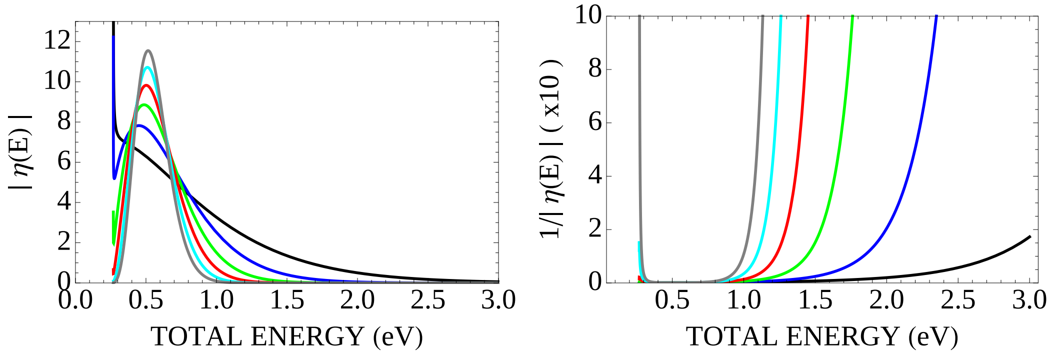

(a) $k_0 = 4.5$ (b) $k_0 = 4.5$

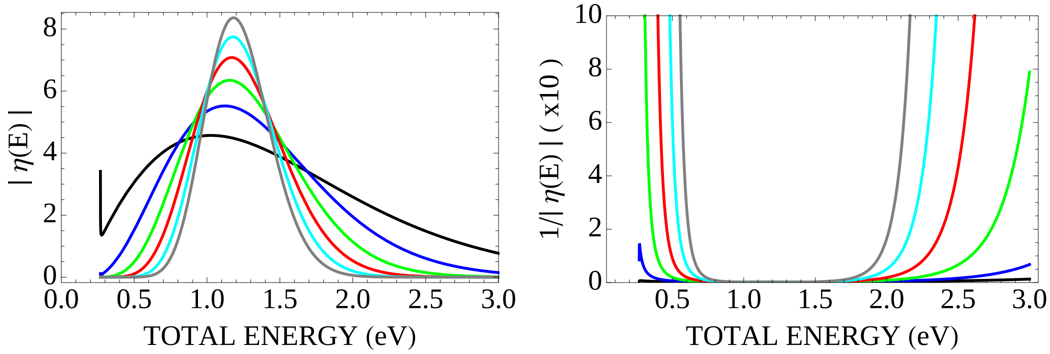

(c) $k_0 = 8.5$ (d) $k_0 = 8.5$

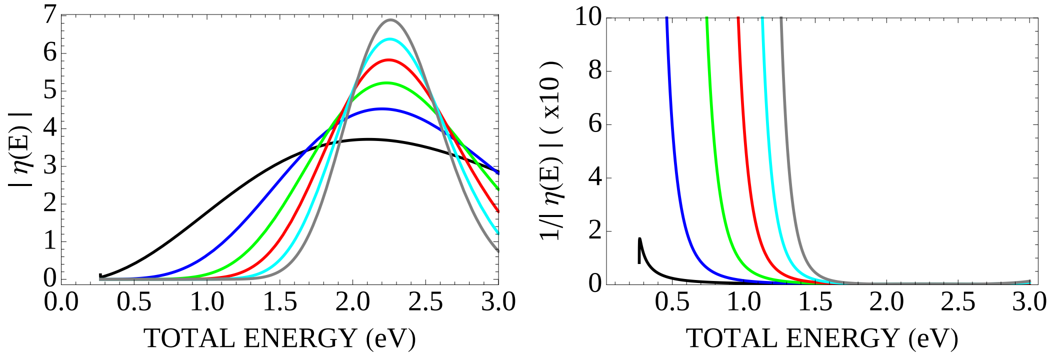

(e) $k_0 = 12.5$ (f) $k_0 = 12.5$

Figure 4.2: Plots of the initial energy distribution and its inverse for different values of σ for $k_0 = 4.5$, 8.5, and 12.5 au.
LEGEND: (BLACK : $\sigma = 0.2$), (BLUE : $\sigma = 0.3$), (GREEN : $\sigma = 0.4$), (RED : $\sigma = 0.5$), (CYAN : $\sigma = 0.6$), (GRAY : $\sigma = 0.7$).

Table 4.2.

For Fig. 4.2a, where $k_0 = 4.5$ au, all the energy distribution curves have significant amplitude as $E \to 0$, and an optimum value of σ would be greater than 0.7. The corresponding inverse in Fig. 4.2b, for $k_0 = 4.5$ au, shows that the energy region of interest for $\sigma > 0.7$ is very narrow and confined to energies below 1.15 eV. Furthermore, as shown in Fig. 4.1, a value of σ greater than 0.7 results in a very broad initial wave packet, which is not desirable, and the wave packet will have amplitude outside the asymptotic region of the PES.

For Fig. 4.2c, where $k_0 = 8.5$ au, all the energy distribution curves for $\sigma \geq 0.4$ go to zero as $E \to 0$, with $\sigma = 0.3$ also being a viable choice. The corresponding inverse in Fig. 4.2d, for $k_0 = 8.5$ au, shows a broad energy region of interest for $\sigma = 0.2$, $\sigma = 0.3$, and $\sigma = 0.4$, and progressively narrower regions of interest exist for $\sigma = 0.5$, 0.6, and 0.7. We would choose $\sigma = 0.3$ or $\sigma = 0.4$, the smallest of the qualifying σ values, so that the initial wave packet is as narrow in coordinate space as possible, and because $\eta_i(E) \to 0$ as $E \to \epsilon_i$.

For Fig. 4.2e, where $k_0 = 12.5$ au, all the energy distribution curves go to zero as $E \to \epsilon_i$. The corresponding inverse in Fig. 4.2f shows that the broadest energy region of interest corresponds to $\sigma = 0.2$, so this would be the best choice. To illustrate the previous conclusions, results for different values of σ will now be presented for $k_0 = 8.5$, 12.5, and 4.5 au.

Fig. 4.3 shows results for different values of σ when $k_0 = 8.5$ au. The divergence of the probabilities in Figs. 4.3a, 4.3c, and 4.3e clearly illustrates the importance of the shape of the inverse of the energy distribution. As σ increases, the energy region of interest narrows, as shown by the curves for $\sigma = 0.5$, 0.6, and 0.7, matching the predictions made previously.

The percent difference plots in Figs. 4.3b, 4.3d, and 4.3f illustrate the accuracy of results for different values of σ when $k_0 = 8.5$. The most prominent

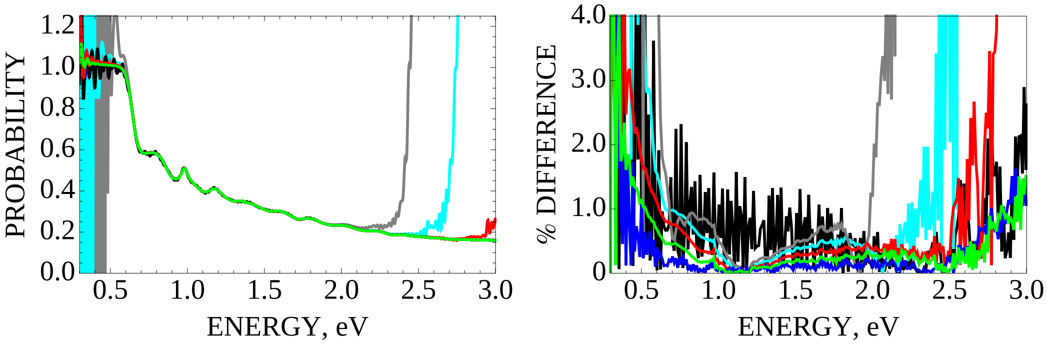

(a) *Non-Reactive Results* (b) *Non-Reactive % Difference*

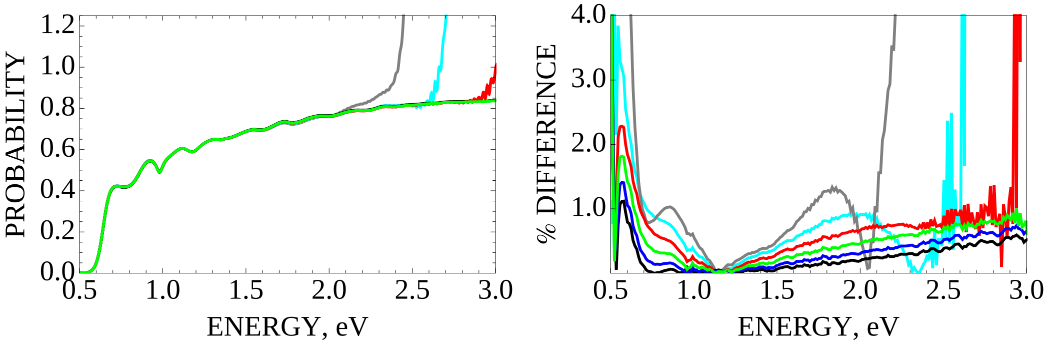

(c) *Reactive Results* (d) *Reactive % Difference*

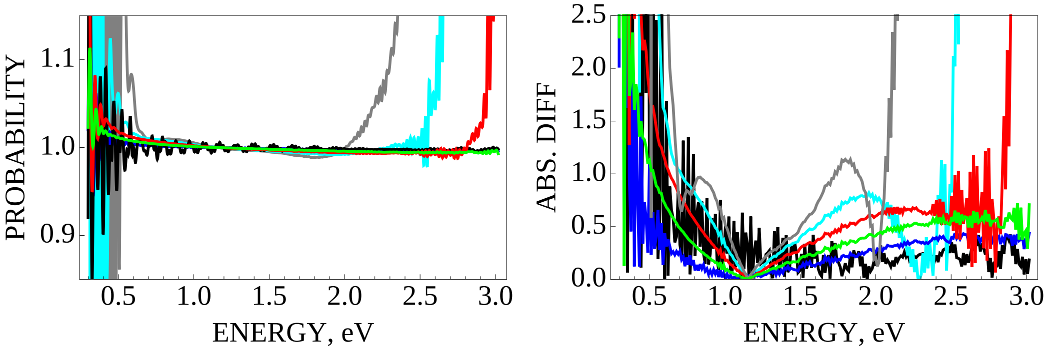

(e) *Normalization* (f) *Norm. % Difference*

Figure 4.3: Convergence of $\mathrm{H} + \mathrm{H}_2(\nu_i = j_i = 0)$ results for different σ values. The other Gaussian parameters are $k_0 = 8.5$ au and $S^0_{\tau_i} = 9.5$ bohr, with $\rho_\infty = 10$ bohr. The APH grid parameters are $N_\rho = 150$, $N_\theta = 65$, and $N_{\chi_i} = 481$. The time parameters are $t_{max} = 10010$ au, $N_t = 1001$, and $t_{delay} = 500$ au.
LEGEND: (BLACK : $\sigma = 0.2$), (BLUE : $\sigma = 0.3$), (GREEN : $\sigma = 0.4$), (RED : $\sigma = 0.5$), (CYAN : $\sigma = 0.6$), (GRAY : $\sigma = 0.7$).

feature of these results is the cusp located around 1.2 eV where the percent difference goes to zero. This cusp is due to the shape of the energy distribution, with the cusp located at the maximum of the energy distributions, as shown in Fig. 4.2c. Note that each σ curve has its own cusp, since the maxima of the energy distributions occur at different energies. Again, the shape of the inverse of the energy distribution is clearly evident, and the accuracy is reduced outside the energy region of interest. The decrease in accuracy as σ increases is most likely due to the broad shape of the initial wave packet, which has amplitude outside the asymptotic region of the PES, located at about 8 bohr and also encroaches into the NIP region at 10.75 bohr.

The non-reactive percent difference plot in Fig. 4.3b shows that the most accurate results are obtained for $\sigma = 0.3$, with $\sigma = 0.4$ providing the next best results, as predicted. The $\sigma = 0.2$ results are very oscillatory due to the presence of very small kinetic energies, shown by the low energy spike in Fig. 4.2c. The presence of these small kinetic energies causes the initial wave packet to have amplitude on the ρ_∞ analysis surface when analysis begins. Adjusting t_{delay} could possibly fix the problem, as is evident by looking at the reactive percent difference plot in Fig. 4.3d, which shows highest accuracy for $\sigma = 0.2$. Since the initial wave packet at $t = 0$ doesn't have amplitude in the reactive arrangement channels, the reactive results are not affected if residual amplitude of the initial wave packet is present. The reactive results for $\sigma = 0.2$, 0.3, and 0.4 show excellent agreement with the ABC results, having a percent difference of $\leq 1\%$ from 0.7 to 3.0 eV.

Fig. 4.4 shows results for different values of σ when $k_0 = 12.5$ au. The divergence of the probabilities in Figs. 4.4a, 4.4c, and 4.4e are now more evident at lower energies, since the center of energy distribution has been shifted to

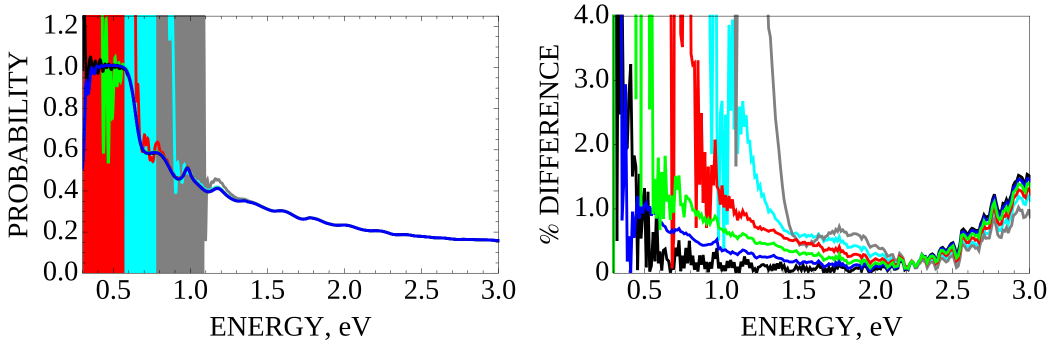

(a) *Non-Reactive Results* (b) *Non-Reactive % Difference*

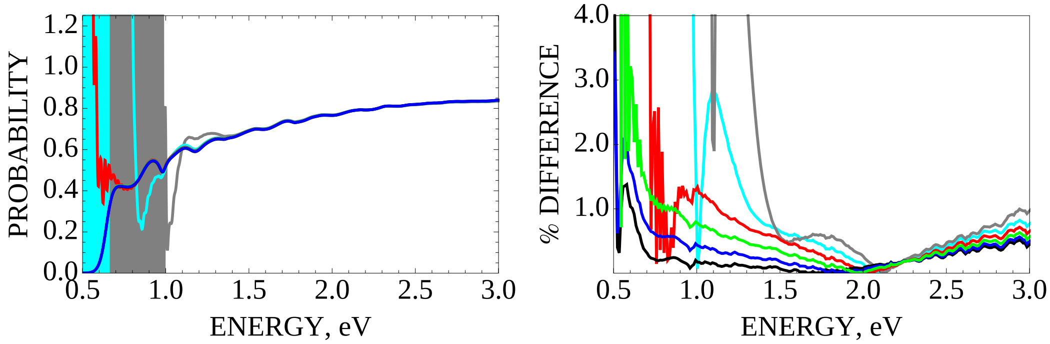

(c) *Reactive Results* (d) *Reactive % Difference*

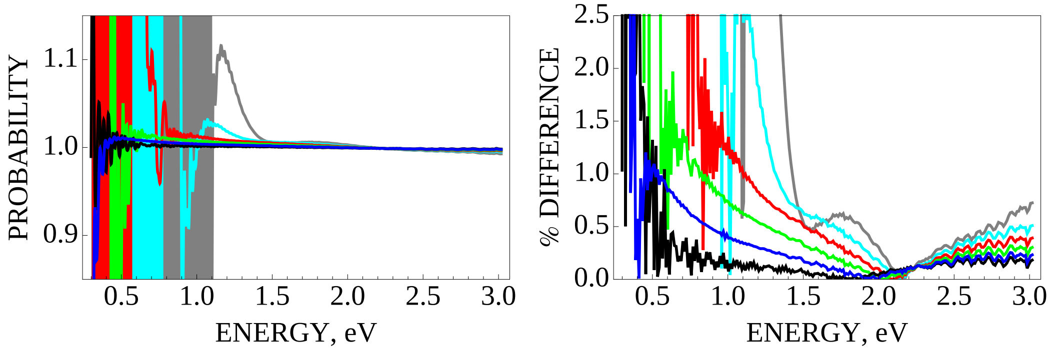

(e) *Normalization* (f) *Norm. % Difference*

Figure 4.4: Convergence of $\mathrm{H} + \mathrm{H}_2(\nu_i = j_i = 0)$ results for different σ values. The other Gaussian parameters are $k_0 = 12.5$ au and $S^0_{\tau_i} = 9.5$ bohr, with $\rho_\infty = 10$ bohr. The APH grid parameters are $N_\rho = 150$, $N_\theta = 65$, and $N_{\chi_i} = 481$. The time parameters are $t_{max} = 10010$ au, $N_t = 1001$, and $t_{delay} = 500$ au.
LEGEND: (BLACK : $\sigma = 0.2$), (BLUE : $\sigma = 0.3$), (GREEN : $\sigma = 0.4$), (RED : $\sigma = 0.5$), (CYAN : $\sigma = 0.6$), (GRAY : $\sigma = 0.7$).

a higher energy. The predicted regions of interest in Table 4.2, for $\sigma = 0.4$, 0.5, 0.6 and 0.7 are reflected in the results. Above their respective energies of divergence, all σ values shown have reasonably accurate results, and there are only small differences in the curves above 2.0 eV.

The percent difference plots in Figs. 4.4b, 4.4d, and 4.4f show the presence of the cusps, as before, that correspond to the energy distribution maxima in Fig. 4.2e. The most accurate results over the entire energy range occur for $\sigma = 0.2$, as predicted, and good results are also present for $\sigma = 0.3$. There is some anomalous behavior in the non-reactive percent difference in Fig. 4.4b, where the $\sigma = 0.2$ results become the least accurate above 2.0 eV. This is due to the presence of higher kinetic energies than in the reactive case, since the majority of the non-reactive probability is in the $\nu_f = 0$ state, so the products have more kinetic energy for a given total energy. For the reactive and normalization percent difference plots, the accuracy is reduced as σ increases due to the increasing width of the initial wave packet as before.

The $k_0 = 12.5$ results differ from the $k_0 = 8.5$ results in that they are much less oscillatory due to the lack of low energy components in the energy distribution, and they are more accurate at higher energies. The reactive results for $\sigma = 0.2$, 0.3, and 0.4 show excellent agreement with the ABC results, having a percent difference of $\leq 1\%$ from 0.7 to 3.0 eV.

Fig. 4.5 shows results for different values of σ when $k_0 = 4.5$ au. The divergence of the probabilities in Figs. 4.4a, 4.4c, and 4.4e are now present at higher energies, since the center of the energy distribution has been shifted to a lower energy. The predicted energy regions of interest in Table 4.2, for $\sigma = 0.3$, 0.4, 0.5, 0.6 and 0.7, are reflected in the results. Below their respective divergences, all σ values shown have reasonably accurate results.

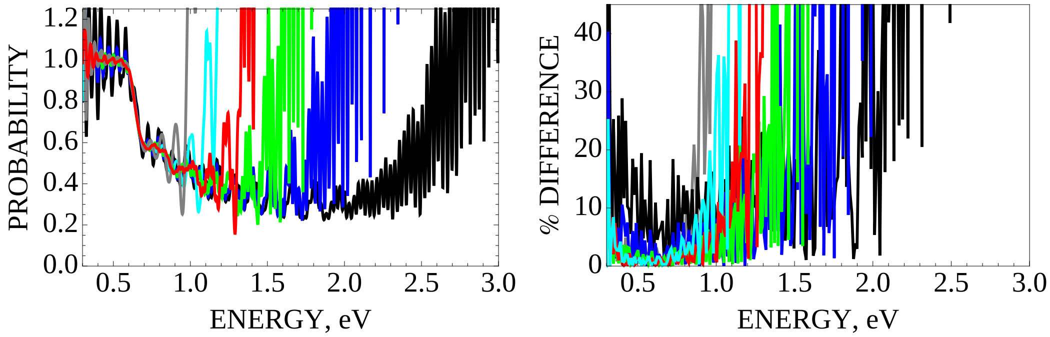

(a) *Non-Reactive Results* (b) *Non-Reactive % Difference*

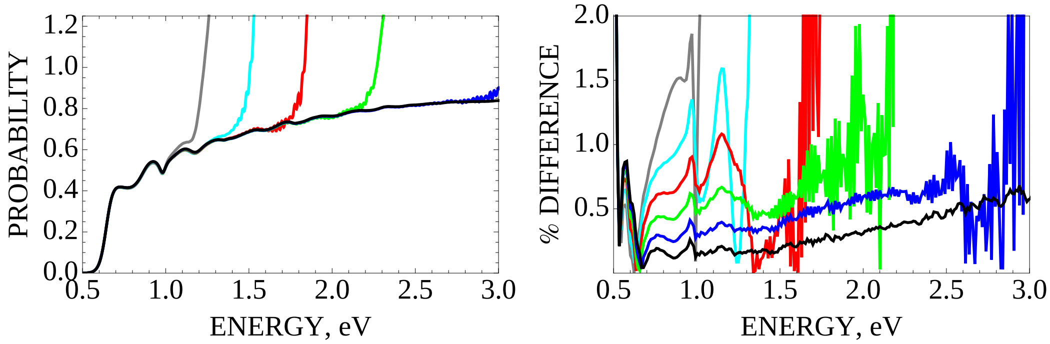

(c) *Reactive Results* (d) *Reactive % Difference*

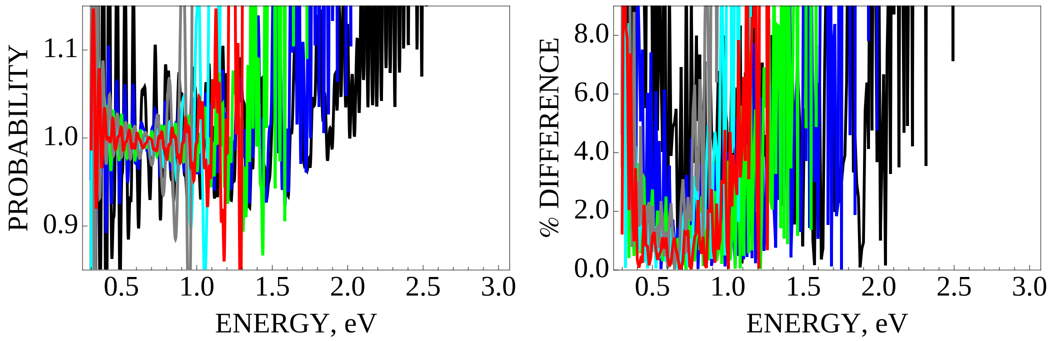

(e) *Normalization* (f) *Norm. % Difference*

Figure 4.5: Convergence of $\mathrm{H} + \mathrm{H}_2(\nu_i = j_i = 0)$ results for different σ values. The other Gaussian parameters are $k_0 = 4.5$ au and $S^0_{\tau_i} = 9.5$ bohr, with $\rho_\infty = 10$ bohr. The APH grid parameters are $N_\rho = 150$, $N_\theta = 65$, and $N_{\chi_i} = 481$. The time parameters are $t_{max} = 10010$ au, $N_t = 1001$, and $t_{delay} = 500$ au.
LEGEND: (BLACK : $\sigma = 0.2$), (BLUE : $\sigma = 0.3$), (GREEN : $\sigma = 0.4$), (RED : $\sigma = 0.5$), (CYAN : $\sigma = 0.6$), (GRAY : $\sigma = 0.7$).

The most apparent feature is present in the non-reactive results, which are overwhelmingly oscillatory, showing very large percent differences in Fig. 4.5b. This is also reflected in the normalization plots. These results are due to the small energies present in the energy distribution, as discussed before, and can be fixed by adjusting t_{delay} or by choosing $S^0_{\tau_i}$ to be much smaller than ρ_∞ so that there is no overlap of the initial wave packet at $t = 0$.

The percent difference plots in Figs. 4.5b, 4.5d, and 4.5f show the presence of cusps, as before, that correspond to the energy distribution maxima in Fig. 4.2a. While the non-reactive results do not provide much information, accurate reactive results are obtained for $\sigma = 0.2$ over the entire energy range, which was not predicted by our initial estimate. For energies below 0.6 eV, the $\sigma = 0.7$ results are the most accurate, which was predicted.

The $k_0 = 4.5$ results differ from the $k_0 = 8.5$ and $k_0 = 12.5$ results in that they are more accurate at lower energies, ≤ 0.7 eV. The reactive results for $\sigma = 0.2$, 0.3, and 0.4 show excellent agreement with the ABC results, having a percent difference of $\leq 1\%$ from about 0.55 to 3.0 eV for $\sigma = 0.2$, from 0.55 to 2.8 eV for $\sigma = 0.3$, and from 0.55 to 1.7 eV for $\sigma = 0.4$.

The behavior of the results for different values of σ has been presented, and the results follow the predictions made by studying the shapes and locations of the initial wave packet, energy distribution, and the inverse of the energy distribution. Deviations from the predictions, usually observed in the non-reactive data, have been explained and can be avoided by changing other parameters such as t_{delay}. This study of σ has also provided information concerning the behavior or the results for different values of k_0, which will be covered next.

4.2.2 Behavior for changing k_0

The input parameter k_0 determines the center of the initial momentum distribution and determines the shape and location of the total energy distribution. It has no effect on the shape or location of the Gaussian initial wave packet. Fig. 4.6 shows the envelope of the initial total energy distribution and its inverse for different values of k_0, for $\sigma = 0.2$, 0.3, and 0.5. The initial energy distribution translates to higher energy and broadens as k_0 increases. The broadening as k_0 increases is due to the $\sqrt{\mu/k_i}$ factor in the energy distribution in Eq. 4.3. We want the broadest energy distribution allowable so that we can obtain results over a large range of energies. Another requirement for obtaining accurate results is that the energy distribution to go to zero as $E \to \epsilon_i$, where ϵ_i is the ro-vibrational energy of the diatom, so that the momentum distribution only contains momentum directed toward the interaction region of the PES. The reasons for this were discussed at the beginning of Sec. 4.2.1. Conversely, the reactive results were shown in Sec. 4.2.1 to not be significantly affected even when the $\eta_i(E) \to 0$ as $E \to \epsilon_i$ requirement is not met.

We can estimate an appropriate value of k_0 by studying the energy distributions and their inverses in Fig. 4.6. For the energy distributions in Figs. 4.6a,

$k_0(au)$	$\sigma = 0.2$	$\sigma = 0.3$	$\sigma = 0.5$
4.5	0.269 - > 3.0	0.269 - 2.35	0.269 - 1.45
6.5	0.269 - > 3.0	0.269 - 3.0	0.3 - 2.0
8.5	0.269 - > 3.0	0.269 - > 3.0	0.4 - 2.6
12.5	0.269 - > 3.0	0.45 - > 3.0	0.95 - > 3.0
16.5	0.45 - > 3.0	1.1 - > 3.0	1.95 - > 3.0
20.5	1.1 - > 3.0	2.2 - > 3.0	N/A

Table 4.3: Energy regions of interest, in eV, for different values of k_0 for $\sigma = 0.2$, 0.3, and 0.5.

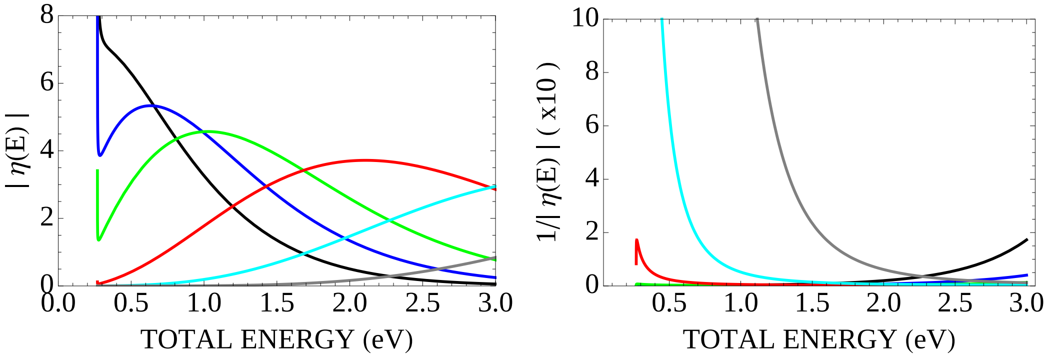

(a) $\sigma = 0.2$ (b) $\sigma = 0.2$

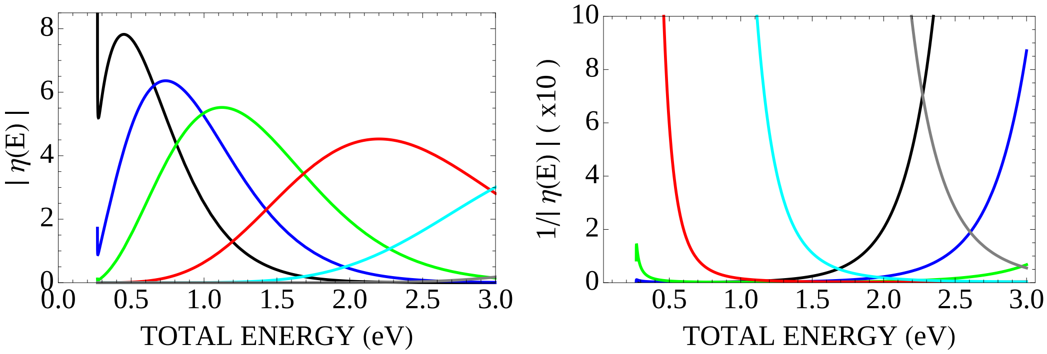

(c) $\sigma = 0.3$ (d) $\sigma = 0.3$

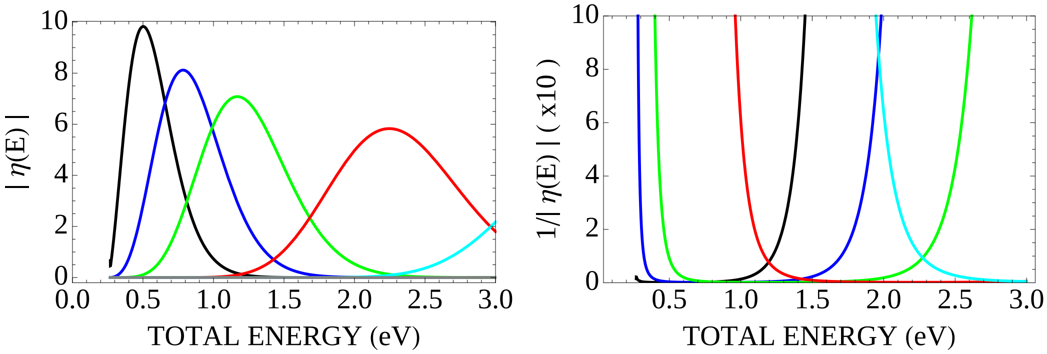

(e) $\sigma = 0.5$ (f) $\sigma = 0.5$

Figure 4.6: Plots of the initial energy distribution and its inverse for different values of k_0 for $\sigma = 0.2$, 0.3, and 0.5.
LEGEND: (BLACK : $k_0 = 4.5$), (BLUE : $k_0 = 6.5$), (GREEN : $k_0 = 8.5$), (RED : $k_0 = 12.5$), (CYAN : $k_0 = 16.5$), (GRAY : $k_0 = 20.5$).

Figs. 4.6c, and Figs. 4.6e, the curves that go to zero as $E \to \epsilon_i$ contain the appropriate momentum distribution. For the inverse energy distributions in

Figs. 4.6b, 4.6d, and 4.6f, the energy regions of interest are located inside the divergences of the curves. We will estimate the energy region of interest boundaries to be where $\eta_i(E)^{-1} = 100$ eV^{-1}, and these are given in Table 4.3.

For Fig. 4.6a, where $\sigma = 0.2$, the energy distribution curves with $k_0 \leq 8.5$ au have significant amplitude as $E \to \epsilon_i$, so the appropriate values of k_0 would be greater than or equal to 12.5 au. For the corresponding inverse in Fig. 4.6b, for $\sigma = 0.2$, the divergences show that the results should be accurate for energies above 0.45 and 1.1 eV for $k_0 = 16.5$ and 20.5 au, respectively. The results for $k_0 = 12.5$ should be accurate over the full range of energies shown. As shown in Sec. 4.2.1, even though the $k_0 \leq 8.5$ energy distributions have significant amplitude for small kinetic energies, we can predict that the reactive results will still be accurate over their respective regions of interest given in Table 4.3.

For Fig. 4.6c, where $\sigma = 0.3$, the energy distribution curves with $k_0 \leq 6.5$ au have significant amplitude as $E \to \epsilon_i$, so the appropriate values of k_0 would be greater than or equal to 8.5 au. However, the energy distribution for $k_0 = 20.5$ au has very little amplitude over the given range of energies, which implies that accurate results will not be present over the shown energy range: 0 to 3.0 eV. For the corresponding inverse in Fig. 4.6d, for $\sigma = 0.3$, the divergences show that the results will be accurate for energies above 0.5, 1.3, and 2.3 eV for $k_0 = 12.5$, 16.5, and 20.5 au, respectively, and for energies below 2.35 for $k_0 = 4.5$ au. The results for $k_0 = 8.5$ and 6.5 should be accurate over the largest range of energies shown.

For Fig. 4.6e, where $\sigma = 0.5$, the energy distribution curves do not have significant amplitude as $E \to \epsilon_i$, and any of the values of σ shown would be appropriate, with the exception of k_0=20.5 au. The energy distribution for

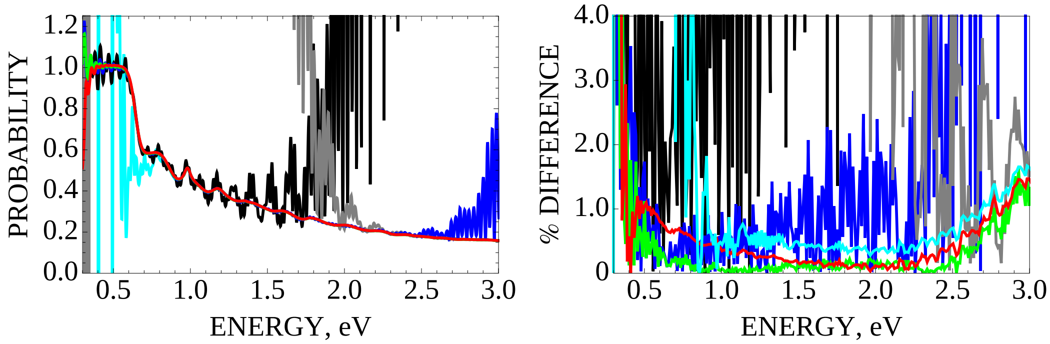

(a) *Non-Reactive Results* (b) *Non-Reactive % Difference*

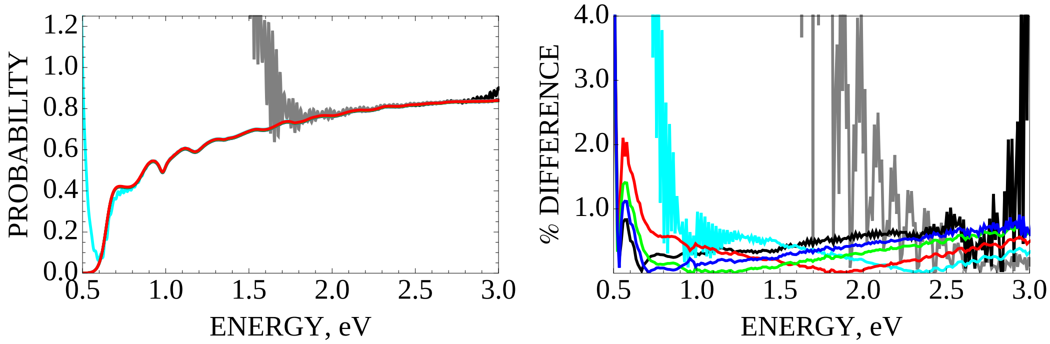

(c) *Reactive Results* (d) *Reactive % Difference*

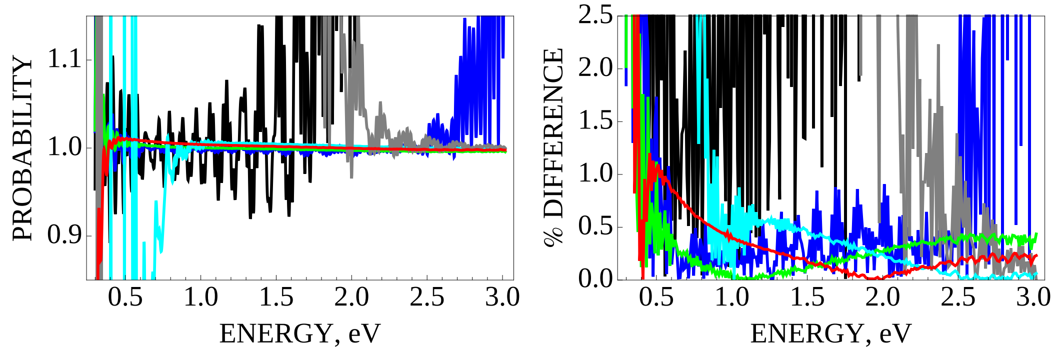

(e) *Normalization* (f) *Norm. % Difference*

Figure 4.7: Convergence of $\mathrm{H} + \mathrm{H}_2(\nu_i = j_i = 0)$ results for different k_0 values. The other Gaussian parameters are $\sigma = 0.3$ and $S^0_{\tau_i} = 9.5$ bohr, with $\rho_\infty = 10$ bohr. The APH grid parameters are $N_\rho = 150$, $N_\theta = 65$, and $N_{\chi_i} = 481$. The time parameters are $t_{max} = 10010$ au, $N_t = 1001$, and $t_{delay} = 500$ au.
LEGEND: (BLACK : $k_0 = 4.5$), (BLUE : $k_0 = 6.5$), (GREEN : $k_0 = 8.5$), (RED : $k_0 = 12.5$), (CYAN : $k_0 = 16.5$), (GRAY : $k_0 = 20.5$).

$k_0 = 20.5$ au has negligible amplitude over the given range of energies and implies that accurate results will not be present over this range: 0 to 3.0 eV.

The benefit of using a larger σ value, as opposed to $\sigma = 0.2$ or 0.3, is that the energy distributions of $k_0 = 4.5$ and 6.5 au do not have appreciable amplitude at $E \to \epsilon_i$. For the corresponding inverse in Fig. 4.6d, where $\sigma = 0.5$, the divergences show that the results will be accurate for energies above 0.95 and 1.95 eV for $k_0 = 12.5$ and 16.5 au, respectively. The curves for $k_0 \leq 8.5$ au, show bounded regions of interest, with their bounds listed in Table 4.3. The optimal choice when $\sigma = 0.5$ depends on the energy range of the desired results, with $k_0 = 8.5$ au having the largest energy region of interest. These parameters will be appropriate for $k_0 = 4.5$ au and $k_0 = 6.5$ au, since they cannot be obtained for the other values of σ shown. Fig. 4.7 shows results for different values of k_0 when $\sigma = 0.3$. The divergence of the probabilities in Figs. 4.7a, 4.7c, and 4.7e show that changing k_0 creates overlapping energy regions of interest, and as k_0 increases, the energy region of interest translates to higher energies. The results for these overlapping regions can be joined to obtain accurate results over the full range of energies from ϵ_i to 3.0 eV. The results in Figs. 4.7a, 4.7c, and 4.7e show that the most accurate results over the full energy range are for $k_0 = 8.5$ and 12.5 au, as predicted.

The percent difference plots in Figs. 4.7b, 4.7d, and 4.7f illustrate the accuracy of results for different values of k_0 when $\sigma = 0.3$. The large oscillations present for $k_0 = 20.5$ au are due to the negligible amplitude of the energy distribution. The large oscillations present in the non-reactive percent difference plot for $k_0 \leq 6.5$ au are due to the presence of the significant amplitude of the energy distribution as $E \to \epsilon_i$. Note that these oscillations are not present in the reactive percent difference plot.

Accurate results for $k_0 = 8.5$, 12.5, and 16.5 au, corresponding to a percent difference $\leq 1\%$ in both the non-reactive and reactive results, are found be-

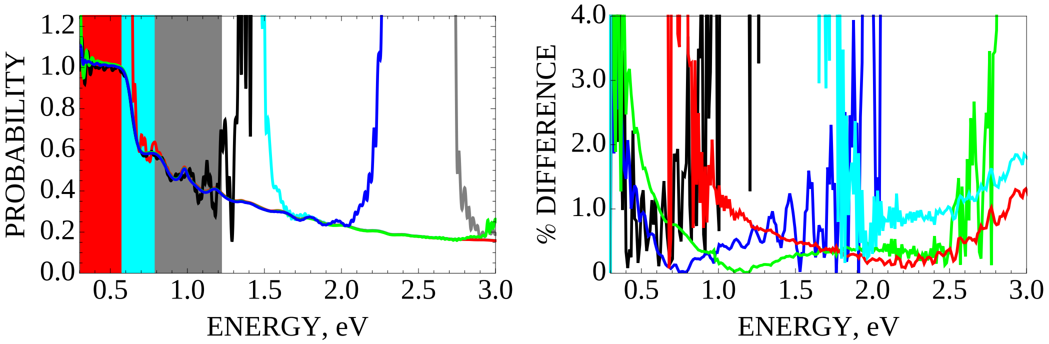

(a) *Non-Reactive Results* (b) *Non-Reactive % Difference*

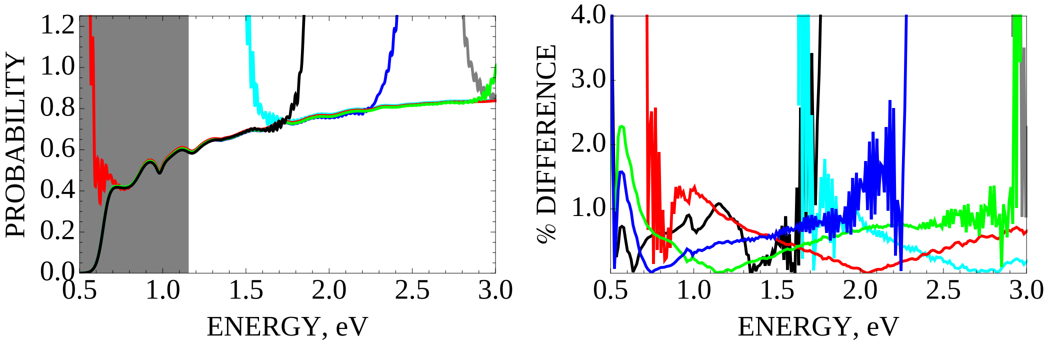

(c) *Reactive Results* (d) *Reactive % Difference*

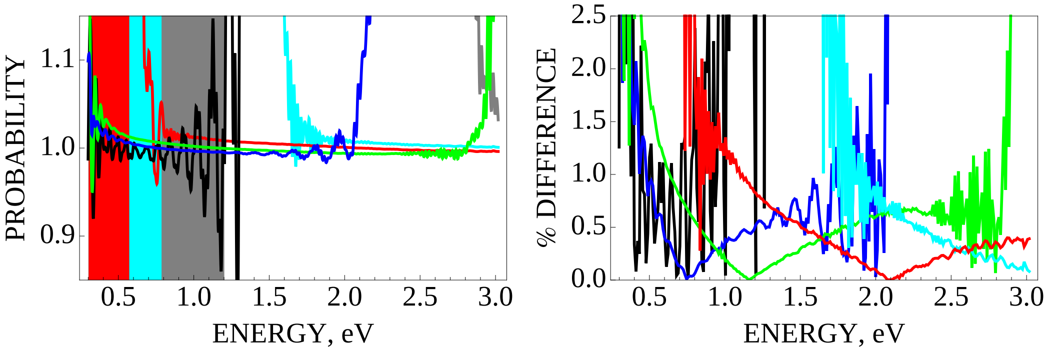

(e) *Normalization* (f) *Norm. % Difference*

Figure 4.8: Convergence of $\mathrm{H} + \mathrm{H}_2(\nu_i = j_i = 0)$ results for different k_0 values. The other Gaussian parameters are $\sigma = 0.5$ and $S^0_{\tau_i} = 9.5$ bohr, with $\rho_\infty = 10$ bohr. The APH grid parameters are $N_\rho = 150$, $N_\theta = 65$, and $N_{\chi_i} = 481$. The time parameters are $t_{max} = 10010$ au, $N_t = 1001$, and $t_{delay} = 500$ au. LEGEND: (BLACK : $k_0 = 4.5$), (BLUE : $k_0 = 6.5$), (GREEN : $k_0 = 8.5$), (RED : $k_0 = 12.5$), (CYAN : $k_0 = 16.5$), (GRAY : $k_0 = 20.5$).

tween about 0.5 and 2.9 eV, 0.6 to 2.8 eV, and 0.9 to 2.7 eV, respectively. Note the accuracy of the reactive $k_0 = 4.5$ and 6.5 au results, which are very accurate even when the energy distribution has amplitude as $E \to \epsilon_i$. Futhermore, the reactive results show that the results for a specific value of k_0 becomes the most accurate, with respect to the other results, around the energy that corresponds to the energy distribution maximum. These regions of maximum accuracy are the "cusps" meentioned in Sec. 4.2.1.

Overall, the best results over the entire energy range are for $k_0 = 8.5$ and 12.5 au. However, the most accurate results for a given energy depend on the location of the energy distribution maximum, corresponding to better accuracy at higher energies as k_0 increases.

Fig. 4.8 shows results for different values of k_0 when $\sigma = 0.5$. Referring to the probabilities in Figs. 4.8a, 4.8c, and 4.8e, the overlapping energy regions of interest are more evident than when $\sigma = 0.3$, since the $\sigma = 0.5$ energy distributions are more narrow. The most accurate results over the full energy range are for $k_0 = 8.5$ au, as predicted. The oscillatory behavior for $k_0 = 4.5$ in the non-reactive and normalization results is due to the significant amplitude of the energy distribution as $E \to \epsilon_i$.

The percent difference plots in Figs. 4.8b, 4.8d, and 4.8f illustrate the accuracy of results for different values of k_0 when $\sigma = 0.5$. The absence of accurate results for $k_0 = 20.5$ au is due to the negligible amplitude of the energy distribution. As discussed for the $\sigma = 0.3$ results, the locations of the high accuracy cusps, especially evident in Fig. 4.8f, correspond to the energy distribution maxima, and each k_0 curve is the most accurate around its cusp. The reactive results in Fig. 4.8d, for $k_0 = 4.5$ au, are more accurate at low energies than the $\sigma = 0.3$ results, as predicted. However, this is not the case for the $k_0 = 6.5$ au results, which disagree with the previous prediction, due to the energy distribution maximum shifting to about 0.6 eV in the $\sigma = 0.5$

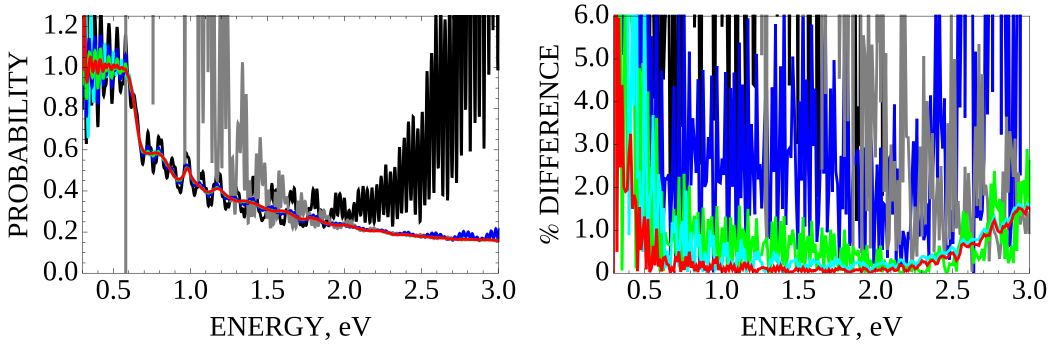

(a) *Non-Reactive Results* (b) *Non-Reactive % Difference*

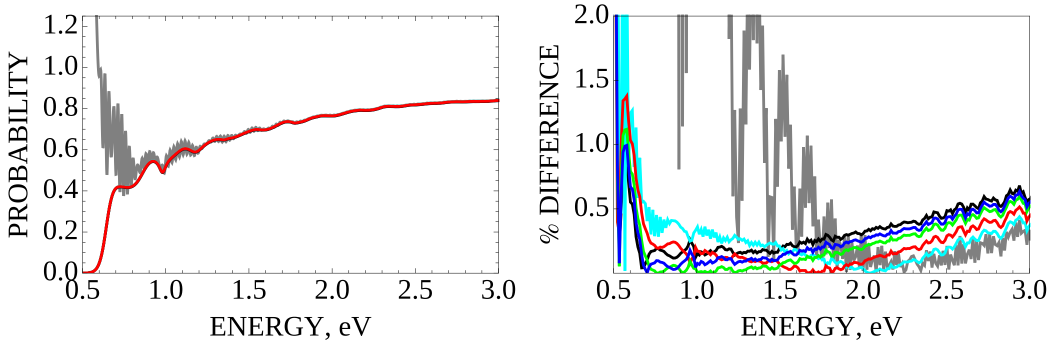

(c) *Reactive Results* (d) *Reactive % Difference*

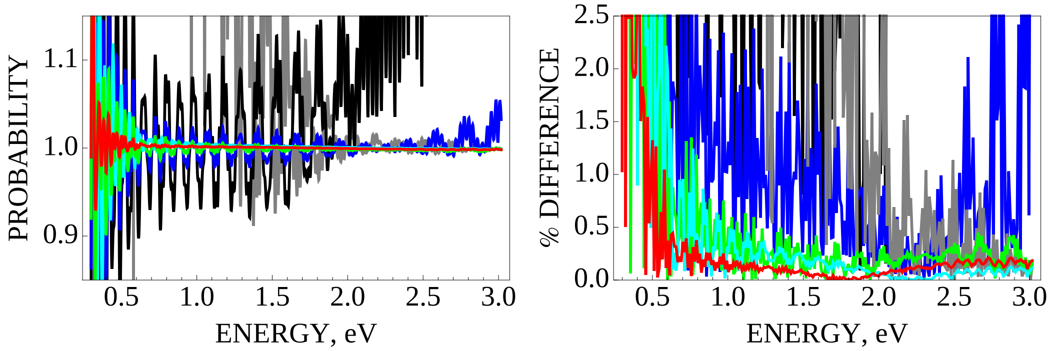

(e) *Normalization* (f) *Norm. % Difference*

Figure 4.9: Convergence of $\mathrm{H} + \mathrm{H}_2(\nu_i = j_i = 0)$ results for different k_0 values. The other Gaussian parameters are $\sigma = 0.2$ and $S^0_{\tau_i} = 9.5$ bohr, with $\rho_\infty = 10$ bohr. The APH grid parameters are $N_\rho = 150$, $N_\theta = 65$, and $N_{\chi_i} = 481$. The time parameters are $t_{max} = 10010$ au, $N_t = 1001$, and $t_{delay} = 500$ au.
LEGEND: (BLACK : $k_0 = 4.5$), (BLUE : $k_0 = 6.5$), (GREEN : $k_0 = 8.5$), (RED : $k_0 = 12.5$), (CYAN : $k_0 = 16.5$), (GRAY : $k_0 = 20.5$).

results.

Fig. 4.9 shows results for different values of k_0 when $\sigma = 0.2$. Referring to the probabilities in Figs. 4.9a, 4.9c, and 4.9e, the overlapping energy regions of interest are much less evident than when $\sigma = 0.3$ or 0.5, since the energy distributions are all very broad. The broad energy distributions for $k_0 = 4.5$, 6.5, and 8.5 au have significant amplitude as $E \to \epsilon_i$, causing the oscillatory behavior present in the non-reactive and normalization results. The most accurate results over the full energy range are for $k_0 = 12.5$ au, as predicted, with the $k_0 = 16.5$ au results also being accurate over a similarly large energy range.

The percent difference plots in Figs. 4.9b, 4.9d, and 4.9f illustrate the accuracy of results for different values of k_0 when $\sigma = 0.2$. The messy non-reactive and normalization precent difference plots, in Figs. 4.9b and 4.9f, only provide significant information concerning the accuracy and stability of the $k_0 = 12.5$ and 16.5 au results. The reactive percent difference plot in Fig. 4.9d, show that the $\sigma = 0.2$ results have the highest accuracy overall, when compared to the previously discussed results for $\sigma = 0.2$ and 0.3. The reactive results have an accuracy $\leq 0.5\%$ between 0.7 and 2.4 eV for all values of k_0. The locations of the high accuracy cusps are not as evident as for previous results, but Fig. 4.9d shows that the most accurate results are achieved by increasing k_0 as the energy increases. Unlike the $k_0 = 20.5$ au results for $\sigma = 0.3$ and 0.5, the $\sigma = 0.2$ results are accurate between 1.7 and 3.0 eV due to the broad energy distribution.

4.2.3 Behavior for changing $S^0_{\tau_i}$

The input parameter $S^0_{\tau_i}$ determines the center of the initial wave packet in coordinate space. It has no effect on the shape or location of the initial momentum or energy distributions. Fig. 4.10 shows the envelope of the initial wave packet for different values of $S^0_{\tau_i}$, for $\sigma = 0.2$, 0.3, 0.5 and 0.7. The wave packet has the same width when σ is fixed and translates to higher S_{τ_i} as $S^0_{\tau_i}$ increases.

Choosing an appropriate value of $S^0_{\tau_i}$ depends primarily on the characteristics of the PES, since the initial wave packet needs to be located in the asymptotic region of the potential energy surface. The next condition depends on the location of the NIP boundary, since we want the initial wave packet to be located outside the NIP region, from ρ_{NIP} to ρ_{max}. The initial wave packet "boundaries" are located at the points where the amplitude of the wave packet is 1% of its maximum value. The boundries $S^{\pm}_{\tau_i}$ are located at

$$S^{\pm}_{\tau_i} = S^0_{\tau_i} \pm 2\sigma\sqrt{\ln 100}, \tag{4.4}$$

where the width is $4\sigma\sqrt{\ln 100}$.

As Eq. (4.4) and Fig. 4.10 show, the value of σ plays a large role in choosing the appropriate value of $S^0_{\tau_i}$. To keep the initial wave packet outside the interaction region of the PES and the NIP region, it is advantageous to choose the smallest σ possible. The widths of the initial wave packets are 1.72, 2.57, 4.29, and 6.01 bohr for $\sigma = 0.2$, 0.3, 0.5, and 0.7, respectively. The results should show a decrease in accuracy as $S^0_{\tau_i}$ decreases, and this loss of accuracy should be amplified as σ increases.

Instead of using t_{delay} to remove overlap of the initial wave packet with the ρ_∞ surface, $S^0_{\tau_i}$ can be chosen such that the entire initial wave packet is located inside the analysis surface. As long as k_0 and σ are appropriately chosen, placing the entire wave packet inside the analysis surface will ensure that the non-reactive results are not ruined by the analysis of the unreacted

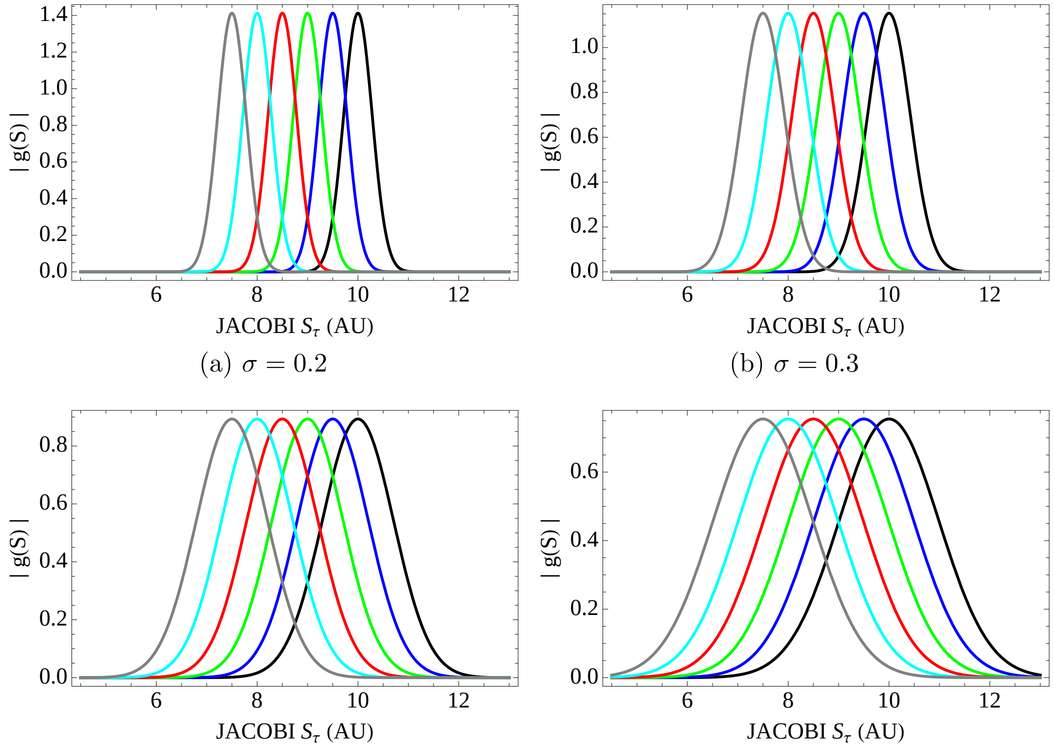

(a) $\sigma = 0.2$

(b) $\sigma = 0.3$

(c) $\sigma = 0.5$

(d) $\sigma = 0.7$

Figure 4.10: Plots of the initial Gaussian wave packet for different values of $S^0_{\tau_i}$ for $\sigma = 0.2$, 0.3, 0.5, and 0.7.
LEGEND: (BLACK : $S^0_{\tau_i} = 10$ bohr), (BLUE : $S^0_{\tau_i} = 9.5$ bohr), (GREEN : $S^0_{\tau_i} = 9$ bohr), (RED : $S^0_{\tau_i} = 8.5$ bohr), (CYAN : $S^0_{\tau_i} = 8$ bohr), (GRAY : $S^0_{\tau_i} = 7.5$ bohr).

wave packet.

First, we will discuss the behavior of the results for different values of $S^0_{\tau_i}$, ranging from 7.5 to 9.5 bohr, when $\sigma = 0.3$ and 0.5. These results will illustrate the importance of choosing the narrowest possible wave packet and show how the results behave when the initial wave packet has amplitude outside the asymptotic region of the PES and inside the NIP region.

We can predict the appropriate values for $S^0_{\tau_i}$ when $\sigma = 0.3$, $\rho = 10$ bohr, and $\rho_{NIP} = 10.75$ bohr by looking at Fig. 4.10b. Accurate non-reactive results can be obtained for $S^0_{\tau_i} \leq 8.5$ bohr, since the only packets with amplitude at or above 10 bohr are for $S^0_{\tau_i} = 9$ and 9.5 bohr. However, for $S^0_{\tau_i} \leq 8.5$ bohr, the non-reactive results should become less accurate as $S^0_{\tau_i}$ decreases and begins to have amplitude outside the asymptotic region of the PES. Since the initial wave packet's overlap with ρ_∞ does not affect the reactive results, the accuracy should decrease as $S^0_{\tau_i}$ decreases.

Note that we are approximating the location of $\rho_\infty = 10$ bohr in this case, since $\rho = S_{\tau_i}$ only when $\chi_i = 0$ and $\theta = \pi/2$. As the results will show, this is a reasonable approximation for illustrating the behavior of the data.

Increasing σ to 0.5 will broaden the initial wave packet, and, as shown in Fig. 4.10c, accurate non-reactive results can be obtained for $S^0_{\tau_i} \leq 8.0$ bohr. However, the accuracy of the non-reactive $S^0_{\tau_i}$ results may be adversely affected since the wave packets are broad and located at small values of $S^0_{\tau_i}$. The reactive results should decrease in accuracy as $S^0_{\tau_i}$ decreases, and this decrease in accuracy should be more pronounced than in the $\sigma = 0.3$ results.

Next, we will look at the convergence of $S^0_{\tau_i}$ as its value is increased for $\rho_\infty = 10$, 11, and 12 bohr. Increasing the value of ρ_∞ will allow observation of higher values of $S^0_{\tau_i}$ without initial overlap with the analysis region, and the results should converge as neighboring values of $S^0_{\tau_i}$ produce initial wave packets that are entirely localized in the asymptotic region of the PES.

Fig. 4.11 shows results for different values of $S^0_{\tau_i}$ when $\sigma = 0.3$. The non-reactive probabilities and normalization plots in Figs. 4.11a and 4.11e show large oscillations when $S^0_{\tau_i} = 9$ and 9.5 bohr. These results have $t_{delay} = 0$ au, so the oscillations are due to the overlap of the initial wave packet with the analysis surface at $\rho_\infty = 10$ bohr, as predicted. This overlap can be seen in Fig. 4.10b. The reactive results in Fig. 4.11c show no noticeable deviations for all values of $S^0_{\tau_i}$.

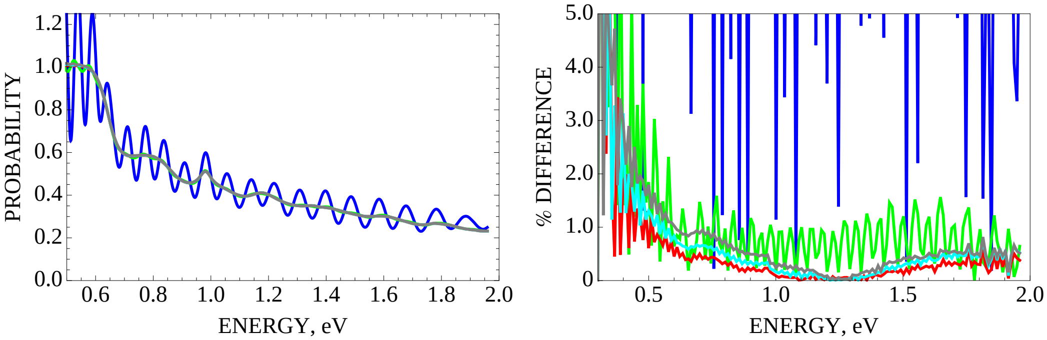

(a) *Non-Reactive Results* (b) *Non-Reactive % Difference*

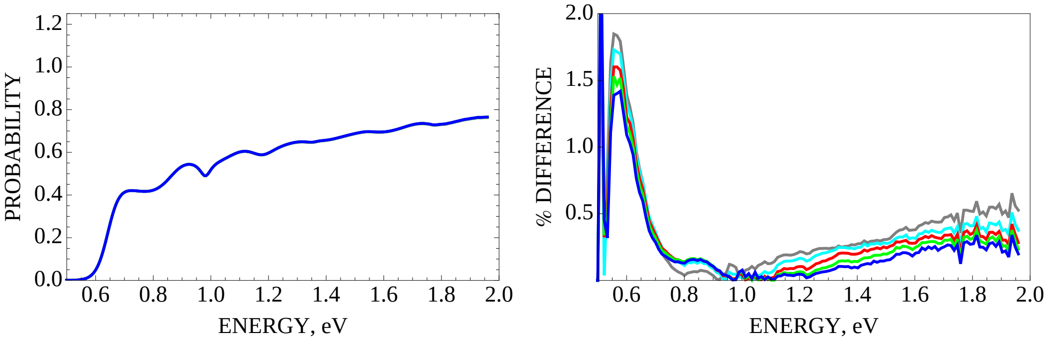

(c) *Reactive Results* (d) *Reactive % Difference*

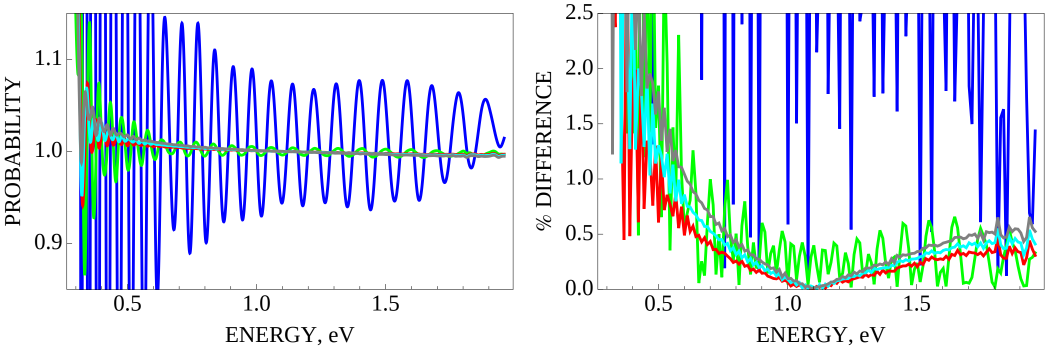

(e) *Normalization* (f) *Norm. % Difference*

Figure 4.11: Convergence of $\mathrm{H}+\mathrm{H}_2(\nu_i = j_i = 0)$ results for different $S^0_{\tau_i}$ values. The other Gaussian parameters are $\sigma = 0.3$ and $k_0 = 8.5$ bohr, with $\rho_\infty = 10$ bohr. The APH grid parameters are $N_\rho = 100$, $N_\theta = 45$, and $N_{\chi_i} = 361$. The time parameters are $t_{max} = 10010$ au, $N_t = 1001$, and $t_{delay} = 0$ au.
LEGEND: (BLACK : $S^0_{\tau_i} = 10$ bohr), (BLUE : $S^0_{\tau_i} = 9.5$ bohr), (GREEN : $S^0_{\tau_i} = 9$ bohr), (RED : $S^0_{\tau_i} = 8.5$ bohr), (CYAN : $S^0_{\tau_i} = 8$ bohr), (GRAY : $S^0_{\tau_i} = 7.5$ bohr).

The percent difference plots in Figs. 4.11b, 4.11d, and 4.11f illustrate the accuracy of results for different values of $S^0_{\tau_i}$ when $\sigma = 0.3$. As predicted, the most accurate reactive results occur when $S^0_{\tau_i} = 9.5$ bohr, with a decrease in accuracy as $S^0_{\tau_i}$ decreases. The reactive results, even for the smallest value of $S^0_{\tau_i} = 7.5$ bohr, are very accurate, with a percent difference less than or equal to about 0.5% above 0.7 eV. The non-reactive results have an accuracy $\leq 1\%$ above 0.65 eV for $S^0_{\tau_i} \leq 8.5$ bohr, with the accuracy decreasing as $S^0_{\tau_i}$ decreases, as predicted.

Fig. 4.12 shows results for different values of $S^0_{\tau_i}$ when $\sigma = 0.5$. The non-reactive probabilities and normalization plots in Figs. 4.12a and 4.12e show large oscillations when $S^0_{\tau_i} \geq 8$ bohr. The increased width of the wave packet decreases the accuracy of the non-reactive results, relative to the $\sigma = 0.3$ results, due to the large amount of overlap with the analysis surface at $\rho_\infty = 10$ bohr shown in Fig. 4.10c. The reactive results in Fig. 4.12c show no noticeable deviations for all values of $S^0_{\tau_i}$.

The percent difference plots in Figs. 4.12b, 4.12d, and 4.12f illustrate the accuracy of results for different values of $S^0_{\tau_i}$ when $\sigma = 0.5$. As predicted, the most accurate reactive results occur when $S^0_{\tau_i} = 9.5$ bohr, with a decrease in accuracy as $S^0_{\tau_i}$ decreases. Compared to the $\sigma = 0.3$ reactive results, the decrease in accuracy is more pronounced when $\sigma = 0.5$ due to the larger width of the initial wave packet. The larger width causes the wave packet to encroach further into the interaction region as $S^0_{\tau_i}$ decreases and also causes the energy distribution to be more narrow than in the $\sigma = 0.3$ case. The non-reactive results are not very accurate and show the problems associated with broad initial wave packets.

Now the convergence of $S^0_{\tau_i}$ will be discussed with respect to increasing $S^i_{\tau_0}$

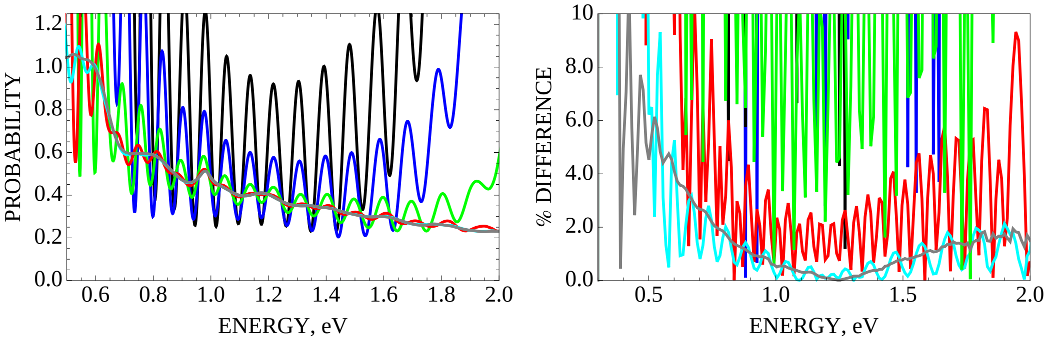

(a) *Non-Reactive Results* (b) *Non-Reactive % Difference*

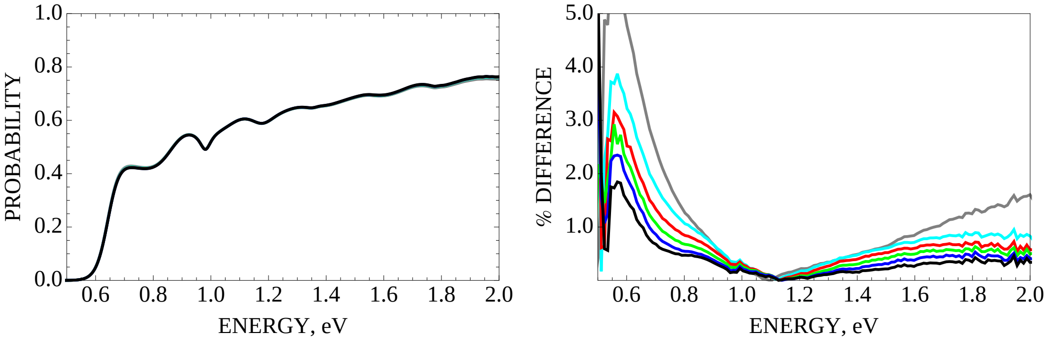

(c) *Reactive Results* (d) *Reactive % Difference*

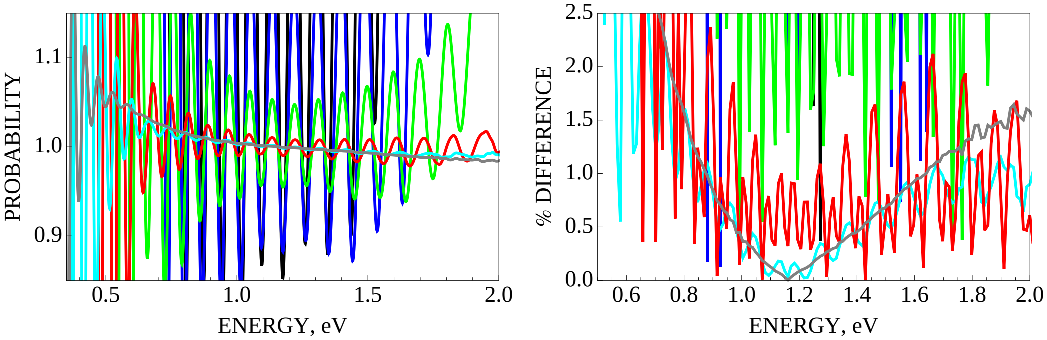

(e) *Normalization* (f) *Norm. % Difference*

Figure 4.12: Convergence of $\mathrm{H}+\mathrm{H}_2(\nu_i = j_i = 0)$ results for different $S^0_{\tau_i}$ values. The other Gaussian parameters are $\sigma = 0.5$ and $k_0 = 8.5$ bohr, with $\rho_\infty = 10$ bohr. The APH grid parameters are $N_\rho = 100$, $N_\theta = 45$, and $N_{\chi_i} = 361$. The time parameters are $t_{max} = 10010$ au, $N_t = 1001$, and $t_{delay} = 0$ au.
LEGEND: (BLACK : $S^0_{\tau_i} = 10$ bohr), (BLUE : $S^0_{\tau_i} = 9.5$ bohr), (GREEN : $S^0_{\tau_i} = 9$ bohr), (RED : $S^0_{\tau_i} = 8.5$ bohr), (CYAN : $S^0_{\tau_i} = 8$ bohr), (GRAY : $S^0_{\tau_i} = 7.5$ bohr).

at a fixed value of $\sigma = 0.2$. Choosing a small value of σ gives a narrow initial wave packet and will provide detailed information on convergence for a narrow region around $S^0_{\tau_i}$. Results will be shown for $\rho_\infty = 10$, 11, and 12 bohr so that accurate results can be shown for larger $S^0_{\tau_i}$ than were previously shown.

Fig. 4.13 shows results for different values of $S^0_{\tau_i}$ when $\sigma = 0.2$, $k_0 = 12.5$ au, and $\rho_\infty = 10$ bohr. The non-reactive probabilities and normalization plots in Figs. 4.13a and 4.13e show large oscillations when $S^0_{\tau_i} = 9.5$ and 10 bohr, due to the overlap of the initial wave packet with the analysis surface at $\rho_\infty = 10$ bohr, as predicted in Fig. 4.10a. The non-reactive results for $S^0_{\tau_i} \leq 9$ bohr show no noticeable difference, and the normalization results are converged above about 0.7 eV. The reactive results in Fig. 4.13c show no noticeable deviations for all values of $S^0_{\tau_i}$.

The percent difference plots in Figs. 4.13b, 4.13d, and 4.13f illustrate the accuracy of results for different values of $S^0_{\tau_i}$ when $\sigma = 0.2$, $k_0 = 12.5$ au, and $\rho_\infty = 10$ bohr. The non-reactive results in Fig. 4.13b, for $S^0_{\tau_i} \leq 9$ bohr, are converged above about 1.5 eV, with the best results obtained when $S^0_{\tau_i} = 9$ bohr at lower energies. The non-reactive results have a percent difference of $\leq 1\%$ from 0.6 to 2.7 eV. The reactive results in Fig. 4.13d are converged above about 2.2 eV, with the best results obtained when $S^0_{\tau_i} = 10$ bohr at lower energies. The reactive results have a percent difference of $\leq 0.5\%$ from 0.65 to 2.85 eV. The key here is that the results are very accurate for all shown values of $S^0_{\tau_i}$ between 0.65 and 2.7 eV as long as the initial wave packet does not overlap ρ_∞. The non-reactive and low energy results are the most sensitive to $S^0_{\tau_i}$.

Fig. 4.14 shows results for different values of $S^0_{\tau_i}$ when $\sigma = 0.2$, $k_0 = 12.5$ au, and $\rho_\infty = 11$ bohr. Here we include $S^0_{\tau_i} = 10.5$ and 11 bohr, and exclude

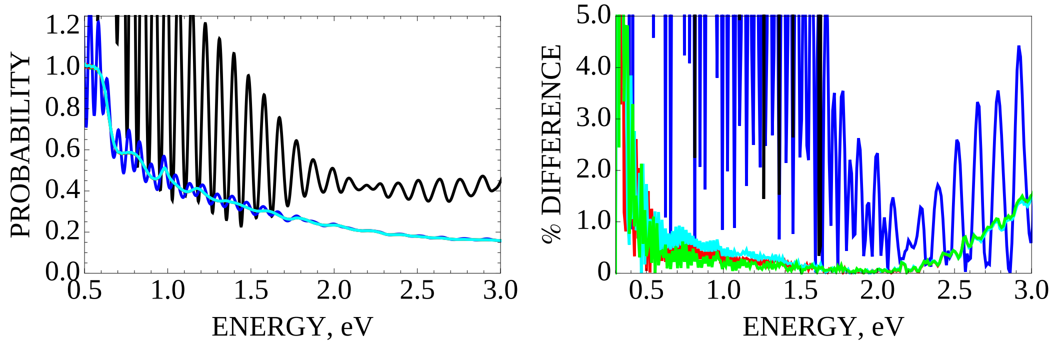

(a) *Non-Reactive Results* (b) *Non-Reactive % Difference*

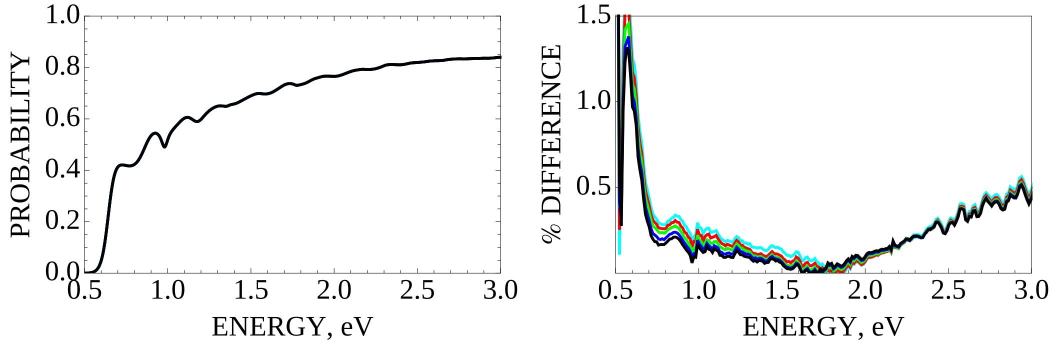

(c) *Reactive Results* (d) *Reactive % Difference*

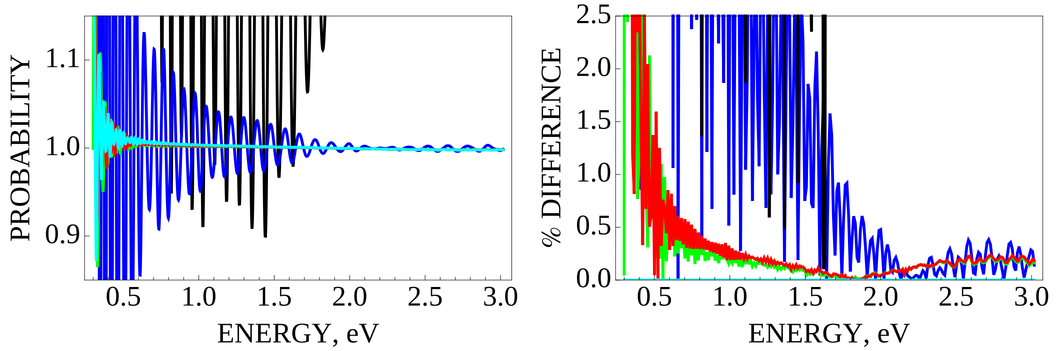

(e) *Normalization* (f) *Norm. % Difference*

Figure 4.13: Convergence of $\mathrm{H}+\mathrm{H}_2(\nu_i = j_i = 0)$ results for different $S^0_{\tau_i}$ values. The other Gaussian parameters are $\sigma = 0.2$ and $k_0 = 12.5$ bohr, with $\rho_\infty = 10$ bohr. The APH grid parameters are $N_\rho = 150$, $N_\theta = 55$, and $N_{\chi_i} = 481$. The time parameters are $t_{max} = 10010$ au, $N_t = 1001$, and $t_{delay} = 0$ au.
LEGEND: (BLACK : $S^0_{\tau_i} = 10$ bohr), (BLUE : $S^0_{\tau_i} = 9.5$ bohr), (GREEN : $S^0_{\tau_i} = 9$ bohr), (RED : $S^0_{\tau_i} = 8.5$ bohr), (CYAN : $S^0_{\tau_i} = 8$ bohr).

$S^0_{\tau_i} = 8$ and 8.5 bohr. The non-reactive probabilities and normalization plots in Figs. 4.14a and 4.14e show large oscillations when $S^0_{\tau_i} = 10.5$ and 11 bohr. The non-reactive results for $S^0_{\tau_i} \leq 10$ bohr show no noticeable difference, and the normalization results are converged above about 0.7 eV. The reactive results in Fig. 4.14c show no noticeable deviations for all values of $S^0_{\tau_i}$.

The percent difference plots in Figs. 4.14b, 4.14d, and 4.14f illustrate the accuracy of results for different values of $S^0_{\tau_i}$ when $\sigma = 0.2$, $k_0 = 12.5$ au, and $\rho_\infty = 11$ bohr. The non-reactive results in Fig. 4.14b, for $S^0_{\tau_i} \leq 10$ bohr, are converged above about 1.4 eV, with the best results obtained when $S^0_{\tau_i} = 10$ bohr at lower energies. The non-reactive results have a percent difference of $\leq 1\%$ from 0.55 to 2.75 eV. The reactive results in Fig. 4.14d are converged above about 1.7 eV, with the best results obtained when $S^0_{\tau_i} = 11$ bohr at lower energies. The reactive results have a percent difference of $\leq 0.5\%$ from 0.65 to 2.8 eV. Compared to the results in Fig. 4.13, the curves for different values of $S^0_{\tau_i}$ in the present results are much more compact as S_{τ_0} decreases. This is due to the higher values of $S^0_{\tau_i}$ that are shown. The results are very accurate for all shown values of $S^0_{\tau_i}$ between 0.65 and 2.75 eV, as long as the initial wave packet does not overlap ρ_∞. The non-reactive and low energy results show sensitivity to increasing $S^0_{\tau_i}$ since they are more convergent and more accurate at lower energies. However, note that there is no real improvement at energies above about 1.5 eV.

Fig. 4.15 shows results for different values of $S^0_{\tau_i}$ when $\sigma = 0.2$, $k_0 = 12.5$ au, and $\rho_\infty = 12$ bohr. Here, we include $S^0_{\tau_i} = 11.5$ and 12 bohr, and exclude $S^0_{\tau_i} = 9$ and 9.5 bohr from the previous results. The non-reactive probabilities and normalization plots in Figs. 4.15a and 4.15e show large oscillations when $S^0_{\tau_i} = 11.5$ and 12 bohr. The non-reactive results for $S^0_{\tau_i} \leq 11$ bohr show no noticeable difference, and the normalization results are converged above about 0.7 eV. The reactive results in Fig. 4.15c show no noticeable deviations for all

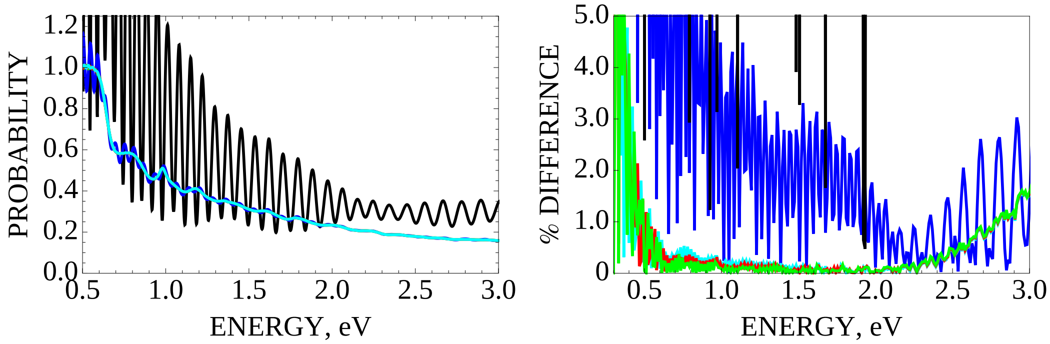

(a) *Non-Reactive Results* (b) *Non-Reactive % Difference*

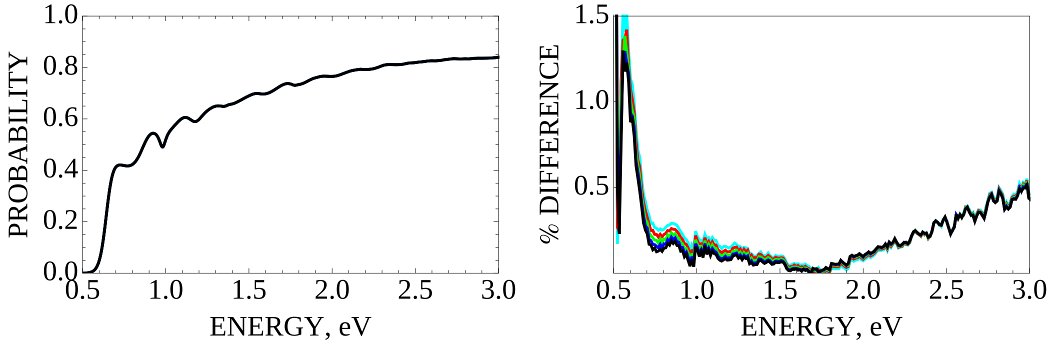

(c) *Reactive Results* (d) *Reactive % Difference*

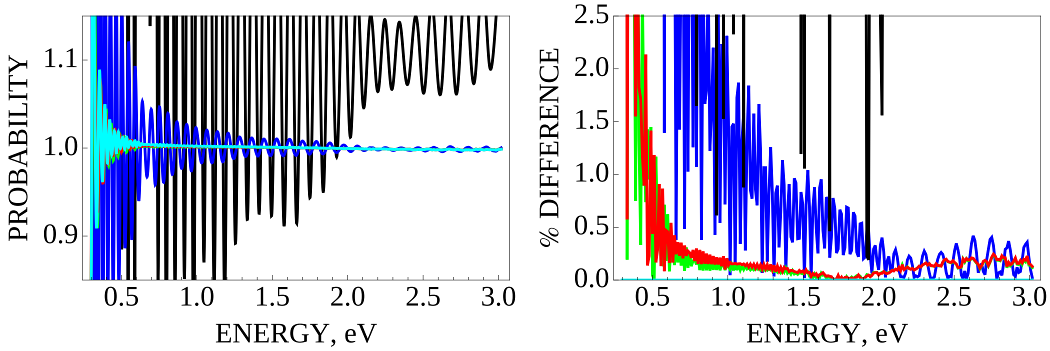

(e) *Normalization* (f) *Norm. % Difference*

Figure 4.14: Convergence of $\mathrm{H}+\mathrm{H}_2(\nu_i = j_i = 0)$ results for different $S^0_{\tau_i}$ values. The other Gaussian parameters are $\sigma = 0.2$ and $k_0 = 12.5$ bohr, with $\rho_\infty = 11$ bohr. The APH grid parameters are $N_\rho = 159$, $N_\theta = 55$, and $N_{\chi_i} = 481$. The time parameters are $t_{max} = 10010$ au, $N_t = 1001$, and $t_{delay} = 0$ au.
LEGEND: (BLACK : $S^0_{\tau_i} = 10$ bohr), (BLUE : $S^0_{\tau_i} = 9.5$ bohr), (GREEN : $S^0_{\tau_i} = 9$ bohr), (RED : $S^0_{\tau_i} = 8.5$ bohr), (CYAN : $S^0_{\tau_i} = 8$ bohr).

values of $S^0_{\tau_i}$.

The percent difference plots in Figs. 4.15b, 4.15d, and 4.15f illustrate the accuracy of results for different values of $S^0_{\tau_i}$ when $\sigma = 0.2$, $k_0 = 12.5$ au, and $\rho_\infty = 12$ bohr. The non-reactive results in Fig. 4.15b, for $S^0_{\tau_i} \leq 11$ bohr, converging above about 0.7 eV, which converges at much lower energy than with the $\rho = 10$ and 11 bohr results. The non-reactive results have a percent difference of $\leq 1\%$ from 0.6 to 2.7 eV. The reactive results in Fig. 4.15d are converged above about 1.55 eV, with the best results obtained when $S^0_{\tau_i} = 12$ bohr at lower energies. Note that the low energy results, below 0.6 eV, are more accurate and better converged than the $\rho = 10$ and 11 bohr results. The reactive results have a percent difference of $\leq 0.5\%$ from 0.65 to 2.8 eV. Compared to the results in Figs. 4.13 and 4.14, the curves for different values of $S^0_{\tau_i}$ in the present results are more compact as $S^0_{\tau_i}$ decreases. Again, this is due to the higher values of $S^0_{\tau_i}$ that are shown. The results are very accurate for all shown values of $S^0_{\tau_i}$ between 0.65 and 2.7 eV as long as the initial wave packet does not overlap ρ_∞. Again, the non-reactive and low energy results show sensitivity to increasing $S^0_{\tau_i}$ since they are better converged and more accurate at lower energies. This shows that the initial wave packet must have a large value of $S^0_{\tau_i}$ in order to obtain accurate low energy results. Also, as will be shown later, the larger value of ρ_∞ also has an effect on the low energy results.

4.3 APH Grid Parameters

4.3.1 Convergence of N_ρ

In this section, we study convergence of the results as the APH ρ grid density is varied. This is accomplished by changing the number of ρ grid points N_ρ, while the grid boundaries ρ_{min} and ρ_{max} remain constant. The ρ grid is uniformly

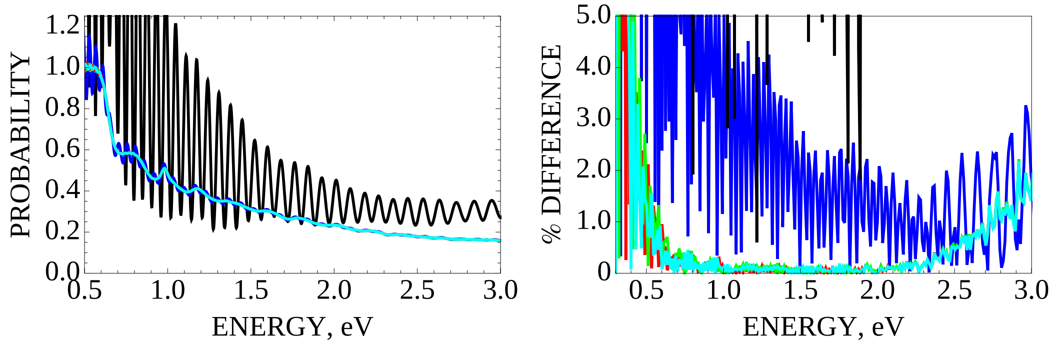

(a) *Non-Reactive Results* (b) *Non-Reactive % Difference*

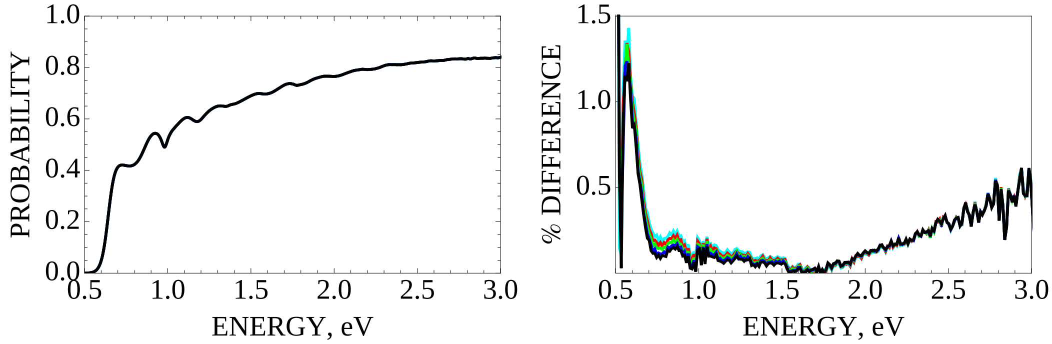

(c) *Reactive Results* (d) *Reactive % Difference*

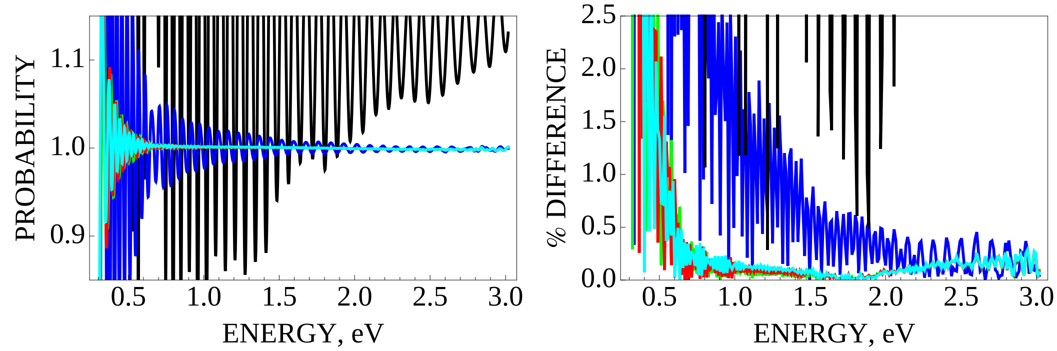

(e) *Normalization* (f) *Norm. % Difference*

Figure 4.15: Convergence of $\mathrm{H}+\mathrm{H}_2(\nu_i = j_i = 0)$ results for different $S^0_{\tau_i}$ values. The other Gaussian parameters are $\sigma = 0.2$ and $k_0 = 12.5$ bohr, with $\rho_\infty = 12$ bohr. The APH grid parameters are $N_\rho = 168$, $N_\theta = 65$, and $N_{\chi_i} = 481$. LEGEND: (BLACK : $S^0_{\tau_i} = 10$ bohr), (BLUE : $S^0_{\tau_i} = 9.5$ bohr), (GREEN : $S^0_{\tau_i} = 9$ bohr), (RED : $S^0_{\tau_i} = 8.5$ bohr), (CYAN : $S^0_{\tau_i} = 8$ bohr).

spaced, with grid spacing:

$$\Delta\rho = \frac{\rho_{max} - \rho_{min}}{N_\rho - 1}. \tag{4.5}$$

For the ρ grid to accurately represent the wave packet, the grid must be dense enough to represent incoming and outgoing waves that possess the highest kinetic energy contained in the wave packet. The maximum eigenvalue of the ρ kinetic energy operator can be used to determine if a given grid density is appropriate.

As discussed in Sec. 2.2.2, in Eq. (2.17), the ρ kinetic energy operator is given by

$$T_\rho = -\frac{\hbar^2}{2\mu\rho^{5/2}}\frac{\partial^2}{\partial\rho^2}\rho^{5/2}, \tag{4.6}$$

which we construct using the DAF representation [32, 33, 34, 35, 36, 37]. The maximum eigenvalues of T_ρ, for different values of N_ρ, are given in Table 4.4.

Results with initial state $\mathrm{H} + \mathrm{H}_2(\nu_i = j_i = 0)$, for various values of N_ρ, are shown in Figs. 4.16 and 4.17, where the boundaries of the ρ grid are $\rho_{min} = 0.64$ and $\rho_{max} = 16.5$ bohr. Fig. 4.16 presents convergence data with $k_0 = 8.5$ au and Fig. 4.17 presents data with $k_0 = 12.5$ au, providing convergence information at lower energies with the former and at higher energies for the latter. It is necessary to present two separate data sets due to the energy width of wave packet. This fact is illustrated by the collective divergence of the data in Fig. 4.16 for energies below 0.5 eV and above 2.4 eV, and by the same phe-

N_ρ	$\Delta\rho$ ($\times 10^{-1}$ au)	Max. Eigenvalue (eV)
100	1.602	2.757
125	1.279	4.324
150	1.064	6.245
175	0.9115	8.514
200	0.7968	11.138

Table 4.4: Maximum eigenvalues of the APH ρ kinetic energy operator for various grid densities. The number of grid points, N_ρ, are uniformly distributed between $\rho_{min} = 0.64$ bohr and $\rho_{max} = 16.5$ bohr.

nomenon in Fig. 4.17 for energies below 0.9 eV. For both figures, plots (a), (c), and (e) present the total non-reactive probability, total reactive probability, and sum of the total non-reactive and reactive probabilities (normalization), respectively. Plots (b) and (d) present the percent difference of the data with respect to the benchmark results of the ABC program [15] and the plots in (f) show the normalization percent difference from unity.

Fig. 4.16 presents data with $k_0 = 8.5$ au. The non-reactive and reactive results, in Figs. 4.16a and 4.16c, show that convergence is reached for all values of $N_\rho \geq 125$. The $N_\rho = 100$ results deviate around 2.8 eV in the non-reactive results and around 2.3 eV in the reactive results. The normalization plot in Fig. 4.16e shows convergence is reached when $N_\rho \geq 150$, with the $N_\rho = 100$ results deviating around 1.95 eV and the $N_\rho = 125$ results deviating around 2.5 eV.

Plots of the percent difference, in Figs. 4.16b, 4.16d, and 4.16f, provide a more detailed picture of convergence. For the non-reactive results, in Fig. 4.16b, the most apparent feature is the deviation of the $N_\rho = 100$ results above about 1.9 eV. While the $N_\rho = 100$ results are converged below 1.9 eV, these results have an accuracy of $\leq 1\%$ between about 0.5 and 2.4 eV. The non-reactive results also show convergence of the $N_\rho \geq 125$ results to about 2.4 eV, with only slight deviations of these results above this boundary, having an accuracy $\leq 1\%$ between 0.5 and 2.75 eV.

The reactive results in Fig. 4.16d show a similar behavior with respect to the $N_\rho = 100$ results, which is convergent to about 1.5 eV, and have an accuracy of $\leq 1\%$ between 0.6 and 2.5 eV. An odd feature is present in the reactive results, with the $N_\rho = 125$ results having a higher accuracy than the $N_\rho \geq 150$ results. This feature should only be viewed as a lack of convergence

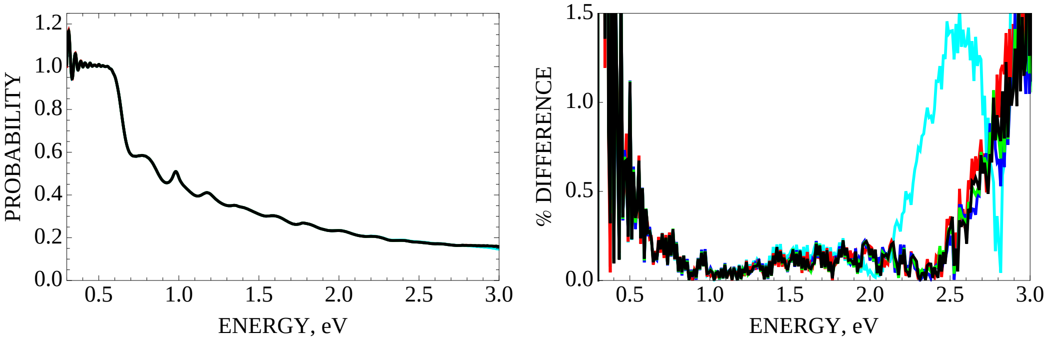

(a) *Non-Reactive Results* (b) *Non-Reactive % Difference*

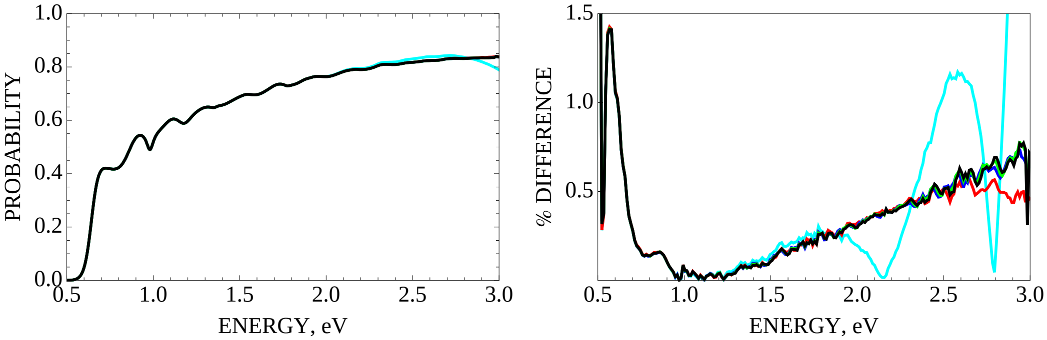

(c) *Reactive Results* (d) *Reactive % Difference*

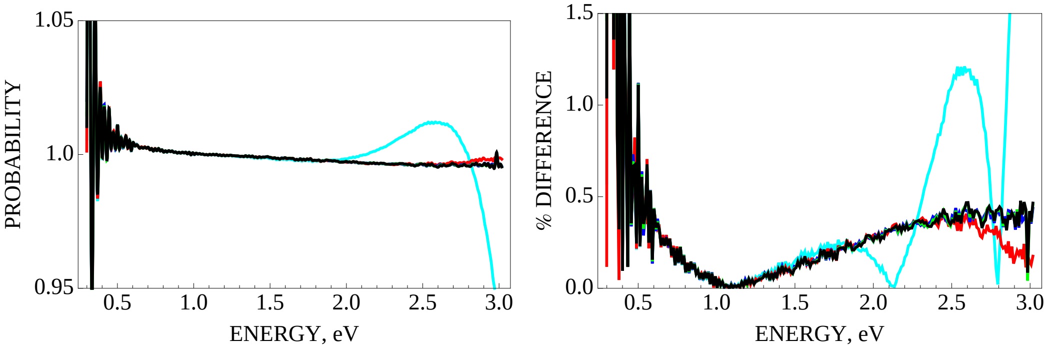

(e) *Normalization* (f) *Norm. % Difference*

Figure 4.16: Convergence of H + $H_2(\nu_i = j_i = 0)$ results for different N_ρ values uniformly distributed between $\rho_{min} = 0.64$ bohr and $\rho_{max} = 16.5$ bohr. The other APH grid parameters are $N_\theta = 65$ and $N_{\chi_i} = 481$. The Gaussian parameters are $\sigma = 0.3$, $k_0 = 8.5$ au, and $S^0_{\tau_i} = 9.5$ bohr, with $\rho_\infty = 10$ bohr. The time parameters are $t_{max} = 10010$ au, $N_t = 1001$, and $t_{delay} = 500$ au. LEGEND: (BLACK : $N_\rho = 200$), (BLUE : $N_\rho = 175$), (GREEN : $N_\rho = 150$), (RED : $N_\rho = 125$), (CYAN : $N_\rho = 100$).

above 2.5 eV, since an increase in accuracy is not present in the non-reactive case. However, even with the lack of convergence, the $N_\rho = 125$ results have an accuracy of $\leq 1\%$ between 0.6 and 3.0 eV. The reactive results are converged for $N_\rho \geq 150$ across the entire energy range and have an accuracy of $\leq 1\%$ between 0.6 and 3.0 eV.

Shifting the energy distribution, with $k_0 = 12.5$ au, allows analysis of the higher energy convergence. Fig. 4.17 shows the results for different values of N_ρ when $k_0 = 12.5$ au. The non-reactive and reactive results in Figs. 4.17a and 4.17c show that convergence is reached for all values of $N_\rho \geq 125$. The deviation of the $N_\rho = 100$ results is much more pronounced, with large oscillations at low energy in the non-reactive results and a distinct separation above about 2.3 eV in the reactive results. The non-reactive results also show deviation of the $N_\rho = 100$ results above about 2.6 eV. The normalization plot in Fig. 4.16e shows a more detailed view of the $N_\rho = 100$ oscillations, and shows the effect of setting $k_0 = 12.5$, since the low energy results are larger than unity.

Plots of the percent difference are given in Figs. 4.17b, 4.17d, and 4.17f. For the non-reactive results, in Fig. 4.17b, the most apparent feature is the deviation of the $N_\rho = 100$ results, which, even though they do drop below 1%, do not properly converge over the entire energy range. The non-reactive results also show convergence of the $N_\rho \geq 125$ results to about 2.0 eV and convergence of the $N_\rho = 150$ results below about 2.0 eV. At higher energies the $N_\rho = 125$ and 150 results have a higher accuracy than the $N_\rho = 175$ and 200 results. As before, this should only be viewed as a lack of convergence, and not that the less dense grids give better results. The results for $N_\rho \geq 125$ have an accuracy $\leq 1\%$ between 0.55 and 2.75 eV.

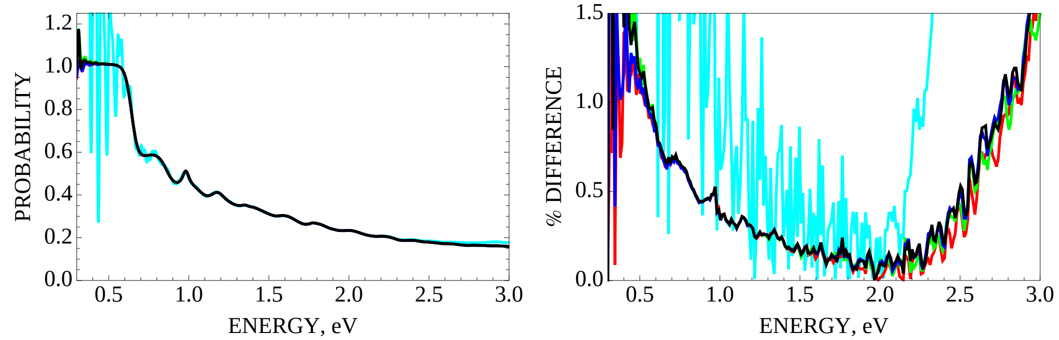

(a) *Non-Reactive Results* (b) *Non-Reactive % Difference*

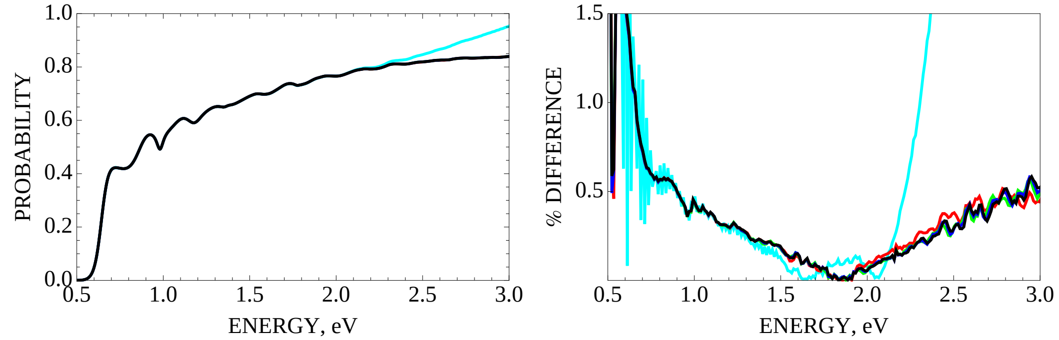

(c) *Reactive Results* (d) *Reactive % Difference*

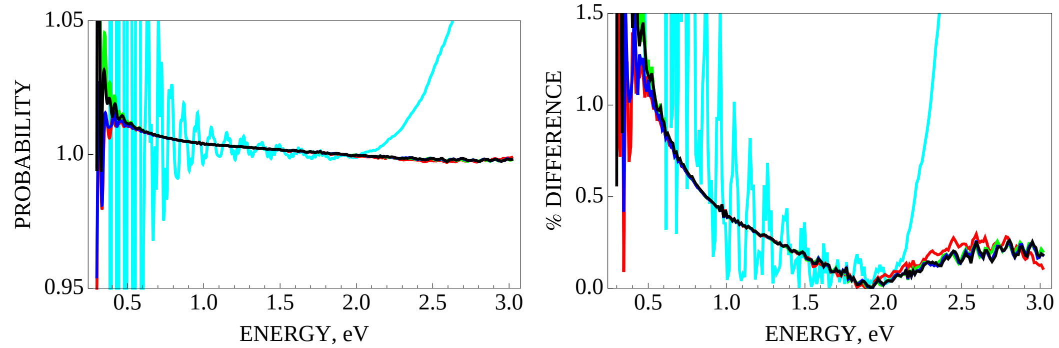

(e) *Normalization* (f) *Norm. % Difference*

Figure 4.17: Convergence of H + $H_2(\nu_i = j_i = 0)$ results for different N_ρ values uniformly distributed between $\rho_{min} = 0.64$ bohr and $\rho_{max} = 16.5$ bohr. The other APH grid parameters are $N_\theta = 65$ and $N_{\chi_i} = 481$. The Gaussian parameters are $\sigma = 0.3$, $k_0 = 12.5$ au, and $S^0_{\tau_i} = 9.5$ bohr, with $\rho_\infty = 10$ bohr. The time parameters are $t_{max} = 10010$ au, $N_t = 1001$, and $t_{delay} = 500$ au. LEGEND: (BLACK : $N_\rho = 200$), (BLUE : $N_\rho = 175$), (GREEN : $N_\rho = 150$), (RED : $N_\rho = 125$), (CYAN : $N_\rho = 100$).

The reactive results in Fig. 4.17d provide a better picture of the higher energy convergence. The $N_\rho = 100$ reactive results only converge between 0.9 and 1.15 eV, but have an accuracy $\leq 1\%$ between 0.7 and 2.3 eV. The $N_\rho = 125$ reactive results are converged below 1.9 eV, which is a lower energy of convergence than is shown in the $k_0 = 8.5$ au results, but have an accuracy $\leq 1\%$ between 0.65 and 3.0 eV. The $N_\rho = 150$ reactive results are converged below 2.6 eV, which is a higher energy of convergence than is shown in the non-reactive results. Due to the oscillatory nature of the non-reactive results, the convergence limit of 2.6 eV for the $N_\rho = 150$ reactive results is the limit that will be chosen. The $N_\rho = 150$ results have an accuracy $\leq 1\%$ between 0.65 and 3.0 eV. The $N_\rho \geq 175$ reactive results are converged for the entire range of energies. The credibility of the higher energy convergence for the $k_0 = 12.5$ au results, relative to the $k_0 = 8.5$ results, is attributed to the higher accuracy of the results at higher energies. Taking both the $k_0 = 8.5$ and 12.5 au results in consideration, the $N_\rho = 100$ results should only be considered for energies ≤ 1.5 eV, even though the non-reactive 12.5 au results are highly oscillatory. Since the energy of the initial diatom, with $\nu_i = j_i = 0$, is 0.269 eV, this convergence is obtained at a maximum kinetic energy of 1.231 eV. Table 4.4 lists a maximum eigenvalue of 2.757 eV for $N_\rho = 100$, and the ratio of this to maximum kinetic energy is about 2.24. The $N_\rho = 125$ results are converged for energies ≤ 1.9 eV, which corresponds to a maximum kinetic energy of 1.63 eV. Table 4.4 lists a maximum eigenvalue of 4.324 eV for $N_\rho = 125$, and the ratio of this to maximum kinetic energy is about 2.65. The $N_\rho = 150$ results are converged for energies ≤ 2.6 eV, which corresponds to a maximum kinetic energy of 2.33 eV. Table 4.4 lists a maximum eigenvalue of 6.245 eV for $N_\rho = 150$, and the ratio of this to maximum kinetic energy is about 2.68. For

$N_\rho \geq 175$, the data is fully converged across the entire shown energy range. Using the highest ratio calculated above, which is 2.68 for $N_\rho = 150$, and the eigenvalues listed in Table 4.4, the highest kinetic energy that can be accurately described for $N_\rho = 175$ is 3.177 eV. For $N_\rho = 200$, the maximum kinetic energy is 4.156 eV. The maximum allowed kinetic energies for $N_\rho \geq 175$ are above the maximum kinetic energies shown in the results. A good estimate on whether a given ρ grid density will provide converged results for the maximum allowed kinetic energy of the energy region of interest is given by

$$E^k_{max} = \mathcal{E}^\rho_{max}/\alpha, \tag{4.7}$$

where $\mathcal{E}^\rho_{max}$ is the maximum eigenvalue of T_ρ, E^k_{max} is the maximum kinetic energy required, and α is empirically assumed to be ≥ 2.68.

However, it should be noted that, for $N_\rho \geq 125$, all the reactive results have an accuracy $\leq 1\%$ above 0.65 eV, and the non-reactive results have an accuracy of $\leq 1\%$ between 0.6 and 2.75 eV, regardless of the convergence. While convergence to the most accurate results is important, the results are reliable across a majority of the energy range shown.

4.3.2 Convergence of N_{χ_i}

In this section, we study convergence of the results as the APH χ_i grid density is varied. This is accomplished by changing the number of χ_i grid points N_{χ_i} over the range 0 to 2π. The χ_i grid is uniformly spaced, with grid spacing:

$$\Delta\chi_i = \frac{2\pi}{N_{\chi_i} - 1}. \tag{4.8}$$

For the χ_i grid to accurately represent the wave packet, as well as the initial and final states, the grid must be dense enough to represent the rovibrational states that are present in the wave packet. The eigenvalues of the diatomic Hamiltonian can be used to determine if a given grid density is appropriate at a given energy, since, as each vibrational state opens, more grid points will be required to represent the added node present in the eigenfunction. The diatomic Hamiltonian is given in Sec. 2.2.4 in Eq. (2.24). The reasoning behind using the asymptotic states to determine the adequacy of a given grid density is a result of the decrease of the χ_i grid density as ρ increases. Since the largest value of ρ at which the wave packet needs to be represented is around ρ_∞, where the wave packet is projected onto its asymptotic eigenfunctions, then we can assume that if the χ_i grid density is appropriate at ρ_∞, it is appropriate at $\rho < \rho_\infty$. Note that this will also be the case for N_θ, which will be discussed in the next section. Table 4.5 lists the energy eigenvalues of the diatomic hamiltonian for seven lowest bound states. Only the lowest seven bound states are shown, since these will be the only open states in the energy region of interest of the results. The energies at which these vibrational states open will provide information on where a particular grid density becomes ineffective at representing that particular eigenfunction.

ν	Eigenvalue (eV)	ν	Eigenvalue (eV)
0	0.269	4	2.160
1	0.782	5	2.563
2	1.269	6	2.939
3	1.728		

Table 4.5: Eigenvalues of the diatomic Hamiltonian for the first seven bound vibrational states with $j = 0$.

Results with initial state $\mathrm{H} + \mathrm{H}_2(\nu_i = j_i = 0)$, for various values of N_{χ_i}, are shown in Figs. 4.18 and 4.19. Fig. 4.18 presents convergence data with $k_0 = 8.5$

au and Fig. 4.19 presents data with $k_0 = 12.5$ au, providing convergence information at lower energies with the former and at higher energies for the latter. It is necessary to present separate data sets due to the energy width of wave packet, as discussed previously in the convergence with respect to N_ρ. For both figures, plots (a), (c), and (e) present the total non-reactive probability, total reactive probability, and sum of the total non-reactive and reactive probabilities (normalization), respectively. Plots (b) and (d) present the percent difference of the data with respect to the benchmark results of the ABC program [15], and the plots in (f) show the normalization percent difference from unity.

Fig. 4.18 presents data with $k_0 = 8.5$ au. The results in Figs. 4.18a, 4.18c, and 4.18e show large oscillations and that no convergence is reached for $N_{\chi_i} = 121$. For $N_{\chi_i} = 241$, the non-reactive and reactive results are convergent below about 1.35 eV, but the normalization results show convergence below 0.9 eV. For $N_{\chi_i} = 361$, the non-reactive results do not show significant evidence of a lack of convergence, but the reactive and normalization results show convergence below 2.75 and 2.1 eV, respectively. The $N_{\chi_i} \geq 481$ results are convergent across the entire range of energies shown.

Plots of the percent difference in Figs. 4.18b, 4.18d, and 4.18f provide a more detailed picture of convergence. For all percent difference plots, the $N_{\chi_i} = 121$ results are only visible at low energy, and show no convergence. Choosing $N_{\chi_i} = 121$ will not provide accurate results for any initial or final value of ν. The $N_{\chi_i} = 241$ nonreactive and normalization results are converged below around 0.9 eV, and have an accuracy of $\leq 1\%$ between 0.5 and 0.9 eV. The reactive results are only converged to around 0.6 eV and have an accuracy $\leq 1\%$ between 0.6 and 1.0 eV. According to Table 4.5, the $N_{\chi_i} = 241$ results

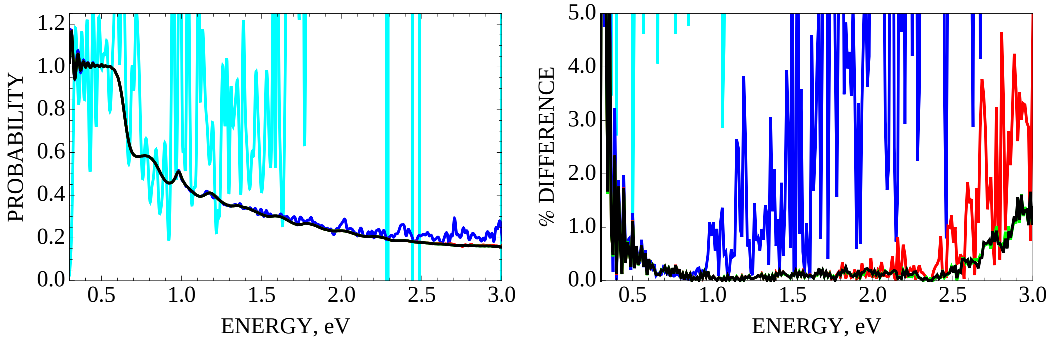

(a) *Non-Reactive Results* (b) *Non-Reactive % Difference*

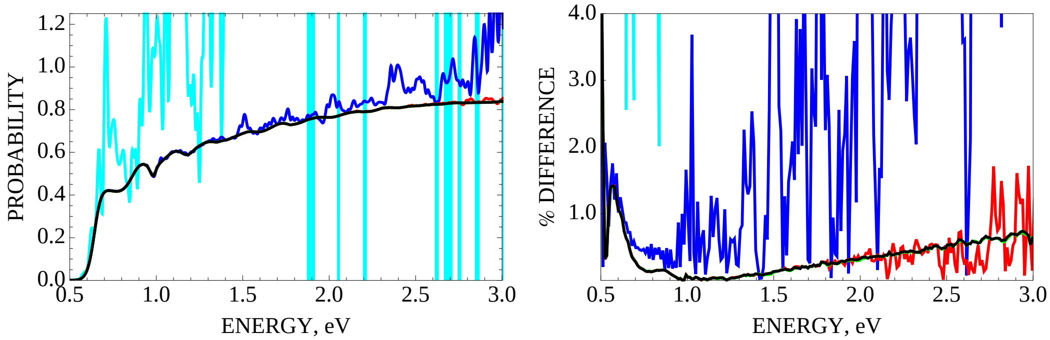

(c) *Reactive Results* (d) *Reactive % Difference*

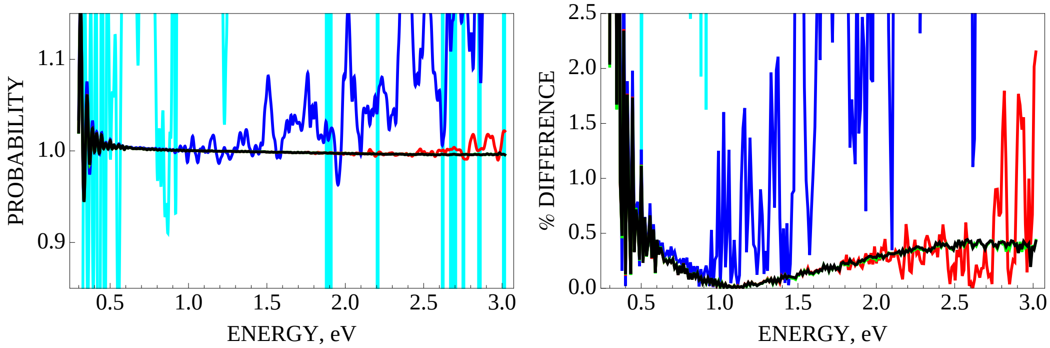

(e) *Normalization* (f) *Norm. % Difference*

Figure 4.18: Results for different N_{χ_i} values with $N_\rho = 150$ and $N_\theta = 65$. The Gaussian parameters are $\sigma = 0.3$, $k_0 = 8.5$ au, and $S^0_{\tau_i} = 9.5$ bohr, with $\rho_\infty = 10$ bohr. The time parameters are $t_{max} = 10010$ au, $N_t = 1001$, and $t_{delay} = 500$ au.
LEGEND: (BLACK : $N_{\chi_i} = 601$), (GREEN : $N_{\chi_i} = 481$), (RED : $N_{\chi_i} = 361$), (BLUE : $N_{\chi_i} = 281$), (CYAN : $N_{\chi_i} = 121$).

lack convergence and have an accuracy $\leq 1\%$ just above the energy where the $\nu = 1$ vibrational state becomes open. Therefore, choosing $N_{\chi_i} = 241$ will only give accurate results for initial or final $\nu = 0$ states.

All the precent difference results in Fig. 4.18 for $N_{\chi_i} = 361$ are converged below 1.8 eV. The results have an accuracy $\leq 1\%$ between 0.5 and 2.4 eV for non-reactive, between 0.6 and 2.75 eV for reactive, and between 0.5 and 2.8 eV for normalization. According to Table 4.5, the $N_{\chi_i} = 361$ results lack convergence between the energies just above the energy where the $\nu = 3$ vibrational state becomes open. However, the results have an accuracy $\leq 1\%$ around the energy of the $\nu = 5$ state. Therefore, choosing $N_{\chi_i} = 361$ will only give converged results for initial or final $\nu \leq 2$ states, but will give accurate results for the $\nu \leq 4$ states.

The percent difference results in Fig. 4.18 for $N_{\chi_i} \geq 481$ are converged across the entire range of energies. The results for $N_{\chi_i} \geq 481$ have an accuracy of $\leq 1\%$ between 0.5 and 2.85 eV for the non-reactive, between 0.6 and 3.0 eV for the reactive, and 0.5 and 3.0 eV for the normalization. According to Table 4.5, the $N_{\chi_i} \geq 481$ results have convergence above where the $\nu = 6$ vibrational state becomes open. The results have an accuracy $\leq 1\%$ just around the energy of the $\nu = 6$ state for the non-reactive results, and above the $\nu = 6$ state for the reactive and normalization results. Therefore, choosing $N_{\chi_i} \geq 481$ will give converged results for initial or final $\nu \leq 6$ states, but will only give $\leq 1\%$ accuracy for the $\nu \leq 5$ states.

The fact that the results become much less accurate as each vibrational channel opens is key feature of the precent difference results. This feature illustrates the initial assumption that the accuracy of the results is dependent on the ability of number of χ_i grid points to represent the asymptotic vibrational eigenfunctions.

Shifting the energy distribution, with $k_0 = 12.5$ au, allows analysis of the

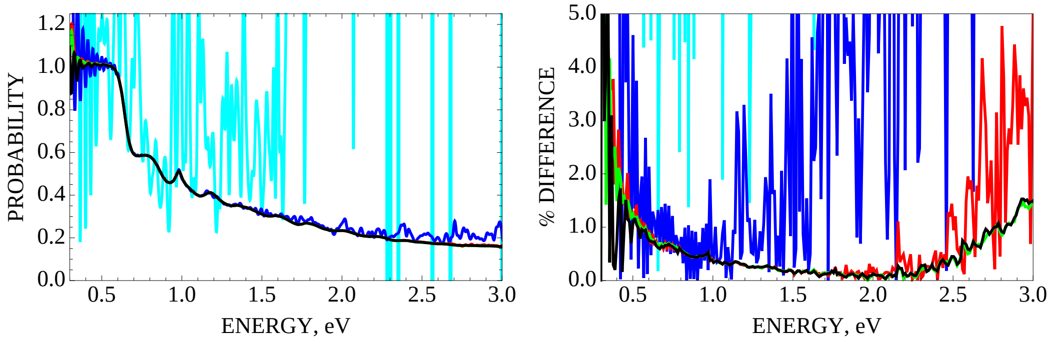

(a) *Non-Reactive Results* (b) *Non-Reactive % Difference*

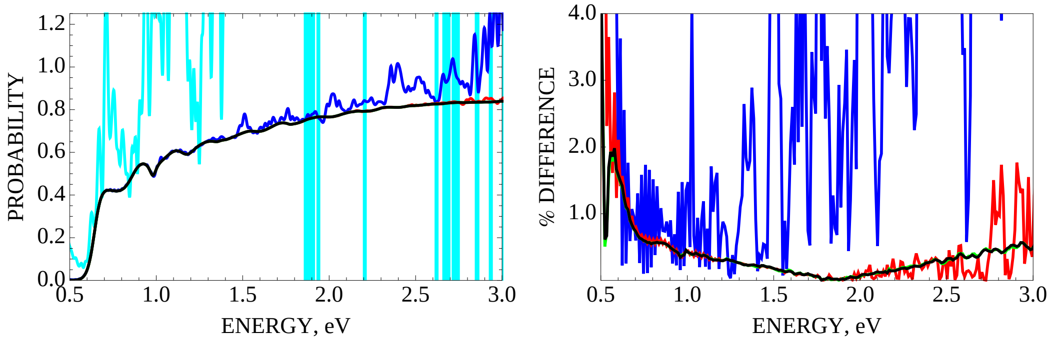

(c) *Reactive Results* (d) *Reactive % Difference*

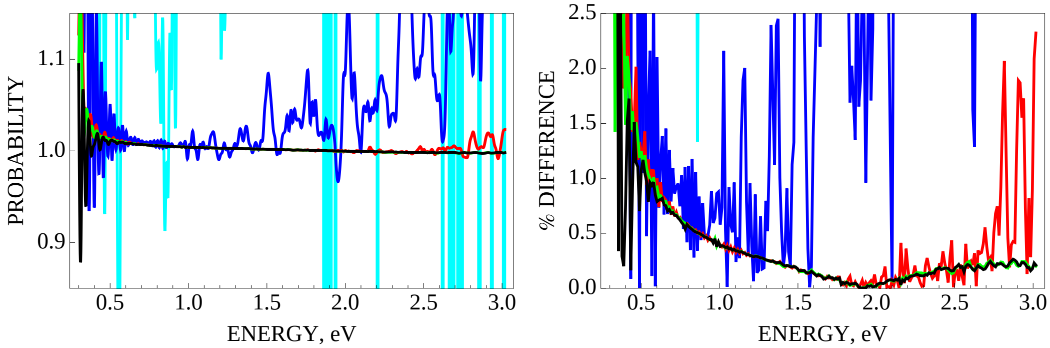

(e) *Normalization* (f) *Norm. % Difference*

Figure 4.19: Results for different N_{χ_i} values with $N_\rho = 150$ and $N_\theta = 55$. The Gaussian parameters are $\sigma = 0.3$, $k_0 = 12.5$ au, and $S^0_{\tau_i} = 9.5$ bohr, with $\rho_\infty = 10$ bohr. The time parameters are $t_{max} = 10010$ au, $N_t = 1001$, and $t_{delay} = 500$ au.
LEGEND: (BLACK : $N_{\chi_i} = 601$), (GREEN : $N_{\chi_i} = 481$), (RED : $N_{\chi_i} = 361$), (BLUE : $N_{\chi_i} = 281$), (CYAN : $N_{\chi_i} = 121$).

higher energy convergence. Fig. 4.19 shows the results for different values of N_{χ_i} when $k_0 = 12.5$ au. The results in Figs. 4.19a, 4.19c, and 4.19e show no new information when compared to the $k_0 = 8.5$ au results.

Plots of the percent difference in Figs. 4.19b, 4.19d, and 4.19f provide a more detailed picture of convergence, but provide no useful information for the $N_{\chi_i} \leq 241$ results. While the high energy results are more accurate in the reactive and normalization plots than when $k_0 = 8.5$ au, the convergence and $\leq 1\%$ accuracy boundaries for $N_{\chi_i} \geq 361$ are the same as before. Therefore, the data favoring the higher energy region of interest reinforces the previous conclusions.

The maximum eigenvalue ν that can be properly represented by a given N_{χ_i} has been determined by analyzing the convergence and accuracy of the results. The assumption that the χ_i grid density can be determined according to its ability to properly represent the diatomic eigenfunctions, and the validity of the conclusions made from the results, can be further reinforced by explicitly looking at how well the χ_i grid density represents the diatomic eigenfunctions. The diatomic eigenfunctions are a function of s_τ, and the relationship between χ_i and s_τ was given in Sec. 2.2.2 in Eq. (2.16b). In order to remove the ρ and θ dependence in Eq. 2.16b, we can set $\rho = \rho_\infty = 10$ bohr, and set $\theta = \pi/2$. Since it is assumed that ρ_∞ is located in the asymptotic region of the PES, choosing $\rho = \rho_\infty$ is appropriate. The least dense χ_i grid corresponds to the edge of the hypersperical surface where $\theta = \pi/2$, providing a picture of the least available representation of the eigenfunctions. Finally, we only need to look at the eigenfunctions in a single arrangement channel, so we choose $\chi_{\tau i} = 0$. With these parameters, Eq. (2.16b) becomes

$$s_{\tau_i} = \frac{10}{\sqrt{2}}\Big\{1 - \cos\left[2\chi_i\right]\Big\}^{1/2}, \tag{4.9}$$

providing a mapping of the χ_i grid points to s_{τ_i} grid points.

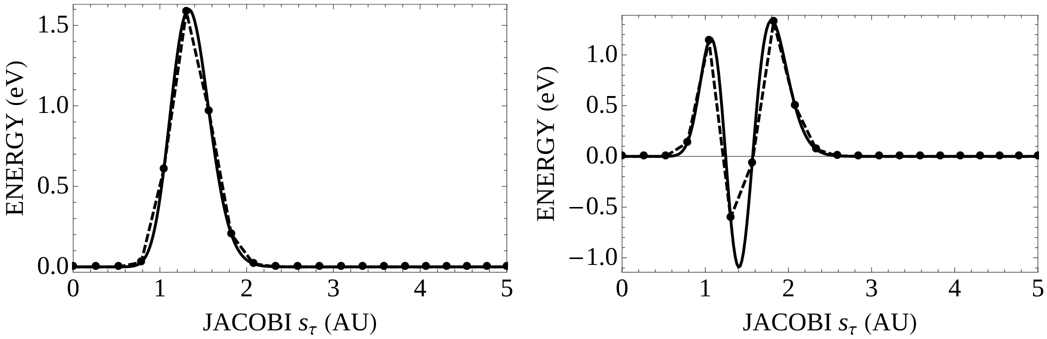

(a) $N_{\chi_i} = 241$; $\nu = 0$ (b) $N_{\chi_i} = 241$; $\nu = 2$

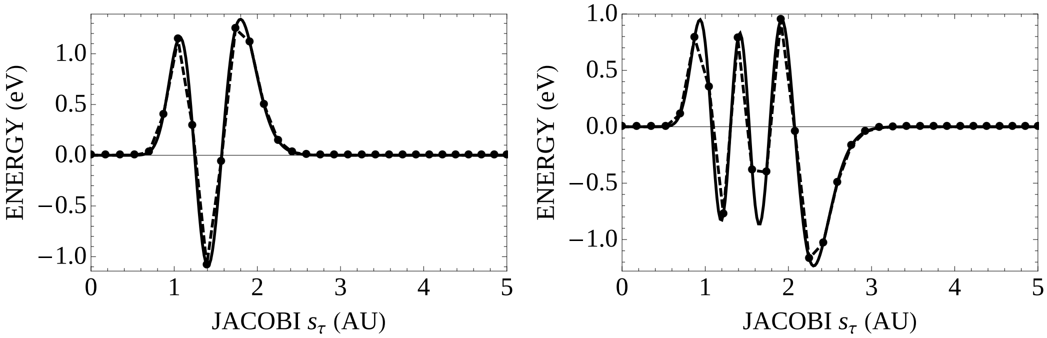

(c) $N_{\chi_i} = 361$; $\nu = 2$ (d) $N_{\chi_i} = 361$; $\nu = 5$

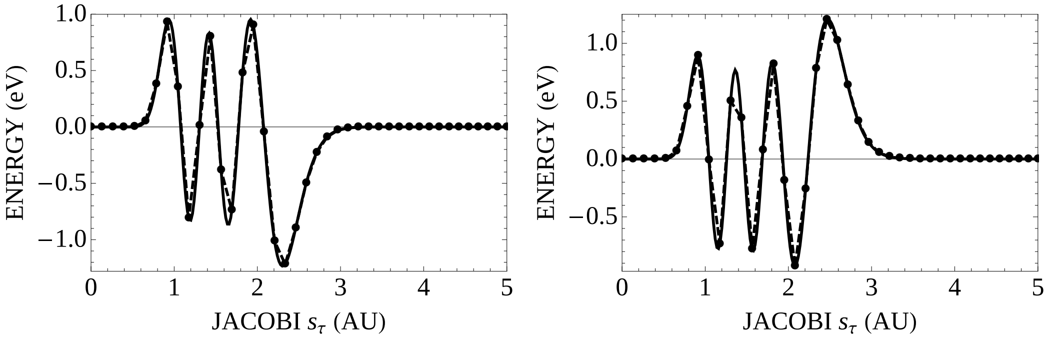

(e) $N_{\chi_i} = 481$; $\nu = 5$ (f) $N_{\chi_i} = 481$; $\nu = 6$

Figure 4.20: Plots of the vibrational eigenfunctions as a function of s_{τ_i} The solid lines are the eigenfunctions determined by diagonalizing the diatomic Hamiltonian and the data points are the χ_i grid points mapped to s_{τ_i} for $\rho = 10$ bohr and $\theta = \pi/2$. The dashed lines are a first order interpolation of the data points.

Fig. 4.20 shows the χ_i grid points used to represent the diatomic eigenfunctions at $\rho = \rho_\infty$ and $\theta = \pi/2$. This figure presents two eigenfunctions for three different values of N_{χ_i}, with the first providing an eigenfunction that is properly represented and the second showing an eigenfunction that is not properly represented. Since the $N_{\chi_i} = 481$ results are converged for all open channels in the energies shown, the two eigenfunctions are both assumed to be properly represented.

Figs. 4.20a and 4.20b show the grid points used to represent the $\nu = 0$ and 2 diatomic eigenfunctions when $N_{\chi_i} = 241$. Previously, it was determined that the $N_{\chi_i} = 241$ results were only appropriate at energies where the $\nu = 0$ vibrational state is open. The $\nu = 0$ eigenfunction is properly represented over the range of its amplitude. The $\nu = 2$ eigenfunction is not properly represented, with a large portion of its amplitude not accounted for, and this is evident in the low accuracy of the results presented earlier.

Figs. 4.20c and 4.20d show the grid points used to represent the $\nu = 2$ and 5 diatomic eigenfunctions when $N_{\chi_i} = 361$. Previously, it was determined that the $N_{\chi_i} = 361$ results were converged at energies where the $\nu \leq 2$ vibrational states are open, and accurate to $\leq 1\%$ for $\nu \leq 4$. The $\nu = 2$ eigenfunction is properly represented with only a small portion of its amplitude left unaccounted. The $\nu = 5$ eigenfunction is not properly represented, with two of its extrema not accurately accounted.

Figs. 4.20e and 4.20f show the grid points used to represent the $\nu = 5$ and 6 diatomic eigenfunctions when $N_{\chi_i} = 481$. Previously, it was determined that the $N_{\chi_i} = 481$ results were converged and accurate at energies where the $\nu \leq 6$ vibrational states are open. The $\nu = 5$ eigenfunction is properly represented. The $\nu = 6$ eigenfunction has a small portion unaccounted for, but the majority of the wave function is properly represented.

Even though the conclusions made using the plots shown in Fig. 4.20 are *ad* *hoc* with respect to the results already presented, they still serve as a useful tool in determining the energies where a chosen grid density not be appropriate. Remember that, since $\theta = \pi/2$, these plots show the minimum number of points that are used to represent the eigenfunctions, and when $\theta < \pi/2$ more points will be available over the range of the eigenfunctions' amplitude.

4.3.3 Convergence of N_θ

In this section, we study convergence of the results as the APH θ grid density is varied. This is accomplished by changing the number of θ grid points N_θ over the range 0 to $\pi/2$. Unlike the ρ and χ_i grids, the θ grid is not uniformly spaced. The θ kinetic energy operator is formed using the discrete variable representation (DVR) [43, 44], and the grid points are determined by the roots of the Legendre polynomials.

As with the χ_i grid, for the θ grid to accurately represent the wave packet, as well as the initial and final states, the grid must be dense enough to represent the rovibrational states that are present in the wave packet. Again, the eigenvalues of the diatomic Hamiltonian can be used to determine if a given grid density is appropriate at a given energy, since, as each vibrational state opens, more grid points will be required to represent the added node present in the eigenfunction. Table 4.5 lists the energy eigenvalues of the diatomic hamiltonian for seven lowest bound states. The energies at which these vibrational states open will provide information on where a particular grid density becomes ineffective at representing that particular eigenfunction. Results with initial state H+H$_2$($\nu_i = j_i = 0$), for various values of N_θ, are shown in Figs. 4.21 and 4.22. Fig. 4.21 presents convergence data with $k_0 = 8.5$ au and Fig. 4.22 presents data with $k_0 = 12.5$ au, providing convergence information at lower energies with the former and at higher energies for the latter.

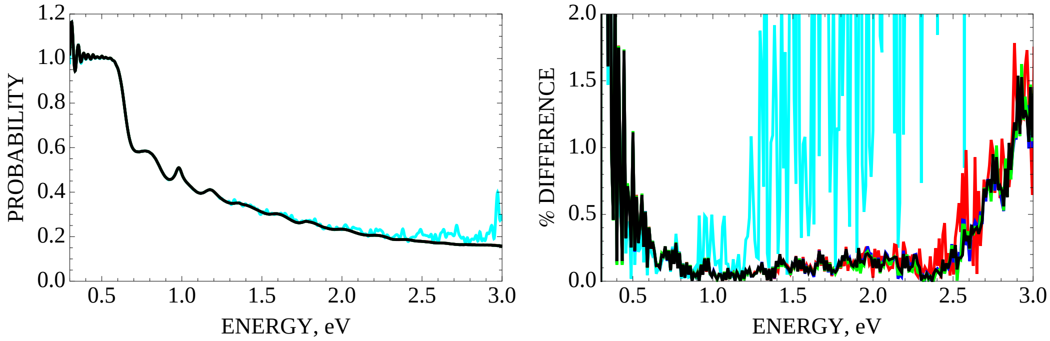

(a) *Non-Reactive Results* (b) *Non-Reactive % Difference*

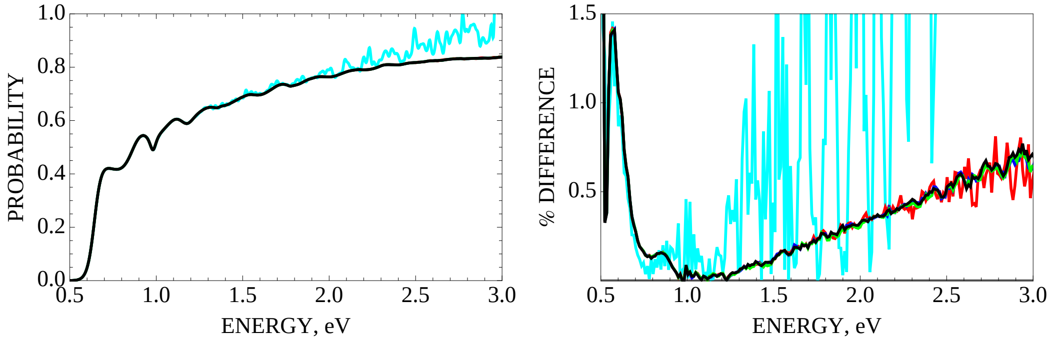

(c) *Reactive Results* (d) *Reactive % Difference*

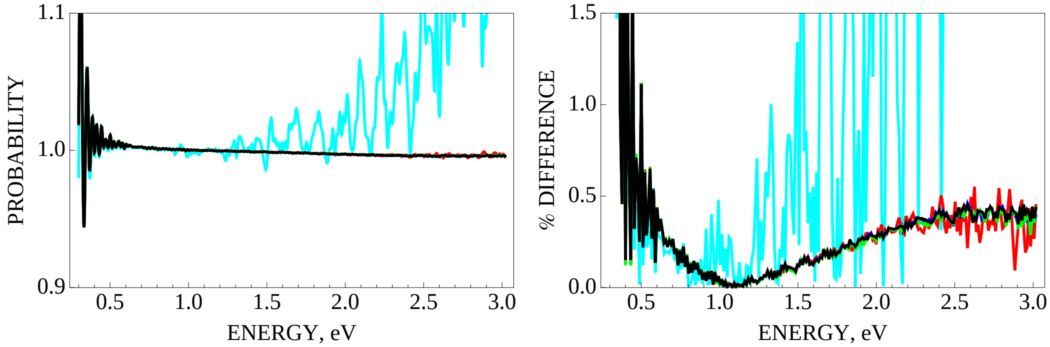

(e) *Normalization* (f) *Norm. % Difference*

Figure 4.21: Results for different N_θ values $N_\rho = 150$ and $N_{\chi_i} = 481$. The Gaussian parameters are $\sigma = 0.3$, $k_0 = 8.5$ au, and $S^0_{\tau_i} = 9.5$ bohr, with $\rho_\infty = 10$ bohr. The time parameters are $t_{max} = 10010$ au, $N_t = 1001$, and $t_{delay} = 500$ au.
LEGEND: (BLACK : $N_\theta = 75$), (GREEN : $N_\theta = 65$), (BLUE : $N_\theta = 55$), (RED : $N_\theta = 45$), (CYAN : $N_\theta = 31$).

Fig. 4.21 presents data with $k_0 = 8.5$ au. The non-reactive and reactive results in Figs. 4.21a and 4.21c show convergence for $N_\theta = 31$ below about 1.3 eV, and the normalization results, in Fig. 4.21e, show convergence below about 0.9 eV. For $N_\theta = 45$, the only a minimal lack of convergence, above about 2.3 eV, is evident in the normalization results. The results for $N_\theta \geq 55$ appear convergent across the entire range of energies.

Plots of the percent difference for $k_0 = 8.5$ au in Figs. 4.21b, 4.21d, and 4.21f provide a more detailed picture of convergence. For all percent difference plots, the $N_\theta = 31$ results do not converge in the traditional sense, but do show a high accuracy below about 0.9 eV before beginning to deviate significantly. The $N_\theta = 31$ results have an accuracy $\leq 1\%$ between 0.5 and 1.3 eV. According to Table 4.5, the $N_\theta = 31$ results lack convergence just above the $\nu = 1$ vibrational state and have an accuracy $\leq 1\%$ up to around the energy where the $\nu = 2$ vibrational state becomes open. Therefore, choosing $N_\theta = 31$ will give converged results for initial or final $\nu = 0$ states, but will give accurate results for $\nu \leq 1$ states.

The $N_\theta = 45$ results for $k_0 = 8.5$ au are converged below around 2.0 eV in all difference plots, and have an accuracy of $\leq 1\%$ between 0.5 and 2.6 eV for the non-reactive results. The reactive and normalization results have an accuracy $\leq 1\%$ above 0.6 eV. According to Table 4.5, the $N_\theta = 45$ results lack convergence between the $\nu = 3$ and $\nu = 4$ vibrational states and have an accuracy $\leq 1\%$ up to around the energy where the $\nu = 5$ vibrational state becomes open for the non-reactive results. The $N_\theta = 45$ results don't follow the usual behavior, where convergence is lost just above the energy where a vibrational channel opens. However, the lack of convergence does increase as each new vibrational channel opens, so the general behavior assumed still applies. Choosing $N_\theta = 45$ will give converged results to around the energy where the $\nu = 2$, or possibly 3, states become open. Since very accurate results $\leq 0.5\%$ are present below 2.3 eV in all plots, it can be assumed that the N_θ grid adequately represents the $\nu \leq 3$ states.

The $N_\theta = 55$ and 65 results for $k_0 = 8.5$ au only show a minor lack of convergence above 2.9 eV, evident in the reactive and normalization plots. These results have an accuracy $\leq 1\%$ above 0.5 eV in the non-reactive and normalization plots, and above 0.6 eV in the reactive plot. Furthermore, the results have an accuracy of $\leq 0.5\%$ between 0.6 and 2.7 eV in the non-reactive plot, between 0.65 and 2.4 eV in the reactive plot, and between 0.6 and 3.0 eV in the normalization plot. According to Table 4.5, the $N_\theta = 55$ and 65 results lack convergence just above the $\nu = 6$ vibrational state and have an accuracy $\leq 1\%$ for all the shown energies. Therefore, choosing $N_\theta = 55$ or 65 will give converged and very accurate results initial or final $\nu \leq 5$ states, but will give adequately accurate results for $\nu \leq 6$ states.

Shifting the energy distribution, with $k_0 = 12.5$ au, allows analysis of the higher energy convergence. Fig. 4.22 shows the results for different values of N_θ when $k_0 = 12.5$ au. The results in Figs. 4.22a, 4.22c, and 4.22e show no new information of significance when compared to the $k_0 = 8.5$ au results.

Plots of the percent difference in Figs. 4.22b, 4.22d, and 4.22f provide a more detailed picture of convergence, but provide no useful information for the $N_\theta = 31$ results. The convergence and $\leq 1\%$ accuracy boundaries for $N_\theta \geq 45$ are the same as for the $k_0 = 8.5$ au results. The only aspect of the $k_0 = 12.5$ au results that is important is the higher accuracy of the higher energy results for the $N_\theta \geq 45$ results. This fact reinforces the previous conclusions, but adds the conclusion that the $N_\theta \geq 45$ grids provide very high accuracy for all shown energies, even in regions that lack convergence.

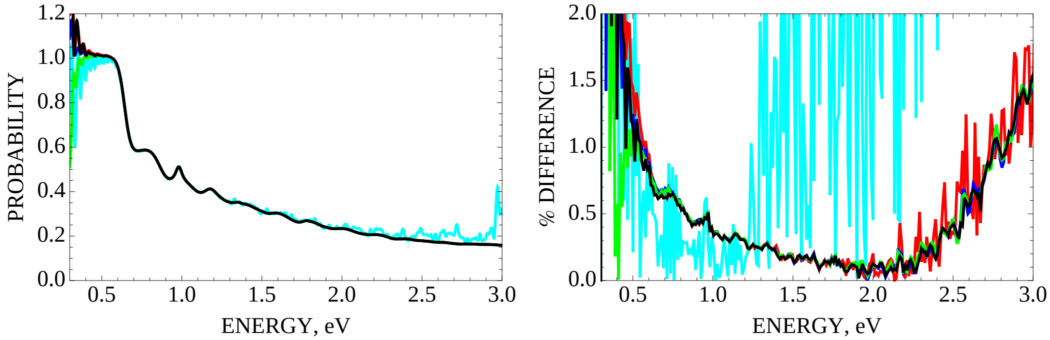

(a) *Non-Reactive Results* (b) *Non-Reactive % Difference*

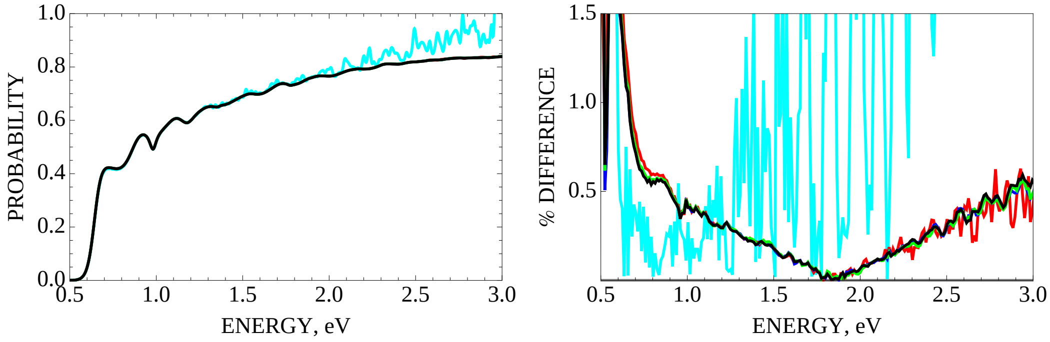

(c) *Reactive Results* (d) *Reactive % Difference*

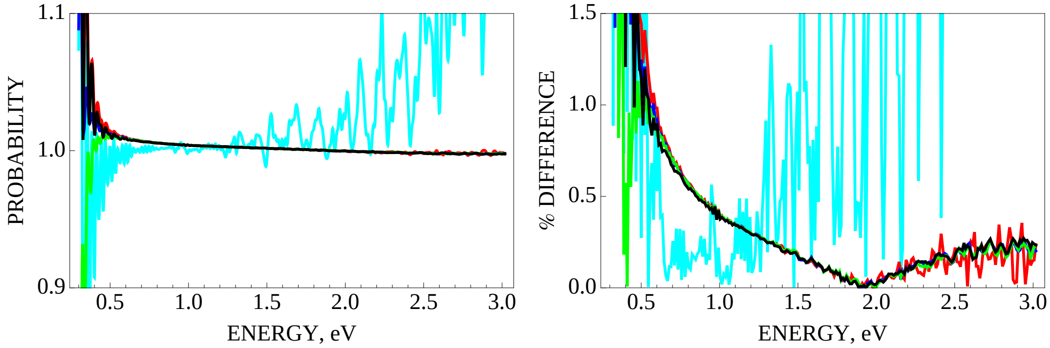

(e) *Normalization* (f) *Norm. % Difference*

Figure 4.22: Results for different N_θ values with $N_\rho = 150$ and $N_{\chi_i} = 481$. The Gaussian parameters are $\sigma = 0.3$, $k_0 = 12.5$ au, and $S^0_{\tau_i} = 9.5$ bohr, with $\rho_\infty = 10$ bohr. The time parameters are $t_{max} = 10010$ au, $N_t = 1001$, and $t_{delay} = 500$ au.
LEGEND: (BLACK : $N_\theta = 75$), (GREEN : $N_\theta = 65$), (BLUE : $N_\theta = 55$), (RED : $N_\theta = 45$), (CYAN : $N_\theta = 31$).

The maximum eigenvalue ν that can be properly represented by a given N_θ has been determined by analyzing the convergence and accuracy of the results. As with N_{χ_i}, the assumption that the θ grid density can be determined according to its ability to properly represent the diatomic eigenfunctions, and the validity of the conclusions made from the results, can be further reinforced by explicitly looking at how well the θ grid density represents the diatomic eigenfunctions. The diatomic eigenfunctions are a function of s_τ, and the relationship between θ and s_τ was given in Sec. 2.2.2 in Eq. (2.16b). In order to remove the ρ and χ_i dependence in Eq. (2.16b), we can set $\rho = \rho_\infty = 10$ bohr, and set $\chi_i = 0$. Since it is assumed that ρ_∞ is located in the asymptotic region of the PES, choosing $\rho = \rho_\infty$ is appropriate. The least dense θ grid corresponds a line on the hypersperical surface where $\chi_i = 0$, providing a picture of the least available representation of the eigenfunctions. These parameters offer look at the eigenfunctions in the entrance arrangement channel, and Eq. (2.16b) becomes

$$s_{\tau_i} = \frac{10}{\sqrt{2}}\Big\{1 - \sin\theta\Big\}^{1/2}, \tag{4.10}$$

providing a mapping of the θ grid points to s_{τ_i} grid points.

Fig. 4.23 shows the θ grid points used to represent the diatomic eigenfunctions at $\rho = \rho_\infty$ and $\chi_i = 0$. This figure presents two eigenfunctions for three different values of N_θ, with the first providing an eigenfunction that is properly represented and the second showing an eigenfunction that is not properly represented.

Figs. 4.23a and 4.23b show the grid points used to represent the $\nu = 0$ and 1 diatomic eigenfunctions when $N_\theta = 31$. Previously, it was determined that the $N_\theta = 31$ results were only appropriate at energies where the $\nu = 0$ vibrational state is open. The $\nu = 0$ eigenfunction is properly represented over the range of its amplitude. The $\nu = 1$ eigenfunction is not properly represented, with a

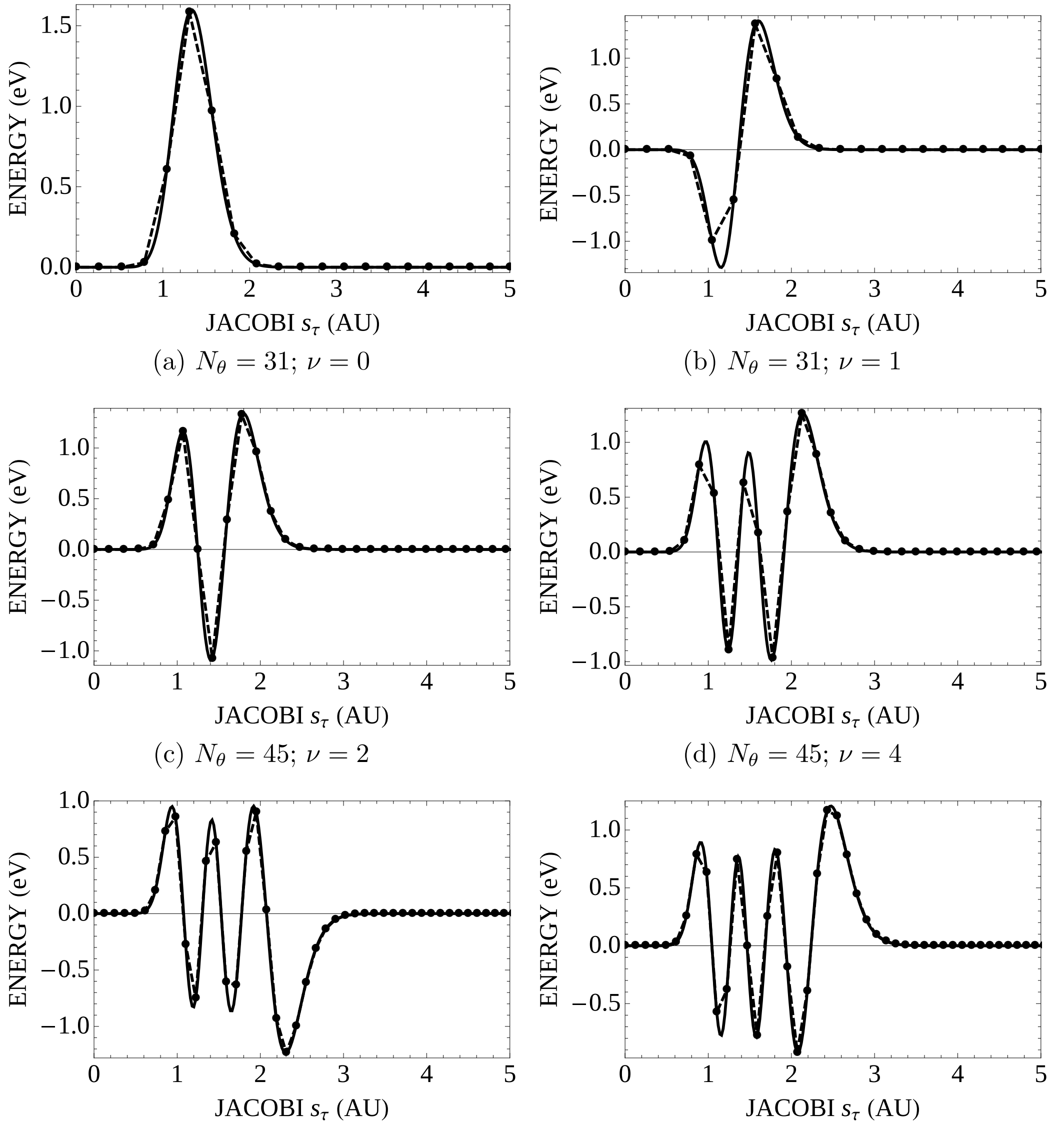

(a) $N_\theta = 31$; $\nu = 0$

(b) $N_\theta = 31$; $\nu = 1$

(c) $N_\theta = 45$; $\nu = 2$

(d) $N_\theta = 45$; $\nu = 4$

(e) $N_\theta = 65$; $\nu = 5$

(f) $N_\theta = 65$; $\nu = 6$

Figure 4.23: Plots of the vibrational eigenfunctions as a function of s_{τ_i} The solid lines are the eigenfunctions determined by diagonalizing the diatomic Hamiltonian and the data points are the θ grid points mapped to s_{τ_i} for $\rho = 10$ bohr and $\chi_i = 0$. The dashed lines are a first order interpolation of the data points.

large portion of its amplitude not accounted for, and this is evident in the low accuracy of the results presented earlier.

Figs. 4.23c and 4.23d show the grid points used to represent the $\nu = 2$ and

4 diatomic eigenfunctions when $N_\theta = 45$. Previously, it was determined that the $N_\theta = 45$ results were converged at energies where the $\nu \leq 2$ vibrational states are open, and accurate to $\leq 0.5\%$ for $\nu \leq 3$. The $\nu = 2$ eigenfunction is properly represented with only almost all of its amplitude accounted. The $\nu = 4$ eigenfunction is not properly represented, with two of its extrema not accurately accounted.

Figs. 4.23e and 4.23f show the grid points used to represent the $\nu = 5$ and 6 diatomic eigenfunctions when $N_\theta = 65$. Previously, it was determined that the $N_\theta = 65$ results were converged and accurate at energies where the $\nu \leq 5$ vibrational states are open. Although minor portions of the $\nu = 5$ eigenfunction, around its extrema, are left unaccounted, the majority of it is properly represented. The $\nu = 6$ eigenfunction shows similar behavior, but this is expected, due to the minimal lack of convergence and the high accuracy of the results.

As with N_{χ_i}, even though the conclusions made using the plots shown in Fig. 4.23 are *ad hoc* with respect to the results already presented, they still serve as a useful tool in determining the energies where a chosen grid density not be appropriate. Remember that , since $\chi_i = 0$, these plots show the minimum point density that is used to represent the eigenfunctions, and, when $\chi_i \neq 0$, more points will be available over the range of the eigenfunctions' amplitude.

4.4 Time Parameters

4.4.1 Convergence of t_{max}

The t_{max} parameter determines the total time the wave packet will be propagated, starting from $t = 0$. t_{max} must be large enough to ensure that the entire wave packet has propagated into the interaction region of the PES and returned to pass ρ_∞. The appropriate value of t_{max} depends primarily upon the attributes of the PES. The asymptotic region of the PES determines where $S^0_{\tau_i}$ and ρ_∞ must be located, and the larger these parameters, the longer the wave packet must be propagated. Furthermore, the properties of the interaction region of the PES can cause the wave packet to be temporarily "trapped", requiring longer propagation times. The initial momentum distribution of the initial wave packet also have an effect on t_{max}, where the presence of small kinetic energies will require longer propagation times. Conversely, an initial wave packet containing higher kinetic energies will decrease the propagation time.

A zeroth-order estimation of t_{max} can be found by analyzing the propagation of a free Gaussian wave packet in one-dimension. The envelope of a free Gaussian wave packet at any time t is given by [55]

$$g(S_{\tau_i}, t) = \left(\frac{1}{2\pi\sigma^2 p(\sigma,t)}\right)^{1/4} e^{-\left[S_{\tau_i} - S^0_{\tau_i} + (k_0 t/\mu)\right]^2 / \left[4\sigma^2 p(\sigma,t)\right]}, \tag{4.11}$$

where

$$p(\sigma, t) = \frac{t^2}{4\mu^2\sigma^4}. \tag{4.12}$$

To determine the zeroth-order value of t_{max}, we find the propagation time required for the free wave packet to travel approximately the round-trip distance from $S^0_{\tau_i}$ to ρ_∞. This is accomplished by plotting the amplitude of the evolving wave packet over the range $S^0_{\tau_i}$ to $S_{\tau_i} = -\rho_\infty$ for various propagation times. The time it takes for the wave packet amplitude to drop below 1% of its initial maximum value, between $S^0_{\tau_i}$ to $S_{\tau_i} = -\rho_\infty$, provides a good estimate of t_{max}. Of course, this estimate doesn't take the PES interactions into account, such as the possibility of resonances, but does help to reduce the amount of parameter space that needs to be explored.

Fig. 4.24 shows "snapshots" of the envelope of two evolving wave packet at different times. The solid curves represent a wave packet with $\sigma = 0.3$ and $k_0 = 8.5$ au, and the dashed curves represent a wave packet with $\sigma = 0.2$ and $k_0 = 12.5$ au. Both wave packets start at $S^0_{\tau_i} = 9.5$ bohr and are propagated toward $S^0_{\tau_i} = -\rho_\infty = -10$ bohr. Fig. 4.24a shows the wave packet at $t = 0$. The maximum amplitude of the $\sigma = 0.3$, $k_0 = 8.5$ au wave packet is about 1.1 and the amplitude of the $\sigma = 0.2$, $k_0 = 12.5$ au wave packet is about 1.4. The time at which the wave packets' maximum amplitudes drop to about 0.011 and 0.014 between -10 and 9.5 bohr is the zeroth order value of t_{max}.

Fig. 4.24b shows the wave packets at $t = 1010$ au. The packets have translated toward -10 bohr and have significant amplitudes in the region of interest. Note that the $k_0 = 12.5$ packet is translating more rapidly since it contains higher kinetic energy components. Also, the packets have broadened as the higher energy components leave the lower energy components behind. Fig. 4.24c shows the wave packets at $t = 2510$ au. A significant amount of the $k_0 = 12.5$ au packet has crossed the -10 bohr boundary, but it still has a maximum amplitude of about10% its initial maximum. The slower moving $k_0 = 8.5$ au packet still has significant amplitude, with a maximum at about 25% of its initial maximum.

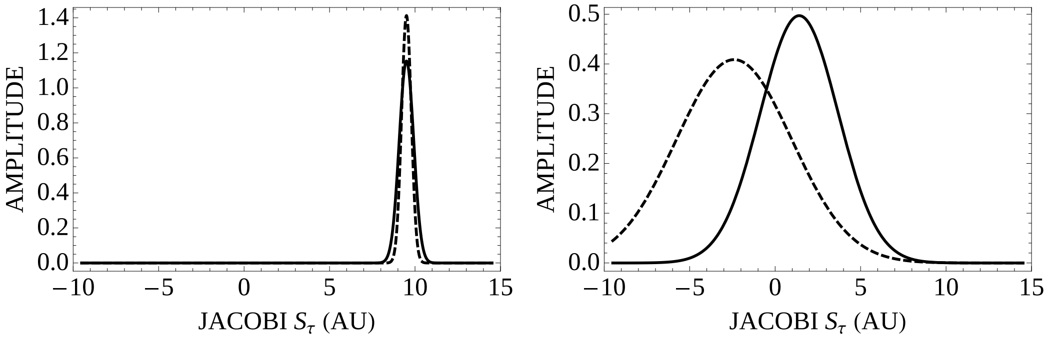

(a) $t = 0$ au (b) $t = 1010$ au

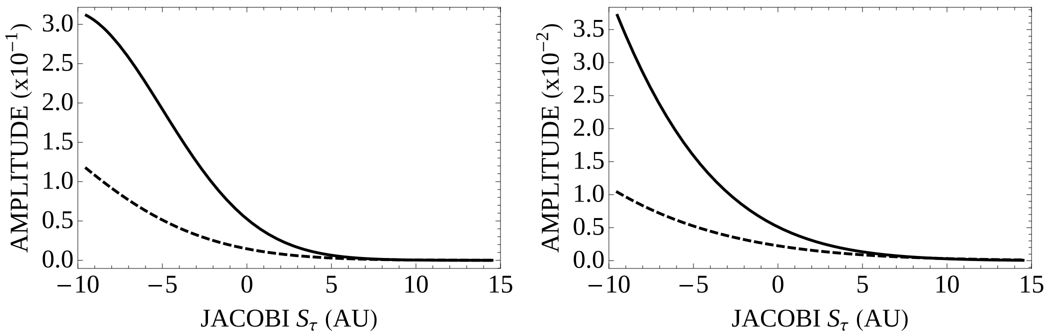

(c) $t = 2510$ au (d) $t = 5010$ au

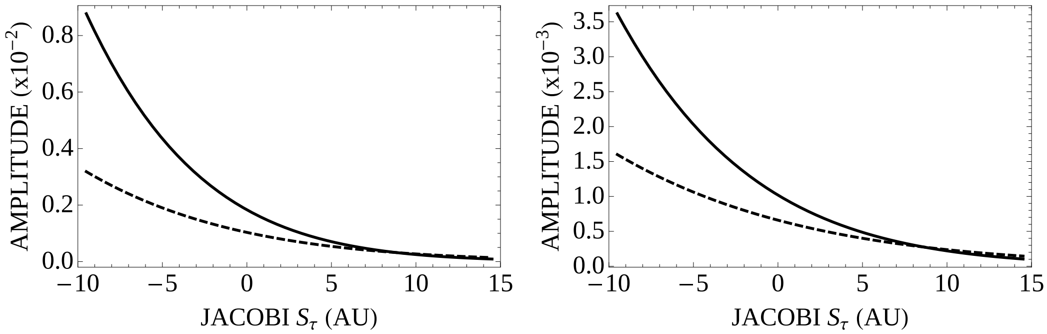

(e) $t = 7510$ au (f) $t = 10010$ au

Figure 4.24: Envelope of the Gaussian wave packet at different propagation times. The initial wave packet starts at $S^0_{\tau_i} = 9.5$ bohr. The solid line is a wave packet with $\sigma = 0.3$ and $k_0 = 8.5$ au, and the dashed line is a wave packet with $\sigma = 0.2$ and $k_0 = 12.5$ au.

Fig. 4.24d shows the wave packets at $t = 5010$ au. The maximum of the $k_0 = 12.5$ au packet is now around 1% its initial maximum, and choosing $t_{max} = 5010$ au would be a suitable choice. However, to account for possible resonances and to be sure that the "entire" wave packet is out of the region of interest, it would be beneficial to propagate it for a little longer. The $k_0 = 8.5$ au packet's maximum has decreased about an order of magnitude between $t = 2510$ and 5010 au, but still needs to be propagated longer as well.

Fig. 4.24e shows the wave packets at $t = 7510$ au. The $k_0 = 12.5$ packet can be assumed to have vacated the region of interest, since its maximum amplitude is about 0.2% of the initial maximum. A maximum propagation time of $t_{max} = 7510$ au is a suitable zeroth-order starting point for the $k_0 = 12.5$ au wave packet. The $k_0 = 8.5$ au packet still has a maximum amplitude of about 1% its initial maximum, so it should be propagated a little longer. Fig. 4.24f shows the wave packets at $t = 10010$ au. Both wave packets have exited the region of interest, so $t_{max} = 10010$ is suitable propagation time for the $k_0 = 8.5$ au packet.

Results with initial state $\mathrm{H}+\mathrm{H}_2(\nu_i = j_i = 0)$, for various values of t_{max}, are shown in Figs. 4.25 and 4.26. Fig. 4.25 presents convergence data with $\sigma = 0.3$ and $k_0 = 8.5$ au, and Fig. 4.26 presents data with $\sigma = 0.2$ and $k_0 = 12.5$ au. The Gaussian parameters of these results are the same as the wave packets discussed above, and the zeroth-order predictions can be tested.

Fig. 4.25 presents the results for $\sigma = 0.3$, $k_0 = 8.5$ au. The non-reactive and reactive results, in Figs. 4.25a and 4.25c, only show a lack of convergence for the $t_{max} = 5010$ au data. The normalization results, in Fig. 4.25e, show a lack of convergence for both the $t_{max} = 5010$ and 7510 au data. The non-reactive and normalization plots show deviations at low energies, around 0.5 eV, and are present because the low kinetic energy portion of the wave packet hasn't reached the analysis surface. All three plots show a lack of convergence around 1.0 eV. The $\nu = 1$ vibrational state opens, at 0.78 eV, just below the

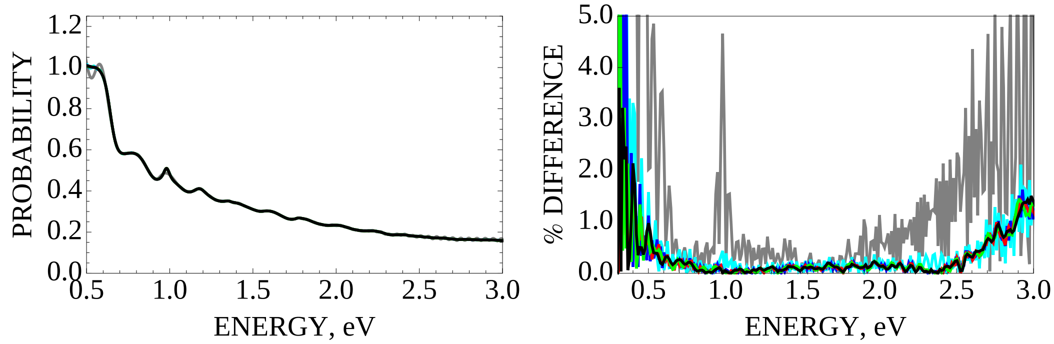

(a) *Non-Reactive Results* (b) *Non-Reactive % Difference*

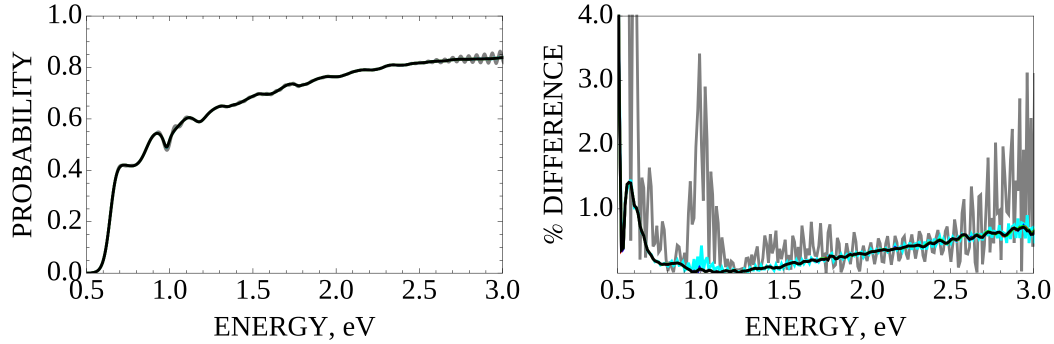

(c) *Reactive Results* (d) *Reactive % Difference*

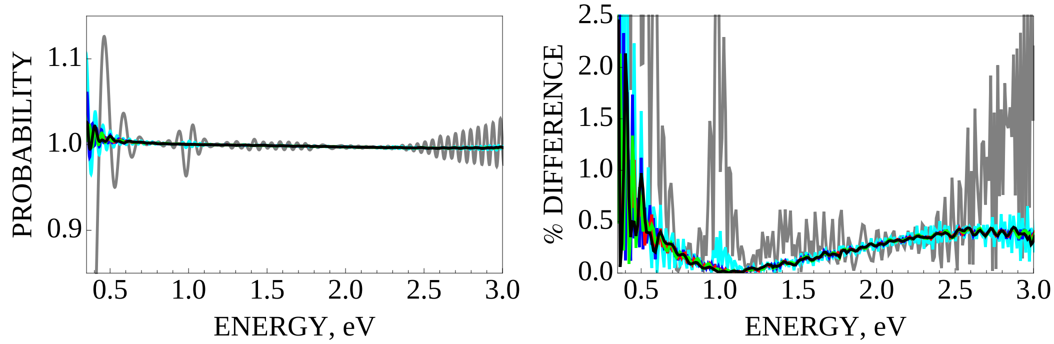

(e) *Normalization* (f) *Norm. % Difference*

Figure 4.25: Results for different values of t_{max}. The APH grid parameters are $N_\rho = 150$, $N_\theta = 55$, and $N_{\chi_i} = 481$. The Gaussian parameters are $\sigma = 0.3$, $k_0 = 8.5$ au, and $S^0_{\tau_i} = 9.5$ bohr, with $\rho_\infty = 10$ bohr. The time parameters are $N_t = 1001$ and $t_{delay} = 500$ au,
LEGEND: (BLACK : $t_{max} = 17510$ au), (GREEN : $t_{max} = 15010$ au), (RED : $t_{max} = 12510$ au), (BLUE : $t_{max} = 10010$ au), (CYAN : $t_{max} = 7510$ au), (GRAY : $t_{max} = 5010$ au)

deviations and the $\nu = 1$ products have a small kinetic energies and don't reach ρ_∞. All three plots also show oscillations above around 2.5 eV and are caused by the lack of higher kinetic energy components in the wave packet.

Plots of the percent difference for $\sigma = 0.3$, $k_0 = 8.5$ au, in Figs. 4.25b, 4.25d, and 4.25f, provide a more detailed picture of convergence. The most prominent features in these plots are the large spikes in the $t_{max} = 5010$ au data. Less pronounced versions of these are present in the $t_{max} = 7510$ au data. As before, these are due to the low kinetic energy of the $\nu = 1$ products at these energies, and these slow moving portions of the wave packet don't reach ρ_∞. The loss of convergence around energies where other vibrational channels open is evident in the large wavelength oscillations in the $t_{max} = 5010$ au data.

The percent difference results show convergence for $t_{max} \geq 10010$ au, as predicted by the zeroth-order estimation discussed previously. Only the reactive results, in Fig. 4.25d, show convergence of the $t_{max} = 7510$ au data, between 0.5 and 0.8 eV. However, even though the $t_{max} = 7510$ au results are not converged elsewhere, in all plots they have a high accuracy of $\leq 0.5\%$ between 0.65 and 2.5 eV and $\leq 1\%$ between 0.6 and 2.7 eV.

Fig. 4.26 presents the results for $\sigma = 0.2$, $k_0 = 12.5$ au. The non-reactive, reactive, and normalization results, in Figs. 4.25a, 4.25c, and 4.25e, are similar to the $k_0 = 8.5$ au results, but lack the high energy oscillations. These oscillations are no longer present since the wave packet's energy region of interest has been shifted and contain higher energy components.

Plots of the percent difference for $\sigma = 0.2$, $k_0 = 12.5$ au, in Figs. 4.26b, 4.26d, and 4.26f, provide a more detailed picture of convergence at higher energies. As in the $k_0 = 8.5$ au results, the $t_{max} = 5010$ au data contains large

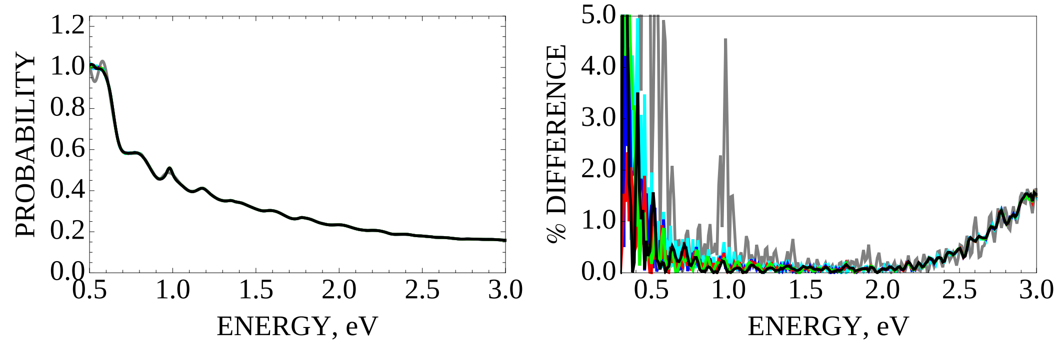

(a) *Non-Reactive Results* (b) *Non-Reactive % Difference*

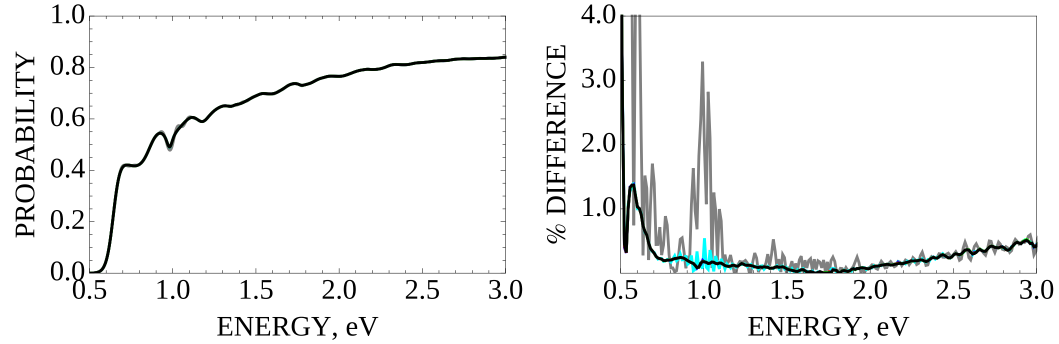

(c) *Reactive Results* (d) *Reactive % Difference*

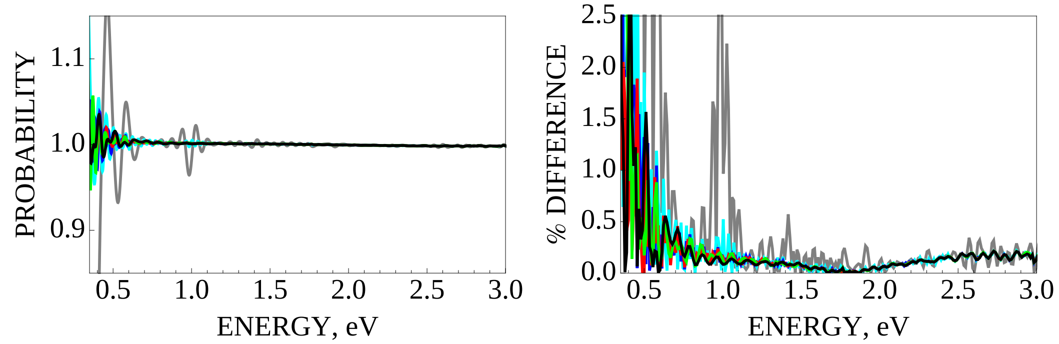

(e) *Normalization* (f) *Norm. % Difference*

Figure 4.26: Results for different values of t_{max}. The APH grid parameters are $N_\rho = 150$, $N_\theta = 55$, and $N_{\chi_i} = 481$. The Gaussian parameters are $\sigma = 0.2$, $k_0 = 12.5$ au, and $S^0_{\tau_i} = 9.5$ bohr, with $\rho_\infty = 10$ bohr. The time parameters are $N_t = 1001$ and $t_{delay} = 500$ au,
LEGEND: (BLACK : $t_{max} = 17510$ au), (GREEN : $t_{max} = 15010$ au), (RED : $t_{max} = 12510$ au), (BLUE : $t_{max} = 10010$ au), (CYAN : $t_{max} = 7510$ au), (GRAY : $t_{max} = 5010$ au)

spikes, with the $t_{max} = 7510$ au data containing smaller versions, around 1.0 eV. Similar, but smaller, features are present in the $t_{max} = 5010$ au data around 1.4 and 1.9 eV, corresponding to energies just above where the $\nu = 2$ and 3 vibrational states open at 1.27 and 1.73 eV, respectively. Another distinct feature of the $k_0 = 12.5$ au results, when compared to the $k_0 = 8.5$ au results, is the accuracy and semi-convergent $t_{max} = 5010$ au data at energies above 2.0 eV. Since the vibrational states that are open above 2.0 eV do not significantly contribute to the total non-reactive and reactive probabilities, the populated lower vibrational states have larger kinetic energies and are moving fast enough to reach ρ_∞.

In all plots, the $t_{max} \geq 7510$ au data is converged above 1.4 eV. The reactive results, in Fig. 4.26d, show convergence for $t_{max} \geq 7510$ au for all energies, except for the 1.0 eV spike in the $t_{max} = 7510$ au data. The zeroth-order estimate above predicted that $t_{max} = 7510$ au should be adequate for converged results, and, since a wave packet with $\sigma = 0.2$, $k_0 = 12.5$ favors results at higher energies, this estimate is validated. The lack of convergence, in the non-reactive and normalization results, for all values of t_{max} below 1.4 eV confirms the high energy favorability.

4.4.2 Convergence of N_t

The N_t parameter determines the total number of grid points between $t = 0$ and t_{max}. The N_t grid is uniformly spaced, with grid spacing:

$$\Delta t = \frac{t_{max}}{N_t}. \tag{4.13}$$

The wave packet is analyzed at ρ_∞ at each time grid point, so the grid must be dense enough to obtain relevant information from the wave packet. For example, if $N_t = 1$, the only grid point is located at t_{max}. When $t = t_{max}$, the entire wave packet has already crossed ρ_∞ and analysis of the packet only at this point provides no information. Therefore, if N_t isn't large enough, significant portions of the wave packet will cross ρ_∞ without being analyzed.

The appropriate value of N_t is primarily dependent upon the Gaussian parameter k_0, with higher values of k_0 requiring larger values of N_t due to the higher kinetic energy components present in the wave packet. Therefore, the faster the wave packet is moving, the denser the time grid must be to properly resolve the information present in the evolving wave packet.

Results with initial state $\mathrm{H} + \mathrm{H}_2(\nu_i = j_i = 0)$, for various values of N_t, are shown in Figs. 4.27 and 4.28. Fig. 4.27 presents convergence data with $\sigma = 0.3$ and $k_0 = 8.5$ au, and Fig. 4.28 presents data with $\sigma = 0.2$ and $k_0 = 12.5$ au. Table 4.6 lists the values of N_t and their corresponding grid spacings Δt when $t_{max} = 10010$ au.

Fig. 4.27 presents the results for $\sigma = 0.3$, $k_0 = 8.5$ au. The non-reactive, reactive, and normalization results, in Figs. 4.27a, 4.27c, and 4.27e, show convergence for all values of N_t. This is to be expected when $k_0 = 8.5$ au, since the wave packet contains low kinetic energies and will slowly evolve in

N_t	Δt (au)	N_t	Δt (au)
401	25.0	1001	10.0
501	20.0	1335	7.5
667	15.0	2002	5.0

Table 4.6: Values of N_t and their corresponding grid spacings Δt when $t_{max} =$ 10010 au.

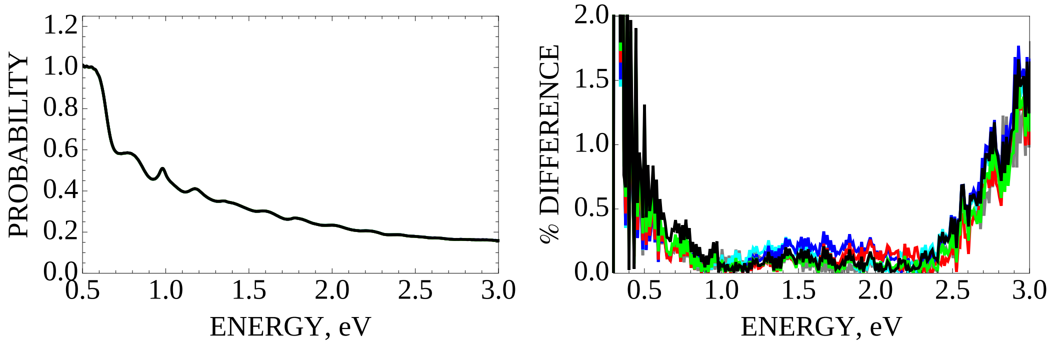

(a) *Non-Reactive Results* (b) *Non-Reactive % Difference*

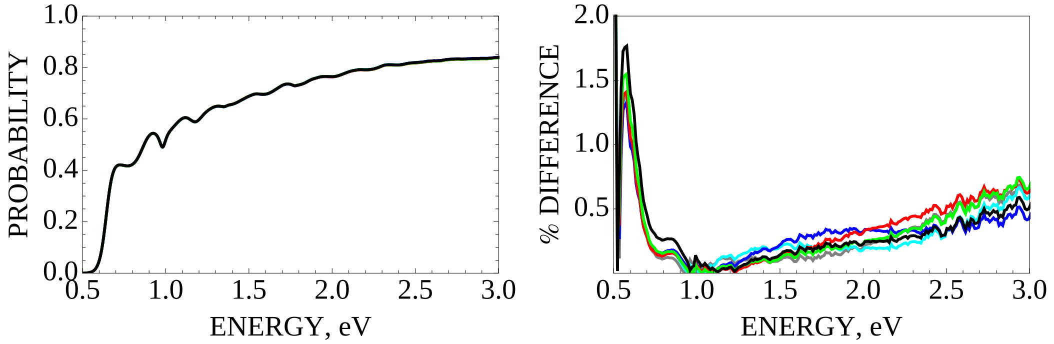

(c) *Reactive Results* (d) *Reactive % Difference*

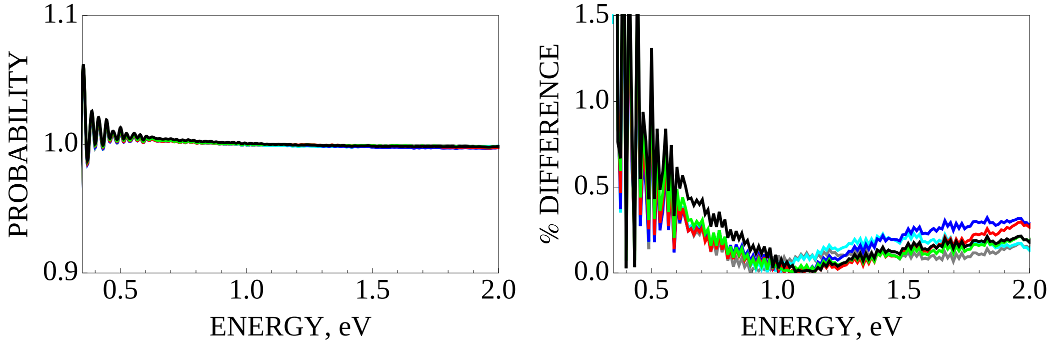

(e) *Normalization* (f) *Norm. % Difference*

Figure 4.27: Results for different values of N_t. The APH grid parameters are $N_\rho = 150$, $N_\theta = 55$, and $N_{\chi_i} = 481$. The Gaussian parameters are $\sigma = 0.3$, $k_0 = 8.5$ au, and $S^0_{\tau_i} = 9.5$ bohr, with $\rho_\infty = 10$ bohr. The time parameters are $t_{max} = 10010$ au, $t_{delay} = 500$ au,
LEGEND: (BLACK : $N_t = 2002$), (GREEN : $N_t = 1335$), (RED : $N_t = 1001$), (BLUE : $N_t = 667$), (CYAN : $N_t = 501$), (GRAY : $N_t = 401$)

time. The slow moving wave packet can be properly analyzed even for small values of N_t.

Plots of the percent difference for $\sigma = 0.3$, $k_0 = 8.5$ au, in Figs. 4.27b, 4.27d, and 4.27f, provide a more detailed picture of convergence. The non-reactive results show convergence for $N_t \geq 1335$ between 1.0 and 2.4 eV. This is to be expected since the largest grid density should extract the most information from the wave packet. However, outside this energy region, the $N_t = 2002$ data is the least accurate, with increased accuracy as N_t decreases. This behavior is not expected, but the difference in accuracy is very small and should not be considered to be significant behavior.

The reactive results in Fig. 4.27d show no convergence in the data. As before, at energies below 1.0 eV, the $N_t = 2002$ data has the lowest accuracy relative to the other data. The reactive results above 1.9 eV show equally odd behavior, where the $N_t = 501$ data is the most accurate between 1.9 and 2.5 eV. No value of N_t establishes itself as being optimal, so it is difficult to classify this behavior. Even though the $\sigma = 0.3$, $k_0 = 8.5$ au non-reactive and reactive results present odd behavior, the results for all values of N_t are very accurate, having an accuracy $\leq 0.5\%$ between 0.6 and 2.5 eV.

Fig. 4.28 presents the results for $\sigma = 0.2$, $k_0 = 12.5$ au. The non-reactive results in Fig. 4.28a show a minor lack of convergence for the $N_t = 401$ and 501 data below 0.9 eV. The reactive results in Fig. 4.28c also show a minor lack of convergence for the $N_t = 401$ and 501 data below 1.2 eV The normalization results in Fig. 4.28e provide a more detailed picture of the convergence, showing large oscillations in the $N_t = 401$ and 501 data across the entire range of energies. The $N_t = 401$ results deviate more than the $N_t = 501$ results, which is expected behavior.

Plots of the percent difference for $\sigma = 0.2$, $k_0 = 12.5$ au, in Figs. 4.28b, 4.28d, and 4.28f, provide a more detailed picture of convergence. The percent difference plots show large oscillations in the $N_t = 401$ and 501 data. This is expected behavior that is not present in the $\sigma = 0.3$, $k_0 = 8.5$ au results. The non-reactive results in Fig. 4.28b show convergence of the $N_t \geq 1335$ data between 1.0 and 2.2 eV, but there is only a small difference in accuracy for the $N_t \geq 667$ data above 1.0 eV.

The reactive results in Fig. 4.28d show convergence of the $N_t \geq 1335$ data between 1.2 and 2.2 eV. The $N_t = 401$ and 501 reactive results are very oscillatory, with the $N_t = 667$ data possessing similar oscillations below 1.5 eV. As in the $\sigma = 0.3$, $k_0 = 8.5$ au results, the $N_t = 2002$ data is less accurate than the $N_t = 1001$ and 1335 data below 1.2 eV and less accurate than the $N_t = 667$ data above 2.5 eV.

The non-reactive and reactive results are very accurate for $N_t \geq 1001$. For $N_t \geq 1001$, the non-reactive results have an accuracy $\leq 0.5\%$ between 0.8 and 2.4 eV, and the reactive results have an accuracy $\leq 0.5\%$ between 0.7 and 3.0 eV. The $\sigma = 0.2$, $k_0 = 12.5$ au results reinforce the observation of odd behavior of the $\sigma = 0.3$, $k_0 = 8.5$ au results. However, the $k_0 = 12.5$ au results do exhibit expected behavior with the low accuracy of the $N_t \leq 667$ data, due to the higher kinetic energies contained in the wave packet.

4.4.3 Convergence of t_{delay}

The t_{delay} parameter determines the time at which to begin analyzing the wave packet. Its primary purpose is to avoid analysis of the unreacted wave packet when the initial wave packet overlaps ρ_∞. t_{delay} is chosen to be large enough so that the its unreacted amplitude has vacated ρ_∞, but small enough so that the returning reacted packet has not yet reached ρ_∞. The non-reactive results are affected the most, since the reactive arrangement channels do not contain

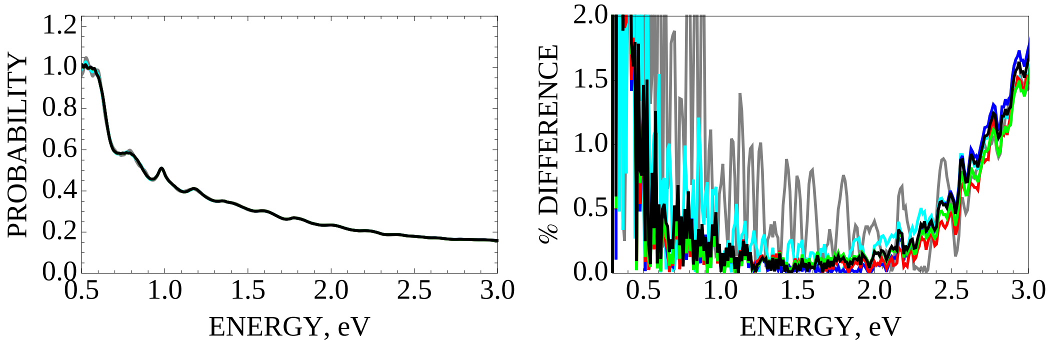

(a) *Non-Reactive Results* (b) *Non-Reactive % Difference*

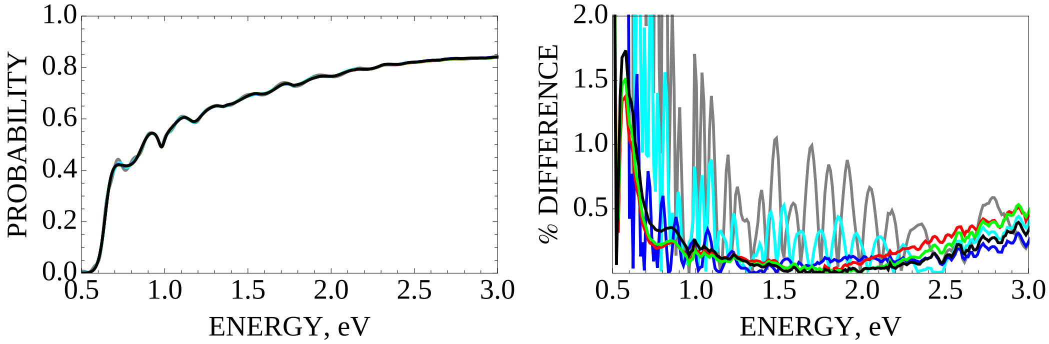

(c) *Reactive Results* (d) *Reactive % Difference*

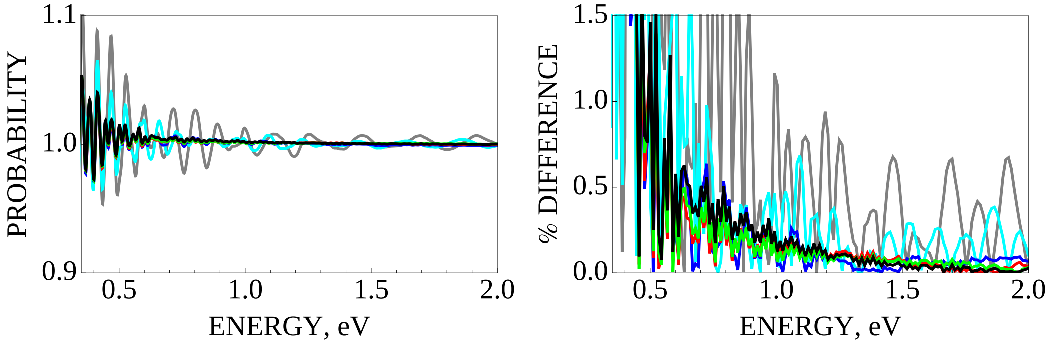

(e) *Normalization* (f) *Norm. % Difference*

Figure 4.28: Results for different values of N_t. The APH grid parameters are $N_\rho = 150$, $N_\theta = 55$, and $N_{\chi_i} = 481$. The Gaussian parameters are $\sigma = 0.2$, $k_0 = 12.5$ au, and $S^0_{\tau_i} = 9.5$ bohr, with $\rho_\infty = 10$ bohr. The time parameters are $t_{max} = 10010$ au, $t_{delay} = 500$ au,
LEGEND: (BLACK : $N_t = 2002$), (GREEN : $N_t = 1335$), (RED : $N_t = 1001$), (BLUE : $N_t = 667$), (CYAN : $N_t = 501$), (GRAY : $N_t = 401$)

any initial wave packet amplitude. However, if t_{delay} is too large, the reacted wave packet could cross ρ_∞ in the reactive channel without being analyzed.

The value of t_{delay} depends on the Gaussian wave packet parameters. As k_0 increases, t_{delay} will decrease due to the increase in the wave packet kinetic energy. The window of appropriate t_{delay} values, between where the wave packet has vacated ρ_∞ and before where the returning wave packet crosses ρ_∞, decreases as $S^0_{\tau_i}$ decreases. This is due to the shorter round-trip the wave packet has to travel. However, if ρ_∞ is held fixed while $S^0_{\tau_i}$ decreases, t_{delay} will decrease since the ρ_∞ overlap of initial wave packet will decrease. As σ increases, t_{delay} increases, since a broader wave packet will take longer to vacate ρ_∞.

The properties of the PES do affect t_{delay}, but since ρ_∞ is located in the asymptotic region of the PES, the wave packet will behave like a free wave packet. A zeroth-order estimation of t_{delay} can be found by analyzing the propagation of a free Gaussian wave packet in one-dimension. To determine the zeroth-order value of t_{step}, we find the propagation time required for the free wave packet to vacate $S_{\tau_i} = \rho_\infty$. This is accomplished by plotting the amplitude of the evolving wave packet in a narrow region around $S_{\tau_i} = \rho_\infty$ for various propagation times. The time it takes for the wave packet amplitude to drop below 1% of its initial maximum value at $S_{\tau_i} = -\rho_\infty$, provides a good estimate of t_{step}. However, this estimate doesn't take into account the approach of the returning reacted wave packet, so it is beneficial to choose the minimal value of t_{delay} that is appropriate. Making plots such as those in Fig. 4.24 provide a good estimate of when the reacted wave packet will return by looking at when it begins to overlap $S_{\tau_i} = -\rho_\infty$.

Fig. 4.29 shows “snapshots” of the envelope of a wave packet at different times. The solid curves represent a wave packet with $\sigma = 0.3$, $k_0 = 8.5$ au and the dashed line marks the line a $S_{\tau_i} = \rho_\infty = 10$ bohr. The wave packet starts

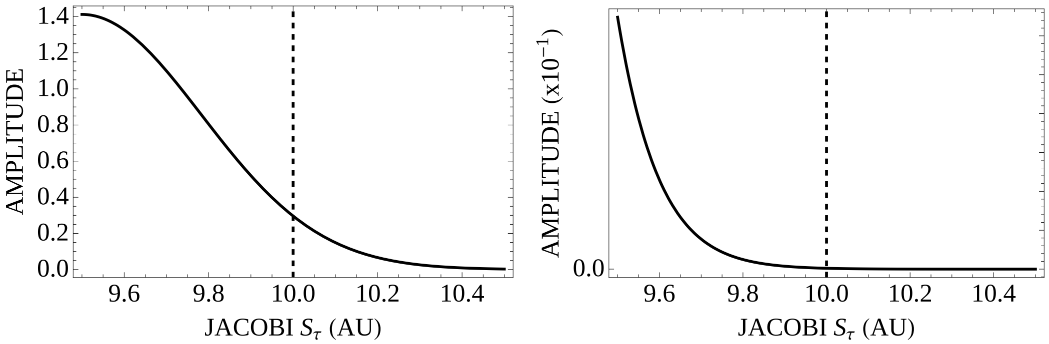

(a) $t = 0$ au (b) $t = 100$ au

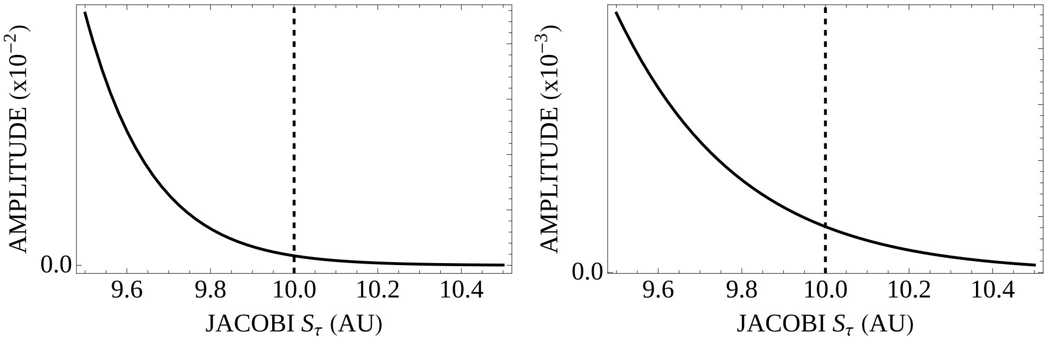

(c) $t = 250$ au (d) $t = 500$ au

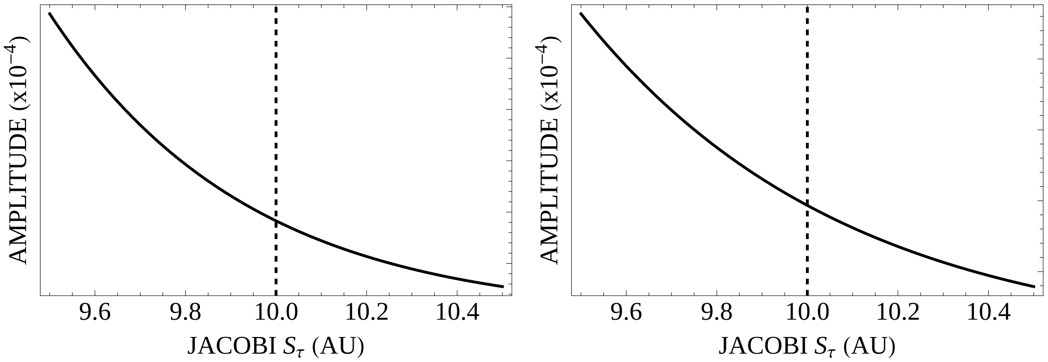

(e) $t = 750$ au (f) $t = 1000$ au

Figure 4.29: Envelope of the Gaussian wave packet around $S_{\tau_i} = 10$ bohr. The initial wave packet starts at $S^0_{\tau_i} = 9.5$ bohr. The solid line is a wave packet with $\sigma = 0.3$ and $k_0 = 8.5$ au. The dashed line locates the $S_{\tau_i} = 10$ bohr boundary.

at $S^0_{\tau_i} = 9.5$ bohr and propagates to the left, toward $S_{\tau_i} = 0$ bohr. Fig. 4.29a shows the wave packet at $t = 0$. The maximum amplitude of the wave packet is about 1.15 and its amplitude at 10 bohr is about 50% of its maximum. The time at which the wave packets' maximum amplitudes drop to below 0.0115 at $S_{\tau_i} = 10$ bohr is the zeroth order value of t_{delay}.

Fig. 4.29b shows the wave packet at $t = 100$ au. The packet amplitude at 10 bohr is about 2.17% of its initial maximum value, so $t_{delay} = 100$ au is too short. Fig. 4.29c shows the wave packet at $t = 250$ au. The packet amplitude at 10 bohr is about 0.13% of its initial maximum value, so $t_{delay} = 250$ au should be sufficient to obtain accurate results. Fig. 4.29d shows the wave packet at $t = 500$ au, and its amplitude at 10 bohr is 0.04% of the initial maximum. Setting $t_{delay} = 500$ au should be more than sufficient. This is probably a better choice for t_{delay} since the wave packet has significantly vacated 10 bohr. Furthermore, $t = 500$ au is short enough that the returning reacted wave packet hasn't returned to ρ_∞. Note that the $t = 750$ and $t = 1000$ au plots in Figs. 4.29e and 4.29f, respectively, both have about the same amplitude of around 4.3×10^{-5} at 10 bohr. This shows that the amplitude of the wave packet has most likely reached its minimum possible value at 10 bohr, since the returning reacted wave packet is close to returning. Results with initial state $\mathrm{H} + \mathrm{H}_2(\nu_i = j_i = 0)$, for various values of t_{delay}, are shown in Fig. 4.30, with $\sigma = 0.3$ and $k_0 = 8.5$ au. The Gaussian parameters of these results are the same as the wave packet discussed above, and the zeroth-order predictions can be tested.

Fig. 4.30 presents the results for $\sigma = 0.3$, $k_0 = 8.5$ au. The non-reactive and normalization results, in Figs. 4.30a and 4.30e, show a lack of convergence for the $t_{delay} = 0$ au data. These oscillations are caused by the overlap of the initial wave packet with ρ_∞. Note that the oscillations are not present in the reactive results, in Fig. 4.30c, since the initial wave packet has no amplitude in the reactive arrangement channels. All three plots show a lack of convergence

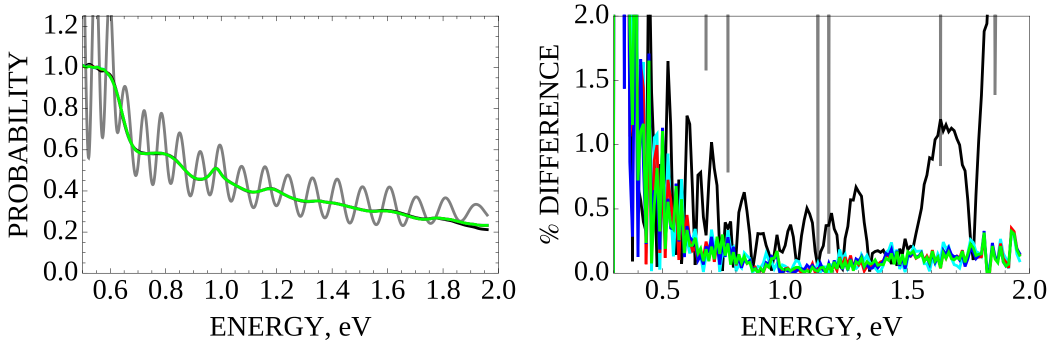

(a) *Non-Reactive Results* (b) *Non-Reactive % Difference*

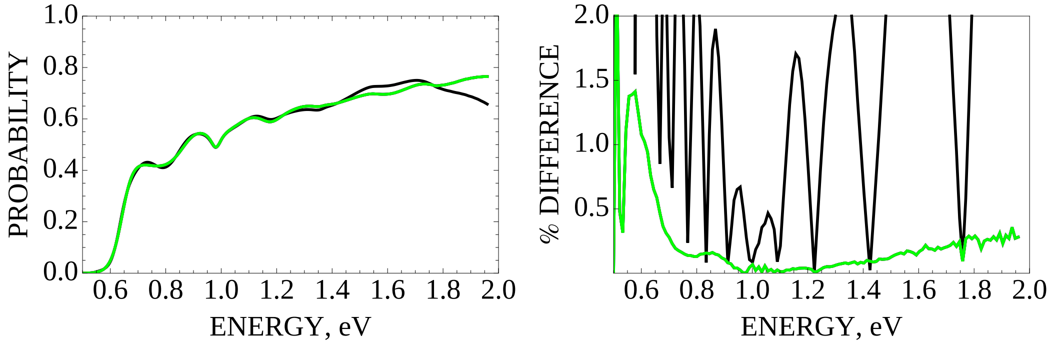

(c) *Reactive Results* (d) *Reactive % Difference*

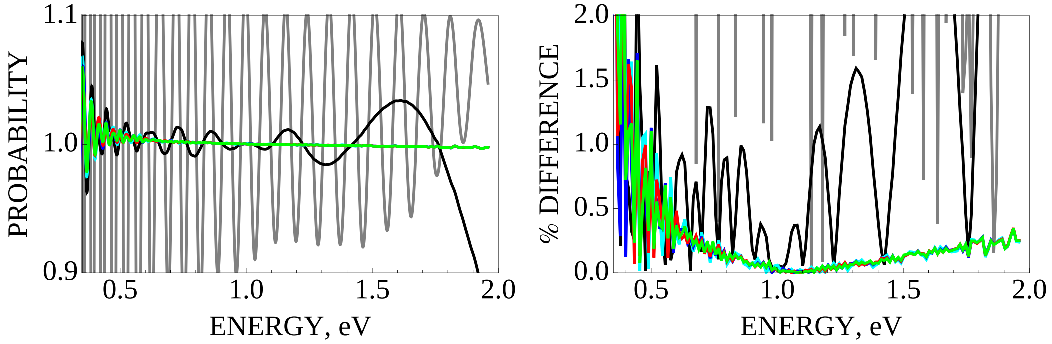

(e) *Normalization* (f) *Norm. % Difference*

Figure 4.30: Results for different values of t_{delay}. The APH grid parameters are $N_\rho = 150$, $N_\theta = 45$, and $N_{\chi_i} = 361$. The Gaussian parameters are $\sigma = 0.3$, $k_0 = 8.5$ au, and $S^0_{\tau_i} = 9.5$ bohr, with $\rho_\infty = 10$ bohr. The time parameters are $t_{max} = 10010$ au, $N_t = 1001$,
LEGEND: (BLACK : $t_{delay} = 1500$ au), (GREEN : $t_{delay} = 1000$ au), (RED : $t_{delay} = 750$ au), (BLUE : $t_{delay} = 500$ au), (CYAN : $t_{delay} = 250$ au), (GRAY : $t_{delay} = 0$ au).

for the $t_{delay} = 1500$ au data. This value of t_{delay} is too large, and the returning reacted wave packet has begun to cross ρ_∞ before analysis begins. The results for t_{delay} between 250 and 1000 au appear to be converged.

Plots of the percent difference for $\sigma = 0.3$, $k_0 = 8.5$ au, in Figs. 4.30b, 4.30d, and 4.30f, provide a more detailed picture of convergence. The most prominent features in these plots are the large oscillations in the $t_{delay} = 1500$ au data, showing what happens when t_{delay} is too large. The non-reactive and normalization results show that the $t_{delay} = 0$ au results are highly divergent, but are converged in the reactive plot. The non-reactive and normalization results also show that the most converged results are for $t_{delay} = 750$ and 1000 au, with the $t_{delay} = 250$ and 500 au data possessing small oscillations. This makes sense since the wave packet amplitude is negligible at $S_{\tau_i} = \rho_\infty = 10$ bohr for $t_{delay} = 750$ and 1000 au in Fig. 4.29. Even though the $t_{delay} = 250$ and 500 au data lack complete convergence, it has very accurate results $\leq 0.5\%$ above 0.6 eV. The reactive results are converged for $t_{delay} < 1500$.

The zeroth-order estimate predicted $t_{delay} = 250$ au should be sufficient to produce accurate results, but that $t_{delay} = 500$ would provide more converged results. The reactive results confirm these predictions, but the non-reactive results favor the larger values of t_{delay}.

CHAPTER 5

RESULTS

5.1 Introduction

In this chapter, we show results obtained by using the h-TDWP method to calculate state-to-state probabilities for the $H + H_2$ and $F + H_2$ systems for total angular momentum, $J = 0$. The results presented are the state-to-state non-reactive and reactive (rearrangement) probabilities, resolved for each ν_f and j_f final states. The total non-reactive and reactive probabilities were given in the convergence study in Chapter 4. Results are shown for two potential energy surfaces belonging to two different point groups. The $H + H_2$ surface possesses the maximum symmetry, belonging to C_{6v}, and the $F + H_2$ surface belongs to C_{2v}. The parameters chosen for the calculations are determined using the convergence study presented in Chapter 4 and are listed in Table 5.1.

To verify our results, we also performed time-independent calculations for these systems using the well-studied ABC reactive scattering program [15]. The state-to-state results show excellent agreement when compared to the time-independent results. The parameters used in the ABC calculations are listed in Table 5.2.

First, the $H + H_2$ state-to-state non-reactive and reactive probabilities are presented for initial states $\nu_i = 0,\ 1,\ 2$, all with $j_i = 0$, to the final states $\nu = 0,\ 1,\ 2$, for all j_f values with appreciable amplitude. Second, the $F + H_2$ state-to-state reactive probabilities are presented for initial state $\nu_i = j_i = 0$, to the final states $\nu = 0$ to 3, for $j_f = 0$ to 10.

Table 5.1: Parameters used in TD calculations. All values in atomic units unless otherwise specified.

Parameter	$H + H_2$	$F + H_2$
t_{max}	10010.0	20010.0
N_t	1001	2001
t_{delay}	500.0	400.0
N_ρ, N_θ, N_χ	150, 65, 481	200, 90, 601
ρ_{min}, ρ_{max}	0.64, 16.0	1.2, 16.0
ρ_∞	10.0	10.5
$S^0_{\tau_i}$	9.5	10.0
k_0	8.5	6.0
σ_0	0.3	0.3
j_{max}	22	29
V_{cut}	0.19	0.225
ρ_{NIP}	10.75	10.75
U_{NIP} (eV)	0.75	0.75

Table 5.2: Parameters used in ABC calculations.

Parameter	$H + H_2$	$F + H_2$
Maximum internal energy (eV)	3.0	4.0
Maximum rotational quantum number	25	40
Maximum hyperradius (a_0)	12.0	14.0
Number of propagation sectors	250	350
Initial scattering energy (eV)	0.3	0.233
Scattering energy increment (eV)	0.015	0.01
Number of scattering energies	114	80

5.2 $\mathrm{H} + \mathrm{H}_2$

The $\mathrm{H}+\mathrm{H}_2$ system is well-studied [59], providing a benchmark platform to test the h-TDWP method. We employ the double many-body expansion (DMBE) potential energy surface for this system [60]. As stated previously, the $\mathrm{H} + \mathrm{H}_2$ PES belongs to the C_{6v} point group. As a result, depending on whether j_i is even or odd, only certain irreducible representation projections of the initial wave packet must be propagated. Here, we deal with $J = j_i = 0$ initial states, which only contain A_1 and E_{2A} components. The A_1 component only requires 41 of the total 481 χ_i points and the E_{2A} only requires 80 χ_i points.

Figs. 5.1 to 5.27 show the state-to-state reactive and non-reactive probabilities for the $\mathrm{H} + \mathrm{H}_2(\nu_i = j_i = 0) \to \mathrm{H}_2(\nu_f, j_f) + \mathrm{H}$ reactions, with $\nu_f = 0$, 1, 2 for appropriate values of j_f. The figures show excellent agreement between the current results and the ABC method. Note that the accuracy of the results is consistent across the full range of energies, which sets our method apart from other hyperspherical TDWP methods [25]. The energy dependence of the accuracy of the other methods is most like due to their asymptotic matching scheme, which analyzes the wave packet at a constant Jacobi coordinate.

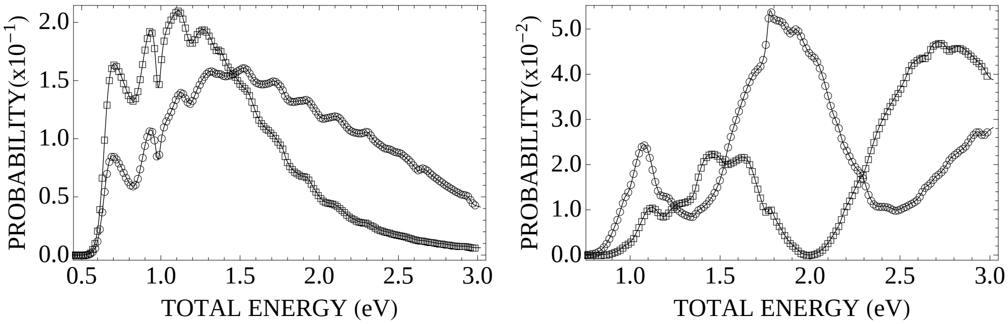

(a) $j_f = 0, 1$ (b) $j_f = 6, 7$

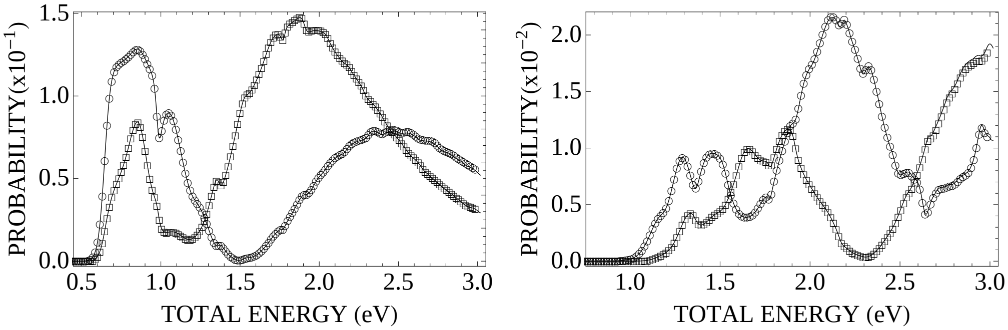

(c) $j_f = 2, 3$ (d) $j_f = 8, 9$

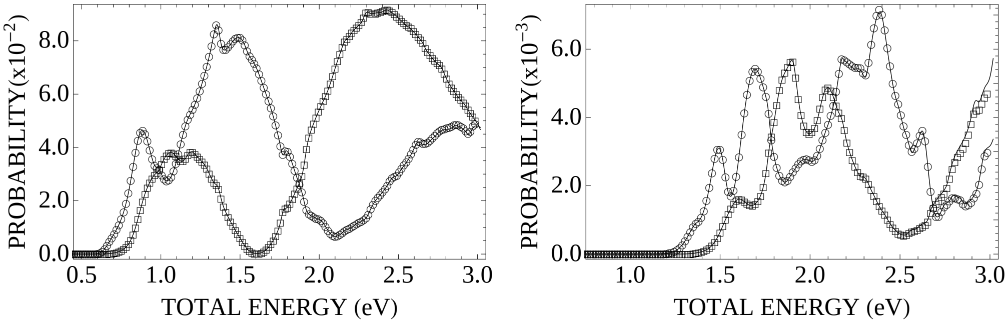

(e) $j_f = 4, 5$ (f) $j_f = 10, 11$

Figure 5.1: State-to-state reaction probabilities for $H + H_2(\nu_i = j_i = 0) \rightarrow H_2(\nu_f = 0, j_f) + H$ on the DMBE potential energy surface when $j_f = 0$ to 11. The solid lines represent our h-TDWP results and the symbols represent the ABC results. The ◯ symbol labels the smaller j_f, and the □ symbol labels the larger j_f in each plot.

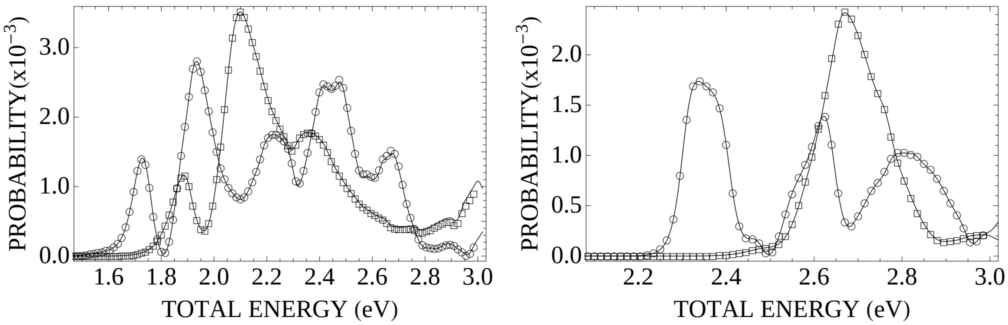

(a) $j_f = 12, 13$ (b) $j_f = 16, 17$

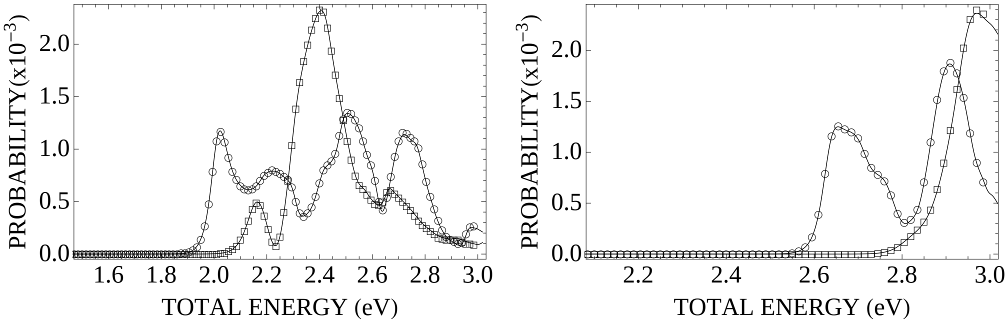

(c) $j_f = 14, 15$ (d) $j_f = 18, 19$

Figure 5.2: State-to-state reaction probabilities for $\mathrm{H} + \mathrm{H}_2(\nu_i = j_i = 0) \rightarrow \mathrm{H}_2(\nu_f = 0, j_f) + \mathrm{H}$ on the DMBE potential energy surface when $j_f = 12$ to 19. The solid lines represent our h-TDWP results and the symbols represent the ABC results. The ◯ symbol labels the smaller j_f, and the □ symbol labels the larger j_f in each plot.

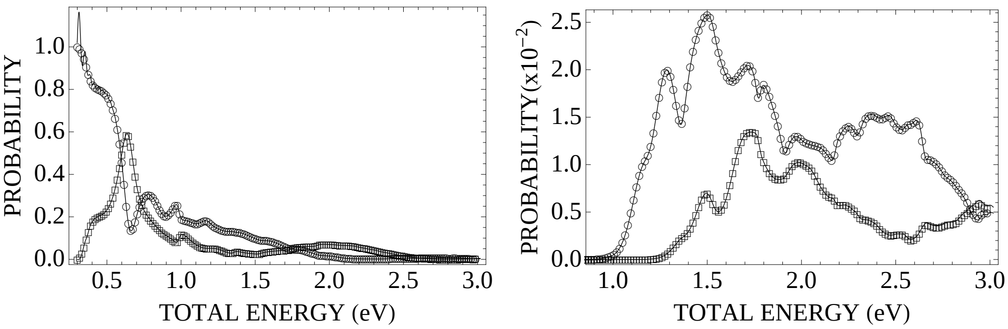

(a) $j_f = 0, 2$ (b) $j_f = 8, 10$

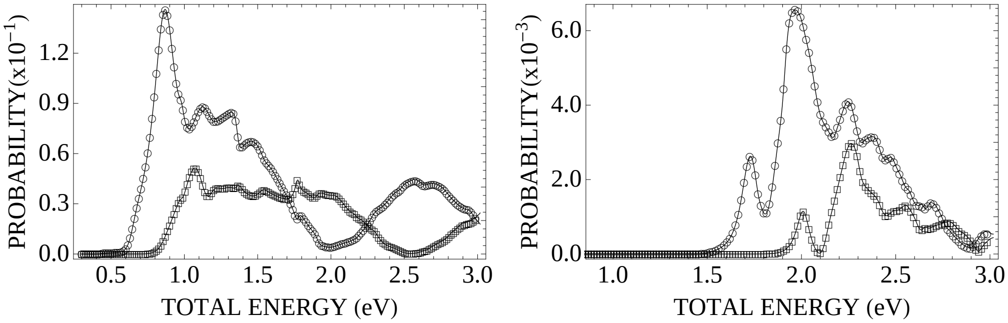

(c) $j_f = 4, 6$ (d) $j_f = 12, 14$

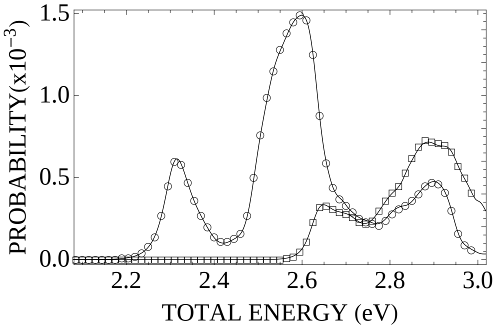

(e) $j_f = 16, 18$

Figure 5.3: State-to-state non-reactive probabilities for $\mathrm{H} + \mathrm{H}_2(\nu_i = j_i = 0) \rightarrow \mathrm{H} + \mathrm{H}_2(\nu_f = 0, j_f)$ on the DMBE potential energy surface when $j_f = 0$ to 18. The solid lines represent our h-TDWP results and the symbols represent the ABC results. The ◯ symbol labels the smaller j_f, and the □ symbol labels the larger j_f in each plot.

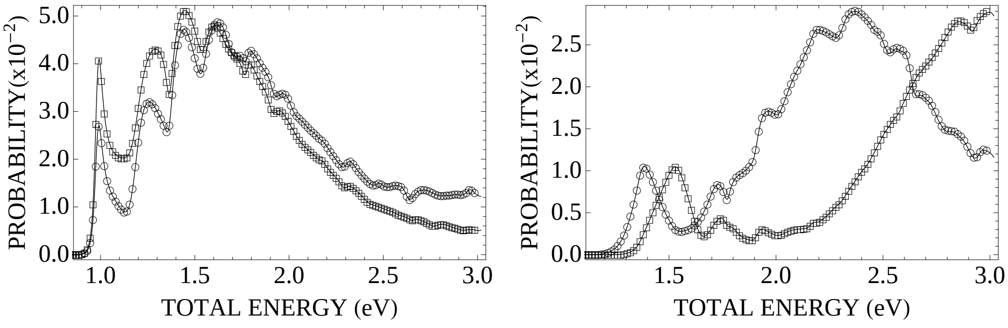

(a) $j_f = 0, 1$

(b) $j_f = 6, 7$

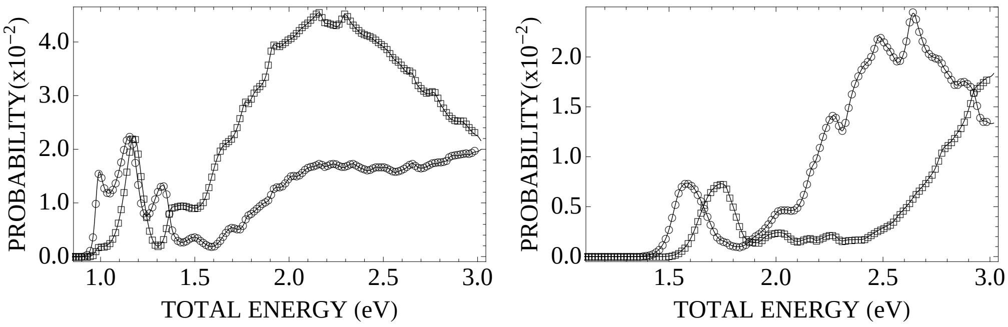

(c) $j_f = 2, 3$

(d) $j_f = 8, 9$

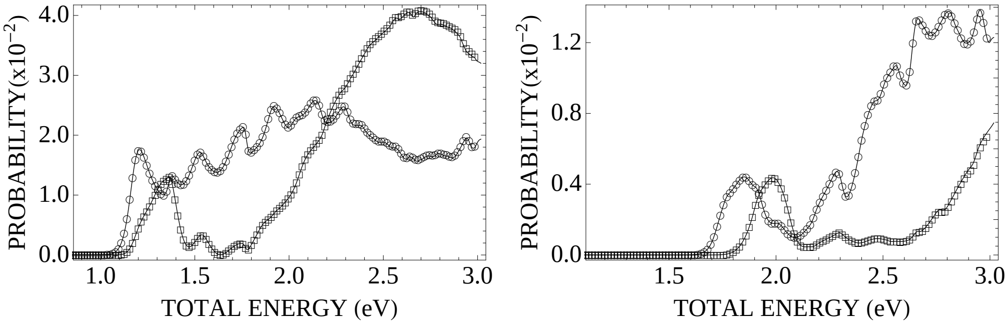

(e) $j_f = 4, 5$

(f) $j_f = 10, 11$

Figure 5.4: State-to-state reaction probabilities for $\mathrm{H} + \mathrm{H}_2(\nu_i = j_i = 0) \rightarrow \mathrm{H}_2(\nu_f = 1, j_f) + \mathrm{H}$ on the DMBE potential energy surface when $j_f = 0$ to 11. The solid lines represent our h-TDWP results and the symbols represent the ABC results. The ◯ symbol labels the smaller j_f, and the □ symbol labels the larger j_f in each plot.

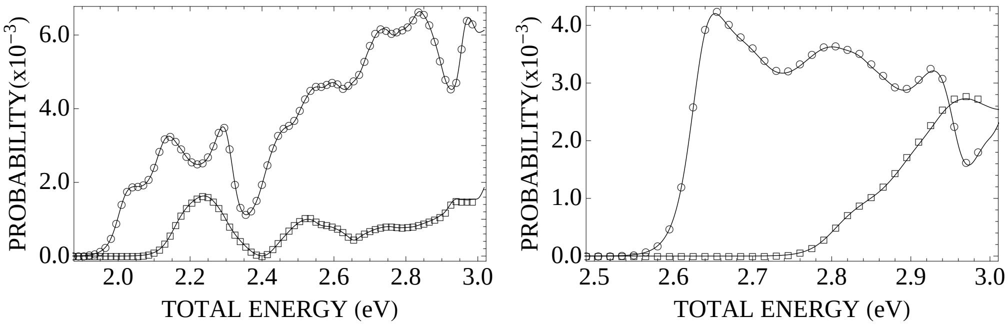

(a) $j_f = 12, 13$ (b) $j_f = 16, 17$

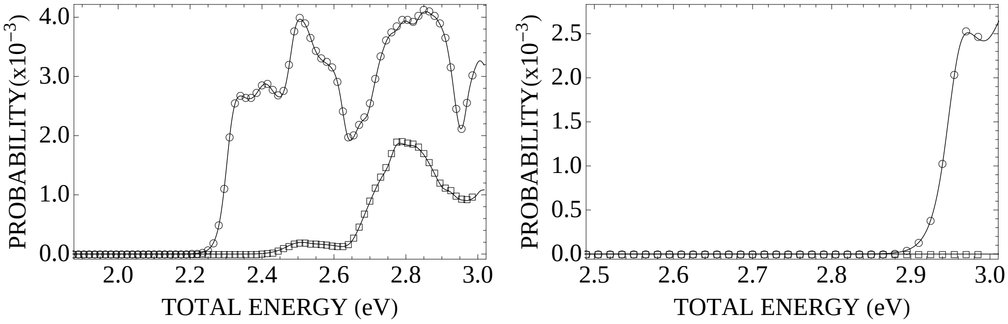

(c) $j_f = 14, 15$ (d) $j_f = 18, 19$

Figure 5.5: State-to-state reaction probabilities for $H + H_2(\nu_i = j_i = 0) \rightarrow H_2(\nu_f = 1, j_f) + H$ on the DMBE potential energy surface when $j_f = 12$ to 19. The solid lines represent our h-TDWP results and the symbols represent the ABC results. The ◯ symbol labels the smaller j_f, and the □ symbol labels the larger j_f in each plot.

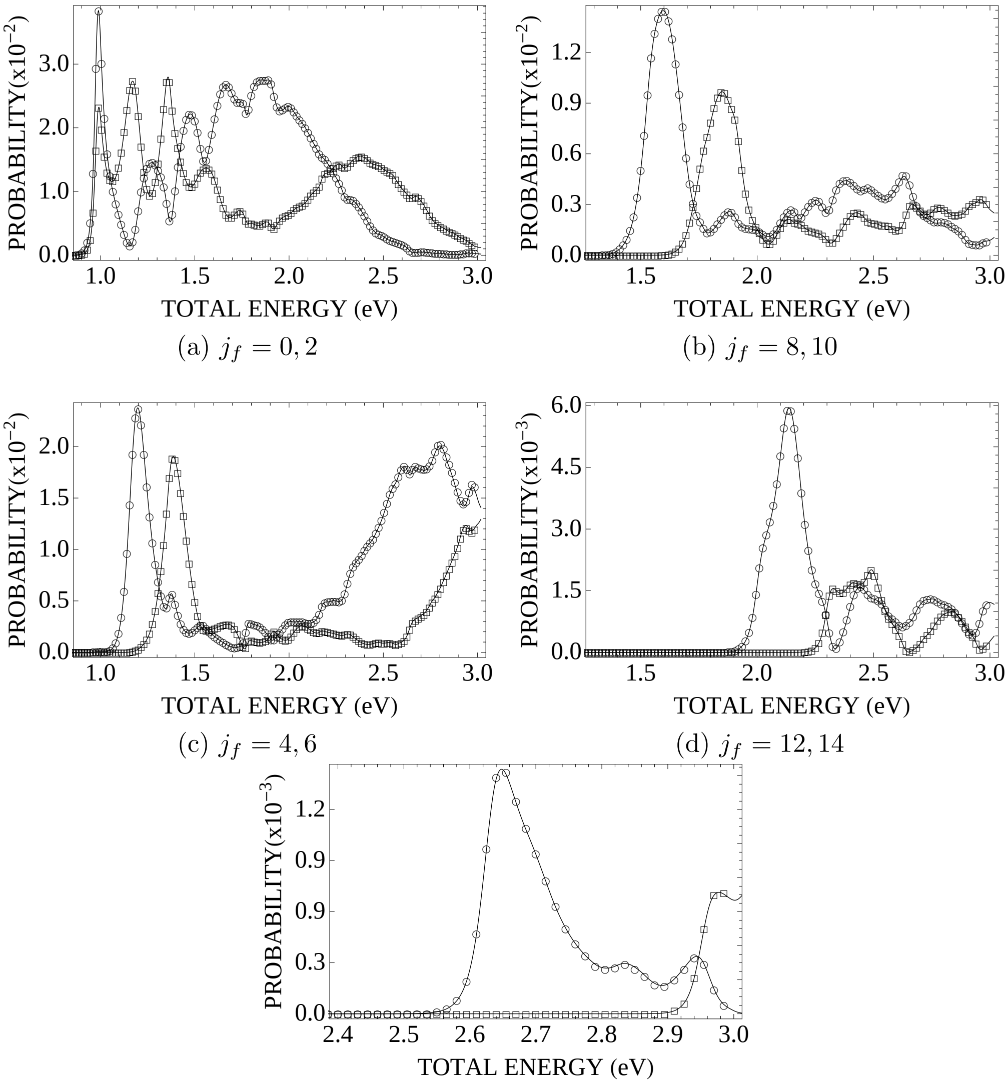

(a) $j_f = 0, 2$

(b) $j_f = 8, 10$

(c) $j_f = 4, 6$

(d) $j_f = 12, 14$

(e) $j_f = 16, 18$

Figure 5.6: State-to-state non-reactive probabilities for $\mathrm{H} + \mathrm{H}_2(\nu_i = j_i = 0) \rightarrow \mathrm{H} + \mathrm{H}_2(\nu_f = 1, j_f)$ on the DMBE potential energy surface when $j_f = 0$ to 18. The solid lines represent our h-TDWP results and the symbols represent the ABC results. The $\bigcirc$ symbol labels the smaller j_f, and the $\square$ symbol labels the larger j_f in each plot.

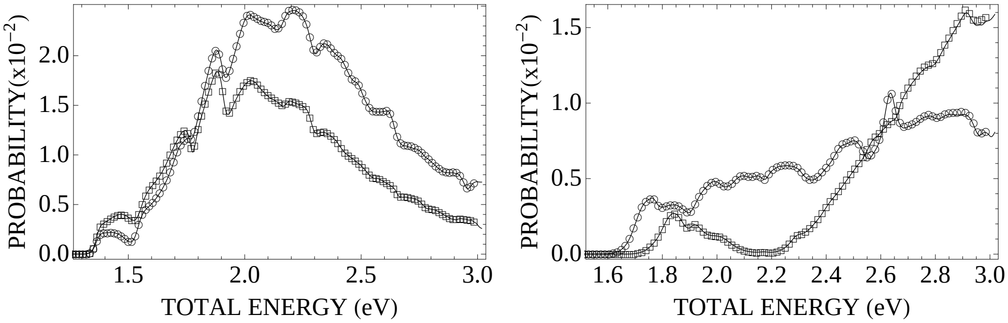

(a) $j_f = 0, 1$ (b) $j_f = 6, 7$

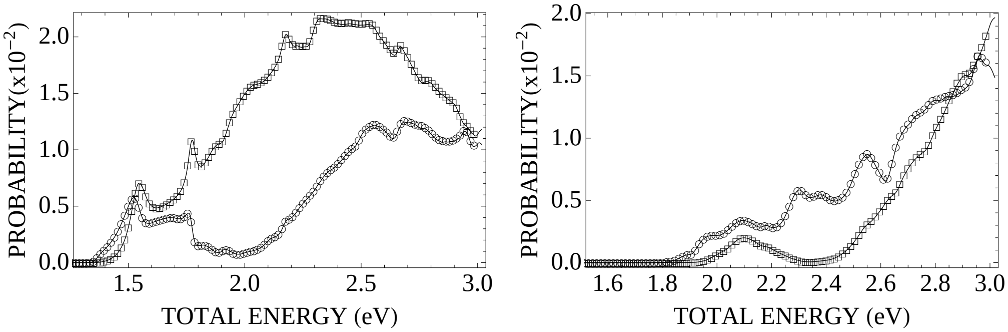

(c) $j_f = 2, 3$ (d) $j_f = 8, 9$

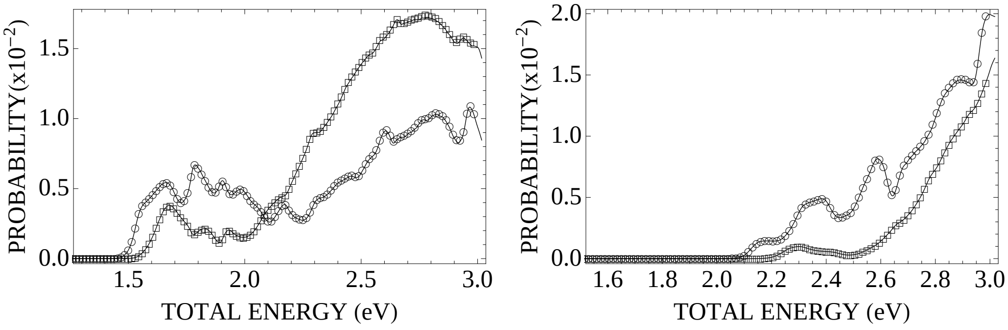

(e) $j_f = 4, 5$ (f) $j_f = 10, 11$

Figure 5.7: State-to-state reaction probabilities for $H + H_2(\nu_i = j_i = 0) \rightarrow H_2(\nu_f = 2, j_f) + H$ on the DMBE potential energy surface when $j_f = 0$ to 11. The solid lines represent our h-TDWP results and the symbols represent the ABC results. The $\bigcirc$ symbol labels the smaller j_f, and the $\square$ symbol labels the larger j_f in each plot.

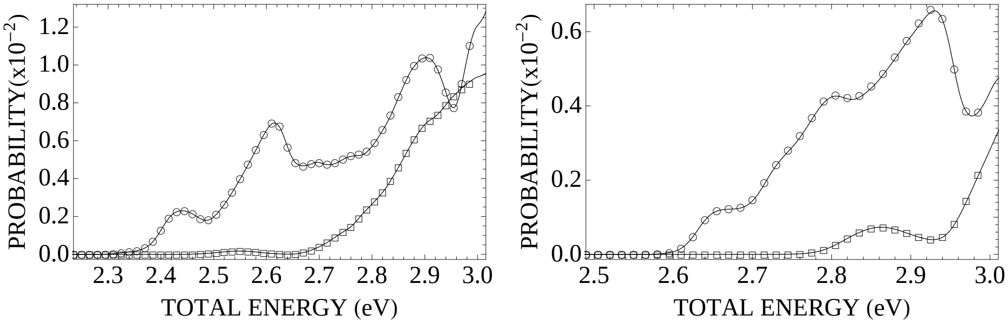

(a) $j_f = 12, 13$ (b) $j_f = 14, 15$

Figure 5.8: State-to-state reaction probabilities for $\mathrm{H} + \mathrm{H}_2(\nu_i = j_i = 0) \rightarrow \mathrm{H}_2(\nu_f = 2, j_f) + \mathrm{H}$ on the DMBE potential energy surface when $j_f = 12$ to 15. The solid lines represent our h-TDWP results and the symbols represent the ABC results. The ◯ symbol labels the smaller j_f, and the □ symbol labels the larger j_f in each plot.

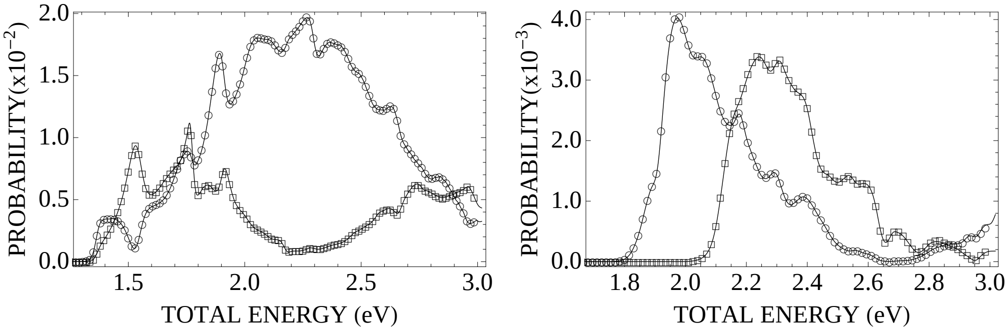

(a) $j_f = 0, 2$ (b) $j_f = 8, 10$

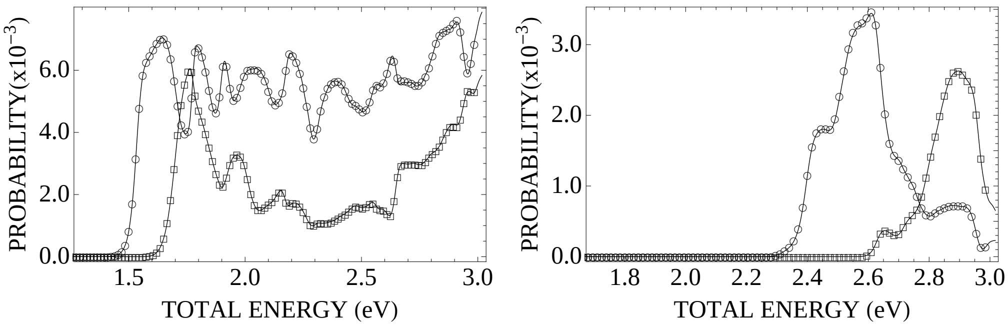

(c) $j_f = 4, 6$ (d) $j_f = 12, 14$

Figure 5.9: State-to-state non-reactive probabilities for $\mathrm{H} + \mathrm{H}_2(\nu_i = j_i = 0) \rightarrow \mathrm{H} + \mathrm{H}_2(\nu_f = 2, j_f)$ on the DMBE potential energy surface when $j_f = 0$ to 14. The solid lines represent our h-TDWP results and the symbols represent the ABC results. The ◯ symbol labels the smaller j_f, and the □ symbol labels the larger j_f in each plot.

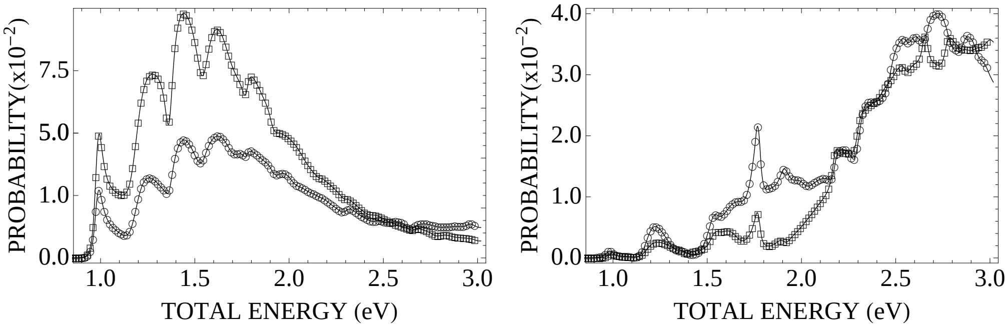

(a) $j_f = 0, 1$

(b) $j_f = 6, 7$

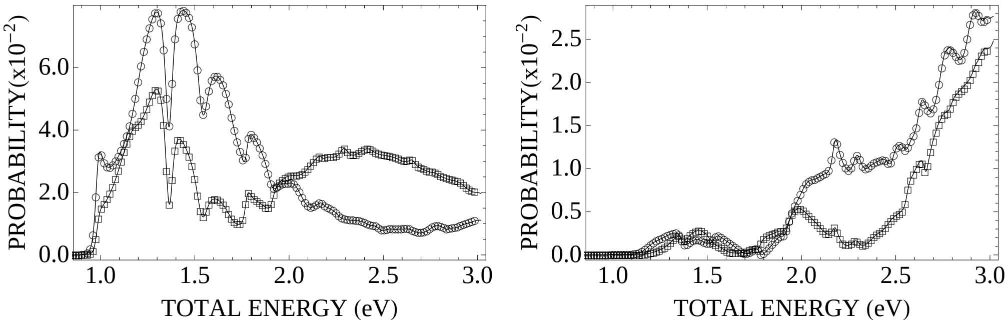

(c) $j_f = 2, 3$

(d) $j_f = 8, 9$

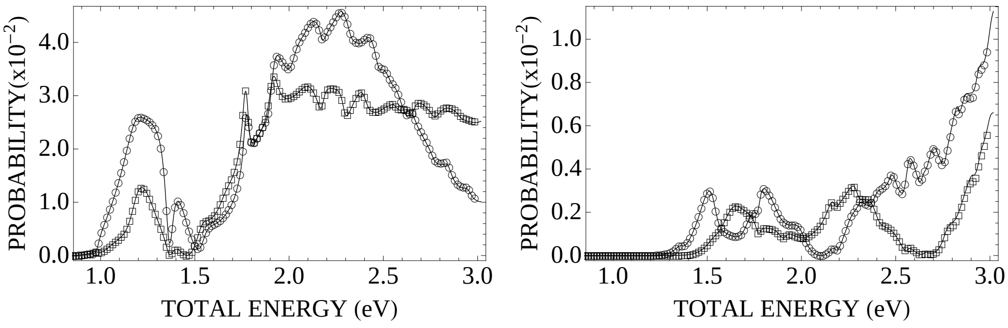

(e) $j_f = 4, 5$

(f) $j_f = 10, 11$

Figure 5.10: State-to-state reaction probabilities for $\mathrm{H} + \mathrm{H}_2(\nu_i = 1, j_i = 0) \rightarrow \mathrm{H}_2(\nu_f = 0, j_f) + \mathrm{H}$ on the DMBE potential energy surface when $j_f = 0$ to 11. The solid lines represent our h-TDWP results and the symbols represent the ABC results. The ◯ symbol labels the smaller j_f, and the □ symbol labels the larger j_f in each plot.

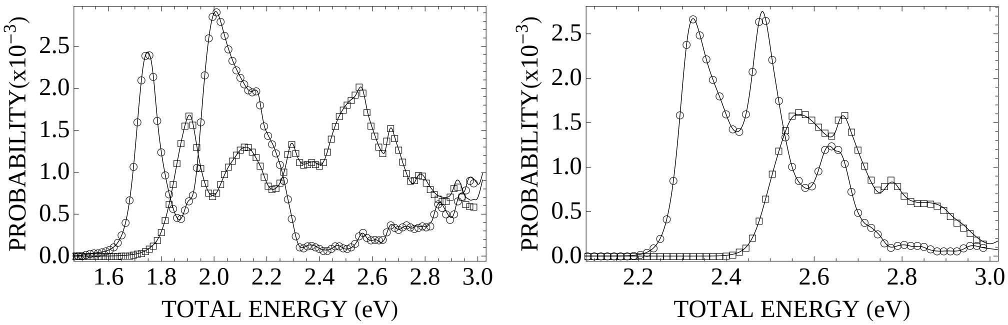

(a) $j_f = 12, 13$ (b) $j_f = 16, 17$

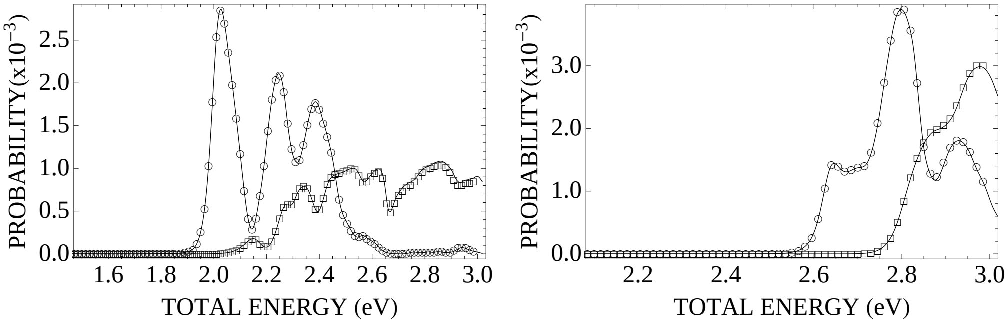

(c) $j_f = 14, 15$ (d) $j_f = 18, 19$

Figure 5.11: State-to-state reaction probabilities for $\mathrm{H} + \mathrm{H}_2(\nu_i = 1, j_i = 0) \rightarrow \mathrm{H}_2(\nu_f = 0, j_f) + \mathrm{H}$ on the DMBE potential energy surface when $j_f = 12$ to 19. The solid lines represent our h-TDWP results and the symbols represent the ABC results. The ◯ symbol labels the smaller j_f, and the ☐ symbol labels the larger j_f in each plot.

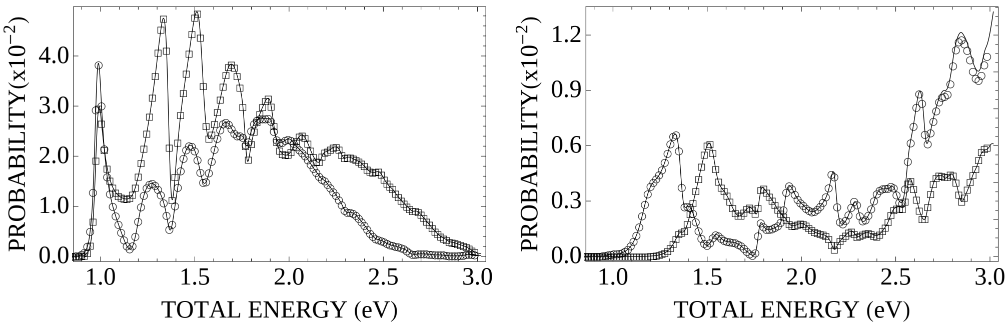

(a) $j_f = 0, 2$ (b) $j_f = 8, 10$

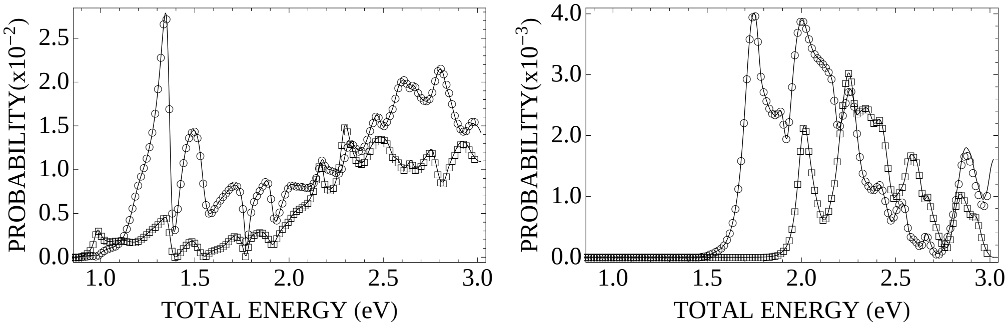

(c) $j_f = 4, 6$ (d) $j_f = 12, 14$

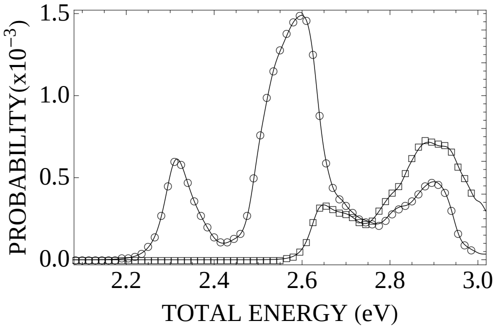

(e) $j_f = 16, 18$

Figure 5.12: State-to-state non-reactive probabilities for $H + H_2(\nu_i = 1, j_i = 0) \rightarrow H + H_2(\nu_f = 0, j_f)$ on the DMBE potential energy surface when $j_f = 0$ to 18. The solid lines represent our h-TDWP results and the symbols represent the ABC results. The ◯ symbol labels the smaller j_f, and the □ symbol labels the larger j_f in each plot.

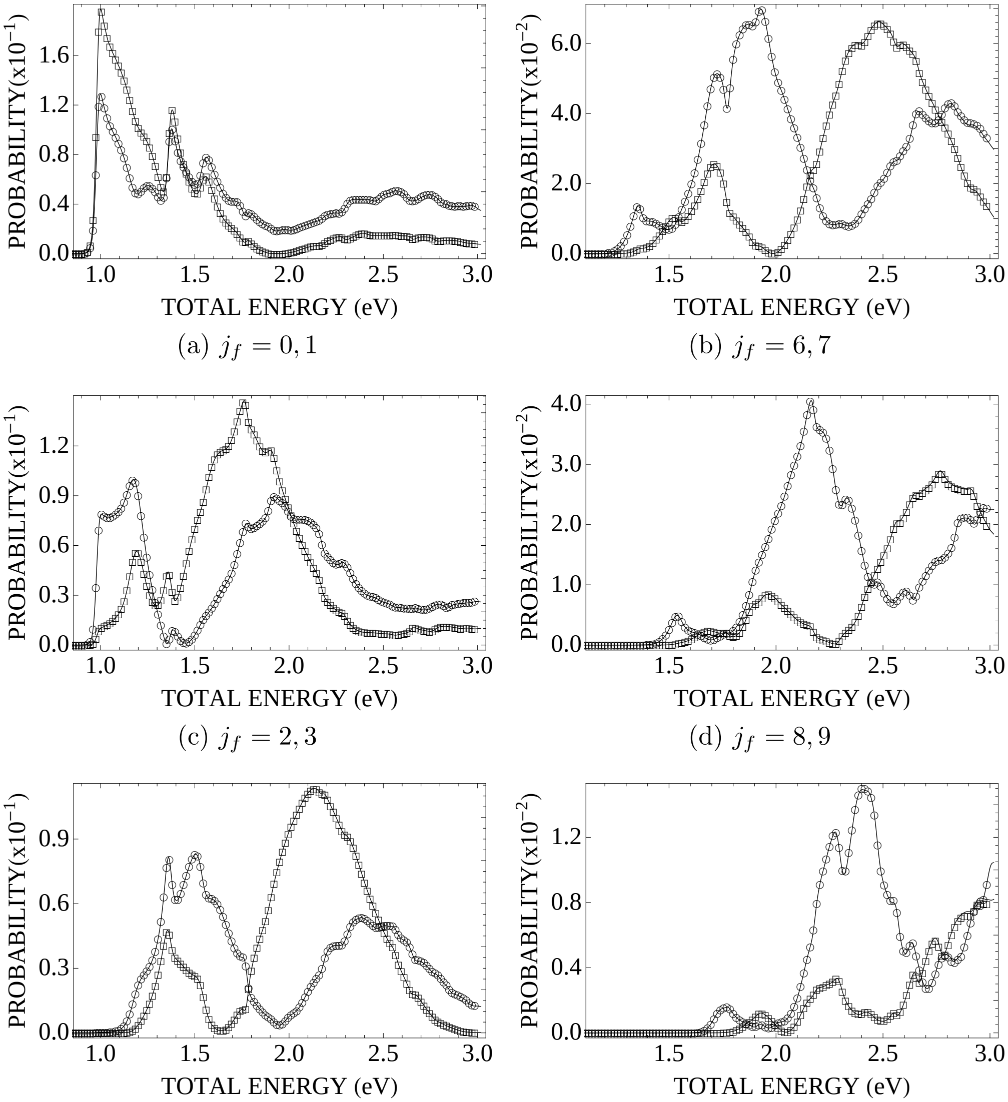

(a) $j_f = 0, 1$

(b) $j_f = 6, 7$

(c) $j_f = 2, 3$

(d) $j_f = 8, 9$

(e) $j_f = 4, 5$

(f) $j_f = 10, 11$

Figure 5.13: State-to-state reaction probabilities for $\mathrm{H} + \mathrm{H}_2(\nu_i = 1, j_i = 0) \rightarrow \mathrm{H}_2(\nu_f = 1, j_f) + \mathrm{H}$ on the DMBE potential energy surface when $j_f = 0$ to 11. The solid lines represent our h-TDWP results and the symbols represent the ABC results. The ◯ symbol labels the smaller j_f, and the □ symbol labels the larger j_f in each plot.

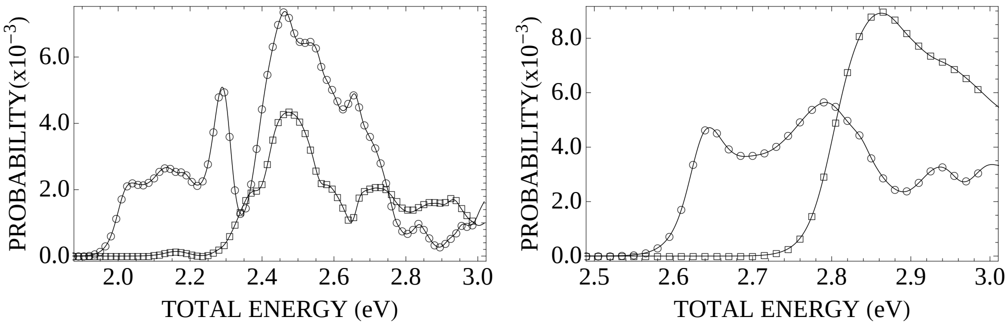

(a) $j_f = 12, 13$ (b) $j_f = 16, 17$

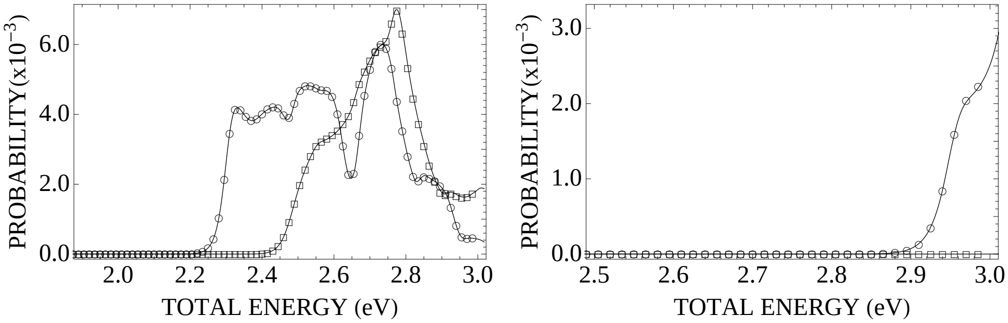

(c) $j_f = 14, 15$ (d) $j_f = 18, 19$

Figure 5.14: State-to-state reaction probabilities for $\mathrm{H} + \mathrm{H}_2(\nu_i = 1, j_i = 0) \rightarrow \mathrm{H}_2(\nu_f = 1, j_f) + \mathrm{H}$ on the DMBE potential energy surface when $j_f = 12$ to 19. The solid lines represent our h-TDWP results and the symbols represent the ABC results. The ◯ symbol labels the smaller j_f, and the □ symbol labels the larger j_f in each plot.

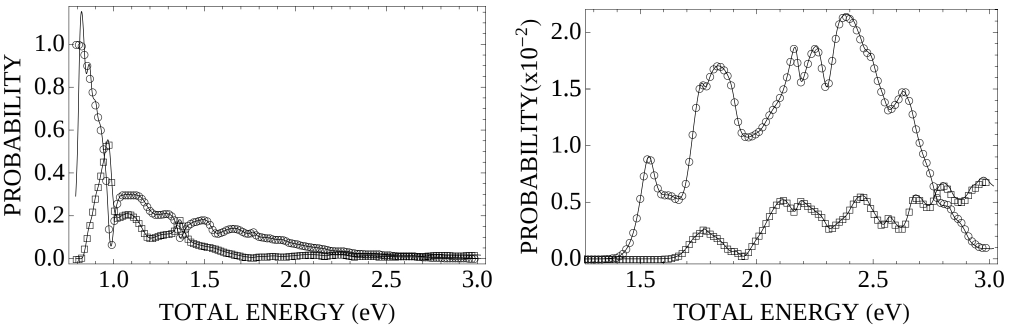

(a) $j_f = 0, 2$ (b) $j_f = 8, 10$

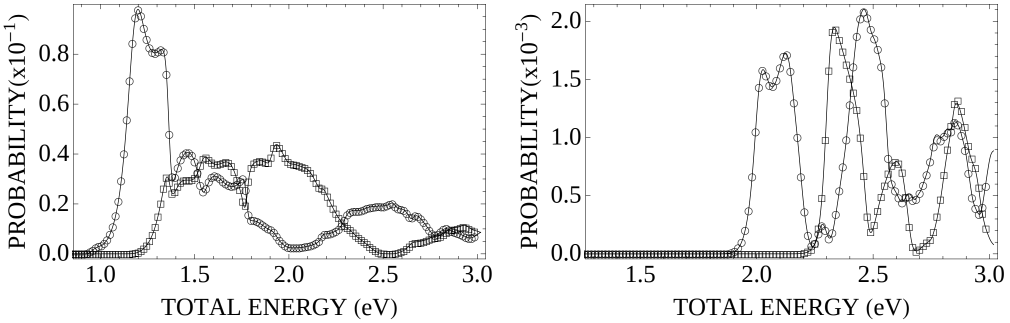

(c) $j_f = 4, 6$ (d) $j_f = 12, 14$

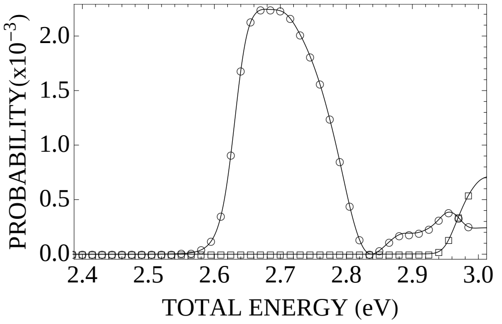

(e) $j_f = 16, 18$

Figure 5.15: State-to-state non-reactive probabilities for $\mathrm{H} + \mathrm{H}_2(\nu_i = 1, j_i = 0) \rightarrow \mathrm{H} + \mathrm{H}_2(\nu_f = 1, j_f)$ on the DMBE potential energy surface when $j_f = 0$ to 18. The solid lines represent our h-TDWP results and the symbols represent the ABC results. The ◯ symbol labels the smaller j_f, and the □ symbol labels the larger j_f in each plot.

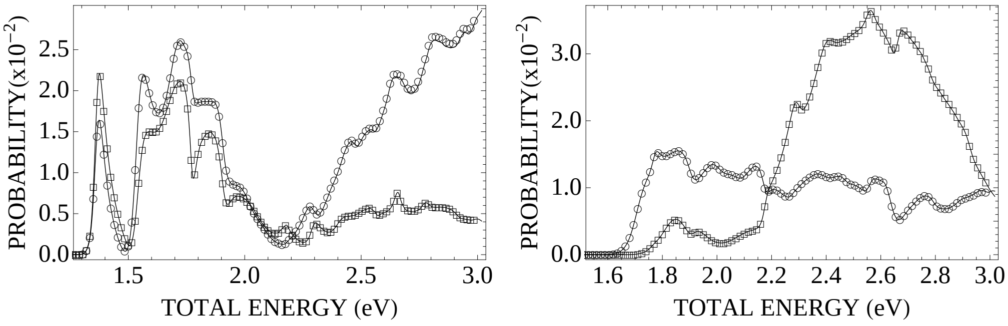

(a) $j_f = 0, 1$ (b) $j_f = 6, 7$

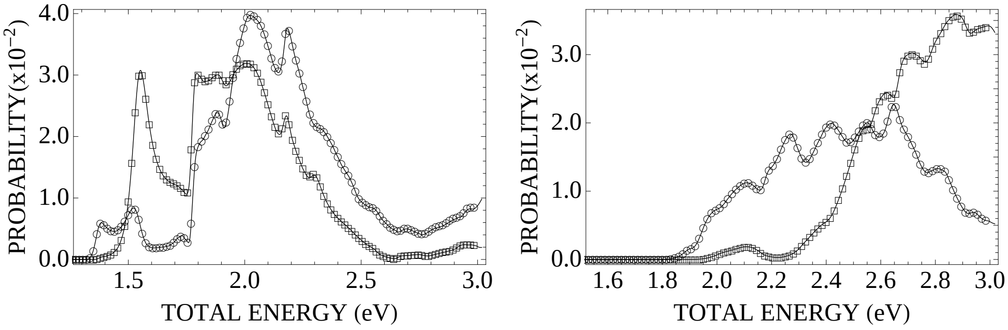

(c) $j_f = 2, 3$ (d) $j_f = 8, 9$

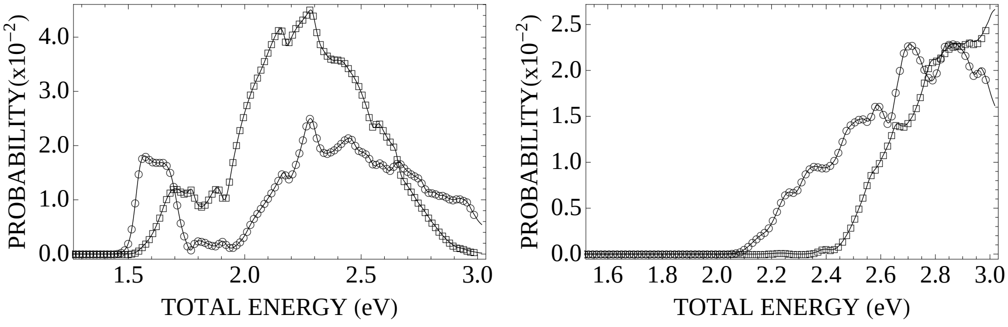

(e) $j_f = 4, 5$ (f) $j_f = 10, 11$

Figure 5.16: State-to-state reaction probabilities for $\mathrm{H} + \mathrm{H}_2(\nu_i = 1, j_i = 0) \rightarrow \mathrm{H}_2(\nu_f = 2, j_f) + \mathrm{H}$ on the DMBE potential energy surface when $j_f = 0$ to 11. The solid lines represent our h-TDWP results and the symbols represent the ABC results. The ◯ symbol labels the smaller j_f, and the □ symbol labels the larger j_f in each plot.

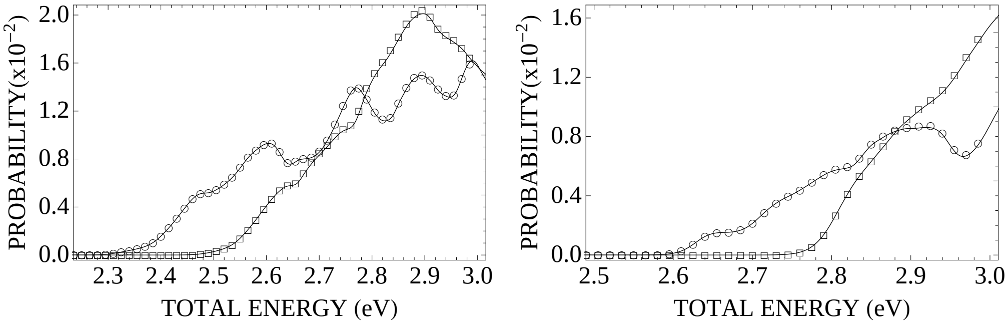

(a) $j_f = 12, 13$ (b) $j_f = 14, 15$

Figure 5.17: State-to-state reaction probabilities for $\mathrm{H} + \mathrm{H}_2(\nu_i = 1, j_i = 0) \rightarrow \mathrm{H}_2(\nu_f = 2, j_f) + \mathrm{H}$ on the DMBE potential energy surface when $j_f = 12$ to 15. The solid lines represent our h-TDWP results and the symbols represent the ABC results. The ◯ symbol labels the smaller j_f, and the □ symbol labels the larger j_f in each plot.

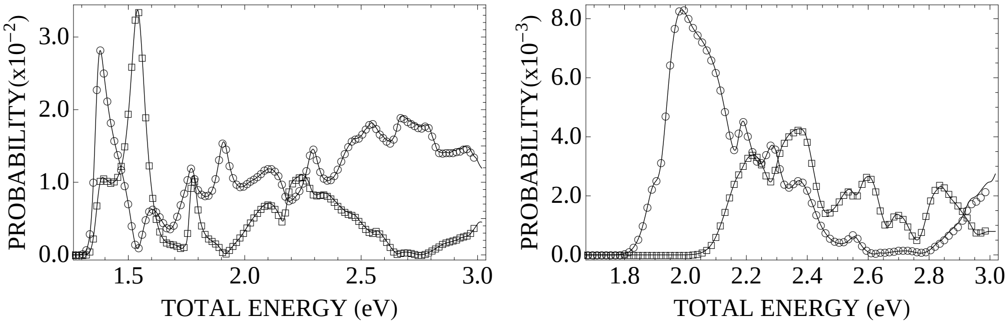

(a) $j_f = 0, 2$ (b) $j_f = 8, 10$

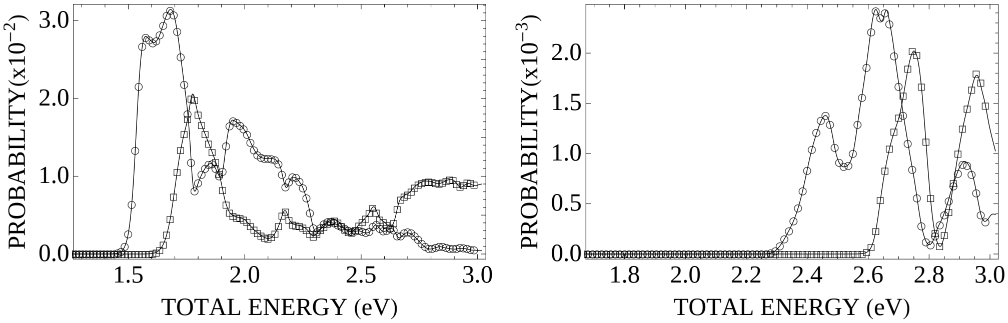

(c) $j_f = 4, 6$ (d) $j_f = 12, 14$

Figure 5.18: State-to-state non-reactive probabilities for $\mathrm{H} + \mathrm{H}_2(\nu_i = 1, j_i = 0) \rightarrow \mathrm{H} + \mathrm{H}_2(\nu_f = 2, j_f)$ on the DMBE potential energy surface when $j_f = 0$ to 14. The solid lines represent our h-TDWP results and the symbols represent the ABC results. The ◯ symbol labels the smaller j_f, and the □ symbol labels the larger j_f in each plot.

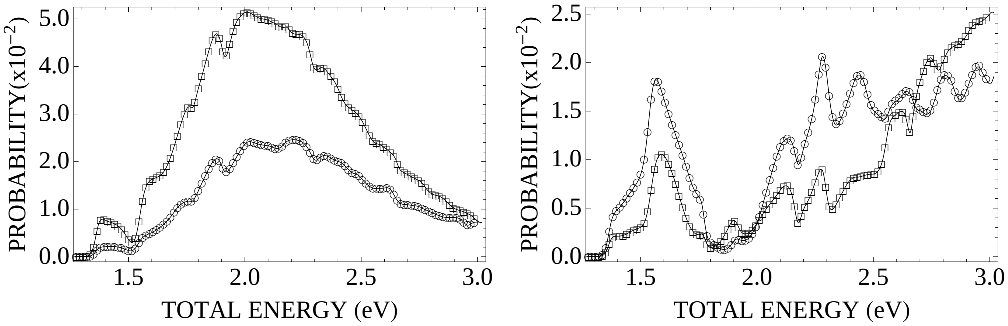

(a) $j_f = 0, 1$ (b) $j_f = 6, 7$

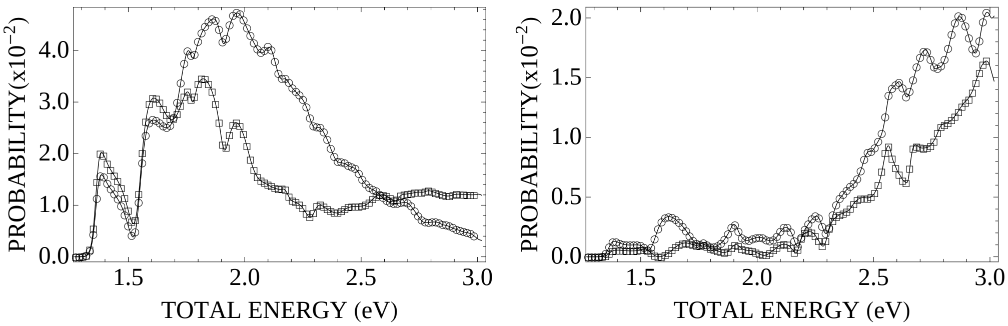

(c) $j_f = 2, 3$ (d) $j_f = 8, 9$

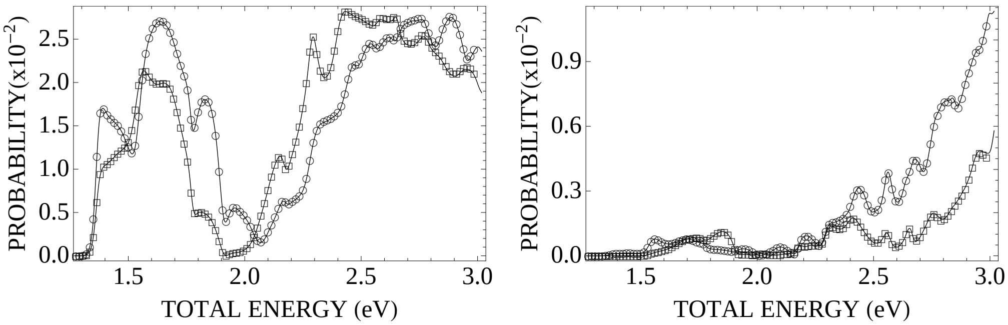

(e) $j_f = 4, 5$ (f) $j_f = 10, 11$

Figure 5.19: State-to-state reaction probabilities for $H + H_2(\nu_i = 2, j_i = 0) \rightarrow H_2(\nu_f = 0, j_f) + H$ on the DMBE potential energy surface when $j_f = 0$ to 11. The solid lines represent our h-TDWP results and the symbols represent the ABC results. The ◯ symbol labels the smaller j_f, and the □ symbol labels the larger j_f in each plot.

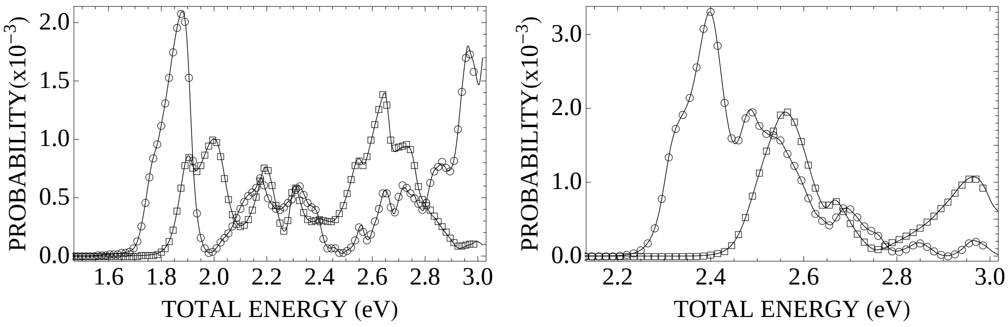

(a) $j_f = 12, 13$ (b) $j_f = 16, 17$

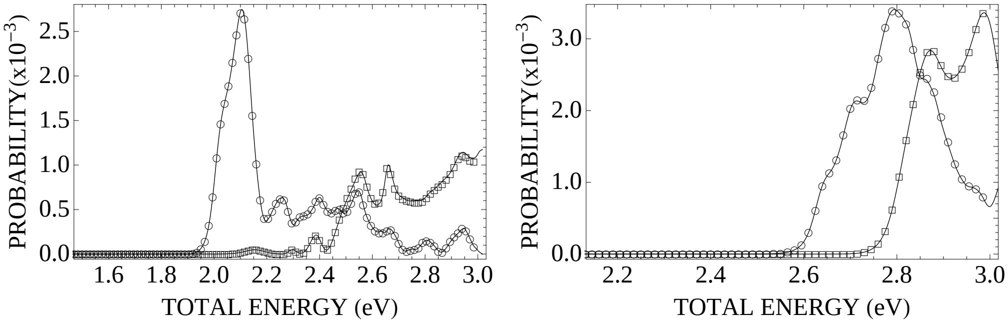

(c) $j_f = 14, 15$ (d) $j_f = 18, 19$

Figure 5.20: State-to-state reaction probabilities for $\mathrm{H} + \mathrm{H}_2(\nu_i = 2, j_i = 0) \rightarrow \mathrm{H}_2(\nu_f = 0, j_f) + \mathrm{H}$ on the DMBE potential energy surface when $j_f = 12$ to 19. The solid lines represent our h-TDWP results and the symbols represent the ABC results. The ◯ symbol labels the smaller j_f, and the □ symbol labels the larger j_f in each plot.

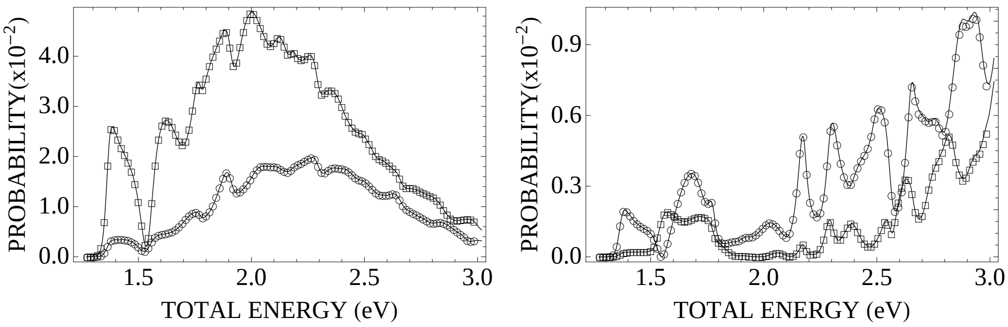

(a) $j_f = 0, 2$

(b) $j_f = 8, 10$

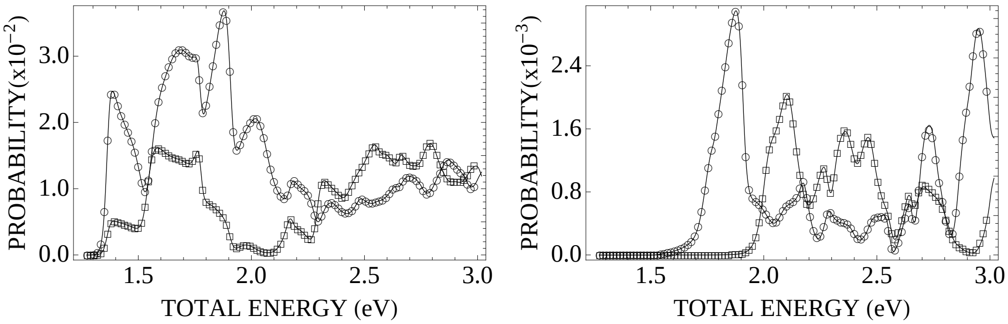

(c) $j_f = 4, 6$

(d) $j_f = 12, 14$

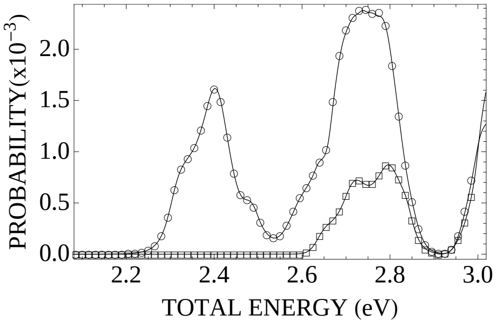

(e) $j_f = 16, 18$

Figure 5.21: State-to-state non-reactive probabilities for $\mathrm{H} + \mathrm{H}_2(\nu_i = 2, j_i = 0) \rightarrow \mathrm{H} + \mathrm{H}_2(\nu_f = 0, j_f)$ on the DMBE potential energy surface when $j_f = 0$ to 18. The solid lines represent our h-TDWP results and the symbols represent the ABC results. The ◯ symbol labels the smaller j_f, and the □ symbol labels the larger j_f in each plot.

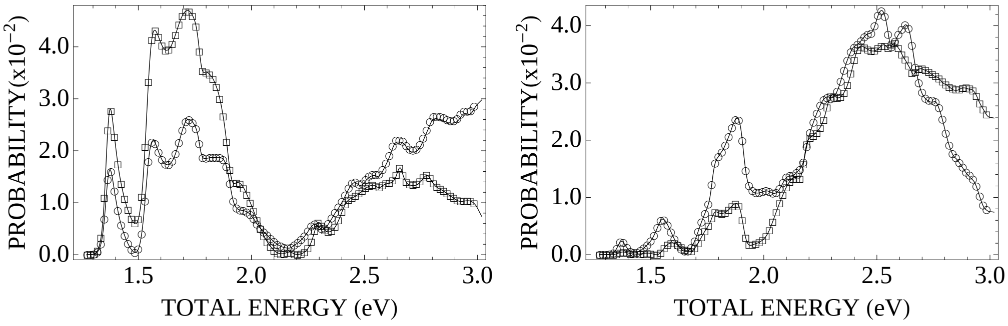

(a) $j_f = 0, 1$ (b) $j_f = 6, 7$

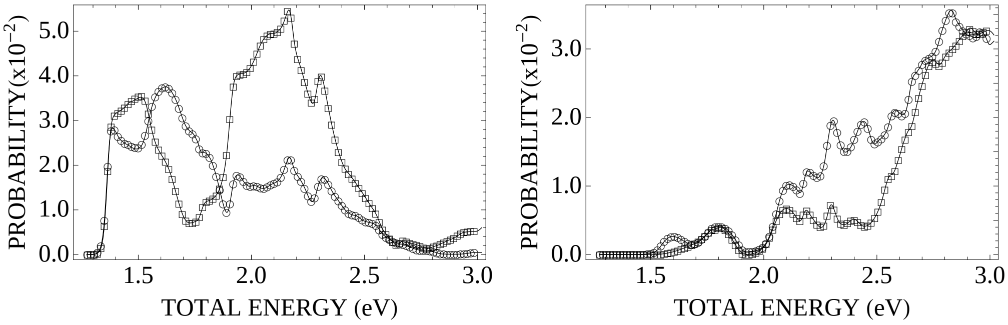

(c) $j_f = 2, 3$ (d) $j_f = 8, 9$

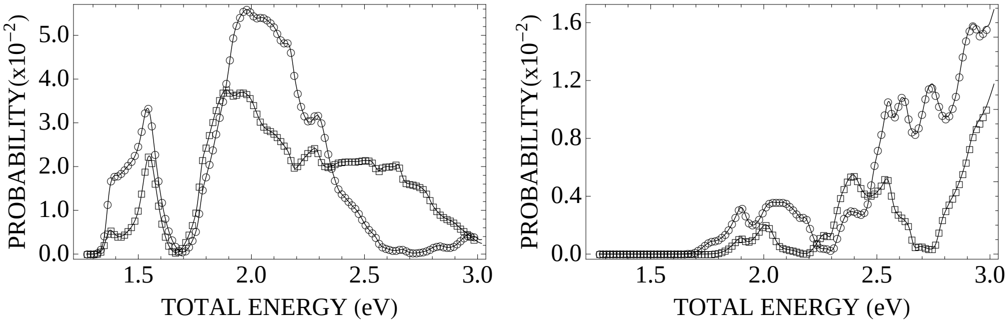

(e) $j_f = 4, 5$ (f) $j_f = 10, 11$

Figure 5.22: State-to-state reaction probabilities for $\mathrm{H} + \mathrm{H}_2(\nu_i = 2, j_i = 0) \rightarrow \mathrm{H}_2(\nu_f = 1, j_f) + \mathrm{H}$ on the DMBE potential energy surface when $j_f = 0$ to 11. The solid lines represent our h-TDWP results and the symbols represent the ABC results. The ◯ symbol labels the smaller j_f, and the □ symbol labels the larger j_f in each plot.

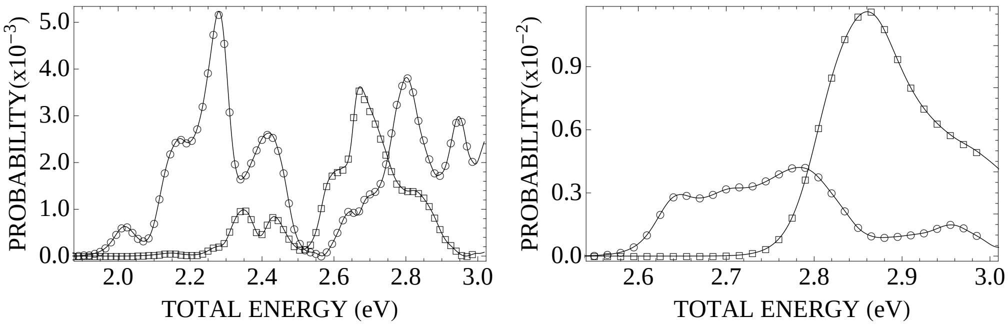

(a) $j_f = 12, 13$ (b) $j_f = 16, 17$

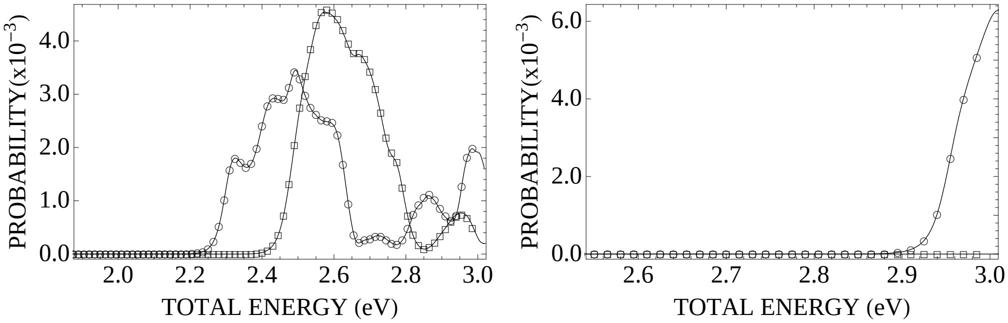

(c) $j_f = 14, 15$ (d) $j_f = 18, 19$

Figure 5.23: State-to-state reaction probabilities for $\mathrm{H} + \mathrm{H}_2(\nu_i = 2, j_i = 0) \rightarrow \mathrm{H}_2(\nu_f = 1, j_f) + \mathrm{H}$ on the DMBE potential energy surface when $j_f = 12$ to 19. The solid lines represent our h-TDWP results and the symbols represent the ABC results. The ○ symbol labels the smaller j_f, and the □ symbol labels the larger j_f in each plot.

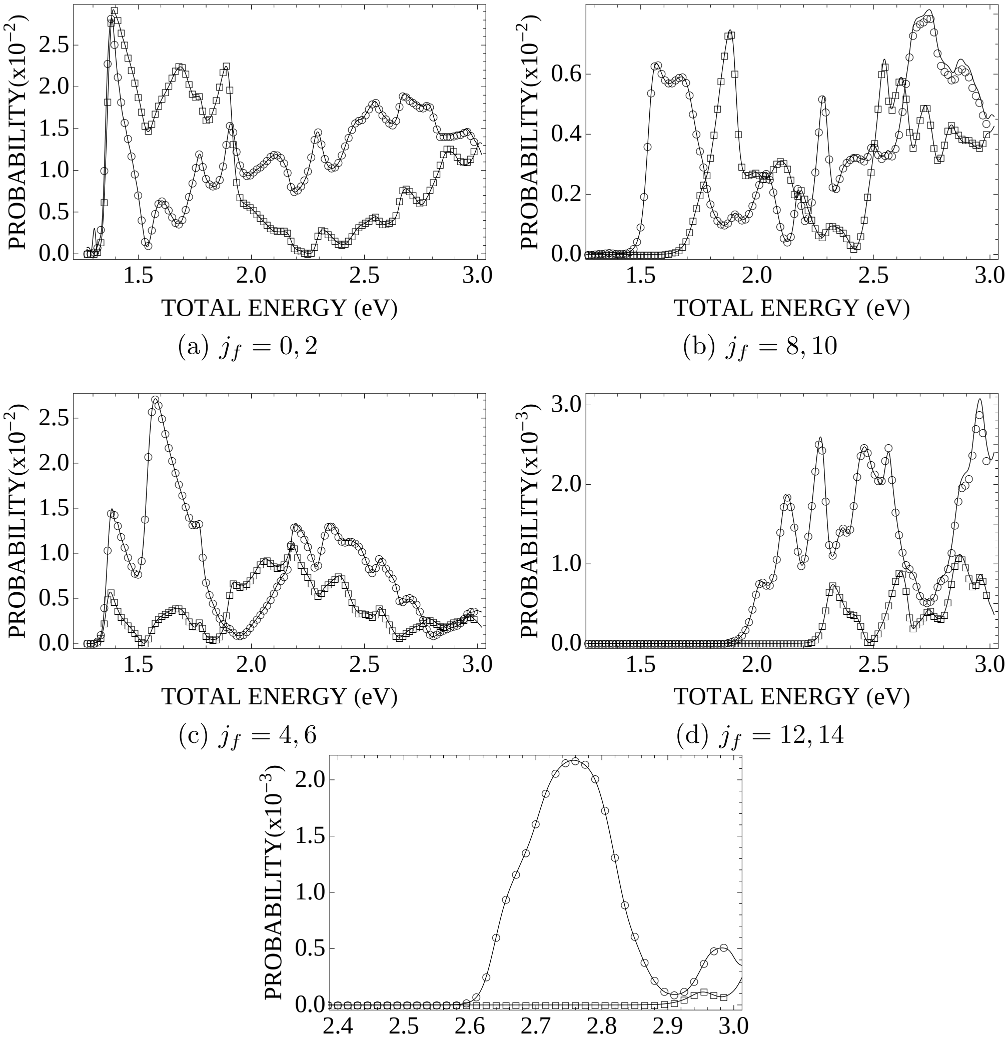

(a) $j_f = 0, 2$

(b) $j_f = 8, 10$

(c) $j_f = 4, 6$

(d) $j_f = 12, 14$

(e) $j_f = 16, 18$

Figure 5.24: State-to-state non-reactive probabilities for $\mathrm{H} + \mathrm{H}_2(\nu_i = 2, j_i = 0) \rightarrow \mathrm{H} + \mathrm{H}_2(\nu_f = 1, j_f)$ on the DMBE potential energy surface when $j_f = 0$ to 18. The solid lines represent our h-TDWP results and the symbols represent the ABC results. The ◯ symbol labels the smaller j_f, and the □ symbol labels the larger j_f in each plot.

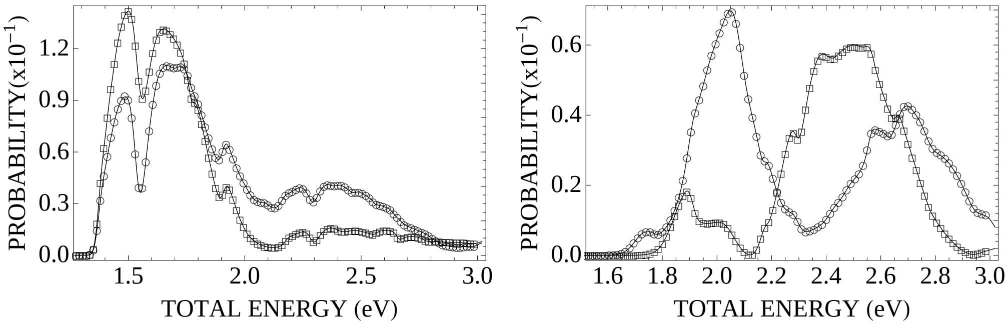

(a) $j_f = 0, 1$ (b) $j_f = 6, 7$

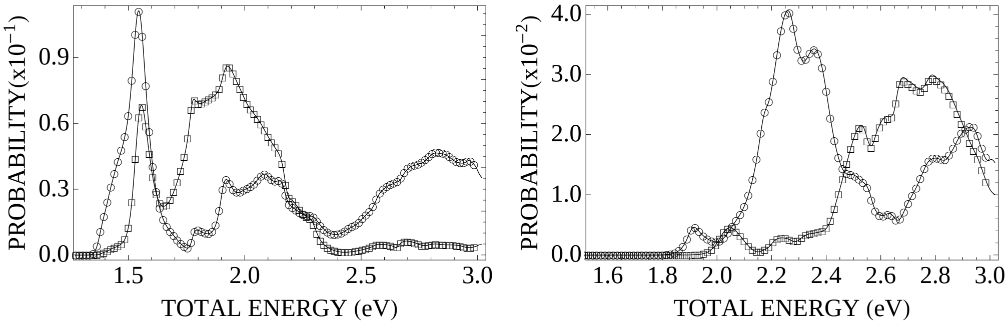

(c) $j_f = 2, 3$ (d) $j_f = 8, 9$

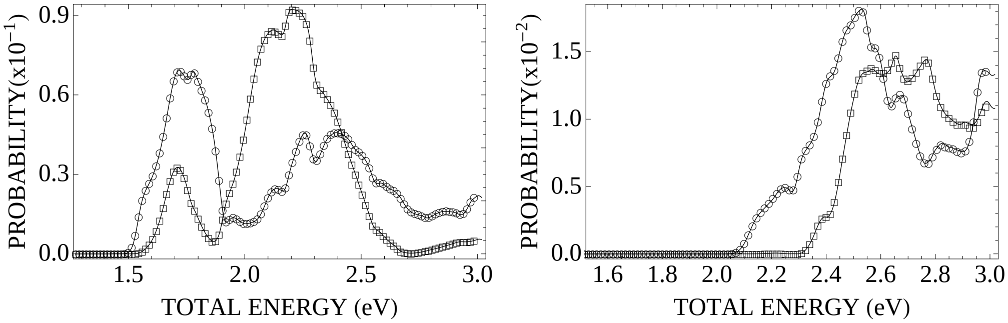

(e) $j_f = 4, 5$ (f) $j_f = 10, 11$

Figure 5.25: State-to-state reaction probabilities for $\mathrm{H} + \mathrm{H}_2(\nu_i = 2, j_i = 0) \rightarrow \mathrm{H}_2(\nu_f = 2, j_f) + \mathrm{H}$ on the DMBE potential energy surface when $j_f = 0$ to 11. The solid lines represent our h-TDWP results and the symbols represent the ABC results. The $\bigcirc$ symbol labels the smaller j_f, and the $\square$ symbol labels the larger j_f in each plot.

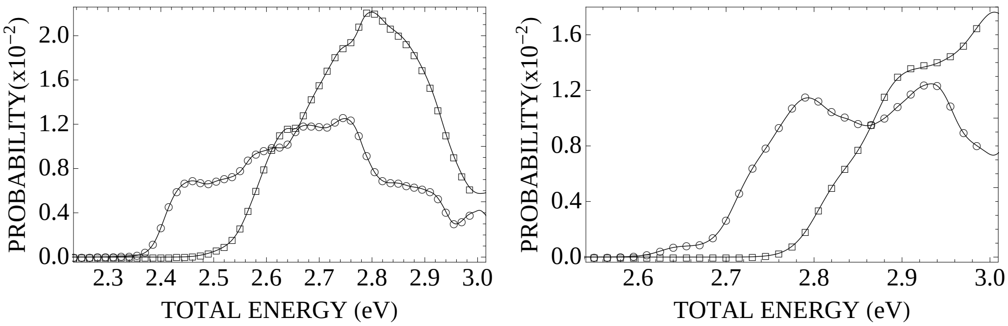

(a) $j_f = 12, 13$ (b) $j_f = 14, 15$

Figure 5.26: State-to-state reaction probabilities for $\mathrm{H} + \mathrm{H}_2(\nu_i = 2, j_i = 0) \rightarrow \mathrm{H}_2(\nu_f = 2, j_f) + \mathrm{H}$ on the DMBE potential energy surface when $j_f = 12$ to 15. The solid lines represent our h-TDWP results and the symbols represent the ABC results. The ◯ symbol labels the smaller j_f, and the □ symbol labels the larger j_f in each plot.

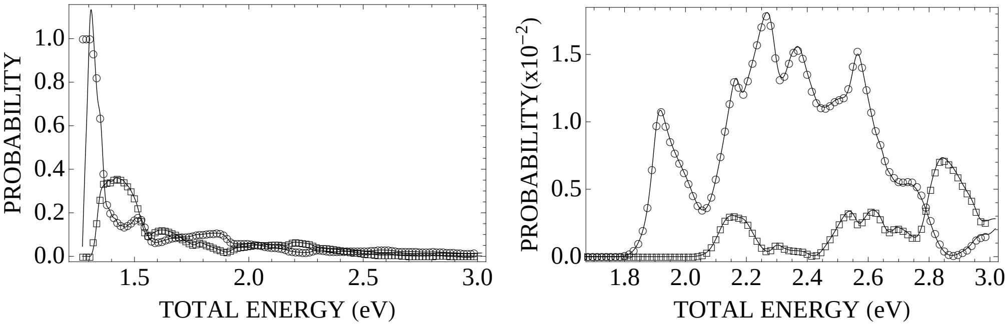

(a) $j_f = 0, 2$ (b) $j_f = 8, 10$

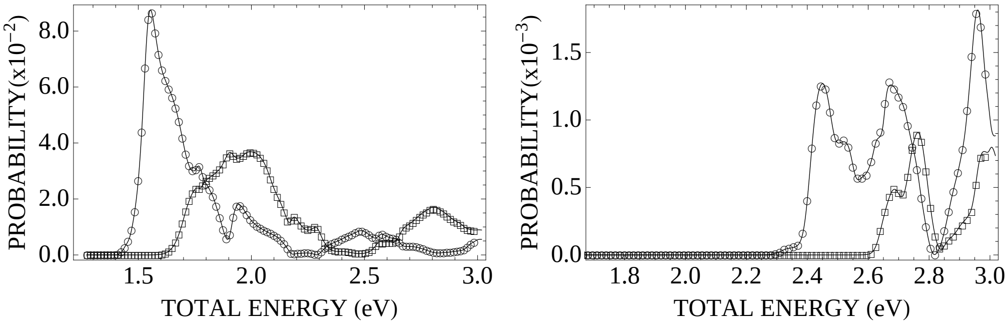

(c) $j_f = 4, 6$ (d) $j_f = 12, 14$

Figure 5.27: State-to-state non-reactive probabilities for $\mathrm{H} + \mathrm{H}_2(\nu_i = 2, j_i = 0) \rightarrow \mathrm{H} + \mathrm{H}_2(\nu_f = 2, j_f)$ on the DMBE potential energy surface when $j_f = 0$ to 14. The solid lines represent our h-TDWP results and the symbols represent the ABC results. The ◯ symbol labels the smaller j_f, and the □ symbol labels the larger j_f in each plot.

5.3 $F + H_2$

The $F + H_2$ system provides a test on a PES belonging to a different symmetry group, but is still similar enough to the $H + H_2$ system that there is no appreciable change to any calculation parameter. We employ the Stark-Werner potential energy surface [2] for this system. The $F + H_2$ PES belongs to the C_{2v} point group. Again, we deal with the $J = j_i = 0$ initial state, which only contains an A_1 component that requires 151 of the total 601 χ_i grid points. The total energy zero is set at the minimum of the HF well. The wave packet parameters provide a total energy region-of-interest from 1.63 to 2.58 eV.

Figs. 5.28 to 5.31 show the state-to-state reactive probabilities for the $H + H_2(\nu_i = j_i = 0) \rightarrow HF(\nu_f, j_f) + H$ reactions, with $\nu_f = 0$ to 3 and $j_f = 0$ to 10. As with the previous system, the figures show excellent agreement between the two methods. Note that the accuracy of the results is once again consistent across the full range of energies.

In comparing the $F + H_2$ parameters to those of $H + H_2$, convergence of the $F + H_2$ results requires more grid points. The increased number of ρ points, when compared to the $H + H_2$ results, is attributed to the higher kinetic energy attributed to the wave packet as it enters the HF arrangement channel. The increased number of θ and χ_i points is due to the number of open vibrational states in the HF channel. Since larger ν values have basis functions with more nodes, a denser grid is needed to accurately represent them in the final state matching.

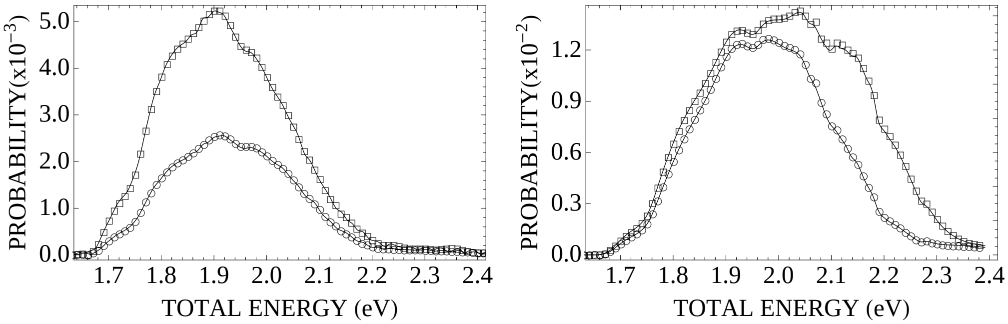

(a) $j_f = 0, 1$ (b) $j_f = 6, 7$

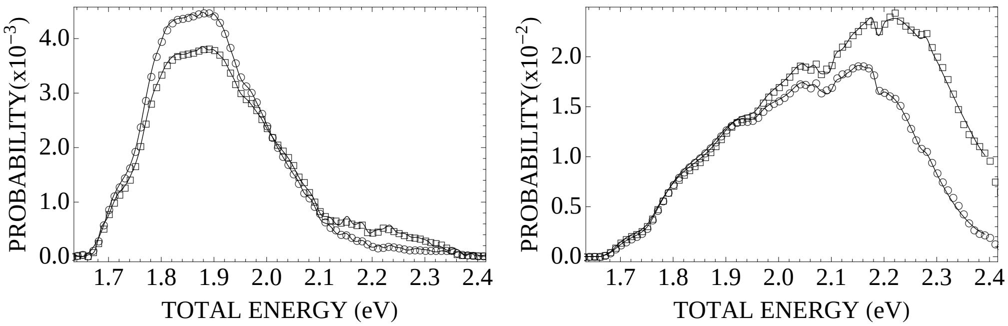

(c) $j_f = 2, 3$ (d) $j_f = 8, 9$

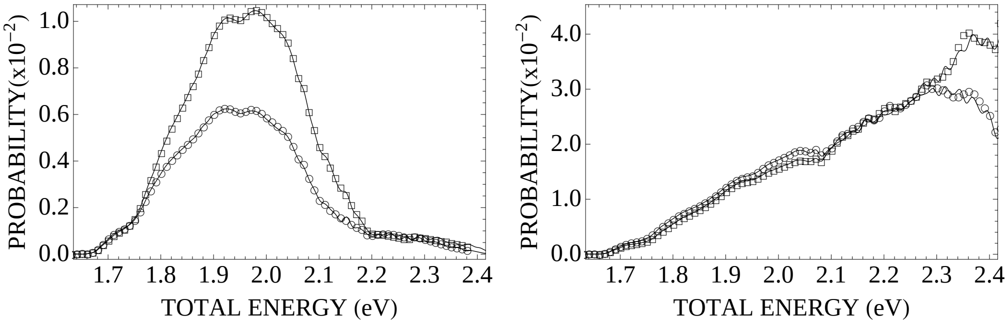

(e) $j_f = 4, 5$ (f) $j_f = 10, 11$

Figure 5.28: State-to-state reaction probabilities for $\mathrm{F} + \mathrm{H}_2(\nu_i = j_i = 0) \rightarrow \mathrm{HF}(\nu_f = 0, j_f) + \mathrm{H}$ on the Stark-Werner potential energy surface when $j_f = 0$ to 11. The solid lines represent our h-TDWP results and the symbols represent the ABC results. The ◯ symbol labels the smaller j_f, and the □ symbol labels the larger j_f in each plot.

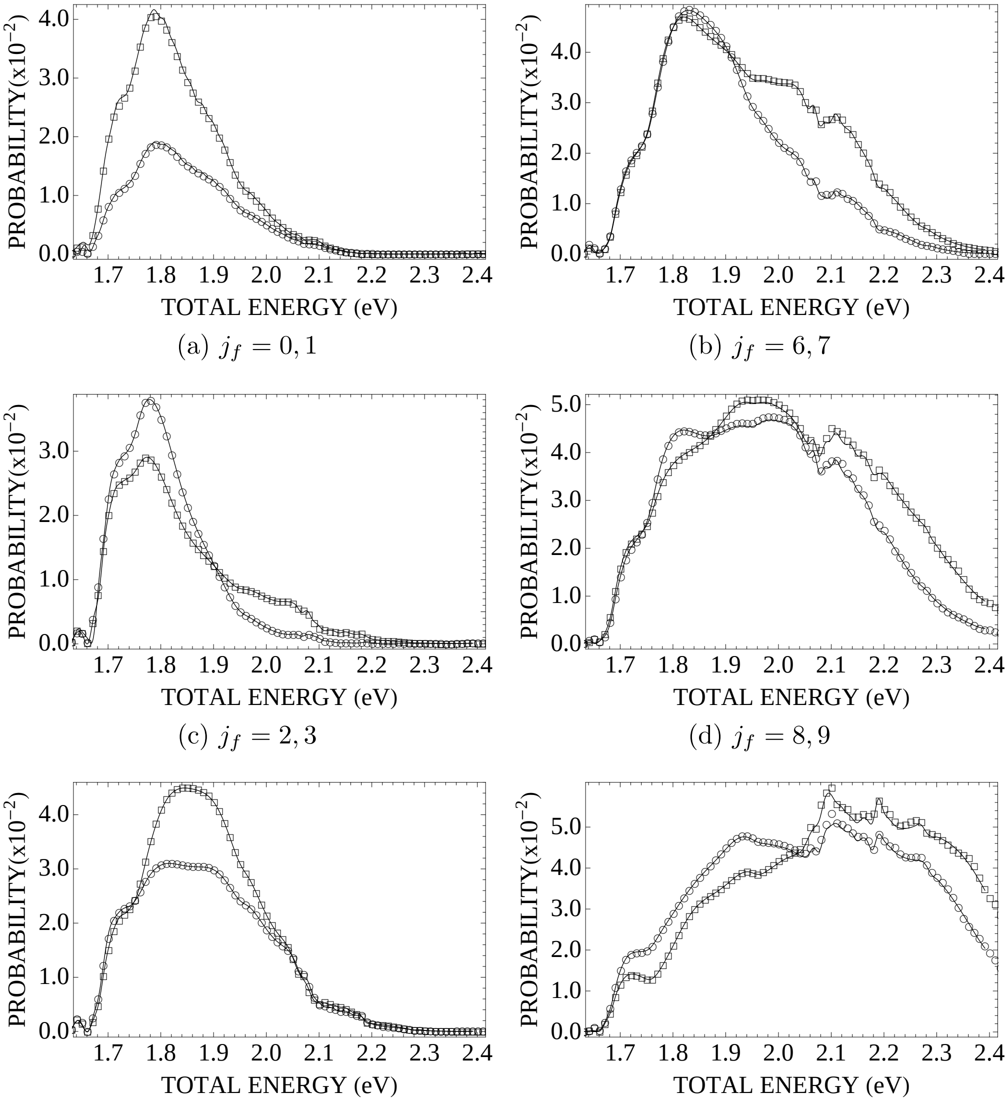

(a) $j_f = 0, 1$

(b) $j_f = 6, 7$

(c) $j_f = 2, 3$

(d) $j_f = 8, 9$

(e) $j_f = 4, 5$

(f) $j_f = 10, 11$

Figure 5.29: State-to-state reaction probabilities for $F + H_2(\nu_i = j_i = 0) \rightarrow HF(\nu_f = 1, j_f) + H$ on the Stark-Werner potential energy surface when $j_f = 0$ to 11. The solid lines represent our h-TDWP results and the symbols represent the ABC results. The ○ symbol labels the smaller j_f, and the □ symbol labels the larger j_f in each plot.

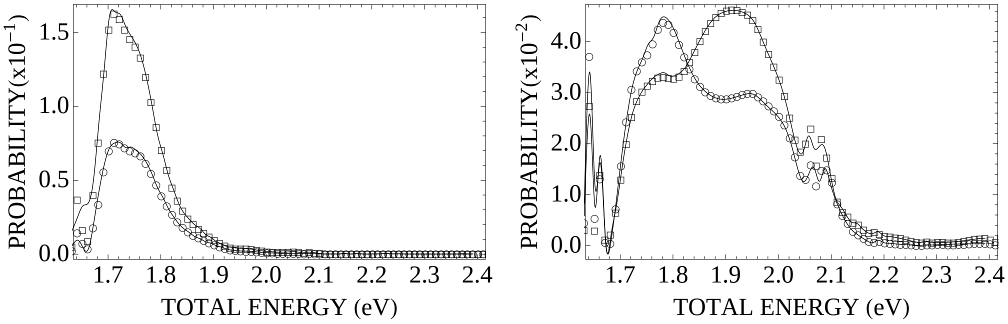

(a) $j_f = 0, 1$ (b) $j_f = 6, 7$

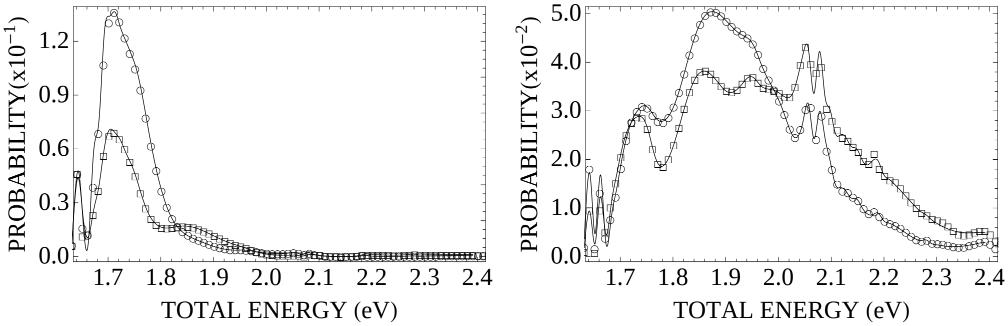

(c) $j_f = 2, 3$ (d) $j_f = 8, 9$

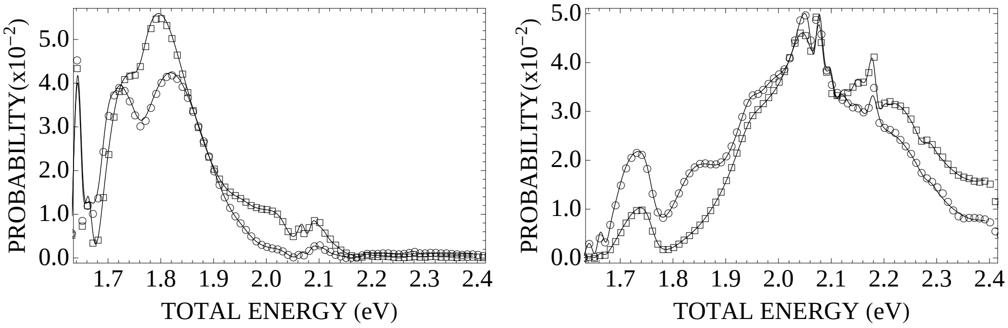

(e) $j_f = 4, 5$ (f) $j_f = 10, 11$

Figure 5.30: State-to-state reaction probabilities for $F + H_2(\nu_i = j_i = 0) \rightarrow HF(\nu_f = 2, j_f) + H$ on the Stark-Werner potential energy surface when $j_f = 0$ to 11. The solid lines represent our h-TDWP results and the symbols represent the ABC results. The ◯ symbol labels the smaller j_f, and the □ symbol labels the larger j_f in each plot.

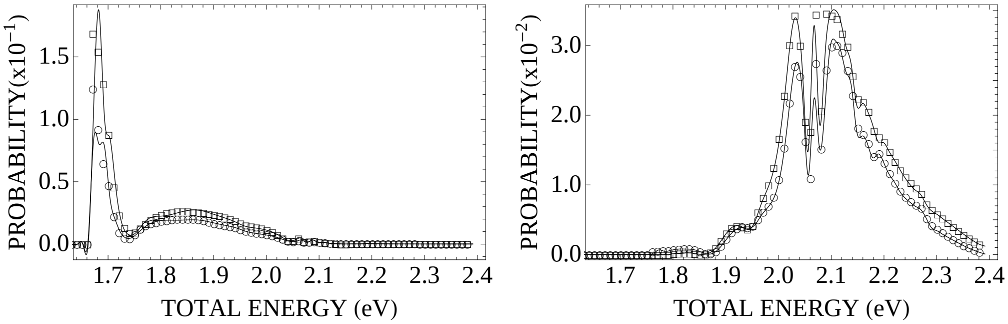

(a) $j_f = 0, 1$ (b) $j_f = 6, 7$

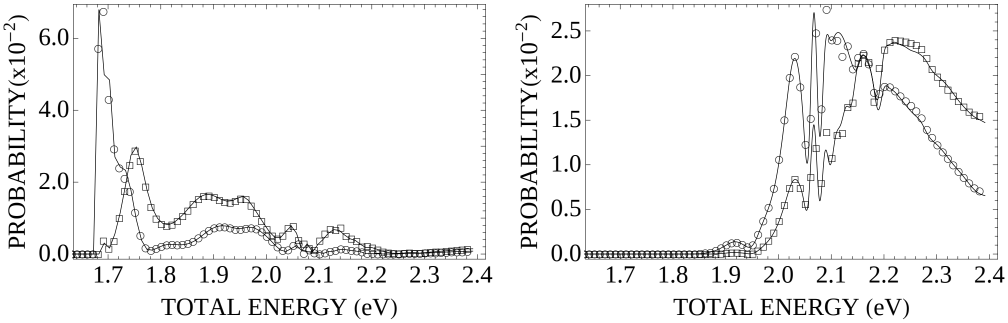

(c) $j_f = 2, 3$ (d) $j_f = 8, 9$

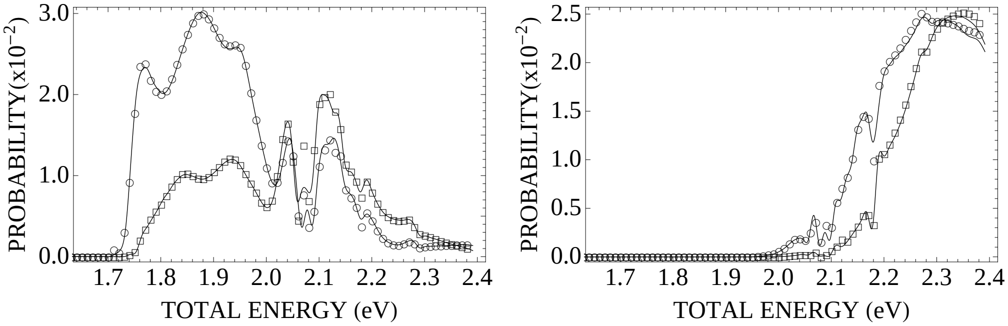

(e) $j_f = 4, 5$ (f) $j_f = 10, 11$

Figure 5.31: State-to-state reaction probabilities for $\mathrm{F} + \mathrm{H}_2(\nu_i = j_i = 0) \rightarrow \mathrm{HF}(\nu_f = 3, j_f) + \mathrm{H}$ on the Stark-Werner potential energy surface when $j_f = 0$ to 11. The solid lines represent our h-TDWP results and the symbols represent the ABC results. The ◯ symbol labels the smaller j_f, and the □ symbol labels the larger j_f in each plot.

CHAPTER 6

CONCLUSION

In this work, a new hyperspherical time-dependent wave packet method was introduced and implemented to produce accurate state-to-state reaction probabilities. Our results show excellent agreement with current benchmark time-independent results, and this agreement is consistent over a large range of energies. The ability of our method to obtain accurate results at higher energies sets our method apart from other hyperspherical TDWP methods [25]. Furthermore, a reviewer from *The Journal of Chemical Physics*, discussing a recently submitted paper that presents the theory and results presented in this dissertation, commented that, "Although hyperspherical wave packet calculations have been presented before, the present paper is leagues ahead in terms of the detail and clarity of the theory and the accuracy of the results."

In Chapter 2, a time-dependent, hyperspherical method for calculating state-to-state S-matrix elements is fully developed for all values of the total angular momentum J. The method is completely general and can treat elastic, rearrangement, and collision induced dissociation reactions. By propagating the wave packet in APH hyperspherical coordinates, all arrangement channels are represented equivalently, and we were able to obtain final state information for all possible products. The complementary relationship between APH and Jacobi coordinates provides simple asymptotic matching expressions for physically accurate boundary conditions. We increased the computational efficiency by taking advantage of the PES symmetry to reduce the region in coordinate space where we must represent the wave packet.

In Chapter 3, the computational details of the program were discussed.

The time propagation of the wave packet is the most computational expensive portion of the program. To decrease this cost, we introduced a method of reducing the eigenvalue range of the APH Hamiltonian by replacing the eigenvalues above an energy cut-off. The number of multiplications involved in applying the Hamiltonian were reduced by developing and implementing a new three-dimensional sylvester-like algorithm. The computational times and time scalings with respect to various input parameters were discussed.

In Chapter 4, the behavior and convergence of the results were discussed. The input values of the Gaussian, APH grid, and propagation time were varied to show how they affected the accuracy of the results. We presented simple methods to estimate the behavior and convergence of the results and showed that these estimates are reasonable.

Currently we are studying systems with nonzero total angular momentum, systems that exhibit collision-induced dissociation (or its time-reversal: three-body recombination), time-dependent Hamiltonians, inclusion of conical intersections, and systems in electromagnetic fields. We are planning to publish articles that discuss the new sylvester-like algorithm, collision induced-dissociation in $\mathrm{H}+\mathrm{H}_2$, a more detailed study of the $\mathrm{F}+\mathrm{H}_2$ resonances. Results for $\mathrm{Li}+\mathrm{Li}_2$, and hopefully other alkali systems, are also being considered in future work.

The program is still not fully optimized. Further optimization of the program can be facilitated through parallelization and use of more efficient numerical and computational procedures. Parallelization can be used where the Hamiltonian is applied to apply each operator simultaneously. Furthermore, for cases with $J > 0$, the propagation of each Λ component of the wave packet can be parallelized. To increase computational efficiency, we are looking into using non-uniform χ_i and time grids. The number of χ_i points required to represent the wave packet and the asymptotic states can be decreased by using a non-uniform grid that concentrates grid points in the well region of the PES. For the time grid, there is a window of time between when the wave packet has no initial overlap with ρ_∞ and when it returns to the asymptotic analysis region. If a less dense grid is used during this window, the smaller Δt results is smaller computational times.

Bibliography

[1] R. T. Pack and G. A. Parker, *J. Chem. Phys.* **87**, 3888 (1987), and references therein.

[2] K. Stark and H.-J. Werner, *J. Chem. Phys.* **104**, 6515 (1996).

[3] C. Chin, R. Grimm, P. Julienne, and E. Tiesinga, *Rev. Mod. Phys.* **82**, 1225 (2010).

[4] Y. Wang, J. P. D'Incao, and B. D. Esry, *Phys. Rev. A* **83**, 032703 (2011).

[5] C. Chin, T. Kraemer, M. Mark, J. Herbig, P. Waldburger, H.-C. Nagerl, and R. Grimm, *Phys. Rev. Lett.* **94**, 123201 (2005).

[6] C. A. Regal, M. Greiner, and D. S. Jin, *Phys. Rev. Lett.* **92**, 040403 (2004).

[7] B. D. Esry, C. H. Greene, and J. P. Burke, *Phys. Rev. Lett.* **83**, 1751 (1999).

[8] G. Roati, M. Zaccanti, C. D'Errico, J. Catani, M. Modugno, A. Simoni, M. Inguscio, and G. Modugno, *Phys. Rev. Lett.* **99**, 010403 (2007).

[9] A. J. Kuppermann and G. C. Schatz, *J. Chem. Phys.* **62**, 2502 (1975).

[10] G. C. Schatz and A. J. Kuppermann, *J. Chem. Phys.* **65**, 4642 (1976).

[11] G. C. Schatz and A. J. Kuppermann, *J. Chem. Phys.* **65**, 4668 (1976).

[12] A. B. Elkowitz and R. E. Wyatt, *J. Chem. Phys.* **62**, 2504 (1975).

[13] A. B. Elkowitz and R. E. Wyatt, *J. Chem. Phys.* **63**, 702 (1975).

[14] V. Aquilanti, S. Cavalli, and D. J. D. Fazio, *J. Chem. Phys.* **109**, 3792 (1998).

[15] D. Skouteris, J. F. Castilo, and D. E. Manolopoulos, *Comp. Phys. Comm.* **133**, 128 (2000).

[16] P. Honvault and J. M. Launay, *J. Chem. Phys.* **109**, 3792 (2001).

[17] R. S. Judson, D. J. Kouri, D. Neuhauser, and M. Baer, *Phys. Rev. A* **42**, 351 (1991).

[18] S. C. ALTHORPE, *J. Chem. Phys.* **114**, 1601 (2001).

[19] S. Y. LIN and H. GUO, *Phys. Rev. A* **74**, 022703 (2006).

[20] S. GÓMEZ-CARRASCO and O. RONCERO, *J. Chem. Phys.* **125**, 054102 (2006).

[21] M. HANKEL, S. C. SMITH, R. J. ALLEN, S. K. GRAY, and G. G. J. BALINT-KURTI, *J. Chem. Phys.* **125**, 164303 (2006).

[22] Z. SUN, X. LIN, S.-Y. LEE, and D. H. ZHANG, *J. Phys. Chem. A* **113**, 4145 (2009).

[23] G. D. BILLING and N. MARKOVIC, *J. Chem. Phys.* **99**, 2674 (1993).

[24] N. MARKOVIC and G. D. BILLING, *J. Chem. Phys.* **100**, 1085 (1994).

[25] S. ADHIKARI and A. J. C. VARANDAS, The coupled 3D wave packet approach for triatomic reactive scattering in hyperspherical coordinates, Comp. Phys. Comm. (unpublished), 2012.

[26] L. M. DELVES, *Nucl. Phys.* **9**, 391 (1959).

[27] L. M. DELVES, *Nucl. Phys.* **20**, 275 (1960).

[28] F. T. SMITH, *Phys. Rev.* **120**, 1058 (1959).

[29] F. D. COLAVECCHIA, F. MRUGALA, G. A. PARKER, and R. T. PACK, *J. Chem. Phys.* **118**, 10387 (2003), and references therein.

[30] N. BALAKRISHNAN, C. KALYANARAMAN, and N. SATHYAMURTHY, *Phys. Rep.* **280**, 79 (1997).

[31] F. A. COTTON, *Chemical Applications of Group Theory*, Wiley, New York, 3 edition, 1990.

[32] D. K. HOFFMAN, N. NAYAR, O. A. SHARAFEDDIN, and D. J. KOURI, *J. Phys. Chem.* **95**, 8299 (1991).

[33] D. K. HOFFMAN and D. J. KOURI, *J. Phys. Chem.* **96**, 1197 (1992).

[34] D. J. KOURI, W. ZU, X. MA, B. M. PETTITT, and D. K. HOFFMAN, *J. Phys. Chem.* **96**, 9622 (1992).

[35] D. J. KOURI and D. K. HOFFMAN, *J. Phys. Chem.* **96**, 9631 (1992).

[36] D. K. HOFFMAN, M. ARNOLD, and D. J. KOURI, *J. Phys. Chem.* **96**, 6539 (1992).

[37] D. K. Hoffman, T. L. M. II, M. Arnold, Y. Huang, W. Zu, and D. J. Kouri, *J. Math. Chem.* **20**, 117 (1996).

[38] M. E. Rose, *Elementary Theory of Angular Momentum*, Wiley, New York, 1957.

[39] M. Abramovitz and I. A. Stegun, editors, *Handbook of Mathematical Functions*, Dover, New York, 1968.

[40] Note that we have used Ω here for the BF_τ z-component of J instead of Λ_τ used in Ref. [1].

[41] The D used in this paper are equal to the $D^\dagger$ of Ref. [38].

[42] Note that we have used κ here to rather than t used in Ref. [1].

[43] J. V. Lill, G. A. Parker, and J. C. Light, *Chem. Phys. Lett.* **89**, 483 (1982).

[44] J. C. Light, I. P. Hamilton, and J. V. Lill, *J. Chem. Phys.* **82**, 1400 (1985).

[45] S. S. Iyengar, G. A. Parker, D. J. Kouri, and D. K. Hoffman, *J. Chem. Phys.* **110**, 10283 (1999).

[46] K. Zhang, G. A. Parker, D. J. Kouri, D. K. Hoffman, and S. S. Iyengar, *J. Chem. Phys.* **118**, 569 (2003).

[47] H. Tal-Ezer and R. Kosloff, *J. Chem. Phys.* **81**, 3967 (1984).

[48] R. T. Pack and J. O. Hirschfelder, *J. Chem. Phys.* **49**, 4009 (1968).

[49] R. T. Pack and J. O. Hirschfelder, *J. Chem. Phys.* **52**, 521 (1970).

[50] M. Hankel, S. C. Smith, S. K. Gray, and G. G. J. Balint-Kurti, *Comput. Phys. Commun.* **179**, 569 (2008).

[51] F. Gögtas, G. G. Balint-Kurti, and A. R. Offer, *J. Chem. Phys.* **104**, 7927 (1996).

[52] $\Phi^{Jp}_{\kappa\Lambda}(\theta,\chi_i;\rho_\xi)$ is a real function, so $\left[\Phi^{Jp}_{\kappa\Lambda}(\theta,\chi_i;\rho_\xi)\right]^* = \Phi^{Jp}_{\kappa\Lambda}(\theta,\chi_i;\rho_\xi)$.

[53] D. Neuhauser and M. Baer, *J. Chem. Phys.* **90**, 4351 (1989).

[54] A. Vibok and G. G. Balint-Kurti, *J. Phys. Chem.* **96**, 8712 (1992).

[55] J. Z. H. Zhang, *Theory and Application of Quantum Molecular Dynamics*, World Scientific, Singapore, 1999.

[56] G. G. Balint-Kurti, R. N. Dixon, and C. C. Marston, *J. Comp. Phys.* **94**, 59 (1991).

[57] K. M. Abadir and J. R. Magnus, *Matrix Algebra*, Cambridge University Press, New York, 2005.

[58] Z. Bacic, J. D. Kress, G. A. Parker, and R. T. Pack, *JCP* **92**, 2344 (1990).

[59] F. J. Aoiz, L. Bañares, and V. J. Herrero, *Int. Rev. Phys. Chem.* **24**, 119 (2005).

[60] A. J. C. Varandas, F. B. Brown, C. A. Mead, D. G. Truhlar, and N. C. Blais, *J. Chem. Phys.* **86**, 6258 (1987).